Design and Development of New Ligands for Imaging P2Y12

A thesis submitted in fulfilment of the

requirements for admission to the degree of

Doctor of Philosophy

by

Ben Biao Ma

School of Chemistry

Faculty of Science

The University of Sydney

December 2024

Declaration

I, Ben Ma, declare that this thesis is entirely my work, contributions from all individuals and published material were acknowledged to the best of my abilities.

This thesis is a summary of the research that I have undertaken in the School of Chemistry, University of Sydney, under the supervision of Dr. Jonathan Danon and Prof. Michael Kassiou between February 2021 and December 2024. This thesis contains less than 80,000 words.

The use of "we" and "our" refers to myself.

Ben Ma

Dr. Jonathan Danon

December 2024

Authorship attribution statement

Portions of the original research presented in this thesis have been published in a peer-reviewed scientific journal, namely:

Ma, B. B.; Montgomery, A. P.; Chen, B.; Kassiou, M.; Danon, J. J. Strategies for targeting the P2Y12 receptor in the central nervous system. *Bioorg. Med. Chem. Lett.* **2022**, *71*, 128837.

Portions of the published work were presented on: Pages 14-18 of **Section 1.4**, pages 23-27 of **Section 2.2**, pages 46-52 of **Section 3.1** and pages 114-116 of **Section 5.2**. I was the main author of the published work, but **Table 5** of page 47 was originally produced by Jonathan Danon.

Ben Ma

As supervisor for the candidature upon which this thesis is based, I can confirm that the authorship attribution statements above are correct.

Dr. Jonathan Danon

December 2024

Acknowledgements

First and foremost, I express gratitude to my supervisor, Dr. Jonathan Danon, for providing me with the opportunity to partake in cutting-edge research under the Danon Group throughout my PhD candidature. I could not have succeeded without your unwavering guidance and support. Thank you for making time throughout the day to proofread my thesis. You have gone above and beyond in your encouragement, and words cannot adequately convey how much it means to me. This entire journey has broadened my perspective, and I recognise that I still have much to learn as a researcher. I am committed to honing my research skills, particularly in effective scientific communication.

I extend my gratitude to Prof. Michael Kassiou for his supervision and the environment that encouraged learning and growth during my time in the Kassiou group. I would like to thank current and former post-doctoral researchers Dr. Andrew Montgomery, Dr. Wendy Tran, Dr. Timothy Callis, Dr. Jakob Lane, and Dr. Tristan Reekie who have given their time to chat during work hours. Your countless feedback, wisdom and guidance will continue to impact the way I work.

I am also appreciative of the Danon and Kassiou group members for their support during my PhD candidature. The banter was fantastic and those fond memories will be remembered. I wish you all the best in your future endeavours, and may be one day we might meet again in the field.

I would like to acknowledge the Australian Government for the Research Training Program Fee Offset, allowing me to partake in this research.

To my parents, I am grateful for your unwavering support and push for me to undertake a PhD degree. Your belief in me has been a driving force, and I am grateful for the sacrifices you made to see me succeed. Now that this chapter is complete, I hope you can relax and focus on your own journeys. I am confident in the knowledge and skills I have gained to face any challenges ahead.

To Tracy, it is unfortunate that we are unable to stay together right until my thesis submission. However, I appreciate the steadfast support and for helping me

maintain my sanity during the most challenging times. You have played a significant role in my growth, and I will strive in the years ahead to find myself and live life on my own terms.

Finally, I would like to thank my friends and family who showed interest in my work and supported me throughout my studies. Special thanks go to Bill Chan for leaving me in a permanent state of car liquidity crisis, Biling for her generosity both in and out of the lab as a trusted friend, and Kris for preaching the gospel of palladium cross-coupling with unwavering passion. As I move on to the next stage of life, I feel ready to face new challenges, armed with the skills and friends that I have gained along the way.

Abstract

Tackling neurodegenerative diseases represent a critical challenge in modern medicine, with conditions like multiple sclerosis, Alzheimer's, Huntington's, and Parkinson's disease presenting complex pathologies and overlapping symptom profiles. Despite over a century of research into these disorders, therapeutic interventions remain predominantly limited to symptom management rather than disease-modifying strategies, underscoring the urgent need for innovative diagnostic and treatment approaches.

Chronic neuroinflammation has been identified as a fundamental pathological mechanism common to all these neurological disorders, contributing to death of brain tissue. Microglia, the central nervous system's primary immune cells, regulate inflammatory responses through complex pro- and anti-inflammatory mechanisms. The P2Y12 protein has been identified as a potential biomarker for monitoring the anti-inflammatory response, offering a promising avenue to developing a deeper understanding of microglial function during neurodegeneration.

Positron Emission Tomography (PET) is a powerful molecular imaging technique that provides insight to biological processes *in vivo* by use of a biomarker-specific radiotracer. Previous attempts to develop P2Y12 PET tracers have repurposed ligands from anti-thrombotic drug discovery campaigns, labelling them with short-lived positron-emitting carbon-11 radionuclides. However, their physicochemical properties were unsuitable for central nervous system (CNS) penetration, effectively halting further pre-clinical or clinical development.

The research in this thesis aims to address these challenges through a comprehensive methodological approach. It first leveraged computer-aided drug design (CADD) to predict optimal binding interactions and physicochemical properties of various known and novel P2Y12 ligands. By rationally modifying literature P2Y12 ligands, our research aimed to enhance CNS penetration and develop a viable tracer. A complementary focus involved the design and synthesis of P2Y12 fluorescent probes for the development of a competitive NanoBRET binding assay, enabling critical

biological evaluation of potential PET tracer candidate molecules.

By systematically addressing the technical barriers in tracer development, this study aimed to support the development of CNS-penetrating P2Y12 PET tracers. A successful tracer could enable more precise elucidation of the anti-inflammatory response *in vivo*, potentially facilitating development of advanced diagnostics, and more targeted therapeutic interventions for neurodegenerative disorders.

Contents

Abbreviations

^{11}C	carbon-11
^{18}F	fluorine-18
2MeS-ADP	2-methylthio-adenosine-5′-diphosphate
^{3}H	tritium
^{33}P	phosphorus-33
Å	angstrom
°C	degrees Celsius
γ	gamma
δ	chemical shift in parts per million downfield
π	pi
Aβ	amyloid beta
AD	Alzheimer's disease
ADP	adenosine diphosphate
AgOAc	silver acetate
APCI	atmospheric pressure chemical ionisation
aq.	aqueous
Arg	arginine
Asn	asparagine
ATP	adenosine triphosphate
Br_2	bromine

BBB	blood brain barrier
Boc-Gly-OH	Boc-glycine
BODIPY	dipyrromethene boron difluoride
BRET	bioluminescence resonance energy transfer
CADD	computer-aided drug design
cat.	catalytic
CD11b	cluster of differentiation molecule 11B
CD45	cluster of differentiation 45
CDI	1,1′-carbonyldiimidazole
ClogD	calculated logD
ClogP	calculated logP
cm^{-1}	wavenumber(s)
CNS	central nervous system
CNS MPO	CNS multiparameter optimisation
CNS PET MPO	CNS PET multiparameter optimisation
$(COCl)_2$	oxalyl chloride
conc.	concentrated
Cy_2NMe	*N*,*N*-docyclohexylmethylamine
CYP	cytochromes P450
CYP2C19	cytochrome P450 2C19
d	doublet

DBU	1,8-diazabicyclo[5.4.0]undec-7-ene
DCE	1,2-dichloroethane
DCM	dichloromethane
DIC	diisopropyl carbodiimide
DMA	*N*,*N*-dimethylacetamide
DMAP	4-dimethylaminopyridine
DME	dimethoxyethane
DMF	*N*,*N*-dimethylformamide
DMF-DMA	*N*,*N*-dimethylformamide dimethyl acetal
DMSO	dimethylsulfoxide
DNP	dinitrophenyl hydrazine
EDC	*N*-(3-Dimethylaminopropyl)-*N*′-ethylcarbodiimide hydrochloride
eq.	equivalent(s)
Et_2O	diethyl ether
Et_3N	triethylamine
EtOAc	ethyl acetate
EtOH	ethanol
ESI	electronspray ionisation
FDG	fluorodeoxyglucose
FRET	Förster resonance energy transfer
g	gram(s)

GCMS	gas chromatography and electron ionisation mass spectrometry
Glu	glutamine
Gly	glycine
GPCR	G protein-coupled receptors
h	hour(s)
H	hydrogen(s)
H_2O	de-ionised water
HA	hydrogen atom(s)
HATU	hexafluorophosphate azabenzotriazole tetramethyl uronium
HBF_4	tetrafluoroboric acid
HCl	hydrochloric acid
HD	Huntington's disease
hERG	human ether-à-go-go-Related Gene
HMBC	heteronuclear multiple-bond coherence
HOBt	hydroxybenzotriazole
HPLC	high-performance liquid chromatography
HRMS	high-resolution mass spectrometry
HSQC	heteronuclear single quantum coherence
HTS	high-throughput screening
*i*PrMgCl·LiCl	isopropylmagnesium chloride lithium chloride
iPr_2NEt	*N*,*N*-diisopropylethylamine

IC_{50}	half maximal inhibitory concentration
IL-1β	interleukin-1β
IL-4	interleukin-4
IL-6	interleukin-6
IL-10	interleukin-10
IR	infrared
K_2CO_3	potassium carbonate
K_d	dissociation constant
KF	potassium fluoride
K_i	inhibitory constant
L	litre(s)
LiOH	lithium hydroxide
LRMS	low-resolution mass spectrometry
Lys	lysine
m/z	mass-to-charge ratio
m	multiplet; milli
M	molar
M^+ & M^-	parent molecular ion
MALDI	matrix-assisted laser desorption/ionisation
MeCN	acetonitrile
MeOH	methanol

mg	milligram
MHz	megahertz
min	minute(s)
mL	millilitre(s)
mol	mole(s)
mp	melting point
MRI	magnetic resonance imaging
MS	multiple sclerosis
MTBE	Methyl tert-butyl ether
MW	molecular weight
N_2	nitrogen
N/A	not available
n-BuLi	*n*-butyllithium
NaOEt	sodium ethoxide
NaOH	sodium hydroxide
NBS	*N*-bromosuccinimide
NHS	*N*-hydroxysuccinimide
NLuc	nanoluciferase
nm	nanometre(s)
nM	nanomolar(s)
NMR	nuclear magnetic resonance

NOESY	nuclear overhauser effect spectroscopy
NR	no reaction
o/n	overnight
P-gp	P-glycoprotein
P2X7	purinergic receptor P2X7
P2Y12	purinergic receptor P2Y12
PD	Parkinson's disease
$Pd(OAc)_2$	palladium(II) acetate
$Pd(PPh_3)_4$	tetrakis(triphenylphosphine)palladium(0)
$PdCl_2$(dbpf)	[1,1′-Bis(diphenylphosphino)ferrocene]palladium(II) dichloride
PEG	polyethylene glycol
PET	positron emission tomography
Phe	phenylalanine
pK_a	acid dissociation constant
pK_b	base dissociation constant
$POCl_3$	phosphoryl chloride
ppm	parts per million
Py-1	pyrylium-1
q	quartet
qPCR	quantitative polymerase chain reaction
quant.	quantitative

quint	quintet
RMSD	root mean square deviation
ROS	reactive oxygen species
rt	room temperature
t_R	retention time
s	singlet
S.M.	starting material
SAR	structure activity relationship
SBDD	structure-based drug design
S_N2	bimolecular nucleophilic substitution
S_NAr	nucleophilic aromatic substitution
SPECT	single photon emission computed tomography
SPR	surface plasmon resonance
SUV	standard uptake value
t	triplet
t-AmylOH	*tert*-amyl alcohol
t-BuOH	*tert*-butanol
TAMRA	5-carboxytetramethylrhodamine
TBA	tertrabuylammonium
TBA(HSO_4)	tetrabutylammonium hydrogensulfate
TBACl	tetrabutylammonium chloride

TBAF	tetrabutylammonium fluoride
Tf_2O	triflic anhydride
TFA	trifluoroacetic acid
Thr	threonine
TPSA	topological polar surface area
Troc	2,2,2-trichloroethyl
Troc-Cl	2,2,2-trichloroethyl chloroformate
TSPO	translocator protein 18 kDa
Tyr	tyrosine
THF	tetrahydrofuran
TLC	thin-layer chromatography
TMS	trimethylsilyl or trimethylsilane
TMSCl	trimethylsilyl chloride
TNF-α	tumor necrosis factor
Ts-Cl	tosyl chloride
UV	ultraviolet
UV-Vis	ultraviolet-visible
v/v	volume for volume
w/v	weight for volume
water	de-ionised water
WT	wild-type

XP	extra precision

Chapter 1

Introduction

1.1 Neurodegenerative diseases and inflammation

1.1.1 Neurodegenerative diseases

Neurodegeneration is characterised by the progressive deterioration of brain function and structure, resulting in the gradual decline of mental and physical condition.[1] The earliest literature on neurodegenerative disease dates back to 1817, authored by James Parkinson.[2] At the time of publication, the disease was referred to as 'shaking palsy', but it is now known as Parkinson's disease (PD). It is characterised by involuntary shaking regardless whether the patient is moving or at rest.[2] At that time, understanding of neuroscience was in its infancy, and diagnostic methods were primarily limited to broad characterisation of symptoms.[2] Scientifically backed research necessary for providing effective treatments to PD patients, let alone finding a cure, was beyond the understanding of researchers at the time. Since the identification of PD, other neurodegenerative conditions such as multiple sclerosis (MS), Huntington's disease (HD) and Alzheimer's disease (AD) have also been recognised, each with their own symptomatic profiles and pathological hallmarks.

Current therapeutic strategies for neurodegenerative diseases are either disease-modifying or symptom management treatments. Disease-modifying treatments aim to intervene in the underlying disease pathology to slow its progression,[3] whereas symptomatic treatments temporarily alleviate the clinical symptoms. However, no drugs have been developed yet that can cure neurodegenerative diseases or reverse the damage caused by degeneration.[4–8] Early intervention is essential for disease-modifying treatments to improve long-term patient outcomes. For instance, the symptomatic onset of AD can occur decades after the initial cerebral amyloid beta (Aβ) aggregation, with pathological changes preceding the clinical symptoms (**Figure 1**).[9] Developing sensitive diagnostic tools capable of detecting early biochemical changes in neurodegenerative diseases could facilitate earlier therapeutic interventions and improve long-term patient outcomes.[10,11] Alternatively, these tools could aid in clinical evaluation for developing more effective treatments.[12]

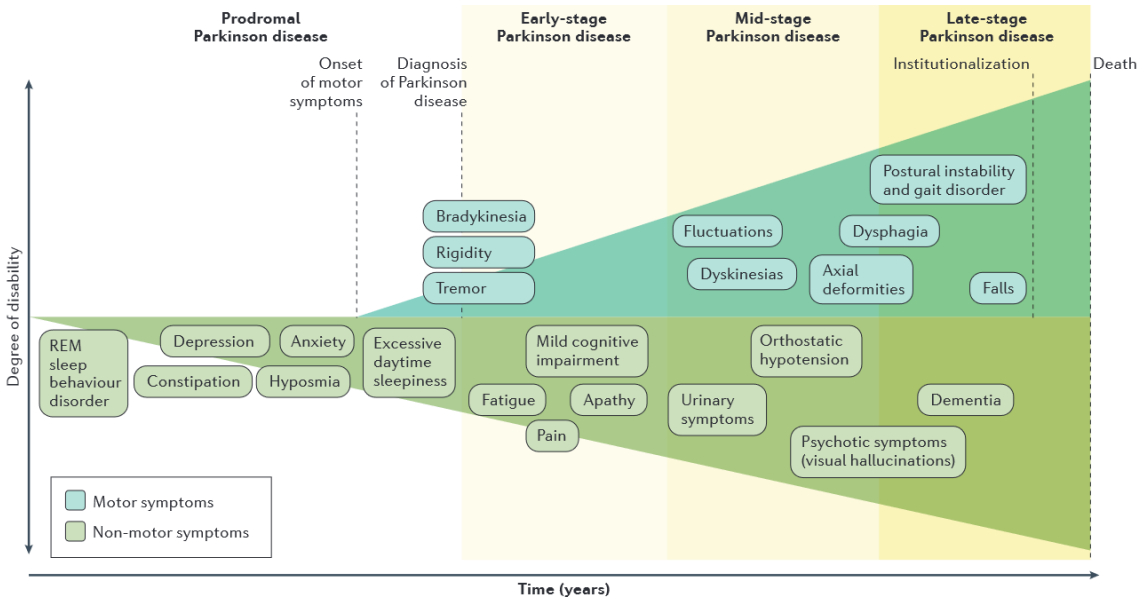

Figure 1: Onset of both motor and non-motor symptoms throughout PD progression with severity.[11]

Capitalising on early biomarkers is as crucial as developing treatments for neurodegenerative diseases. Modern imaging techniques that assist in patient diagnosis include positron emission tomography (PET) imaging, single photon emission computed tomography (SPECT) and magnetic resonance imaging (MRI).[11,13,14] While MRI is effective at aiding diagnosis of neurodegenerative diseases, it typically identifies them in the progressive stages through anatomical changes.[15] PET imaging often uses [^{18}F]fluorodeoxyglucose ([^{18}F]FDG) to monitor biochemical changes resulting from increased metabolic activity, but neither technique can diagnose a specific neurodegenerative condition alone.[16] SPECT has found success in aiding diagnosis of PD but lacks resolution.[17] Genetic sequencing is used to diagnose HD, but ethical concerns have limited its widespread adoption.[10] Novel diagnostic techniques that employ fluorescent probes and genetic sequencing for other neurodegenerative diseases have yet to be proven robust for clinical applications.[13,18]

A comprehensive diagnostic toolbox is needed to target molecular biomarkers of neurodegenerative diseases for differential diagnosis.[10,19] Establishing a correlation between biomarkers and disease states is critical. Chronic inflammation is a prominent pathological hallmark of all neurodegenerative diseases, and its dysregulation

contributes towards neuronal death.[20,21] Imaging inflammation via PET has the potential to be extremely useful to understand underlying causes of disease, as a diagnostic tool, but current gaps in understanding chronic neuroinflammatory responses remain.[10,19,22,23]

1.1.2 Neuroinflammation

Neuroinflammation is a complex and essential process for maintaining homeostasis in the central nervous system (CNS).[24] Typically, an exogenous or endogenous insult will trigger a neuroinflammatory response.[25] Cells such as microglia and astrocytes are immediately recruited to mediate the repair process by secreting cytokines, chemokines, secondary messengers and reactive oxygen species (ROS).[26,27] Historically, neuroinflammation was characterised as two distinct phases: the pro-inflammatory response, which is neurotoxic and contains neural insults, and the anti-inflammatory response, which is neuroprotective.[21] However, it is now understood that these responses exist on a heterogenous spectrum, coexisting in a delicate balance.[28]

ROS such as hydroxyl radicals, superoxide anions and peroxides are generated as a part of the pro-inflammatory response mechanism. Lipid oxidation inhibits glucose transporter type-3 signalling and activates mitogen-activated kinases that leads to apoptosis.[29] Direct ROS reactions can occur with proteins, inhibiting receptors and enzymatic functions.[29] DNA mutations caused by ROS have contributed to accelerated ageing, exacerbating the already poor regenerative capabilities of the CNS.[30,31] ROS induce downstream excitotoxic conditions by elevating the calcium levels, resulting in glutamate receptors activation and cell death.[29] ROS are promiscuous and can disrupt cellular functions.[29]

Cytokines are the primary messengers in modulating cellular behaviours, secreted by both microglia and astrocytes.[32] They alone do not cause damage but activate cells downstream to perform unique tasks in pro- and anti-inflammatory cascades. Occasionally, cytokines may open ion channels and create excitotoxic conditions leading to apoptosis.[33] In post-mortem PD cerebrospinal fluid and AD peripheral

blood samples, elevated levels of pro-inflammatory cytokines such as interleukin-1β (IL-1β), IL-6 and tumour necrosis factor (TNF-α) have been observed.[33] The self-perpetuating mechanism in neurodegenerative diseases will have persistent cytokine signalling.[32]

Repetitive inflammation inflicts substantial damage upon healthy cells through necroptosis[34] and dysregulated repair.[35] However, the anti-inflammatory response to quell the pro-inflammatory counterpart remains poorly understood. The anti-inflammatory response mainly regulates the pro-inflammatory response and minimises damage, allowing the limited regenerative capacity of neurotrophic factors to retain CNS functions.[36] IL-4 has been implicated in regulating ROS generation by the microglia via stimulating apoptosis,[37] while IL-10 has been shown to regulate the pro-inflammatory cytokine production.[38] Current *ex vivo* studies do not provide insight into the changes in the anti-inflammatory response that supposedly attenuate the chronic inflammatory response in neurodegenerative diseases. Post-mortem examinations have shown that microglial activation is largely responsible for the upregulation of various inflammatory mediators in neurodegenerative diseases, closely corresponding with neuroinflammation.[39,40]

The most widespread cells in the CNS are glial cells,[41] such as astrocytes, microglia and oligodendrocytes. These cells are highly adaptable, capable of responding to even the smallest changes in the local micro-environment to effectively combat CNS insults.[41] Communication and coordination among glial cells are indispensable for modulating the neuroinflammatory response.[41,42] In particular, intercellular communication between microglia and astrocytes form the cornerstone of neuroinflammation, but precise mechanisms and downstream effects remain poorly understood.[43,44] Among glial cells, microglia have garnered the most attention due to their versatility and active frontline role in regulating CNS functions.[45]

1.2 Microglia

Microglia are the most populous immune cell in the CNS,[46] often referred to as the macrophages of the CNS.[47] These cells originate from prenatal invasion of macrophages into the CNS, but have distinct characteristics that differentiate them from macrophages.[21,46] Monocytes, progenitor cells to macrophages, are also distinguishable from microglia based on their expression of cluster of differentiation (CD) markers, particularly CD45 and CD11b (higher expression levels in monocytes versus microglia).[46] Microglia survey the local micro-environment by following adenosine diphosphate (ADP) gradients towards sites of insult.[48] Beyond its surveillance function, microglia clear neural debris, mediate neuroinflammation, promote repair and perform many other functions as presented in **Figure 2**.[11,49]

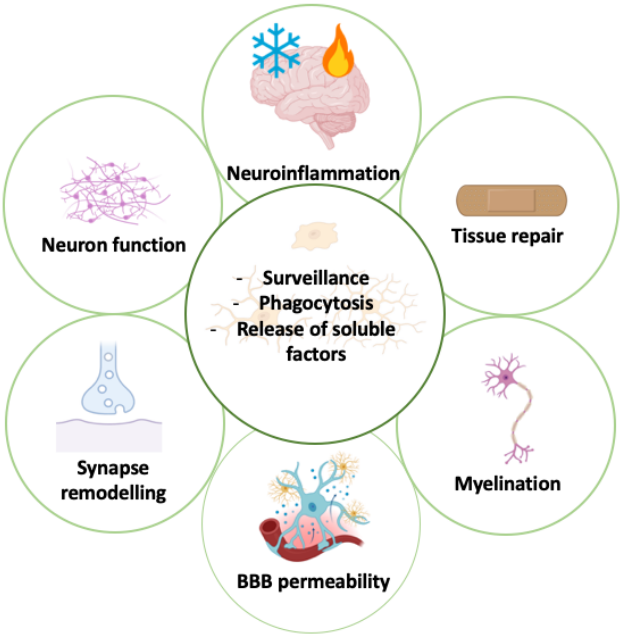

Figure 2: Phagocytosis, surveillance and release of soluble factors are the core microglial properties (inner ring) that promote various biological processes (outer rings).[49]

Microglial morphology is directly related to stimuli from the local micro-environment, resulting in distinct morphologies generally categorised as ramified, hyper-ramified, amoeboid and phagocytic.[48,49] However, the current consensus suggests that microglial morphology is much more dynamic and requires quantitative tools to

differentiate them precisely. Walker and coworkers have acknowledged the need for better tools to discriminate microglia based on their phenotypic state, as morphology alone provides limited information.[48]

Historically, microglia were thought to exist in two distinct phenotypic states: M1 pro-inflammatory and M2 anti-inflammatory. Each state was believed to have specific functional roles, with microglia exclusively secreting cytokines corresponding to their state. Recent consensus between Paolicelli and coworkers suggests that classifying microglia solely based on the M1/M2 paradigm is an oversimplification.[49] They reiterated the heterogenous model of microglial phenotypes in which both the pro- and anti-inflammatory responses can occur simultaneously, reflecting the dynamic nature of microglia as shown in **Figure 3**.[49]

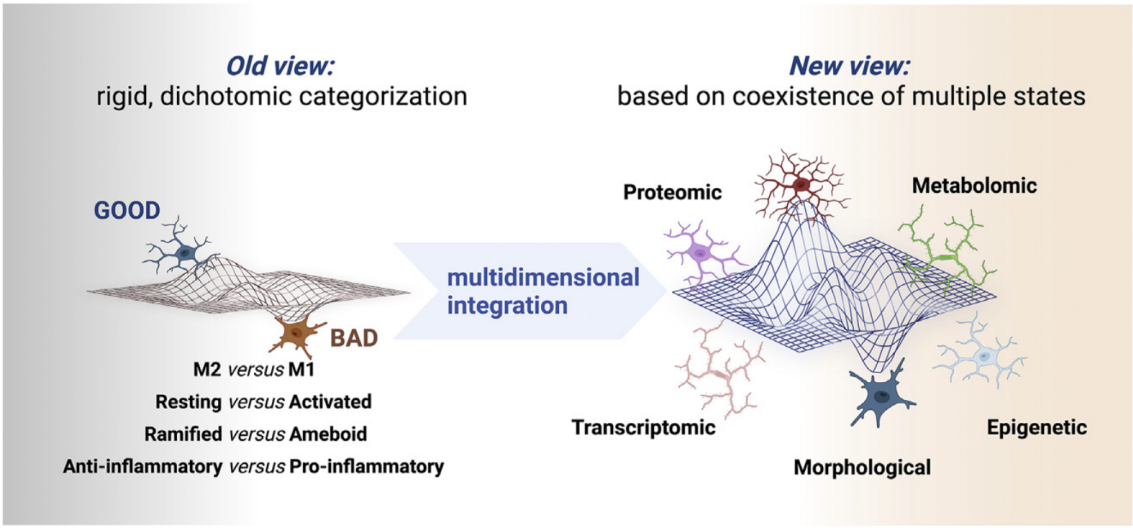

Figure 3: Classical perception encompassed clearly defined states of microglia (left), while the current model suggests a dynamic activation of microglia that closely adapts to the local micro-environment.[49]

Microglial states are also shaped by a combination of intrinsic and extrinsic factors, spatiotemporal context, and various additional layers of complexity. Intrinsic determinants include species, ontogeny, sex, and genetic background. The specific context in which the organism exists is also important, encompassing factors such as age, spatial location, and environmental influences such as nutrition, microbiota, pathogens, and drugs. These intrinsic and extrinsic factors collectively impact

microglia above levels, including epigenomic, transcriptomic, proteomic, metabolomic, and phenomic, ultimately determining their functions as shown in **Figure 4**.[49]

This complexity is not yet fully understood, particularly in the context of neurodegenerative diseases. Chronic activation of microglia has been implicated in conditions such as AD, PD, HD, and MS.[50–52] To elucidate the pathology of neurodegenerative disease, it is essential to monitor the phenotypic state of microglia throughout disease progression.[48,49] Developing molecular imaging tools to visualise these changes *in vivo*, such as radiotracers for use in PET imaging, is crucial for advancing our understanding of microglial roles in neurodegeneration and the development of more effective therapeutic strategies.[53]

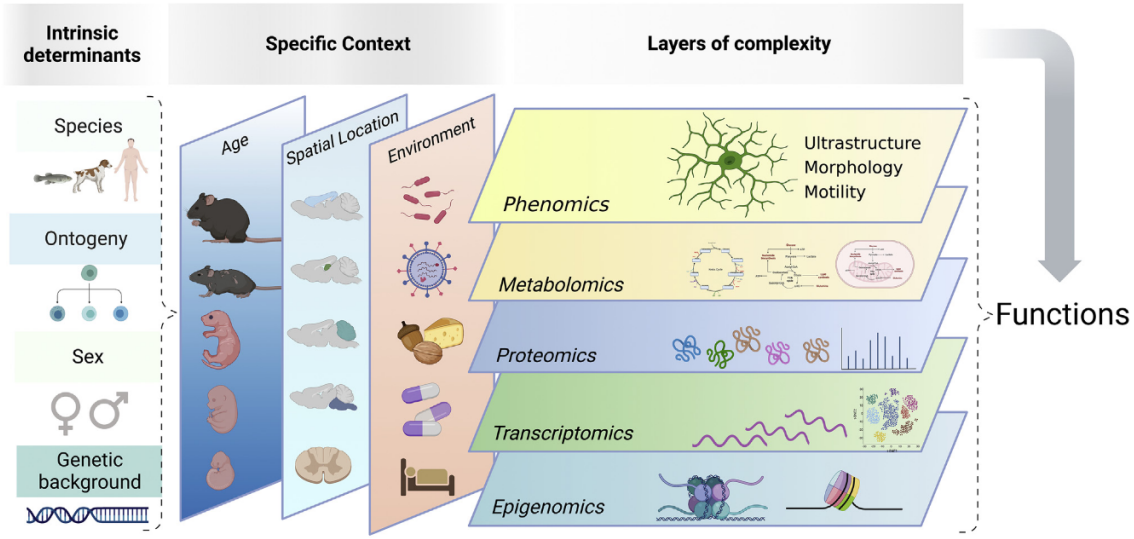

Figure 4: Summary of the effects of extrinsic and intrinsic determinants on the overall microglial state.[49]

1.2.1 PET imaging

PET is a powerful non-invasive molecular imaging technique for measuring receptor expression *in vivo* through the use of a targeted radiolabelled ligand. A patient is injected with a sub-therapeutic dose to ensure no functional response is elicited,[54] allowing occupancy of the receptor of interest by the tracer to reflect its innate intrinsic response. The radionuclide emits positrons, colliding with electrons

typically within 0.5 mm,[54] generating two 511 keV γ-rays that travel in opposite directions perpendicular to the collision pathway in an event called annihilation.[55] These γ-rays are captured by a sensor encircling the patient, and the detected signal is traced back to the source of the annihilation event (**Figure 5**).[54] A three-dimensional image of tracer distribution can be generated using the detected γ-radiation signals. SPECT uses a γ-ray emitting radionuclide that can be tracked similarly to PET imaging but at the cost of resolution.[14]

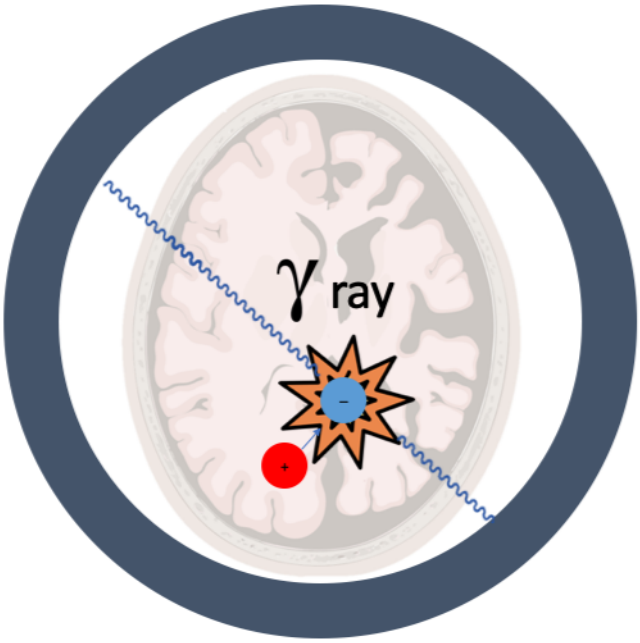

Figure 5: For CNS imaging purposes, typically either a carbon-11 or fluorine-18 labelled radiotracer emits positrons, colliding with electrons and emitting two 511 keV γ-rays perpendicular from the trajectory pathway.

PET tracers are typically small organic molecules, making carbon-11 (^{11}C) a frequently used radionuclide. Carbonyls or methyl groups in tracers can be replaced with carbon-11 via intermediates such [^{11}C]carbon dioxide, [^{11}C]carbon monoxide, or [^{11}C]methyl iodide.[56] However, the short half-life of carbon-11 (20.39 minutes) requires on-site synthesis due to rapid decay, subsequently requiring a cyclotron to be on premises to generate the necessary radiosynthons.[57] An alternative radionuclide is fluorine-18 (^{18}F), which has a radioactive half-life (109.8 minutes) five times longer

than carbon-11, allowing easier manufacture and distribution of the radiotracer.[56] The extended half-life of fluorine-18 also allows for prolonged scanning times, increasing the diagnostic versatility.[58] The advantages of fluorine-18 make it a practical choice for PET tracers whenever feasible.[56,57]

Clinically, PET scans are often performed at a specific time point and within a limited tissue area, commonly assessed using standardised uptake value (SUV) imaging. This method estimates receptor expression but provides limited insights into the kinetics of the radiotracer.[59,60] Dynamic imaging overcomes this limitation by monitoring the signal over time, resulting in a better understanding of ligand kinetics and enhancing quantification accuracy.[60] Total-body imaging further advances dynamic imaging by improving the signal sensitivity,[61] reducing the required radiotracer dosage and shortening scan times.[62,63] This approach may help discern dysfunctional microglia in chronically diseased states compared to healthy models.[64] It may also be conceivable to further differentiate various neurodegenerative diseases based on the biomarker characteristics.[65]

Microglial pro-inflammatory responses have been actively studied through PET imaging of biomarkers such as translocator protein 18 kDa (TSPO) and the purinergic receptor P2X7 (P2X7) as shown in **Figure 6**.[66–69] TSPO has shown great promise in identifying neuroinflammation localised in the cortico-limbic system in conditions like AD, PD, MS, and HD, but its expression is not specific to a particular microglial phenotype.[70] There is therefore growing interest in understanding the intricacies of the innate immune response to neurological insults to develop better treatment strategies.[70] In particular, the anti-inflammatory microglial response has been overlooked in its significance in neurodegenerative diseases for the past two decades.

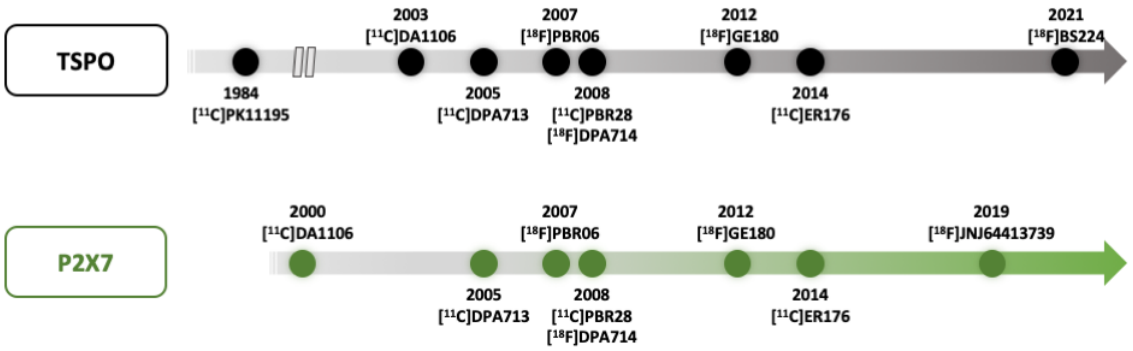

Figure 6: Literature radiotracers used to targeting microglial TSPO and P2X7 for monitoring pro-inflammatory responses in the CNS.[69]

1.2.2 Purinergic receptors and anti-inflammatory response

Purinergic receptors are membrane-bound receptors activated by purines, categorised as either P1 or P2 receptors. Adenosine serves as the endogenous agonist for P1 receptors, while phosphorylated nucleosides like adenosine triphosphate (ATP) and ADP activate P2 receptors.[71] These receptors are further subcategorised as either ligand-gated ion channels (P2X receptors) or G protein-coupled receptors (GPCRs or P2Y receptors).[71]

P2X ligand-gated ion channels typically function as multimeric complexes,[72] responding rapidly to extracellular ATP by opening ion channels that allow cation influx.[73] This influx subsequently triggers immediate response microglial responses. For example, activation of P2X4 facilitates chemotaxis, while P2X7 promotes the release of pro-inflammatory cytokine IL-1β.[74] In contrast, GPCRs modulate intracellular pathways to induce prolonged downstream responses that adapt to the gradual changes in the micro-environment.[75] These include the regulation of microglial phagocytic activities *via* P2Y2 and P2Y6, and attenuate glutamate-induced excitotoxicity signalling through activation of P2Y1 and P2Y12.[74,76] The diverse functional response of microglia resulting from purinergic receptor activation present opportunities to investigate and understand their nuanced roles.

Table 2: Receptors expressed on microglia that are biomarkers for pro- and anti-inflammatory responses. Multiple endogenous ligands are sorted in the order of affinity toward the receptor.[71,77]

Receptor		Endogenous ligand(s)[77]	Receptor expression
P2X	P2X4	ATP	Up-regulated under pro-inflammatory response[78]
	P2X7	ATP	Up-regulated under pro-inflammatory response[45,79]
P2Y	P2Y1	ADP > ATP	Up-regulated under pro-inflammatory response[78]
	P2Y2	UTP = ATP	Up-regulated under pro-inflammatory response[80]
	P2Y6	UDP > UTP » ATP	Up-regulated under pro-inflammatory response[81]
	P2Y12	ADP	Up-regulated under anti-inflammatory response[45,79]

Beaino and coworkers explored the receptor expression of microglia under anti-inflammatory stimulation to identify potential biomarkers for use in PET imaging. Using IL-4 to stimulate an anti-inflammatory response, they measured relative protein expression through quantitative polymerase chain reaction (qPCR), comparing it to non-stimulated microglia as a control.[79,82,83] This analysis uncovered a four-fold increase in purinergic receptor P2Y12 (P2Y12) expression.[45,79] Western blotting experiments were subsequently performed to estimate protein expression levels, indicating a two-fold increase in P2Y12 under anti-inflammatory conditions.[79] Given its role in neuroinflammatory response modulation, P2Y12 is a potential biomarker for imaging the anti-inflammatory response in the CNS.[74] Currently, microglial P2Y12 studies are limited to *in vitro* settings due to limitations of PET radiotracers, see **Section 1.4**. Extending this research to *in vivo* models with PET imaging could

offer a more comprehensive understanding of microglial phenotypes across various physiological conditions.

1.3 P2Y12

P2Y12 was uncovered by Hollopeter and coworkers in an effort to identify the target receptor for anti-thrombotic drugs clopidogrel and ticlopidine.[84] Surprisingly, P2Y12 was found to be expressed both in the brain and on platelets. This discovery prompted Sasaki and coworkers to conduct a follow-up study, identifying that microglia are the sole cell-type that expresses P2Y12 in the brain.[85] Mildner and coworkers further elucidated that P2Y12 was expressed throughout all brain regions, age groups and stages of life.[86] Despite microglia originating from the prenatal macrophage invasion to the brain, P2Y12 was not found to be expressed on macrophages.[86]

ADP is the endogenous agonist of P2Y12, stimulating platelets and initiating a biochemical cascade to affect thrombosis.[87] This process is beneficial in preventing excess blood loss by clotting the blood externally, but internal clotting in blood vessels could cause significant harm. Antagonising P2Y12 can disrupt the event chain and is the cornerstone strategy for developing anti-thrombotic drugs.[88]

1.3.1 Therapeutics

In the decade following the identification of P2Y12 as the drug target for clopidogrel and ticlopidine, there was a surge in the discovery of anti-thrombotic ligands. Up until 2022, around 1,000 P2Y12 ligands have been synthesised through anti-thrombotic drug campaigns, with AstraZeneca, Pfizer, and Sanofi leading the efforts to design the first reversible P2Y12 antagonist with increased efficacy and overcoming drug resistance against clopidogrel.[89] Recently, interest in developing new anti-thrombotic drugs waned due to the unclear clinical benefits over existing drugs.[90] Given that P2Y12 was validated as a key drug target in the periphery, it is not

surprising that the ligand physicochemical properties were not refined for CNS applications.

Functional studies on microglial P2Y12 are rare, making its potential as a therapeutic target in this context uncertain. Webster and coworkers generated P2Y12 knockout models, treated them with clopidogrel, and observed microglial responses to cerebral ischemia. Homozygous P2Y12 knockout mice did not survive bilateral common carotid artery occlusion to induce ischemia.[91] Interestingly, clopidogrel-treated and heterozygous P2Y12 knockout mice models exhibited higher neuronal viability, attributed to the immobilisation of microglia, which prevented microglia-to-neuron contact leading to neuronal death.[91] Lou and coworkers delved further into the mechanism of action, finding that persistent antagonism and homozygous P2Y12 knockout models suffered excessive bleeding from an inability of microglia to chemotax towards damaged sites and repair lesions. However, delayed P2Y12 antagonism or limited P2Y12 availability post-lesion enhanced lesion repair.[92] Tozaki-Saitoh and coworkers administered cangrelor through spinal injection and orally dosed clopidogrel in mice models, observing a reduction in neuropathic pain.[93] Instances of P2Y12 antagonism have demonstrated potential therapeutic benefits in animal models, leading some researchers to speculate about possible translation to humans.[94]

1.3.2 PET imaging studies

The prospects of disease-modifying therapeutics have drawn attention to P2Y12, but its functional role in neuroinflammation remains enigmatic. Over the past decade, growing interest in developing a CNS-penetrant P2Y12 PET tracer to better understand its expression and relevance to brain disease.[79] Evidence supporting P2Y12 as a useful imaging target has been accumulating with each attempt. Beaino and coworkers identified P2Y12 as a biomarker for the anti-inflammatory response.[79] Villa and coworkers concluded that P2Y12 was exclusively expressed on microglia among other peripheral immune cells.[45] Maeda and coworkers observed decreased P2Y12 expression in PS19 and rTg4510 tauopathy mice compared to wild-type and

non-transgenic mice models.[95] However, all attempts to image CNS P2Y12 *in vivo* have been unsuccessful, therefore strategies for developing CNS-penetrant P2Y12 radiotracers must be revisited and analysed to address their shortcomings.

1.4 Microglial P2Y12 PET tracers

CNS exposure remains the biggest challenge that current strategies for P2Y12 PET tracers have yet to overcome. Typically, CNS penetrating ligands need to have a delicate balance between lipophilicity and hydrophilicity. A ligand that is too lipophilic will often lead to off-target binding, which may be a substrate for efflux transporters, making it unable to accumulate in brain parenchyma.[96] Downstream toxicity may ensue from efflux transporter binding such as deactivation of human ether-à-go-go-Related Gene (hERG) cardiac potassium channel and cytochromes P450 (CYP) inhibition.[96,97] Overly hydrophilic ligands are unable to diffuse across the tight lipophilic BBB junctions.[96]

In this work, BBB permeability refers to the passive diffusion into the CNS, whereas CNS penetration describes the ability of a ligand to both permeate the BBB and be retained within the CNS. Enzymatic metabolism and efflux by endothelial transporters also affect the retention of a ligand within the CNS after passively diffusing across the BBB.[98] Careful consideration has been made to accurately discuss challenges in the design of CNS-penetrating P2Y12 PET tracers in this thesis.

1.4.1 Previous attempts towards CNS P2Y12 PET tracers

In the past decade, re-purposing anti-thrombotic drug candidates have been the main strategy towards CNS-penetrating P2Y12 PET tracers. Anti-thrombotic drug candidates do not account for BBB permeability in their design brief, let alone retention in the CNS. Rather, anti-thrombotic drugs are typically designed to avoid BBB permeability, minimising the likelihood of off-target effects. Despite this, the sheer wealth of P2Y12 ligands discovered through anti-thrombotic drug

discovery offers researchers opportunities to identify ligands with the potential for CNS penetration.

The first reported attempt towards the design of a CNS-penetrating P2Y12 PET tracer was by Villa and coworkers, who approached the design by re-purposing literature ligands. Non-radiolabelled azetidine **1** was identified as their PET lead from Bach and coworkers anti-thrombotic drug campaign (**Figure 7**).[99] This ligand possessed single digit nanomolar affinity toward P2Y12 and was radiolabelled for PET imaging studies in rat models.[45] Incorporating a carbon-11 radionuclide into the lead ligand was straightforward, as the urea moiety could be conveniently synthesised through a carbon monoxide radiosynthon.[56] Despite the promising binding affinity, azetidine **1** failed to show CNS penetration, halting further investigations.

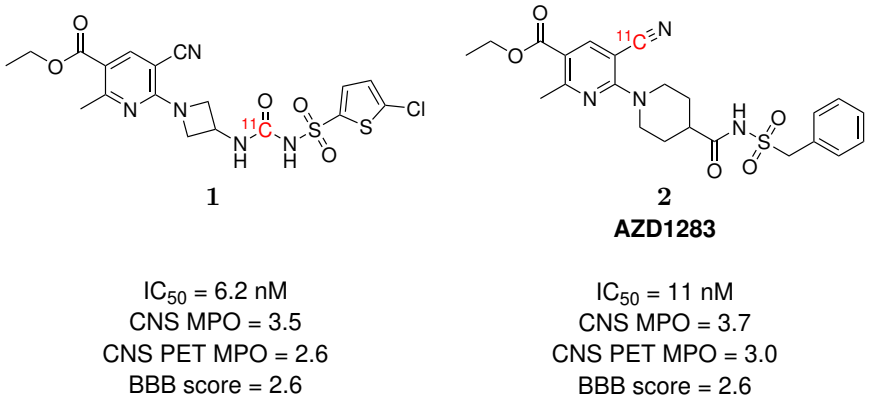

Figure 7: Structures of P2Y12 binding ligands from previous PET tracer studies,[45,95] radionuclides of the analogues are coloured red. Left: Villa and coworkers carbon-11 radiolabelled azetidine analogue from Bach and coworkers. CNS MPO and CNS PET MPO scores were obtained from Wildt and coworkers.[45,99,100] Right: Maeda and coworkers carbon-11 radiolabelled AZD1283 analogue from Bach and coworkers.[95,99,101] CNS MPO and CNS PET MPO were calculated using the algorithm described by Zhang and coworkers.[102] The LogD value was obtained from Jackson and coworkers,[103] while other physicochemical properties were predicted using Marvin for the CNS MPO and CNS PET MPO algorithms.[104]

Maeda and coworkers approached the development of a CNS-penetrating P2Y12 PET tracer with a similar strategy, re-purposing AZD1283 **2** from Bach and coworkers due to its high-affinity toward P2Y12 (**Figure 7**).[95,99,101] AZD1283 was carbon-11 radiolabelled via nitrile substitution of a bromonicotinate precursor.[95] Despite the

high-affinity of AZD1283, their radiotracer also failed to accumulate in the CNS in their rTg4510 mouse models.[95]

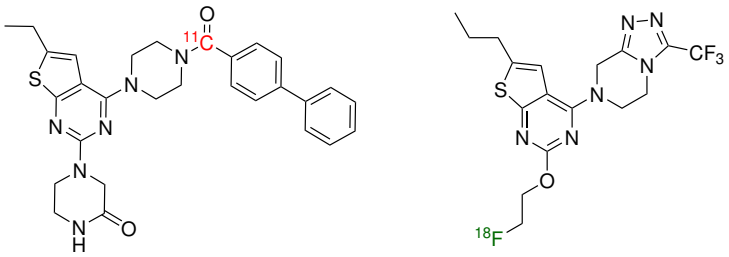

3
K_i = 9 nM
CNS MPO = 2.6
CNS PET MPO = 2.0
BBB score = 2.9

4
K_i = 0.3 nM
CNS MPO = 4.5
CNS PET MPO = 2.5
BBB score = 4.3

Figure 8: Structures of P2Y12 binding ligands from Van der Wildt and coworkers.[100] Radionuclides of the analogues are coloured red (^{11}C) and green (^{18}F). Left: Van der Wildt and coworkers carbon-11 radiolabelled thienopyrimidine analogue from Lee and coworkers.[100,105] Right: Van der Wildt and coworkers fluorine-18 radiolabelled thienopyrimidine analogue from Lee and coworkers.[100,105]

Van der Wildt and coworkers took a more strategic approach towards CNS-penetrating P2Y12 PET tracers, guided by CNS multiparameter optimisation (MPO) and CNS PET MPO scoring to predict CNS penetration through physicochemical property calculations. They were interested in the thienopyrimidine compounds from an LG Life Sciences patent for their high-affinity P2Y12 ligands. Ultimately they decided on thienopyrimidines **3** and **4** based upon further refinement with MPO calculations. MPO scores are presented in **Figure 8** with thienopyrimidine **4** scoring 4.5 at best with CNS MPO (molecules are scored between 0 to 6, with scores $\geq$4 being favourable for CNS penetration),[106] while displaying high binding affinity (K_i = 0.3 nM). Despite their careful approach, none of their ligands showed appreciable CNS accumulation. However, co-administrating tariquidar, a P-glycoprotein (P-gp) efflux blocker, allowed them to observe limited BBB permeability with thienopyrimidines **3** and **4**. This indicated that the thienopyrimidines were at least partially permeating through the BBB but were removed from the brain parenchyma by efflux transporters. However, it has been speculated that mouse and human efflux transporters may

be different, requiring further investigations or modifications to conclude on CNS penetration of the thienopyrimidine **4**.

In 2022, Jackson and coworkers attempted to design and synthesise a CNS-penetrating P2Y12 PET tracer, repeating the approach with piperidine **2** by Maeda and coworkers.[95,103] The radiotracer was administered to wild-type (WT) and P2Y12 knockout mice, but it did not accumulate in the CNS due to rapid metabolism and accumulation in the liver.[103] They also highlighted the necessity of using trifluoroacetic acid (TFA) as a buffer in high-pressure liquid chromatography (HPLC) purity analysis, suggesting that AZD1283 was likely in its anionic form in physiological conditions,[103] making it unlikely to permeate the BBB even if metabolism issues were resolved.[107]

In summary, re-purposing anti-thrombotic drug candidates has been the predominant strategy in the design of CNS penetrating P2Y12 PET tracers. Attempts to date have been unsuccessful due to the inability of the ligands to display CNS penetration. Van der Wildt and coworkers were the first group to use predictive algorithms in their design approach, improving the likelihood of identifying a successful CNS penetrating PET tracer. Despite the favourable CNS MPO score of thienopyrimidine **4**, it was unable to accumulate in the CNS. However, thienopyrimidine **4** was the first to show moderate BBB permeability. The use of CNS-penetration predictive algorithms is likely to increase the chances of selecting the appropriate ligand for this application. Computer-aided strategies should be further investigated to better use them for the next iteration of designing a CNS-penetrating P2Y12 PET tracer.

1.5 Computer-aided drug design

High attrition rates in clinical drug development and rising costs have led to the adoption of alternative methods for prudent drug design.[108,109] Computer-aided drug design (CADD) methodologies have become an indispensable part of the modern drug discovery process. Virtual screening can be used to triage otherwise impractical numbers of molecules to select compounds for *in vitro* screening (hit identification).[110,111] Hit-to-lead and lead optimisation campaigns also use predictive

in silico methods to help refine desired pharmacological activity, reduce the likelihood of off-target effects, and improve druglikeness and bioavailability of drug candidates.[112]

1.5.1 CNS-penetration predictive algorithms

CNS-penetration predictive algorithms such as CNS MPO,[113] CNS PET MPO[102,114] and BBB score[115,116] have been developed to use sets of calculated physicochemical properties to predict various physiochemical and pharmacokinetic parameters of small molecule drug candidates for CNS penetration. These predictive algorithms were trained to discriminate common physicochemical trends between CNS-penetrating drugs and non-CNS-penetrating ligands. Each predictive algorithm assigns physicochemical properties with different weightings, with the caveat that property prediction values differ across various software packages. Re-purposing ligands from anti-thrombotic drug discovery campaigns for CNS applications would make predictive CNS accumulation algorithms integral to the campaign, especially given the current challenges in achieving CNS accumulation of P2Y12 PET tracers.

CNS MPO and CNS PET MPO are considered gold standards for CNS-penetration predictive algorithms, scoring compounds based on properties like calculated logP (ClogP), calculated logD (ClogD), molecular weight (MW), topological polar surface area (TPSA), number of hydrogen bond donors, and pK_{a}. The aggregate score ranks the compound between 0 and 6, with greater scores indicating increased likelihood of CNS penetration.[106] A cut-off score of $\geq$4 captures approximately 74% of all known CNS drugs for CNS MPO,[113] whereas a score $\geq$3 captures approximately 79% of all known PET tracers for CNS PET MPO algorithms.[114]

Gupta and coworkers scrutinised the CNS MPO predictive algorithm, criticising the approach to train the model exclusively on ligands that successfully enter the CNS and the lack of a standardised physicochemical calculation software package. They highlighted the flaws of excluding valuable training data from non-CNS penetrating ligands and the inconsistencies in physicochemical property calculations from individual software packages (e.g. pK_{a} and logP).[117] Although the CNS PET MPO

method was specifically designed for assessment of CNS PET tracers, both MPO scoring systems use similar predicted physicochemical properties as their inputs and therefore suffer from the same variability in scores.

QikProp logBB was developed by Jorgensen and coworkers as part of the Maestro suite, a complete package for *in silico* aided drug design.[118] While the specifics of the training dataset remain proprietary, the developers report that 95% of CNS-penetrant drugs score between -3 and 1.2.[118] External benchmarking has suggested that higher scores generally correspond with increased CNS penetration likelihood.[117] QikProp integration within Schrödinger Maestro suite resolves scoring discrepancies between physicochemical prediction software, a key issue discussed with the CNS MPO algorithm. Fan and coworkers conducted a randomised test with 1,403 unique ligands, and the algorithm successfully predicted 82% of the compounds to be either CNS accumulating or inactive.[119] These results suggest that QikProp logBB is a robust tool for assessing CNS penetration and may provide more consistent predictions than CNS MPO.

In the design of a CNS penetrating P2Y12 PET tracer, computer-aided ligand design should be considered. This could guide the ligand selection process by identifying candidates with favourable physicochemical properties for CNS penetration. Efforts toward CNS P2Y12 PET tracers without computer-aided tools failed to demonstrate CNS penetration.[45,67,103] Van der Wildt and coworkers incorporated CNS penetration predictive algorithms in their selection strategy, showing promising results in identifying suitable ligands.[100]

1.6 Aims of this work

Microglia exhibit increased P2Y12 expression in response to anti-inflammatory signalling, yet the precise role of this receptor in CNS diseases remains unclear. Developing a PET tracer to monitor P2Y12 expression *in vivo* could provide valuable insights into its function, regulation and dynamics. However, there are currently no CNS-penetrating PET tracers available for imaging P2Y12. Efforts to repurpose

literature P2Y12 ligands for microglial P2Y12 PET imaging applications have yet to produce a successful tracer. Furthermore, the reliance on carbon-11 radiolabelling limits the practicality and versatility for CNS PET imaging studies. As such, this thesis aims to design and synthesise fluorinated P2Y12 ligands tailored for CNS PET tracing applications.

The work in **Chapter 2** describes the rational design of a potential CNS penetrating and fluorinated P2Y12 ligand library using CADD methodologies. Fluorine was incorporated to facilitate the eventual development of a fluorine-18 PET tracer that is practical and versatile. Effective PET imaging of microglial P2Y12 requires the ligand to achieve CNS penetration without compromising binding affinity. CADD-guided modifications facilitated rational design of CNS-penetrating fluorinated P2Y12 ligands. A divergent synthetic strategy was developed to access an initial library of compounds.

The lack of an accessible assay for evaluating affinities of the fluorinated P2Y12 ligands developed in **Chapter 2** prompted the development of NanoBRET P2Y12 probes. **Chapter 3** addresses the selection and virtual screening of suitable literature P2Y12 ligands to guide NanoBRET P2Y12 probe design. Initial selection criteria focused on identifying ligands with a known binding pose and high-affinity binding at P2Y12. Docking studies using a published P2Y12 crystal structure were used to refine structures that maintain high-affinity to the target.

Building upon the findings, a P2Y12 ligand was chosen based on predicted affinity and synthetic accessibility. In **Chapter 4**, a library of NanoBRET P2Y12 probes was generated from this selected ligand, focusing on probing linker interactions. This involved exploring various linker lengths and types to identify the optimal configuration for the fluorescent probe, as well as evaluating different fluorophores for their suitability. The development of a NanoBRET fluorescent probe will not only facilitate biological evaluation of new P2Y12 ligands such as those in **Chapter 2**, but also provides a scalable platform for high-throughput screening to identify new CNS-penetrating P2Y12 PET tracers.

Chapter 2

P2Y12 PET Tracers

2.1 Introductory remarks

The link between the P2Y12 expression and the CNS anti-inflammatory response has made it a target for imaging neurodegenerative conditions throughout disease progression. As discussed in **Chapter 1**, current strategies for designing P2Y12 PET tracers have been isolated to repurposing anti-thrombotic drug candidates. The strength of this strategy is the known pharmacokinetics profiles of these molecules, particularly for those that were progressed further through clinical trials. However, the main drawback was the lack of consideration toward CNS penetration. CADD could help us determine whether the modification is tolerable at the binding pocket and predict whether the ligand would accumulate in the CNS.

2.1.1 Chapter aims and objectives

The work described in this chapter aimed to synthesise fluorinated P2Y12 ligands that would retain affinity to P2Y12 and accumulate in the CNS. The workflow for this chapter comprised lead identification, ligand docking, CNS penetration predictions, retrosynthetic analysis, and chemical synthesis of a focused library of P2Y12 ligands. As a starting point, we focused on adapting high-affinity ligands that have functional groups that could be modified to incorporate a fluorine atom, to aid PET tracer

development in the future.

2.2 Lead identification and library design

Literature P2Y12 ligands may not have been viable drugs for various reasons, such as limited clinical response or toxicity.[120] However, these considerations are less critical in the development of PET tracers. Typically, the sub-therapeutic dosage would rather avoid the elicitation of pharmacological effects, providing an accurate reflection of biological response under neurodegenerative conditions. Additionally, toxicity is less concerning due to the low doses required for imaging.[121] For CNS PET tracers, high-affinity and selective binding are essential, alongside structural features that facilitate high CNS uptake. Literature P2Y12 ligands and anti-thrombotic drugs provide many high-affinity options, granting the opportunity to triage and identify promising candidates for CNS PET tracer development.

A challenge with the selection process was the variance in the reported binding affinity values. Ideally, binding affinities for these ligands would be reported as standardised inhibition or dissociation constants (K_i or K_d), enabling direct comparisons across studies.[107] Binding half maximal inhibitory concentration (IC_{50}) values are subject to variability depending on experimental conditions, which may complicate cross-study comparisons.[122] We made attempts to take into account the variability of available data when performing our ligand selection.

2.2.1 Selecting a lead candidate

We began by investigating reported anti-thrombotic drugs to identify a lead compound suitable for CNS applications. At first glance, small irreversible P2Y12 antagonists appear promising (**Figure 9**). Clopidogrel, for example, has demonstrated CNS penetration in mice models.[93] However, patients taking CYP enzyme inhibitors or with CYP2C19 polymorphisms, accounting for 30% of the population, were unable to metabolise clopidogrel to its active thiol form.[89,90,123] Furthermore, irreversible

PET tracers are prone to off-target binding interactions and are commonly known as flow limited tracers.[124] This means perfusion governing tissue distribution will result in a gradient effect from the injection site.[58] This makes it impractical to repurpose such irreversible P2Y12 PET ligands for CNS PET applications.

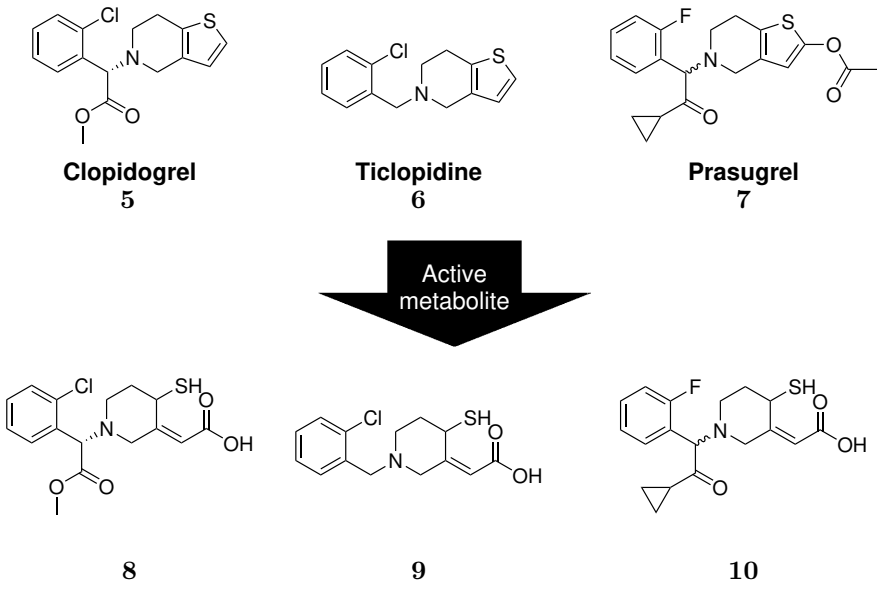

Figure 9: Structures of anti-thrombotic drugs that are irreversible P2Y12 antagonists. These are prodrugs that are metabolised to reveal the respective reactive thiol species that irreversibly binds to P2Y12.

Reversible anti-thrombotic drugs are alternatives that could display more favourable pharmacological profiles as PET tracers and higher affinity at P2Y12. Repurposing these drugs, which includes ticagrelor **11** and cangrelor **12**, appeared unlikely to penetrate the CNS due to their relatively large size and high polarity. Significant modifications to ticagrelor **11** or cangrelor **12** would be required to make them CNS active, deviating from their well characterised pharmacological profile.

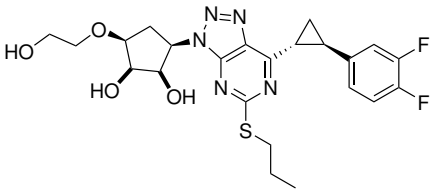

Ticagrelor
11
IC_{50} = 10 nM
MW = 507.56 g/mol
TPSA = 122.6

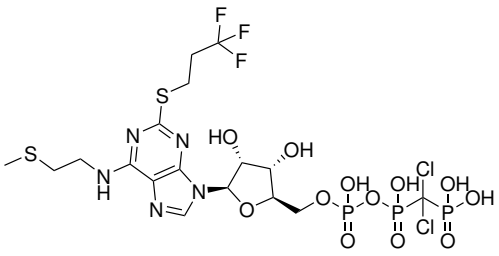

Cangrelor
12
IC_{50} = 0.45 nM
MW = 776.35 g/mol
TPSA = 252.6

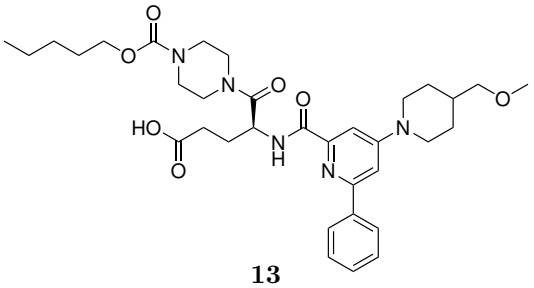

13
K_i = 3.5 nM
MW = 637.78 g/mol
TPSA = 141.1

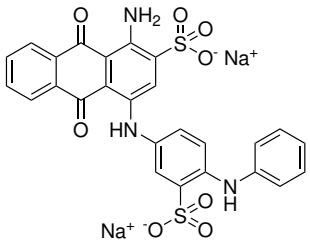

14
K_i = 25 nM
MW = 609.53 g/mol
TPSA = 198.6

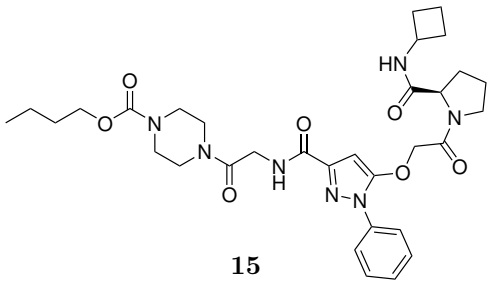

15
K_i = 7.7 nM
MW = 637.74 g/mol
TPSA = 153.2

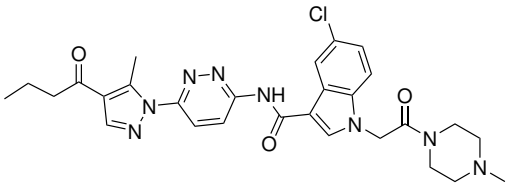

16
IC_{50} = 17 nM
MW = 563.06 g/mol
TPSA = 113.3

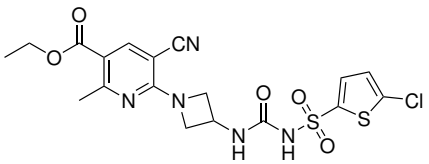

17
IC_{50} = 6.2 nM
MW = 483.94 g/mol
TPSA = 141.0

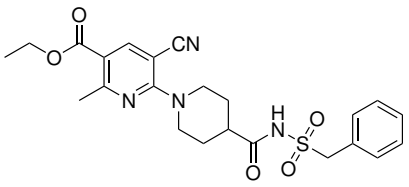

18
IC_{50} = 11 nM
MW = 470.54 g/mol
TPSA = 128.9

Figure 10: Selected structures of reported drugs and drug candidates with associated binding affinities (IC_{50} or K_i) at P2Y12.[110] MW = molecular weight. TPSA = topological polar surface area. The TPSA was predicted using ChemDraw.[125]

Industry efforts to develop more effective anti-thrombotic drugs have resulted

in a broad selection of reversible P2Y12 ligands. The structural diversity among these ligands offers an opportunity to identify a lead with suitable physicochemical properties for CNS penetration (**Figure 10**). Piperidine **13** and anthraquinone **14** are likely to be charged under physiological conditions, which would prevent BBB penetration.[126] Pyrazole **15** was also considered suboptimal for CNS applications, as its large size hinders both CNS penetration and synthetic accessibility. In contrast, indole **16** and nicotinates **17** and **18** were evaluated as promising candidates for repurposing in CNS PET imaging, given their smaller molecular size. Notably, both nicotinates **17** and **18** have previously been investigated for CNS PET imaging, making them appealing for further exploration. While binding affinities measured as K_i or K_d values would allow for accurate comparisons, nicotinate **17** was selected as the lead from the available binding data. At the time of lead selection, the work by Van der Wildt and coworkers was yet to be published, and we were unaware that nicotinate **17** was BBB impermeable.[100]

2.2.2 Modifications to the lead

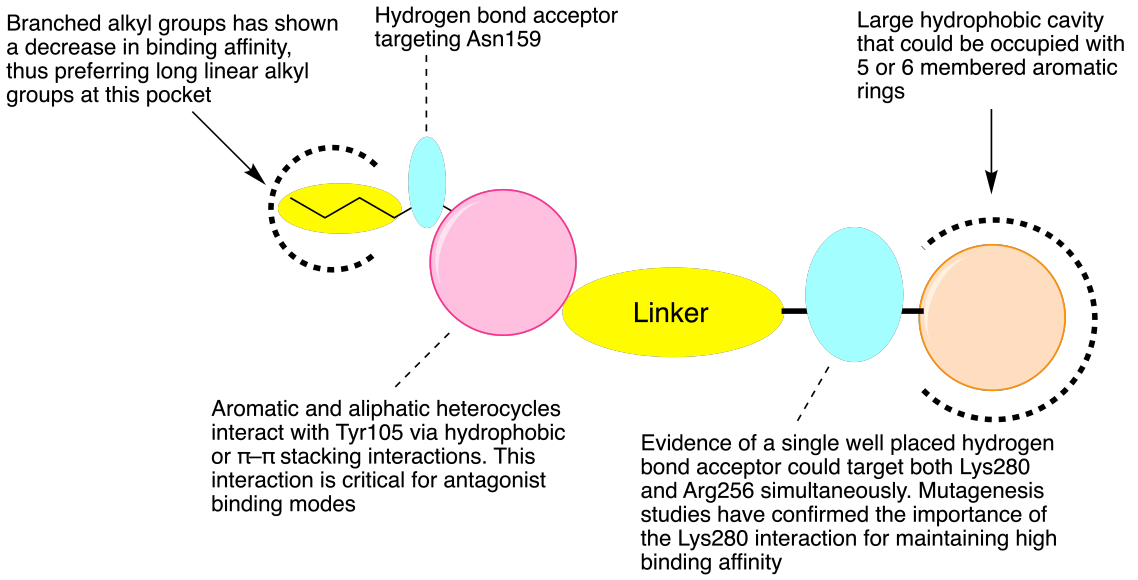

Figure 11: Schematic of the general antagonist binding interactions with the P2Y12R. Yellow = hydrophobic functional groups, blue = polar functional groups, pink = heterocycles and orange = carbocycles. The key amino acid residue interactions are represented with dashed lines. Bold dashed lines are the hydrophobic pockets or cavities within the binding site.[110]

Before proceeding with modifications to the lead, we reviewed the literature to identify tolerable positions for fluorine incorporation. Experimental data from P2Y12 drug discovery campaigns and docking studies provided insights into the binding pocket, directing us towards sites where functional group alterations might be tolerated. Paoletta and coworkers' docking studies elucidated key binding interactions with residues within the P2Y12 binding pocket, correlating them with experimental data.[127] This aided our design of a general pharmacophore model, as shown in **Figure 11** summarising common structural motifs across drug candidates. This model highlighted the importance of key amino acid interactions, including hydrogen bonding with Asn159, Arg256 and Lys280, and hydrophobic interactions with Tyr105. Our chosen lead **17** fits this pharmacophore model.

Literature has reported that the narrow hydrophobic pocket on the western half of the lead could accommodate alkyl esters up to eight carbons in length.[128] Across the docking studies, the carbonyl was deemed essential for H-bonding interactions with Asn159.[127] A fluorine atom was introduced at the terminal position of the alkyl chain for synthetic accessibility as a radiolabelling handle. We proposed a library to incorporate an alkyl chain attached to either an ester or ketone moiety, with a terminal fluorine (**Figure 12**). Despite esters may hydrolyse *in vivo*,[45] these modifications were incorporated in our library due to the synthetic accessibility to rapidly probe out the fluorine tolerability at the binding pocket. Then we performed docking studies on the modified compounds to evaluate likely affinity for P2Y12 and helped to guide optimal rational molecular design.

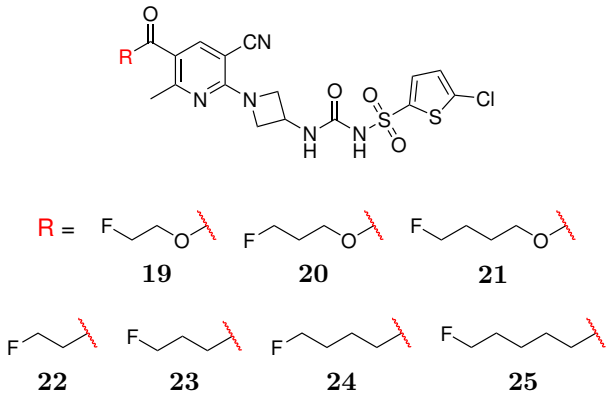

Figure 12: Planned modifications on the lead compound based on predicted physicochemical properties, its effect on CNS accumulation and predicted P2Y12 binding affinity.

CADD tools such as docking studies and physicochemical predictors are powerful tools to incorporate in a structure-based drug design (SBDD) campaign. The Glide package within Schrödinger Maestro enables *in silico* exploration of ligand-protein interactions. QikProp is a powerful tool within the Schrödinger suite for CNS drug discovery that predicts BBB permeability from the aggregation of 36 unique physicochemical parameters.[117] We submitted the modified ligands to docking and physicochemical predictive algorithms to evaluate whether they were suitable for synthesis and further investigation.

To perform *in silico* docking studies, the protein and ligand were prepared using the tools within Schrödinger Maestro. First, the antagonist-bound P2Y12 crystal structure (PDB ID: 4NTJ) was selected as the protein, given the similarity of the bound nicotinate antagonist to our compound library **17**. The protein was then manually inspected to remove detergents, water and steroids to reduce computational cost and interference from extraneous substances. The protein was then prepared using the in-built Protein Preparation Wizard in the Schrödinger Maestro suite. Finally, the ligands were prepared using the LigPrep package (generating 3D structures and ionisation states), multiple conformers of the ligands were generated using Confgen, a Glide grid was generated with the bound ligand as the centroid, and Glide docking was carried out with the extra precision (GlideXP) scoring function. For the detailed

procedure and protocols, see **6.1**.

Table 3: Table of lead azetidine compound **17** with proposed modifications. Schrödinger QikProp logBB is a predictor of CNS druggability (95% of all orally available drugs score between -3 to 1.2). Schrödinger Maestro Glide predicts ligand-protein interactions and outputs a score based on the calculated free energy of binding (the more negative the score, the stronger the predicted binding affinity).

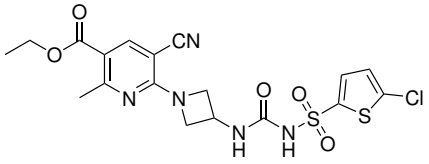

17
IC_{50} = 6.2 nM
logBB = -2.7
GlideXP = -12.4

Compound code	logBB	GlideXP
17	-2.7	-12.4
19	-2.7	-13.7
20	-2.6	-13.5
21	-2.9	-15.0
22	-2.4	-12.3
23	-2.5	-15.1

The docking studies predicted almost all the modified ligands to have greater affinity than lead compound **17** (**Table 3**). Compound **22** scored closely with the lead compound, so it would be difficult to conclusively say how well the fluorine-modified compound would perform in biological assays. The shorter length of the fluoroethyl ketone analogue followed the experimental data, suggesting the loss of binding affinity when chain lengths were shorter than those of ethyl esters. Besides the fluoroethyl ketone, all other compounds follow the expected results, with the general trend toward increased binding affinity with longer alkyl chains. Based on the QikProp logBB scores, all the compounds showed potential to penetrate the CNS. Fluorinated ketones **24** and **25** were subsequently added to the proposed library to serve as length-matched comparatives to the ester series. This addition aimed to establish trends between the ester and ketone functionalities in binding at P2Y12.

2.3 Lead synthesis

We opted to develop a divergent synthetic strategy to access our proposed library of fluorinated P2Y12 ligands. This could be divided in two phases: a convergent approach to access the lead compound and divergent synthesis to furnish our modified compounds. The key intermediates are broken down into smaller fragments as shown in **Scheme 1**. Although nicotinate **27** needed to be synthesised, azetidine **28** and thiophene **29** were commercially available.

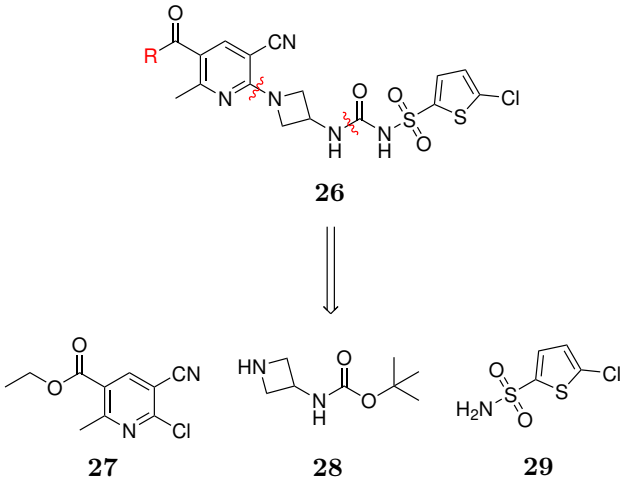

Scheme 1: Key fragments for synthesis of our P2Y12 ligand library identified by retrosynthetic analysis.

In Bach's approach to the lead compound (**Scheme 2**), the cumulative 3.5% yield over six steps was an inefficient strategy. The low overall yield was exacerbated by the final sulfonylurea forming step (11% yield), resulting in the significant loss of late stage materials in the process. Purifying this material to obtain larger amounts of the divergent intermediate would require large scale column chromatography and solvent volumes to isolate the product, both of which are challenging to scale up. Optimisation of the synthetic route was therefore investigated to improve the yield toward the divergent intermediate. We initially took inspiration from Bach and coworkers' approach to link the fragments and access lead **17**.[99]

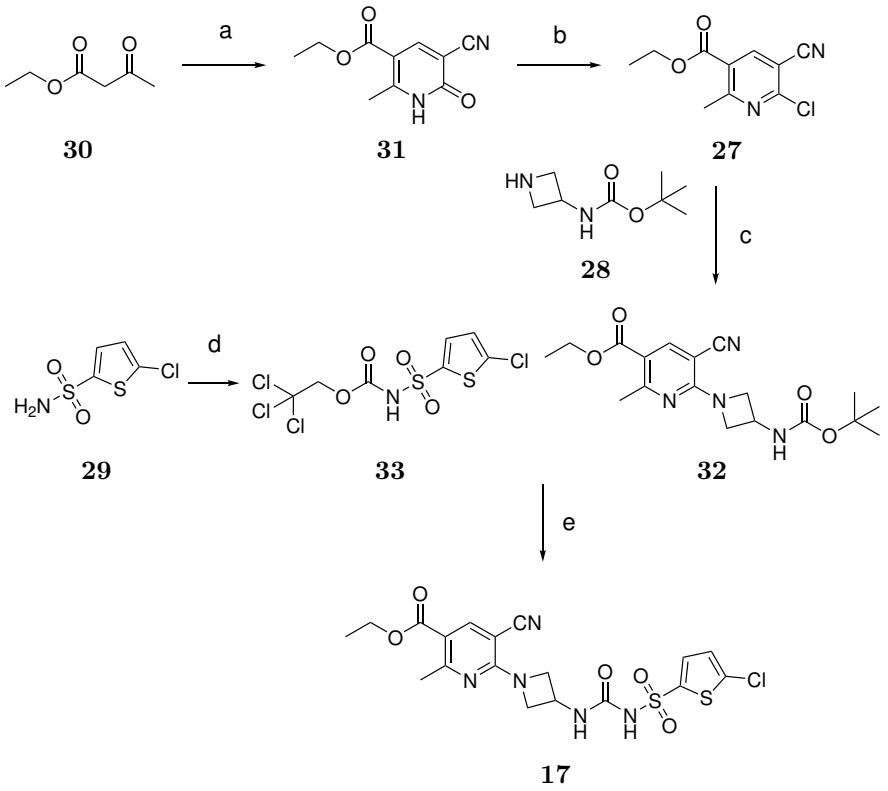

Scheme 2: Bach's synthetic route to lead **17**. (a) Cyanoacetamide, NaOEt, EtOH, rt, 24 h, 67%; (b) $(COCl)_2$, cat. DMF, DCM, reflux, 18 h, 98%; (c) iPr$_2$NEt, DCE, rt, o/n, 66%; (d) Troc-Cl, NaOH, DCE/H_2O, 0 °C - rt, 7 h, 73%; (e) i) 4 M HCl in dioxane, DCM, rt, 30 min, ii) Et_3N, MeCN, reflux, 1 h, 11% (over 2 steps).

Our divergent synthetic strategy to access the fluorinated analogues **17**-**25** is shown in **Scheme 3**. Hydrolysis of lead **17** gives access to divergent acid intermediate **34**. Carboxylic acid **34** undergoes Steglich esterification to furnish our leads **19**-**21**, and amide coupling to form the Weinreb amide **35**. Subsequently, treating Weinreb amide **35** with the respective fluorinated Grignard reagent would access both fluorinated ketone analogues **22**-**25**.

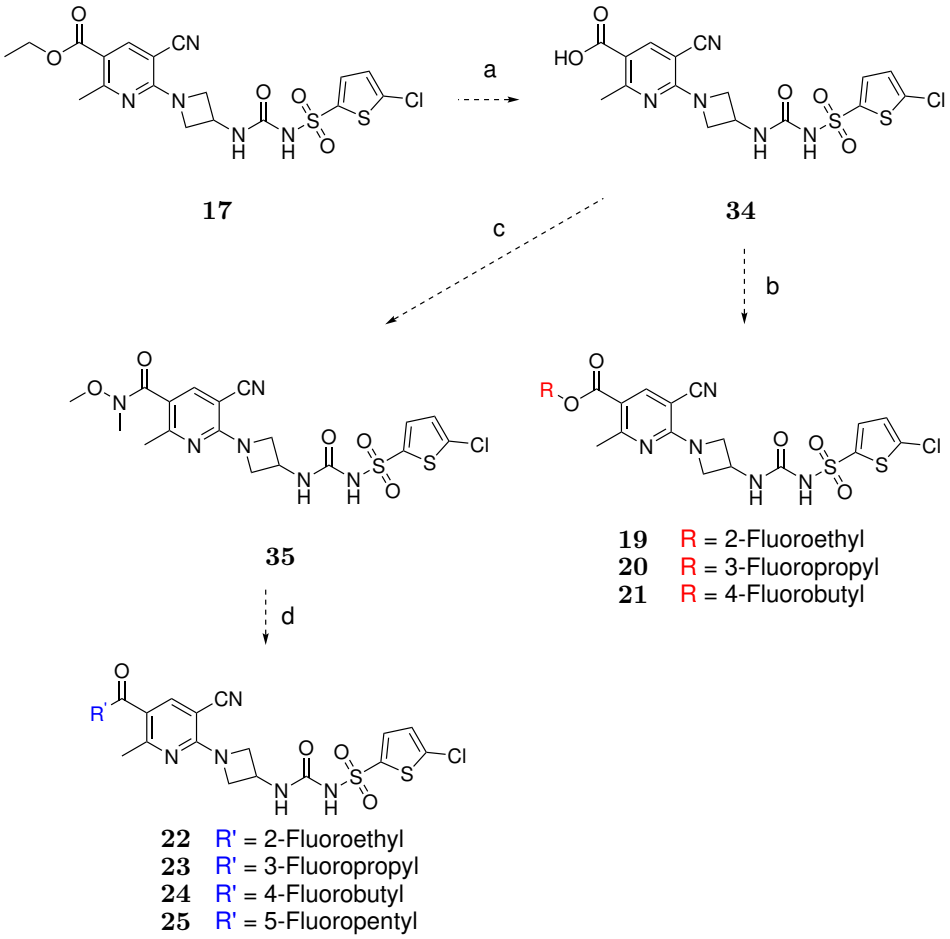

Scheme 3: Our divergent synthetic strategy to access fluorinated analogues of lead **17**. (a) NaOH, H_2O/THF, rt, o/n; (b) Fluorinated alcohol, EDC, THF, 0 °C - rt, o/n; (c) *N,O*-Dimethylhydroxylamine, EDC, THF, 0 °C - rt, o/n; (d) Fluorinated alkyl Grignard reagents, Et_2O, rt.

2.3.1 Nicotinate core synthesis

Following literature procedures,[129,130] we treated ethyl acetoacetate with dimethylformamide dimethylacetal (DMF-DMA) to append dimethylamine to ethyl acetoacetate *in situ* (**Scheme 4**). Malononitrile and Et_3N were then added to cyclise pyridone **31** and recrystallisation afforded the pure product with fair yields (67%, over 2 steps). NMR spectra confirmed the pyridone cyclisation from the aromatic proton at 8.43 ppm and broad amide peak at 12.95 ppm (**Appendix 6**). Despite our rigorous attempts to recrystallise product obtained from the liquors of crystallisation to improve the overall yield, we could not achieve the yields reported in the literature. Nevertheless, a yield sacrifice on the first step of the synthesis was not detrimental

in our synthetic strategy to access lead **17**.

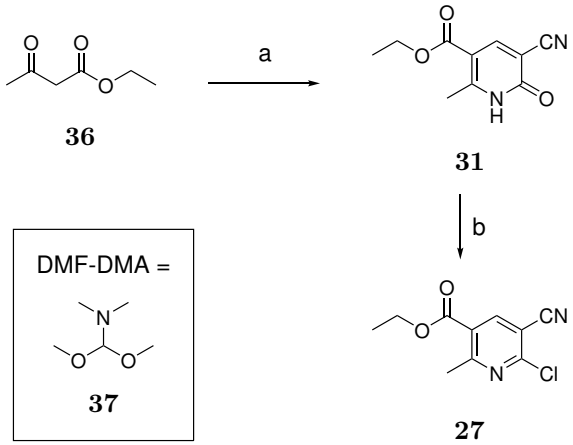

Scheme 4: Synthesis of the nicotinate core starting from ethyl acetoacetate **36** via pyridone **31**. (a) i) DMF-DMA, EtOH, 42 °C, 6 h, ii) Malononitrile, Et_3N, EtOH, 30 °C, 18 h, 67%; (b) $POCl_3$, MeCN, 80 °C, 22 h, 87%.

Pyridone **31** was subjected to chlorination conditions using $POCl_3$, yielding nicotinate **27** in good yields, comparable to the literature (87%). The absence of the pyridone broad amide proton (12.95 ppm, **Appendix 7**) and chlorine MS splitting pattern (**Appendix 8**) suggested the chlorination was successful. Nicotinate **27** was accessed over two steps, without requiring chromatographic purification. This was well-suited for gram-scale synthesis. Both the pyridone **31** and nicotinate **27** were bench-stable and synthesised in advance of the nucleophilic aromatic substitution (S_NAr) with azetidine **28**.

Azetidine **28** was treated with nicotinate **27** under basic conditions (**Scheme 5**), and the reaction was monitored via thin-layer chromatography (TLC) analysis until complete consumption of starting material was observed. The crude product was purified by flash chromatography to access compound **32** in excellent yields (93%). This substantially improved upon the reported yields (67%) by allowing sufficient time for complete consumption of starting material. Upon scaling up the reaction, concentrating the fractions using a rotovap resulted in an oil, which did not crystallise until it was dried vigorously under high vacuum pressure. Recrystallisation from EtOAc afforded free-flowing crystalline material which was easier to isolate and handle for subsequent reactions.

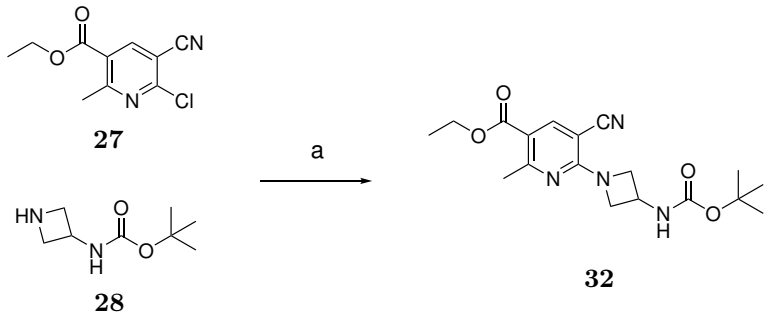

Scheme 5: Nucleophilic aromatic substitution of nicotinate **27** with azetidine **28**. (a) $i\mathrm{Pr}_2\mathrm{NEt}$, DCE, rt, o/n, 93%.

2.3.2 Sulfonylurea formation

In situ generation of isocyanate *via* Troc-carbamate

In preparation for the sulfonylurea formation, we attempted synthesis of compound **33** *via* dropwise treatment of sulfonamide **29** with Troc-Cl under biphasic conditions (entry 1, **Table 4**). TLC analysis indicated rapid formation of a new product, but stirring overnight revealed complete reversion to the starting material. Flash chromatography and subsequent spectroscopic analysis confirmed that the isolated product was predominantly the unreacted starting material.

Formation of the Troc-carbamate on sulfonamide **29** was complicated by competing deprotection reaction. A large excess of Troc-Cl was added to drive the reaction to completion (entry 2, **Table 4**), but the reaction progress stalled (as observed by TLC analysis), and was therefore halted. This resulted in only 27% isolated yield of the desired product alongside recovery of starting material (entry 2, **Table 4**) after flash chromatography.

Table 4: Optimisation of Troc-carbamate formation of sulfonamide **29**. [a] The reaction mixture was analysed by TLC, and quantities of recovered starting material (SM) were not calculated.

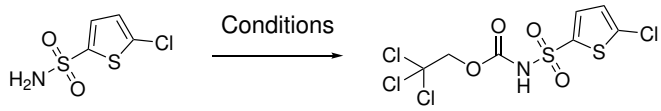

29 **33**

Entry	Scale (g)	Conditions	Outcome
1	0.15	NaOH, Troc-Cl (2 eq.), DCM/H_2O, rt, o/n	SM[a]
2	0.15	NaOH, Troc-Cl (14.3 eq.), DCM/H_2O, rt, 2 h	27% yield + SM[a]
3	0.15	NaOH, Troc-Cl (2 eq.), DCE/H_2O, 0 °C - rt, 2 h	72% yield + SM[a]
4	1.5	NaOH, Troc-Cl (2 eq.), DCE/H_2O, 0 °C - rt, 2 h	66% yield + SM[a]
5	15	NaOH, Troc-Cl (2 eq.), DCE/H_2O, 0 °C - rt, 2 h	34% yield + SM[a]

The proposed Troc-deprotection mechanism under basic biphasic conditions is shown in **Scheme 6**. Due to the acidic nature of the carbamate proton (predicted $pK_a = 3.1$),[131] deprotonation by a base drives the formation of the deprotonated intermediate **38**. A reversible equilibrium exists between this intermediate and liberated 2,2,2-trichloroethanol **40** and isocyanate **39**. This can be attacked by hydroxide ions, driving the reaction toward a decarboxylation pathway as shown by intermediates **41-43**, regenerating sulfonamide **29**. Literature has reported similar heat-driven decomposition for isocyanates.[132] The *in situ* formation of isocyanates under basic conditions was reported by Azad, Dauvergne, Caplow and coworkers.[133–135]

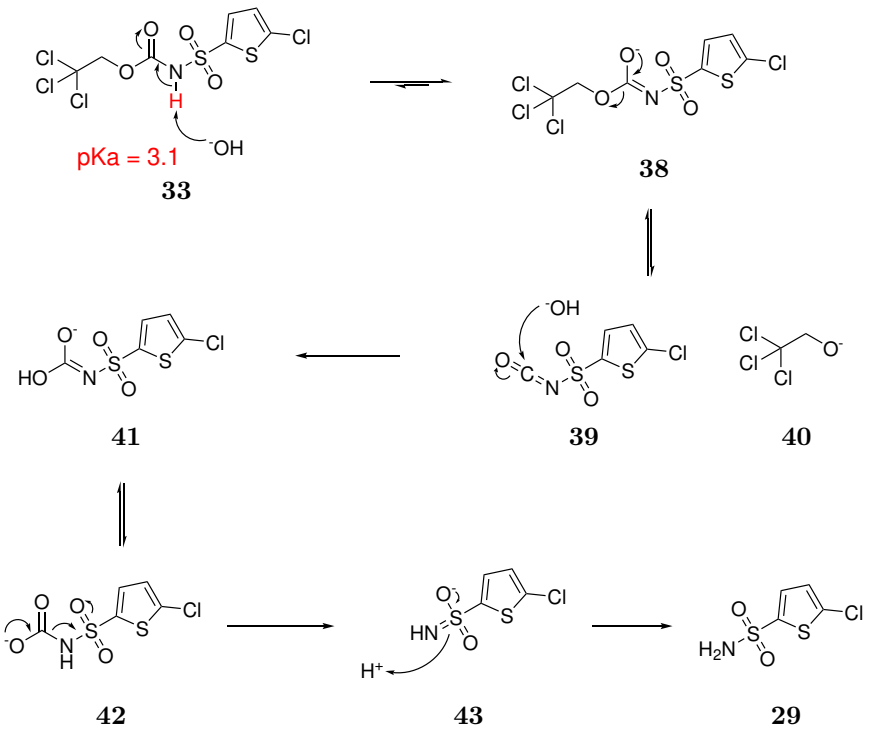

Scheme 6: Proposed mechanism of the *in situ* isocyanate formation of carbamates in the presence of NaOH and water. The pK_a of the sulfonamide was predicted using MolGpka following the protocol laid out by Pan and coworkers.[131]

The biphasic Troc-carbamate formation was optimised by reducing the reaction temperature (entries 3-5, **Table 4**). Lowering the temperature helped stabilise Troc-carbamate **33** throughout product formation, while attenuating the competing deprotection reaction. This adjustment led to improved yields (72%, entry 3, **Table 4**) and prompted subsequent scale-up reactions. However, during purification by flash chromatography, the desired product eluted rapidly and coeluted with traces of an unknown brown impurity. Despite the inefficient separation, adequate quantities of Troc-carbamate **33** were obtained for sulfonylurea formation studies.

To access nicotinate **17** (**Scheme 7**), Boc-deprotection of compound **32** was performed under acidic conditions. Crude amine **44** was found to be unstable on the bench, necessitating refrigeration to prevent degradation if storage was required. Otherwise, it could be telescoped immediately to the sulfonylurea formation without further purification. It was combined with Troc-sulfonamide **33** and heated at reflux under basic conditions. Purification by flash chromatography, using an eluent system buffered with acetic acid to elute the fractions, afforded the desired product **17** in

low yield (13%), confirming the literature-reported low conversion. In addition to nicotinate **44**, sulfonamide **29** was identified in the product mixture, while no Troc-carbamate **33** was detected. Competing decomposition mechanisms may therefore have contributed to poor yield despite the complete consumption of **33**.

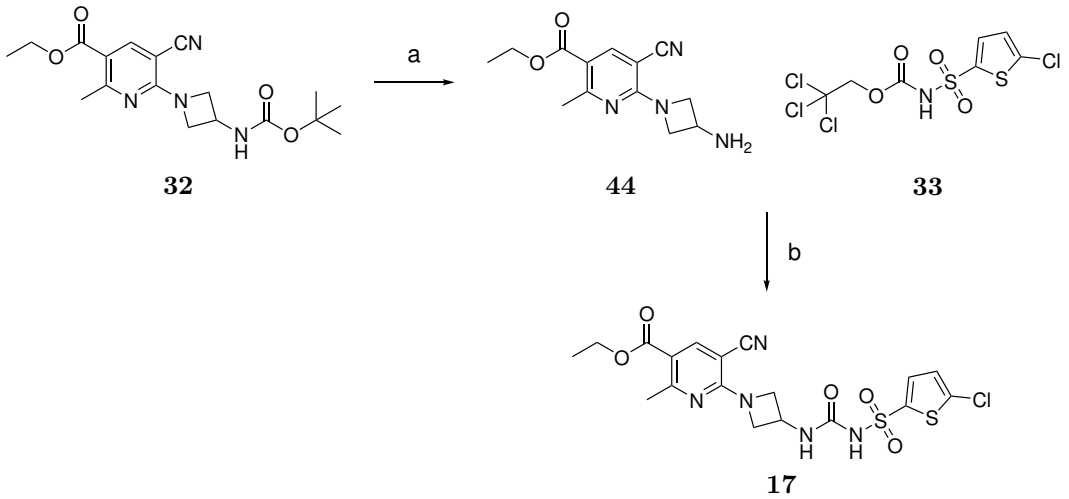

32 **44** **33** **17**

Scheme 7: Synthesis of lead **17** from Boc-carbamate **32** *via* telescoped strategy. (a) 4 M HCl in dioxane, DCM, rt, 30 min, quant.; (b) Et_3N, MeCN, reflux, 13%.

In summary, attempts to access divergent intermediate **34** *via* the Troc-carbamate route **33** proved inefficient. Scaling up the reaction highlighted challenges in Troc-carbamate formation and purification, limited yield of the final sulfonylurea formation step complicated efforts to produce sufficient quantities of the divergent intermediate **34**.

In situ generation of isocyanate from nicotinate 32

In an effort to improve sulfonylurea formation, the reaction partners were reversed by generating an isocyanate *in situ* from azetidine **44** and using sulfonamide **29** as the nucleophile. This approach circumvented the presence of the highly acidic proton of sulfonamide carbamates, which previously led to product decomposition. Spyropoulos and coworkers reported the *in situ* generation of isocyanates *via* a Boc-protecting group, providing a one-pot method for asymmetric urea synthesis.[136]

Azetidine **32** was treated with triflic anhydride and 2-chloropyridine, stirring until the complete consumption of starting material was observed by TLC analysis.

Sulfonamide **29** and triethylamine (Et_3N) were added. The reaction mixture was purified by flash chromatography and afforded the desired product in fair yields (49%, over 2 steps).

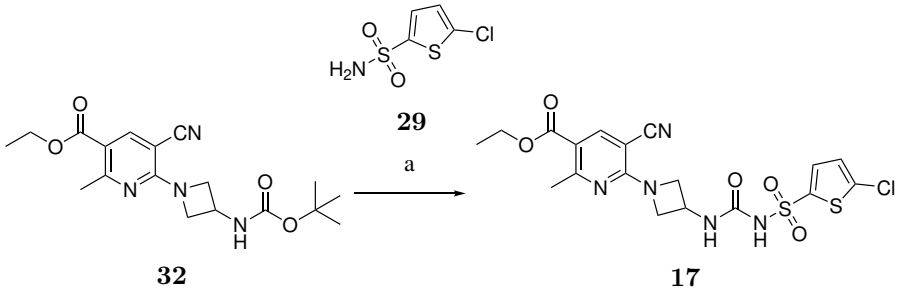

Scheme 8: Synthesis of lead **17** *via in situ* generation of isocyanate, followed by nucleophilic attack by sulfonamide **29**. (a) i) Tf_2O, 2-chloropyridine, DCM, rt, 50 min, ii) Sulfonamide **29**, Et_3N, rt, o/n, 49%.

The *in situ* isocyanate generation was initially uncovered by Banwell and coworkers as an adaptation of Bischler–Napieralski reaction.[137] Isolation of intermediate species contributed toward understanding the mechanism for this reaction (**Scheme 9**).[136,138–140] The triflic anhydride, a strong and oxophilic electrophile, reacts with the carbonyl of the Boc-group despite its low nucleophilicity. Under the acidic conditions, the *tert*-butyl group then likely dissociates, reforming a mixed anhydride **46**. Subsequent attack of 2-chloropyidine at the labile sulfinate group could produce intermediate **47**, which equilibrates with the protonated isocyanate **48**. A base then abstracts the proton, resulting in the formation of isocyanate intermediate **49**.

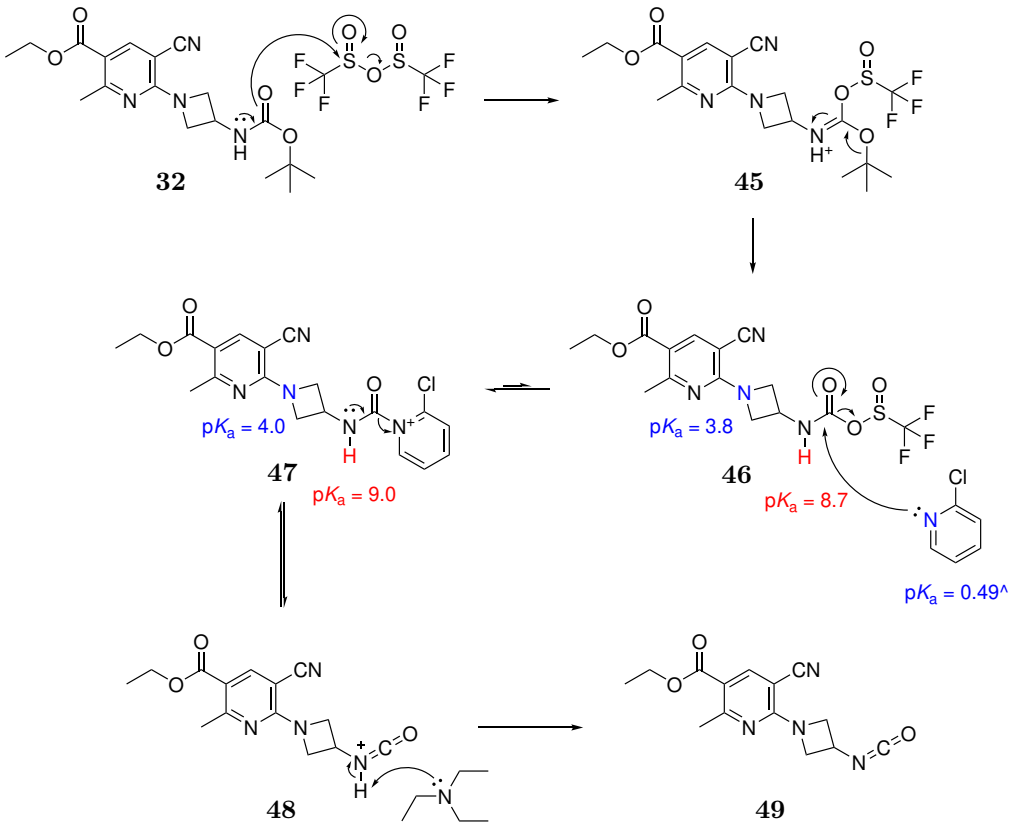

Scheme 9: Proposed mechanism for the *in situ* generation of isocyanate **49** from Boc-carbamate **32** in the presence of triflic anhydride. Blue represents a base and red for acids, pK_a were predicted with MolGpKa.[131] ^ Experimental pK_a obtained from Linnell and coworkers.[141]

Another plausible mechanism involves a Mukaiyama-like condensation. In this model, 2-chloropyridine forms an adduct with carbamate proton, facilitating a concerted mechanism for the isocyanate formation (**Scheme 10**).[142] This mechanism presumes that the low nucleophilicity of chloropyridine makes it unlikely to directly attack the anhydride intermediate **46**. Therefore, the Mukaiyama-like condensation could be an alternative mechanistic pathway to result in isocyanate **49**.

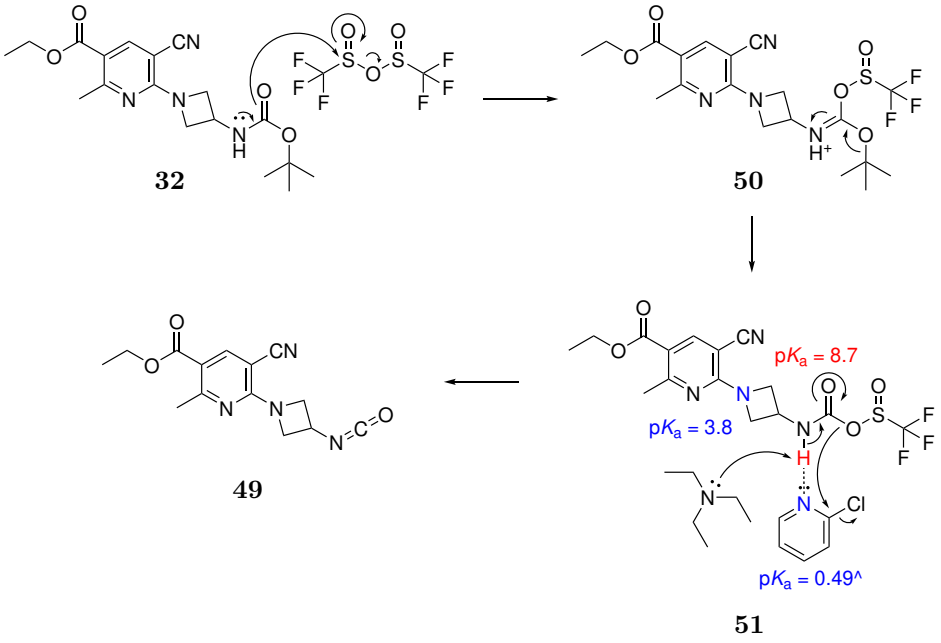

Scheme 10: Proposed mechanism for the *in situ* generation of isocyanate **49** from Boc-carbamate **32** in the presence of triflic anhydride via the Mukaiyama condensation-like reaction. Blue represents a base and red for acids, pK_a were predicted with MolGpKa.[131] ^ Experimental pK_a obtained from Linnell and coworkers.[141]

2.4 Fluorinated analogue synthesis

2.4.1 Towards ketone analogues

To access divergent intermediate **34**, ethyl ester **17** was hydrolysed under basic conditions with lithium hydroxide (LiOH) as shown in **Scheme 11** (step a). The product was isolated in quantitative yields.

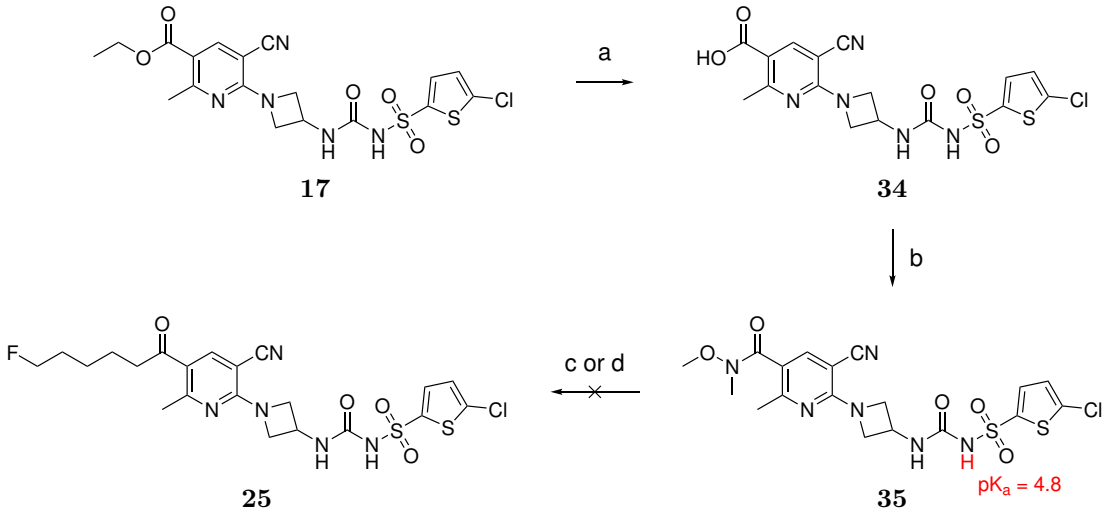

Scheme 11: Weinreb ketone synthesis strategy on divergent intermediate **34** to obtain the ketone series. (a) LiOH, H_2O/THF, rt, o/n, quant.; (b) EDC, *N*,*O*-dimethylhydroxylamine, pyridine, THF, 0 °C - rt, o/n, 83%; (c) i) 1-Bromo-5-fluoropentane, magnesium, Et_2O, reflux, 1 h, ii) THF, -78 °C - rt, o/n; d) i) 1-Bromo-5-fluoropentane, *i*PrMgCl·LiCl, THF, -40°C, 1 h, ii) THF, -78 °C - rt, o/n. Red indicates the proton was predicted to be acidic and pK_a was predicted with MolGpKa.[131]

For the ketone series, divergent intermediate **34** was coupled with *N*,*O*-dimethylhydroxylamine under standard 1-ethyl-3-(3-dimethylaminopropyl)carbodiimide (EDC)-mediated amide coupling conditions (step b, **Scheme 11**). The crude product was separated in aqueous acidic conditions to remove the urea byproduct and purified with flash chromatography to afford Weinreb amide **35** in good yields (83%).

The ketone synthesis began with focus toward ketone **25** (**Scheme 11**). This was prioritised due to the relative ease of handling the Grignard reagent precursor, 1-bromo-5-fluoropentane **52**, which is less volatile than the shorter bromofluoroalkanes. The Grignard reagent was presumably generated *in situ* by treating bromoalkane **52** with magnesium and refluxed until full consumption of magnesium was observed. However, after treating Weinreb amide **35** with two-fold excess of the Grignard reagent — accounting for one equivalent to neutralise the acidic urea proton (pK_a = 4.8, **Scheme 11**) — showed no consumption of starting material was observed. To enhance the reactivity, a Turbo-Grignard reagent was prepared by treating bromoalkane with isopropylmagnesium chloride-lithium chloride, yet once again no consumption of Weinreb amide **35** was observed.

Subsequent investigations confirmed that the Grignard reagent was not forming. Both standard Grignard (condition a, **Scheme 12**) and Turbo-Grignard conditions (condition b, **Scheme 12**) were used to generate a Grignard reagent. These were titrated in 1,10-phenanthroline and menthol solution as per the literature,[143] but the colour remained unchanged. The addition of a commercially prepared isopropylmagnesium chloride-lithium chloride successfully turned the solution purple. Therefore, Grignard reagent was unable to form, likely due to halogen exchange or coupling reactions with alkyl fluorides as reported in literature.[144] Consequently, the strategy to generate the fluoroalkyl ketones *via* the Weinreb ketone synthesis was likely incompatible and was temporarily shelved. We instead turned our attention to fluoroalkyl ester series synthesis through Steglich esterification.

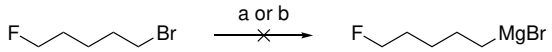

52 **53**

Scheme 12: Generation of the Grignard reagent **53** *via* standard conditions and Turbo Grignard conditions. The reagents were titrated with 1,10-phenanthroline and menthol to calculate the concentration of the Grignard reagent. (a) 1-Bromo-5-fluoropentane, magnesium, Et_2O, reflux, 1 h; (b) 1-Bromo-5-fluoropentane, *i*PrMgCl·LiCl, THF, -40 °C, 5 min.

2.4.2 Synthesis of ester analogues

To synthesise the ester analogues **19-21**, divergent intermediate **34** was treated with hydroxybenzotriazole (HOBt), *i*Pr_2NEt and EDC. HOBt was necessary to catalyse the Steglich esterification by generating an active HOBt ester *in situ*, facilitating the nucleophilic attack by the fluorinated alcohols. DCM was used as a solvent to drive the reaction by decreasing the urea byproduct solubility in solution. This furnished our ester series **19-21** from low to very good yields (32-86%).

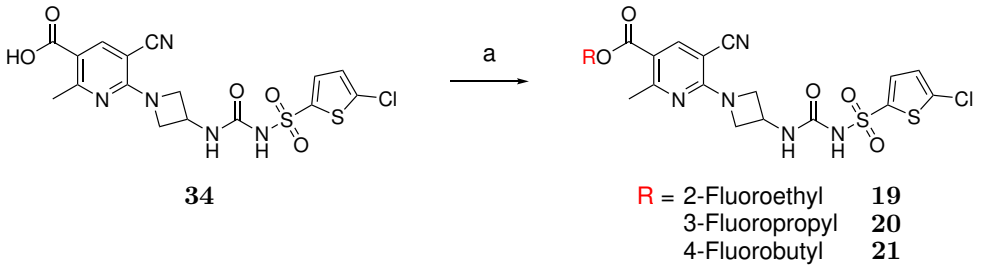

34

Scheme 13: Synthesis of ester analogues **19-21** *via* ester hydrolysis and then furnished by Steglich esterification. (a) Fluorinated alcohol, HOBt, iPr$_2$NEt, EDC, DCM, 0 °C - rt, o/n, 32-86%.

2.5 Concluding remarks

This chapter focused on the design and synthesis of fluorinated P2Y12 ligands that could retain binding at P2Y12 and enter the CNS. The proposed library of fluorinated P2Y12 compounds was based on the structural modification of lead **17**. A divergent synthetic strategy was developed to efficiently access the compound library. The initial reported synthetic pathway suffered from a poor cumulative yield (4% over 6 steps), which was impractical for a divergent synthetic strategy. The synthetic route for lead **17** was optimized, resulting in a significant improvement in overall yield (28% over 4 steps) and a reduction in the number of steps (**Scheme 14**). Further investigation in the urea coupling step could, particularly whether the exothermic quench decompose the isocyanate intermediate or stabilisation of the reactive isocyanate intermediate by lowering the reaction temperatures could improve the yields further.

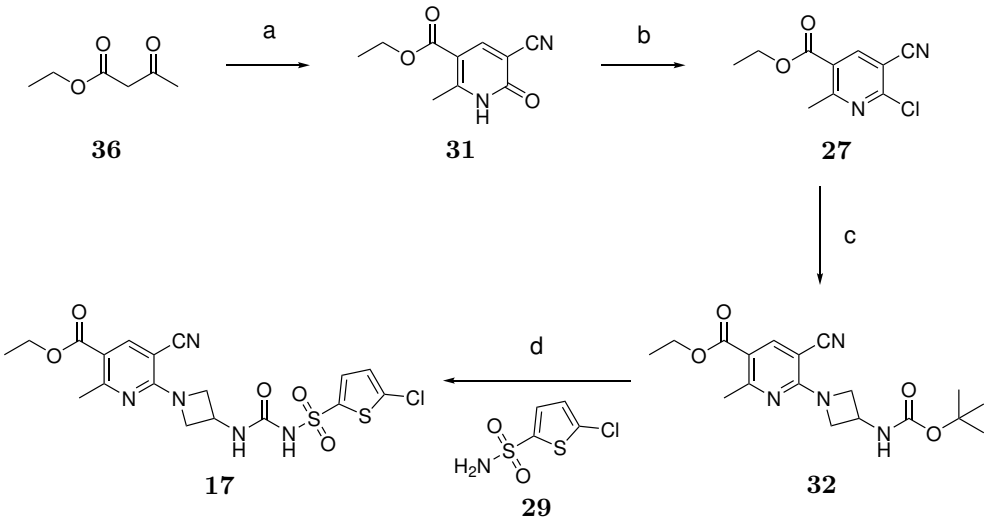

Scheme 14: Our pathway to access gram scale of lead **17** with a cumulative yield of 28% over 4 steps. (a) i) DMF-DMA, EtOH, 42 °C, 6 h, ii) Malononitrile, Et_3N, EtOH, 30 °C, 18 h, 67% (over 2 steps); (b) $POCl_3$, MeCN, 80 °C, 22 h, 87%; (c) *Tert*-butyl azetidin-3-ylcarbamate, $i Pr_2NEt$, DCE, rt, o/n, 93%; (d) i) Tf_2O, 2-chloropyridine, DCM, rt, 50 min, ii) 5-Chlorothiophene-2-sulfonamide **29**, Et_3N, rt, o/n, 49%.

Despite our efforts towards synthesising the ketone series, analogues **22**-**25** were not accessible *via* the Weinreb ketone synthesis pathway. To address this challenge, an alternative route is proposed in **Scheme 15**. This approach involves using a trimethylsilyl (TMS)-protected alcohol to perform the Weinreb ketone synthesis. Subsequent mild acidic deprotection would reveal the alcohol, which could be activated with tosyl chloride (TsCl). Finally, fluorination could be achieved using a nucleophilic fluorine source such as tetrabutylammonium fluoride (TBAF) or potassium fluoride (KF).

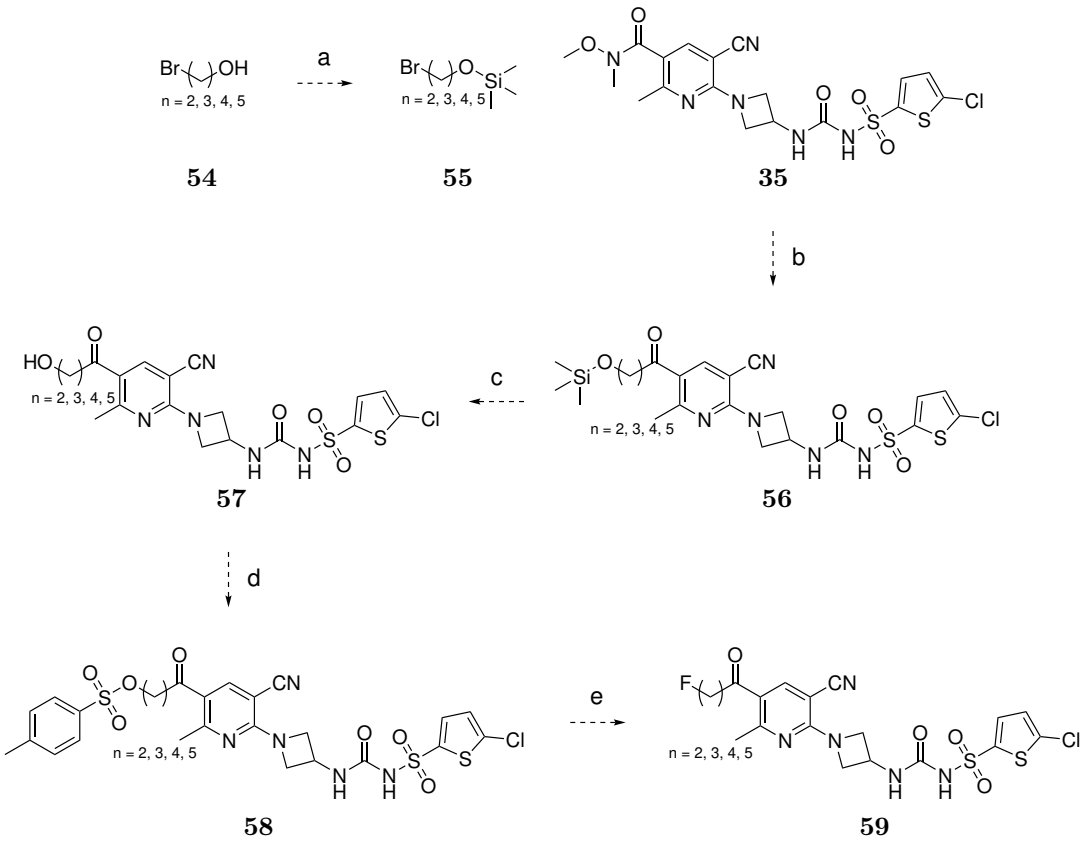

Scheme 15: Proposed synthetic route to access the ketone analogues **22**-**25**. (a) TMSCl, Et_3N, DCM, rt; (b) i) Magnesium, Et_2O, reflux, ii) THF, -78 °C - rt; (c) HCl, H_2O, rt; (d) TsCl, Et_3N, DCM, rt; (e) TBAF or KF, THF, rt.

Given the difficulties encountered in synthesising the ketone series, attention was turned to synthesising the fluorinated ester analogues **19**-**21**, which were successfully synthesised using Steglich esterification. These compounds are now intended for biological evaluation. However, the limited availability of P2Y12 radioligands for competitive binding assays halted further progression. As a more feasible alternative, the development of a fluorescence-based assay was considered more suitable given the available facilities.

Chapter 3

Computational studies for the development of fluorescent P2Y12 probes

3.1 P2Y12 Binding assays

Following the design and synthesis of fluorinated P2Y12 ligands discussed in **Chapter 2**, biological evaluation emerged as the next critical step. P2Y12 binding assessment methods are constrained to competitive radioligand binding assays,[110] relying on the displacement of a radioactive ligand with the ligand of interest to determine binding affinities (reported as K_{i} values). However, radioligands used for these assays are bespoke to individual organisations, as shown in **Table 5**, and are therefore inconvenient for research groups with limited resources to use in campaigns to develop novel P2Y12 ligands.[145] Further drawbacks for radioligand binding assays include the additional clearances, limited shelf-life, specialist training and equipment required to conduct these types of assays.[107,110,145,146] Surface plasmon resonance (SPR), fluorescent-based competition, and flux-based binding assays are developed as alternatives to circumvent these challenges.[146,147]

A useful binding assay for PET tracer development would evaluate binding affinity

Table 5: Reported radioligands used in competition binding assays for evaluating binding affinities of synthetic P2Y12 ligands. Asterisks (*) denote the locations of ^{3}H radionuclides. Binding affinities (K_{i}) measured by displacement of [^{3}H]PSB-0413 on human platelets.[157⊕] ADP and 2MeS-ADP were shown to bind proximately, but distinct sites on P2Y12.[158∝] Saturation binding assays allowed determination of the dissociation constant of [^{3}H]PSB-0413 on P2Y12 on human platelets (K_{d} = 6.5 nM).[158]

Radioligand (type of ligand)	K_{i} (nM)	Structure	Example References
[^{33}P]ADP (endogenous agonist)	75000⊕	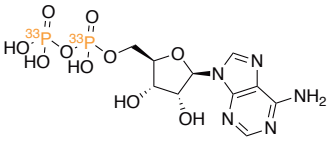	128,148,149
[^{33}P]2MeS-ADP (synthetic agonist)	32.1	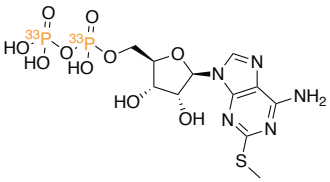	150–152
[^{3}H]2MeS-ADP (synthetic agonist)	32.1	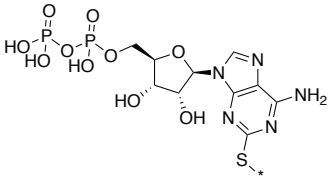	105
[^{125}I]AZ11931285 (non-competitive antagonist of ADP, competitive antagonist of 2MeS-ADP)	0.125	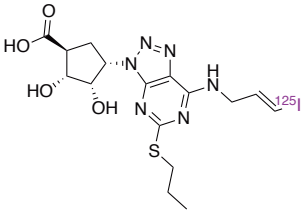	99,101,153–155
[^{3}H]PSB-0413 (competitive antagonist of ADP)	N/A∝	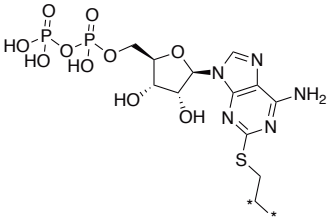	128,148,156

through receptor occupancy. Flux-based assays report on downstream ion-releasing mechanisms for binding affinity evaluation; this indirect evaluation technique is sub-optimal for PET tracer development.[159] SPR is a rapid method that can evaluate the binding affinity of a ligand when bound to the protein by detecting subtle energy changes.[160] Although, this strategy directly correlates with receptor occupancy, it is complex and requires specialist expertise for establishing a robust protocol. Fluorescent probes are user-friendly, have a long shelf life, and are readily accessible,

making them ideal for routine analysis of biological systems using fluorescence spectroscopy in modern research. Therefore, to achieve widespread accessibility and open up opportunities for future high-throughput screening (HTS) to enable discovery of CNS P2Y12 PET tracers, fluorescence-based competition binding assays would be the ideal choice.[146,161]

3.1.1 Fluorescence-based binding assays

Fluorescence-based assays fall either under direct or indirect measurement categories: Förster resonance energy transfer (FRET) and Bioluminescence resonance energy transfer (BRET) respectively.[162] Traditional FRET-based binding assays rely on direct laser excitation of the fluorescent probe, measuring the associated emission intensity to evaluate binding affinity.[163] However, FRET ligands are prone to photobleaching over the course of data collection and poor signal-to-noise ratio from non-specific binding,[164] and require controlled storage conditions away from light to maintain their fluorescence activity.[163]

BRET-based assays were developed to address the fundamental limitations of FRET-based assays.[162,165–168] The BRET approach involves tagging a protein with a bioluminescent enzyme, also referred to as the BRET donor, and pairing it with a suitable fluorescent ligand acceptor.[165] When the distance between BRET donor and acceptor is positioned within 10 nm (**Figure 13a**), light emitted by the BRET donor is absorbed by the BRET acceptor, which will subsequently fluoresce with a bathochromic shift as shown in **Figure 13b**.[165,167] This proximity-based fluorescence drastically reduces the background signal from non-specific binding, resulting in an improved signal-to-noise ratio.

The BRET ratio is a measurement used to quantify the binding affinity for BRET-based assays. It is calculated as the relative emission intensity of the acceptor compared to the donor.[169] A dose-response curve could be generated with BRET-ratio against the compound of interest concentration. This can be used to determine an IC_{50} value by extracting the data where 50% BRET-ratio was observed. Using the

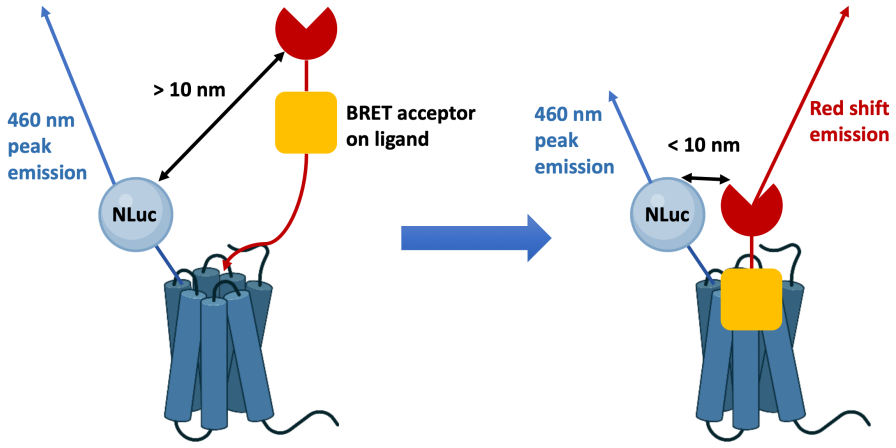

(a)

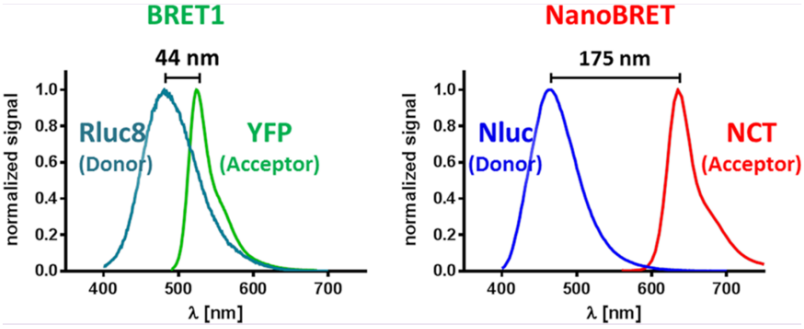

(b)

Figure 13: (a) The NLuc exhibits peak emission around 460 nm. When the BRET acceptor is within 10 nm of the donor, it absorbs emitted light and fluoresces at a longer wavelength, resulting in a bathochromic shift. (b) The peaks appear further apart on the NanoBRET than BRET, resulting in better signal-to-noise ratio when the BRET ratios are taken.[165]

Cheng-Prusoff equation, the IC_{50} can be converted to a K_i value. This approach allows for the evaluation of non-labelled ligands by assessing their ability to displace the fluorescent ligand.

NanoBRET represents the most advanced of the BRET-based assays, employing a small (19.1 kDa) bioluminescent enzyme, dubbed nanoluciferase (NLuc).[162,165–167] Its smaller size reduces the impact of the tag on both the protein's folded structure and ligand binding.[167] Additionally, pairing NLuc with a suitable fluorescent probe minimises spectral overlap, significantly improving the signal-to-noise ratio.[167] Therefore, the NanoBRET system was chosen as a platform for the development of a novel P2Y12 binding assay.

3.1.2 P2Y12 NanoBRET probe design

Designing a NanoBRET probe requires careful consideration of three fundamental structural components: the ligand, fluorophore, and linker (**Figure 14**). Our design approach for a P2Y12 NanoBRET probe followed a similar strategy exemplified by Toy and coworkers,[145,170] focusing on preserving receptor affinity while maximising the signal-to-noise ratio.[145,170]

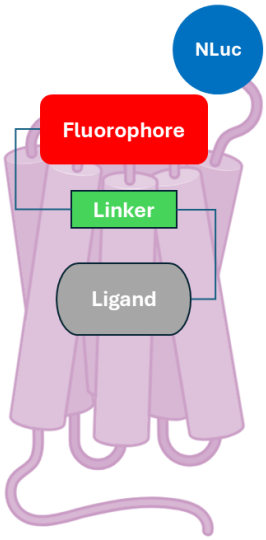

Figure 14: The general structure of a NanoBRET ligand, which consists of a ligand, linker and a fluorophore.

Considerations for the ligand

The inclusion of a linker and fluorophore can compromise receptor affinity compared to the parent ligand.[162] Therefore, selecting a high-affinity ligand with a well-characterised binding pose serves as the foundation for creating a successful NanoBRET probe.[171] Ligands with high-affinity (K_i in the low nanomolar range) are optimal for preserving receptor affinity.[162] The linker attachment site should be directed toward the extracellular space to facilitate BRET fluorescence while maintaining receptor compatibility. Additionally, the chosen site should feature suitable synthetic handles to enable reliable probe synthesis.

Considerations for the fluorophore

The fluorophore must align with the bioluminescence profile of NLuc to ensure compatibility with NanoBRET assays.[168] A small-molecule fluorophore is preferred to preserve the receptor affinity of the ligand when attached. Common small-molecule fluorophores used in NanoBRET probes include rhodamine, boron difluoride and pyridinium moieties.[172] Notably, rhodamine-based 5-TAMRA (often simply referred to as TAMRA) and difluoride-based BODIPY are widely used due to their reliable conjugation strategies, suitable fluorescence profiles, and commercial availability (**Figure 15**). The pyridinium-based Py-1 features an inbuilt synthetic conjugation handle, enabling direct fluorescent probe formation by stirring a free amine with the fluorophore precursor and base. The Py-1 precursor is not commercially available, but it can be made *via* a short synthetic sequence using common reagents.[173]

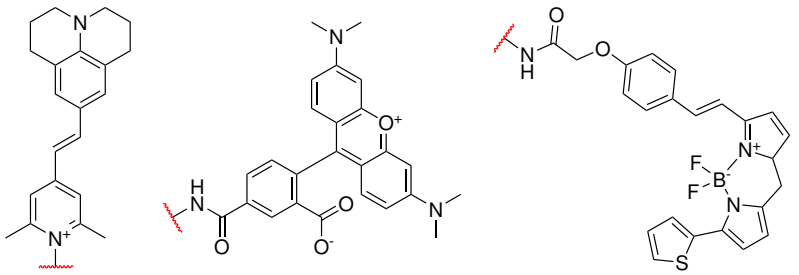

Figure 15: Structure of fluorophores that were investigated by Grätz and coworkers in their design of NanoBRET fluorescent probes.

Grätz and coworkers evaluated probes containing BODIPY, Py-1 and TAMRA fluorophores in their development of a histamine H2 receptor NanoBRET binding assay.[172] Although, the binding affinity was relatively 10-fold greater for probes containing BODIPY versus Py-1 or TAMRA, the latter two probes displayed significantly better BRET ratios. Furthermore, the BODIPY conjugate was unstable under incubation conditions, undergoing complete degradation within 24 h and making it unsuitable for biological evaluation.[172] Grätz and coworkers ultimately abandoned BODIPY-conjugated probes due to fluorophore instability and poor BRET ratio. This work emphasises that the practicality and accuracy of the NanoBRET probes

under assay conditions are other important factors to consider in the design.

Considerations for the linkers

The linker bridges the fluorophore and ligand, requiring careful optimisation of its length and structure to balance BRET efficiency and binding affinity.[167,171] Among the three probe components, rational linker design for linker type and length is the most challenging to achieve. Often this requires iterative adjustments through molecular modelling, synthesis, or both to determine the most appropriate attachment site for the linker.[145,167,170] It is generally accepted that the linker design is best determined on a case-by-case basis.[145,167,170] In saying that, SBDD approaches allow for efficient use of resources to predict the binding pose. This enables subsequent identification of the optimal attachment position and evaluation of whether the linker modifications are tolerable at the binding pocket.

Structure-based design approach

SBDD involves the use of computational tools to model ligand interactions, guiding ligand design, and therefore reducing the need for costly and time-consuming synthesis steps.[170] For the purposes of this work, protein-ligand interaction prediction tools were the primary focus for the design of a P2Y12 fluorescent probe. Previously published P2Y12 crystal structures serve as excellent models for this, as they accurately reflect the conformation of the protein bound to different agonists and antagonists.[174,175] More details on this are provided in **Section 3.2.3**. The industry-standard Glide package from Schrödinger's Maestro suite was used due to its user-friendly interface, high accuracy, and minimal training requirements.

Given the limited literature on linker and fluorophore effects when extending into extracellular space, a standardised docking protocol has yet to be established.[176,177] Most studies simplify docking simulations by considering only the truncated ligand-linker combination, excluding the fluorophore, to focus on optimal attachment points and potential binding site interactions.[145,168,170]

3.1.3 Chapter aims and objectives

The aim of this chapter was to identify a suitable structure for developing a NanoBRET ligand library. The selected structure should possess a synthetically tractable handle that extends toward extracellular space and can tolerate linker and fluorophore modifications. The first step involved selection of potential high-affinity antagonists with established binding poses. A docking library was constructed from ligand, linker, and fluorophore combinations, alongside an analogous library of truncated structures. These ligands were docked into an appropriate P2Y12 crystal structure using Glide to evaluate how structural modifications were tolerated within the receptor's binding site.

3.2 NanoBRET P2Y12 probe library

3.2.1 Ligand triage

Literature ligands provided a useful starting point for developing a fluorescent probe in a resource-efficient manner. After manually tabulating structures and affinities of hundreds of P2Y12 ligands from the peer-reviewed and patent literature, we identified high affinity P2Y12 ligands **60** and **61** in a patent from Actelion.[178] These ligands appeared synthetically tractable, potentially allowing a convergent synthetic strategy towards the core structure, and subsequent late-stage functionalisation to synthesise a range of analogues *via* amide coupling reactions.

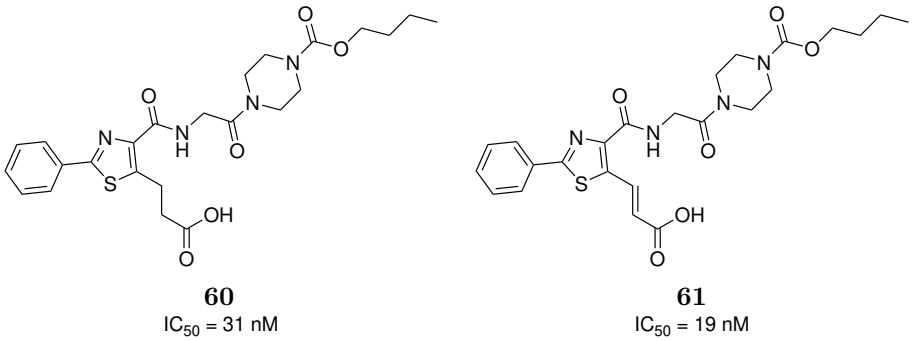

Figure 16: Lead ligands identified from Caroff and coworkers resembling the general antagonist structure of **Figure 11**.

Upon visual inspection, we identified key similarities between antagonist **60** and antagonist pharmacophore model as shown in the overlay of **Figure 17**. While the carbonyl of the carbamate forms a H-bond with Asn159, the butyl chain is likely stabilised in the narrow hydrophobic crevice. Typically, antagonists have π–π stacking interactions with Tyr105, but in this case, piperazine binds via hydrophobic interactions. The linker retained the critical Lys280 interaction, while the phenylthiazole moiety occupied the large hydrophobic pocket at opposite end of the binding site, stabilising the ligand in the antagonist binding pose. The propanoate moiety could either extend deeper into the receptor or orient towards the extracellular space, warranting further investigation in molecular docking studies.

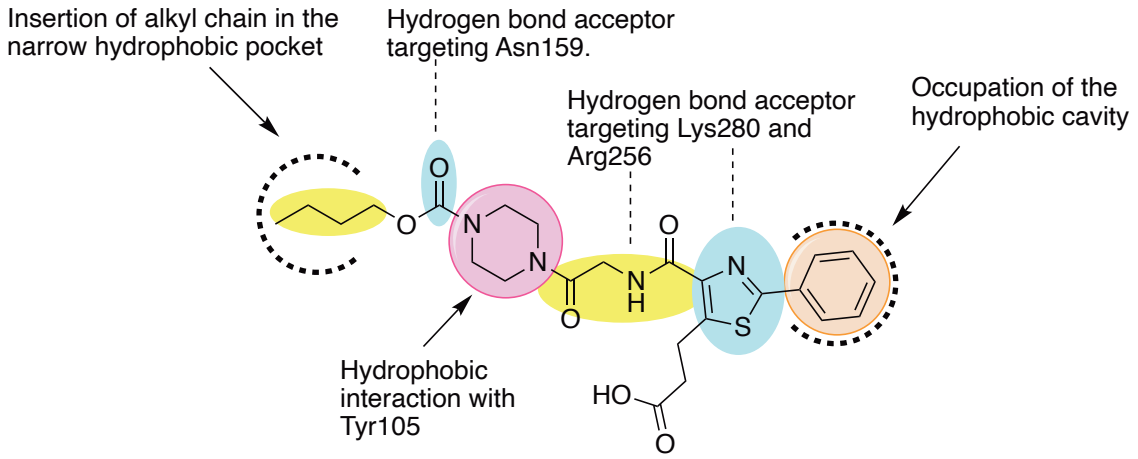

Figure 17: Lead ligand **60** overlay over the general antagonist pharmacophore structure.[178] The propanoate falls outside the crucial bonding interactions and could be facing deeper towards the receptor or point outwards towards extracellular space. The carboxylic acid serves as a convenient handle to divergently synthesise our library.

3.2.2 Ligand library

To construct the ligand library, the components that remained to be considered were the fluorophore and linker. Py-1 and TAMRA were selected due to their superior stability and BRET ratios compared to BODIPY. However, selecting a single fluorophore proved challenging due to insignificant differences in their reported properties. Consequently, both fluorophores were subjected to molecular docking studies to assess potential variations in binding interactions.

Polyethylene glycol (PEG) and linear alkyl chains are commonly used linkers for NanoBRET probes in bridging fluorophores with ligands.[145,172] These linkers were selected as starting points for further investigation. The resulting combinations of ligands, linkers, and fluorophores are summarised in **Table 6**, following the design considerations discussed in **Section 3.1.2**.

Table 6: Summarised general structure of the P2Y12 fluorescent probe combinations. S = Single bond; D = Double bond (*E*-isomer).

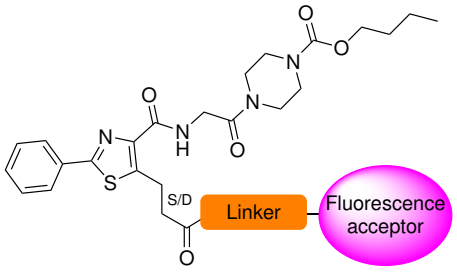

S/D	Fluorescence acceptor	Linker	Compound number
S	TAMRA	C_2H_4	**62**
		C_3H_6	**63**
		C_4H_8	**64**
		PEG1	**65**
		PEG2	**66**
	Py1	C_2H_4	**67**
		C_3H_6	**68**
		C_4H_8	**69**
		PEG1	**70**
		PEG2	**71**
D (*E*-isomer)	TAMRA	C_2H_4	**72**
		C_3H_6	**73**
		C_4H_8	**74**
		PEG1	**75**
		PEG2	**76**
	Py1	C_2H_4	**77**
		C_3H_6	**78**
		C_4H_8	**79**
		PEG1	**80**
		PEG2	**81**

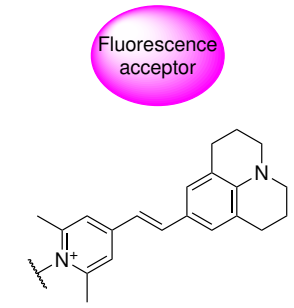

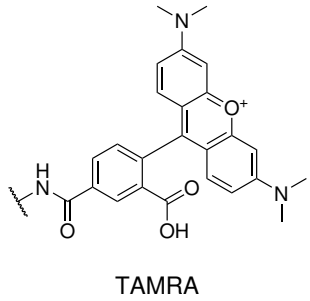

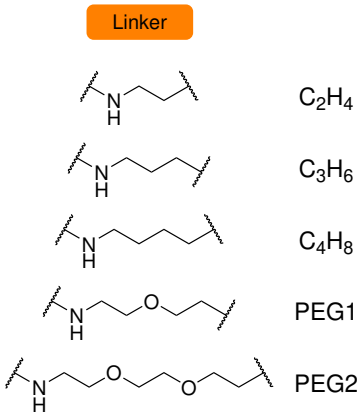

Additionally, an analogous series of this library excluding the large fluorophores is shown in **Figure 18**. This was designed as an initial *in silico* screening library to simplify docking calculations. Ethyl ester analogues **82a** and **83a**, previously synthesised and evaluated for P2Y12 binding by Caroff and coworkers,[178] served as benchmarking compounds in molecular docking studies.

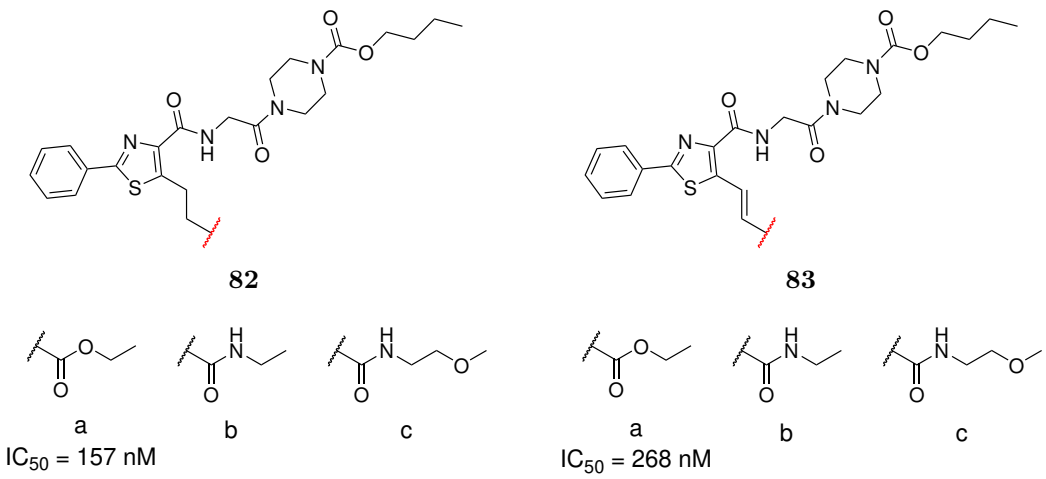

Figure 18: Truncated linker structures submitted to molecular docking studies to investigate linker tolerability at P2Y12. Binding IC_{50} values were obtained from a displacement binding assay using Chinese hamster ovary cells expressing human P2Y12 with [^{3}H]2MeS-ADP.[178]

3.2.3 Protocol

The molecular docking studies were conducted with the Glide package within the Schrödinger Maestro suite. Available P2Y12 crystal structures from the literature were reviewed to identify a suitable template for docking simulations. Zhang and coworkers resolved several P2Y12 crystal structures, including antagonist-, agonist-, and inverse agonist-bound conformations.[174,175] Among these, the competitive antagonist-bound structure (PDB ID: 4NTJ; crystallised ligand (AZD1283 **18**)) was selected as the template for molecular docking studies. The resolution of 4NTJ (2.62 Å) is considered sub-optimal for docking studies (crystal structures with < 2 Å are typically preferred) due to poor details of the electronic structure.[179] However, Paoletta and coworkers successfully rationalised the observed binding data for a range of structurally diverse P2Y12 antagonists in their *in silico* docking studies.[127] This was the clear choice, as our chosen lead compounds from the Actelion patent were also competitive P2Y12 antagonists with similar pharmacophore that occupy the same binding pocket **Figure 19**.

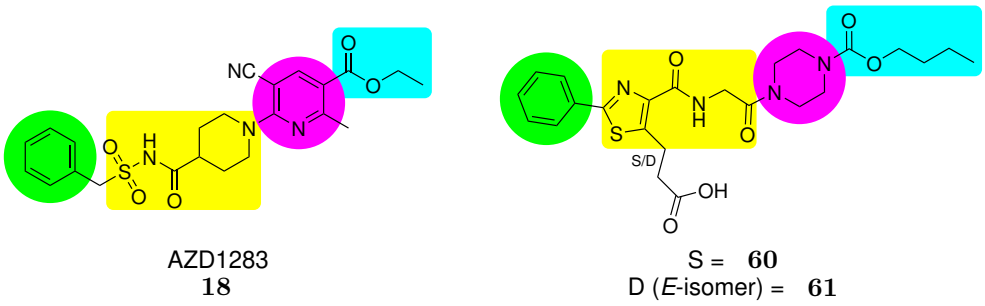

Figure 19: Structure of the antagonist-bound co-crystallisation ligand (AZD1283 **18**) and thiazoles **60** and **61**. The structural similarities between the compounds are matched with the corresponding highlighted colour. S = Single bond, propanoic acid **60**; D = Double bond (*E*-isomer), propenoic acid **61**.

The Protein Preparation Wizard tool was used for protein preparation and Prime was used to fill in missing side chains, loops, or hydrogen atoms (HA). PROPKA predicted and adjusted protonation states of the protein at pH 7 and then the overall structure was minimised to relax HA movement, bonds, angles and clashes using OPLS3 force field. Ligands, water, detergents, fatty acids, and cholesterol molecules were manually removed. All that remained was the optimised protein structure, which was used for ligand-protein binding modelling.

Ligand preparation was performed using the LigPrep package, which predicted likely ionisation states at pH 7 ± 2 using Epik.[180] Tautomers were generated and geometries were optimised using OPLS3 force field. Conformers were subsequently generated using the Confgen tool, generating 64 conformers for each individual ligand. For well-defined binding pocket/ligand pairings, different conformers typically converge upon a single binding pose regardless of initial conformation.

A Glide grid was generated with the Receptor Grid Generation tool, with the co-crystallised ligand referenced as the centroid for the modelling study. The grid was centred around the ligand and defined by a 20 $Å^3$ box as we expected the ligand was likely to bind within the vicinity of other literature antagonists. Setting a boundary limit speeds up calculations by limiting the search space and restricts the generation of erroneous results from Glide attempting to over-fit to all potential binding pockets.

With the individual components for the docking prepared, we then submitted

our prepared ligand conformers to the prepared protein with extra precision (XP) protocols. The top scoring docking conformations were visually inspected to verify the ligand docking depicts the expected binding pose and interactions reported by Paoletta, Zhang and coworkers.[127,174]

3.3 Docking results

3.3.1 Validation and benchmarking of modelling

Redocking AZD1283 to 4NTJ showed that the top-scoring predictions unanimously converged upon the binding pose depicted in **Figure 20a**. Asn159 was able to form H-bonding interactions with the carbonyl of the ester group, while the ethyl ester inserts into the hydrophobic pocket and the pyridine π–π stacking interactions with Tyr105. The sulfonamide was calculated to be anionic under physiological conditions and forms an ionic interaction with Arg256. The sulfonyl and carbonyl groups of the sulfonamide form H-bonding interactions with Lys280 and Arg256. Finally, the benzyl group occupies the large hydrophobic cavity anchoring the structure as shown in **Figure 20b**. This validation study replicated the experimental binding pose in the crystal structure and conforms with the results obtained by Paoletta and coworkers,[127] allowing us to perform molecular docking studies for our ligand library.

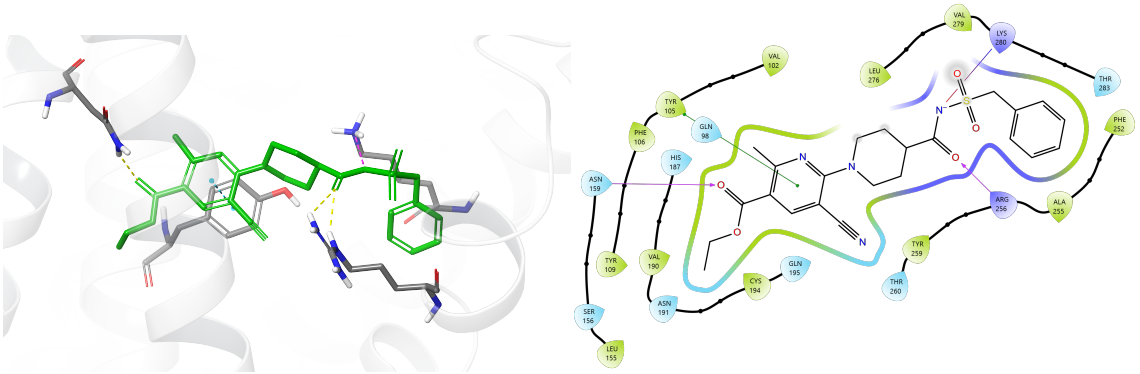

(a) **(b)**

Figure 20: Validation of binding pose and interactions with the antagonist bound P2Y12 crystal structure (4NTJ). a) AZD1283 was redocked for model validation. b) 2D residue interactions between AZD1283 at the antagonist binding pocket.

The orientation of the propanoate and propenoate moieties of leads **60** and **61** were first investigated to determine whether additional binding interactions could be picked up by this ligand scaffold. Both compounds shared the same core binding interactions (**Figure 21a-d**). The carbonyl of the carbamate exhibits H-bonding interactions with Asn159, while the narrow hydrophobic pocket accommodates the *n*-butyl chain. The thiazole exhibits π–cationic bond interactions with Lys280 and the carbonyl of the secondary amide exhibits hydrogen bonding interactions with Arg256. The phenyl ring inhabits the large hydrophobic cavity, stabilising the ligand in a binding pose similar to that of the co-crystallised ligand. Predictably, the propanoate is more flexible than its unsaturated counterpart, allowing the alkyl chain to fold back on itself and enabling ionic bonds to form between both oxygens of the carboxylic acid and Lys280. On the other hand, the propenoate remains rigid and points towards extracellular space, permitting ionic bonds with a single oxygen of the carboxylic acid with the Lys280.

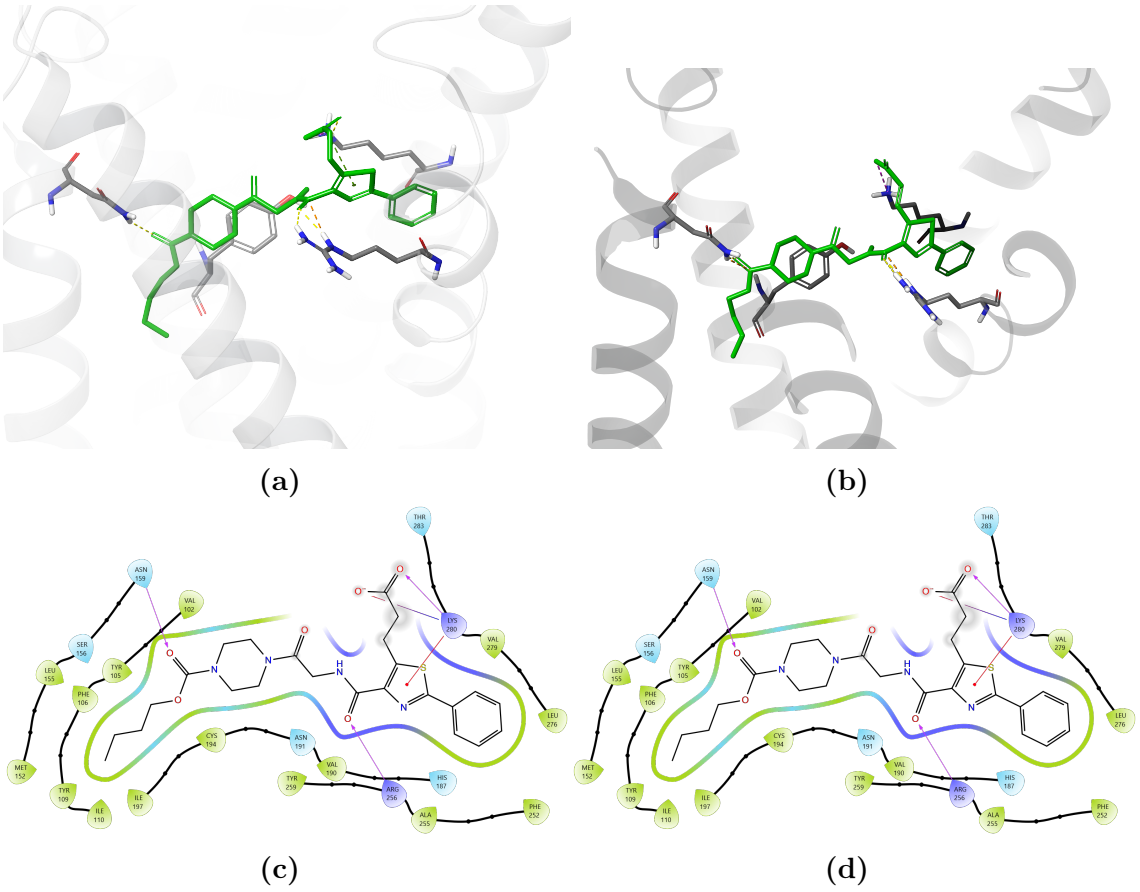

Figure 21: Glide docking of ligands at the antagonist bound P2Y12 crystal structure (4NTJ). a) 3D binding pose of thiazole **60**. b) 3D binding pose of thiazole **61**. c) Thiazole **60** key residue binding interactions. d) Thiazole **61** key residue binding interactions.

The GlideXP scores suggest that propanoate **60** (GlideXP score = -9.9, **Appendix 1**) exhibits stronger affinity compared to propenoate **61** (GlideXP score = -8.9, **Appendix 1**). However, these predictions were inconsistent with experimental findings, which demonstrated that the propenoic derivative (IC_{50} = 19 nM) possessed a 2-fold higher affinity for P2Y12 than its propanoic counterpart (IC_{50} = 31 nM).[178] It was speculated that scoring function may not have adequately penalised the strained folding of the propanoate moiety around Ly280. Additionally, Ma and Dougherty suggested the π–cationic bonding interaction strength could be similar to hydrogen and ionic bonding interactions.[181,182] However, GlideScore could undervalue contributions from the electron donating propenoate group *via* π-bonds to thiazole, which further enhances π–cationic bonding interaction.[183]

Docking ethyl ester analogues **82a** and **83a** was expected to reveal similar binding

interactions. However, discrepancies were flagged by the rigid ethyl propenoate analogue (**Figure 22a and c**). This analogue sacrificed the π–cationic bonding interaction with Lys280 in favour of a H-bonding interaction between the carbonyl of the secondary amide. Consequently, all interactions with Arg256 were lost and contorted the binding pose to fit within the pocket as shown in **Figure 22**.

In contrast, ethyl propanoate analogue **82a** sacrificed the ionic interactions with Lys280 (**Figure 22a and b**), but conserved the rest of the binding interactions. The GlideXP scores suggested ethyl propanoate **82a** (GlideXP = -8.8, **Appendix 1**) bound with higher affinity to P2Y12 than ethyl propenoate **83a** (GlideXP = -7.9, **Appendix 1**), reflecting previously reported experimental data (ethyl propanoate **82a** IC_{50} = 157 nM and ethyl propenoate **83a** IC_{50} = 268 nM).[178] These data served as a benchmark for the amide linker modifications discussed in the following sections.

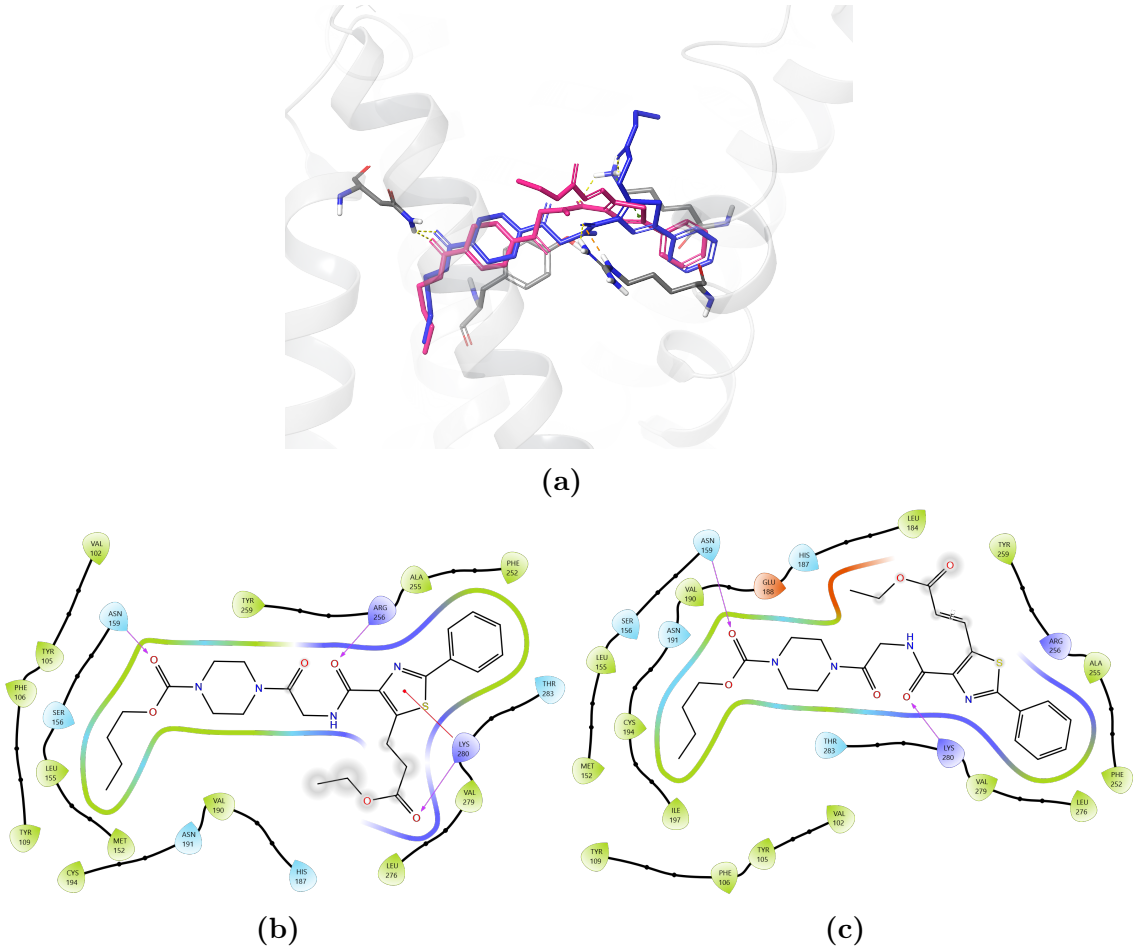

Figure 22: Glide docking of ligands at the antagonist bound P2Y12 crystal structure (4NTJ). a) 3D binding poses of propanoate **82a** (blue) and propenoate **83a** (pink). b) Ethyl propanoate **82a** key residue binding interactions. c) Ethyl propenoate **83a** key residue binding interactions.

3.3.2 Docking of truncated NanoBRET probes

The tolerability of truncated amides in the P2Y12 binding pocket was investigated by referencing to ester analogues of identical or similar atomic length. Ethyl propanamide **82b** was predicted to lose both H-bonding interactions with Asn159 and Arg256 to accommodate the ethyl amide (**Figure 23a and b**). Instead, the binding interaction became centred around the π–cationic bond with Lys280. This change facilitated additional H-bonding interactions with Tyr259 and Lys280. However, the piperazine group became exposed to the non-charged polar environments, reducing the hydrophobic stabilisation with Tyr105. The loss of these stabilisation interactions and H-bonding penalties were reflected in the reduced GlideScore (GlideXP = -7.7,

Appendix 1).

In contrast, ethyl propenamide **83b** was rewarded for its rigidity, occupying the binding pocket in a similar pose to that predicted from inspection of the co-crystallised ligand and pharmacophore model (**Figure 23a and c**). H-bonding interactions with Asn159 and Arg256 were preserved, while an additional H-bond with Tyr259 was established. The GlideScore for ethyl propenamide **83b** (GlideXP = -8.6, **Appendix 1**) was the highest among the truncated linker series, likely due to the additional hydrophobic stabilisation.

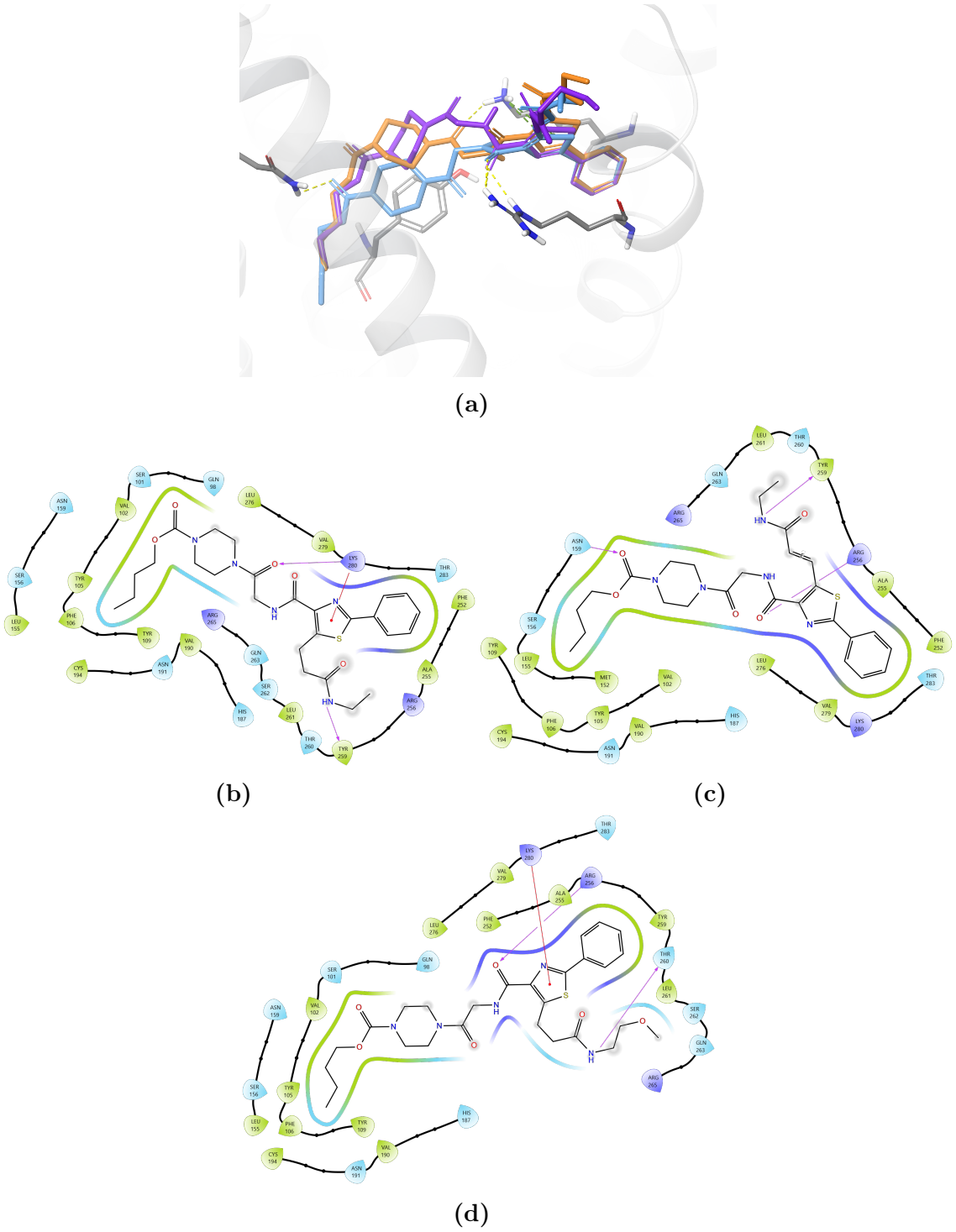

Figure 23: Glide docking of ligands at the antagonist bound P2Y12 crystal structure (4NTJ). a) 3D binding poses of propamides **82b** (orange) and **82c** (purple), and propenamide **83b** (light blue). b) Ethyl propanamide **82b** key residue binding interactions. c) Ethyl propenamide **83b** key residue binding interactions. d) Methoxyethyl propanamide **82c** key residue binding interactions.

Methoxyethyl propanamide **82c** introduced additional polar interactions along an extended linker. We predicted that this moiety may clash with the bulky hydrophobic

Tyr259 residue, rather than H-bonding to it, resulting in a reduced docking score. This clash was observed on inspection of the docking interaction map, where the amide of the truncated linker instead participated in H-bonding to Thr260. Additionally, the π–cationic bond with Lys280 was conserved, and an H-bonding interaction with Arg256 was gained. The GlideScore suggested higher affinity for the methoxyethyl moiety (GlideXP = -8.0, **Appendix 1**) compared to ethyl propanamide **82b**, likely due to additional polar interactions introduced by the ether group.

Upon visual inspection, methoxyethyl propenamide **83c** failed to display a binding pose similar to that of the co-crystallised ligand. The structural rigidity of the propenamide appeared to restrict its ability to flex and rotate compared to methoxyethyl propanamide **82c**. This rigidity suggested that methoxyethyl propenamide **83c** was likely to adopt another binding pose to avoid unfavourable interaction with Tyr259. Consequently, PEG linker modifications on propenamide **61** were predicted to result in reduced affinity.

Overall, Glide docking results indicated that most amides modifications to carboxylic acid and ester lead compounds were tolerated within the P2Y12 binding pocket. Propanamide analogues **82b** and **82c** were predicted to maintain affinity at P2Y12 by forming H-bonds with either Tyr259 or Thr260. Ethyl propenamide **83b** was predicted to be higher affinity than the parent ethyl ester analogue **83a**.

3.3.3 Docking of NanoBRET probes

We chose to further investigate whether it would be possible to dock some of the full-length fluorescent probes following a similar methods to obtain further information. After processing the fluorescent probe library through LigPrep, a protonated series (protonated at the nitrogen of the julolidine headgroup) of the Py-1 compounds were generated. Conformers of neutral and protonated compounds were then created and docked following the standard protocol (**3.2.3**).

Propanamide series

From the truncated docking studies, it was observed that a propanamide moiety demonstrated greater tolerance to linker modifications due to the increased flexibility of the synthetic handle. This flexibility was evident in the binding interactions of the ethyl linker derivative **67**, which adopted a binding pose to allow for the protonated julolidine headgroup to occupy a hydrophilic pocket (**Figure 24b**). Meanwhile, the thiazole moiety maintained crucial π–cationic interactions with Lys280, and the amide H-bonded with Arg256. However, the butyl chain was unable to fully insert into the narrow hydrophobic pocket, potentially limiting additional hydrophobic stabilisation interactions (**Figure 24a**).

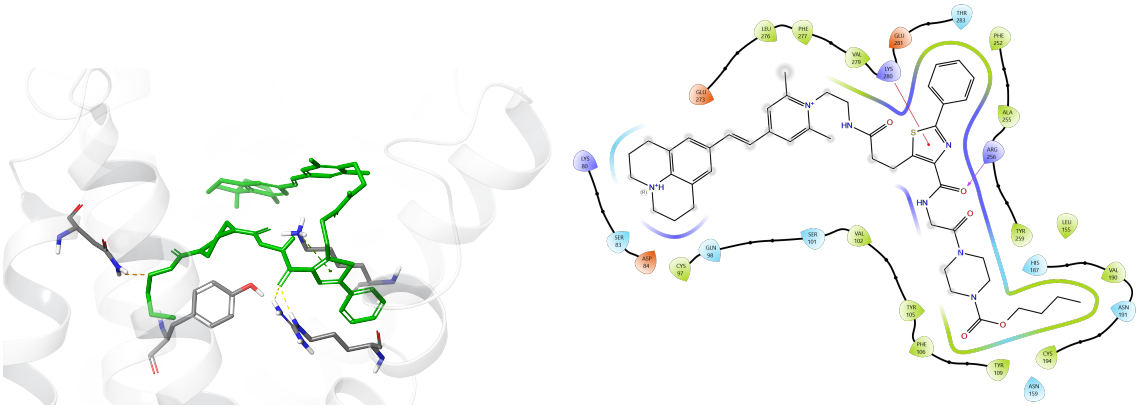

(a) **(b)**

Figure 24: Glide docking of fluorescent probe **67** at the antagonist bound P2Y12 crystal structure (4NTJ). a) 3D binding pose of ethyl propanamide **67**. b) Key residue binding interactions of ethyl propanamide **67**.

The PEG1 derivative **70** (GlideXP = -7.9, **Appendix 2**) achieved the highest score among the P2Y12 fluorescent probe library. As shown in **Figure 25b**, it conserved interactions with Lys280 through H-bonding and π–cationic bonding interactions, while hydrophobic stabilisation from the alkyl chain and phenyl ring persisted. Interestingly, the Py-1 fluorophore moiety displayed H-bonding with Glu273 and π–π stacking interactions with Phe277. The PEG1 linker was predicted to afford the longest tolerable fluorescent ligand from the docked library.

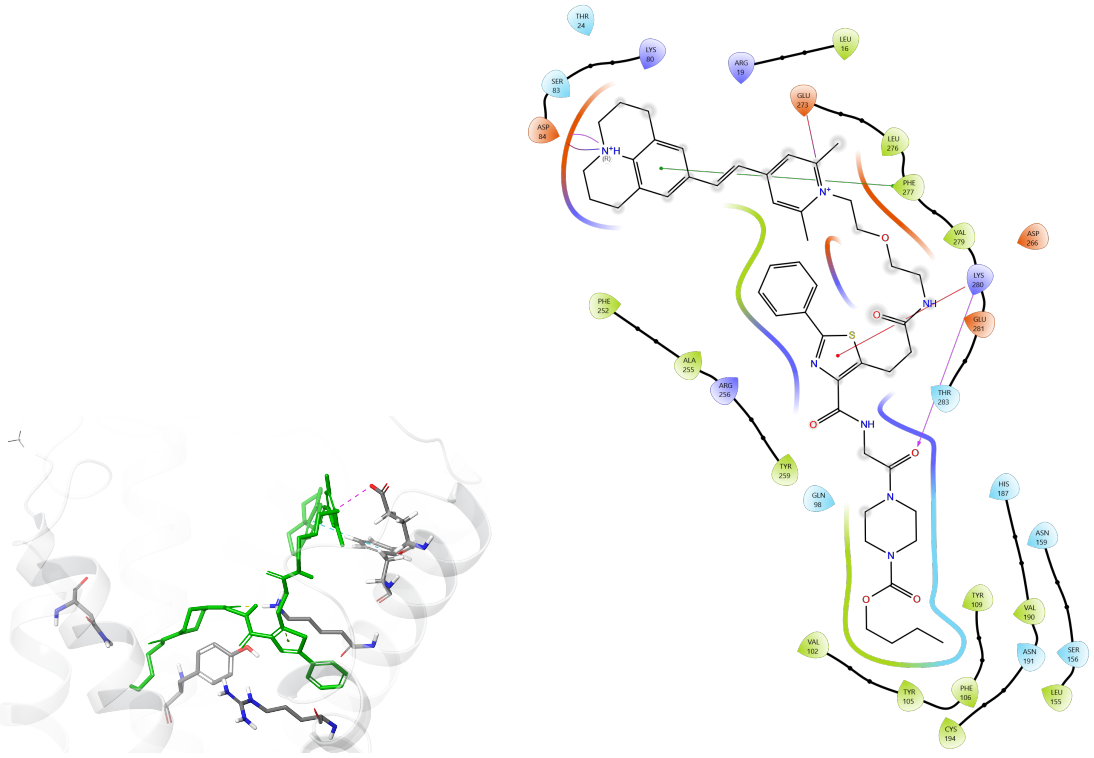

(a) **(b)**

Figure 25: Glide docking of fluorescent probe **70** at the antagonist bound P2Y12 crystal structure (4NTJ). a) 3D binding pose of PEG1 propanamide **70**. b) Key residue binding interactions of PEG1 propanamide **70**.

For TAMRA propanamide probe **70**, π–π stacking interactions with Tyr192 were gained at the expense of interactions with Glu273 and Phe277 (**Figure 26**). Consequently, phenyl ring hydrophobic interactions were disturbed, pushing the phenyl ring toward extracellular space. Despite adopting an unexpected binding pose, critical H-bonds with Arg256 and Lys280 were preserved. Regardless, this fluorescent probe displayed the lowest score of all compounds in the propanamide series (GlideXP = -5.6, **Appendix 2**).

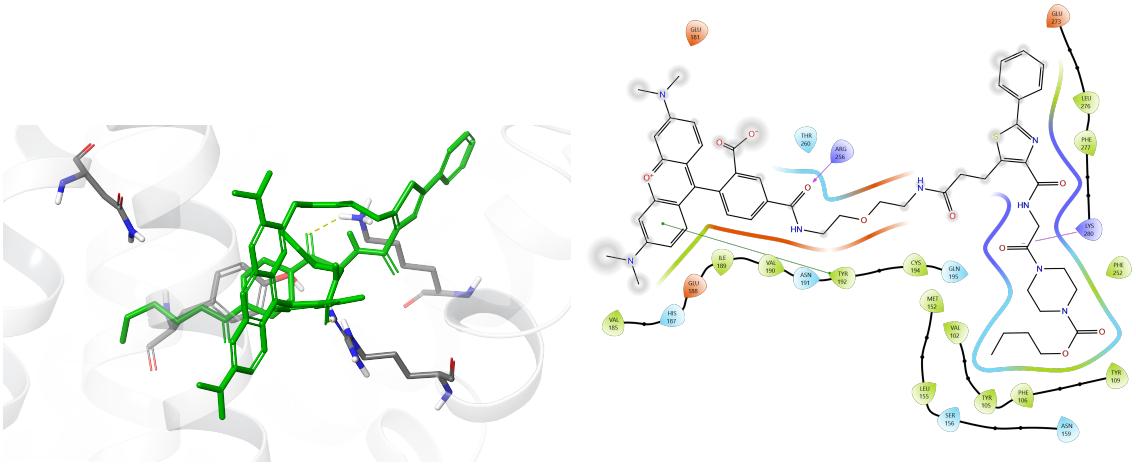

(a) **(b)**

Figure 26: Glide docking of fluorescent probe at the antagonist bound P2Y12 crystal structure (4NTJ). a) 3D binding pose of TAMRA-propanamide **65**. b) Key residue binding interactions of TAMRA-propanamide **65**.

Propenamide series

Propenamide **77** was the only fluorescent probe that appeared to occupy the P2Y12 binding pocket by the ligand moiety adopting the pose of the co-crystallised ligand. It conserved H-bonding interactions with Arg256 and Lys280, while the alkyl chain inserted into the hydrophobic pocket. The phenyl ring and julolidine moiety of the Py1 fluorophore also occupied hydrophobic cavities, contributing to its favourable binding at P2Y12 (GlideXP = -6.4, **Appendix 2**).

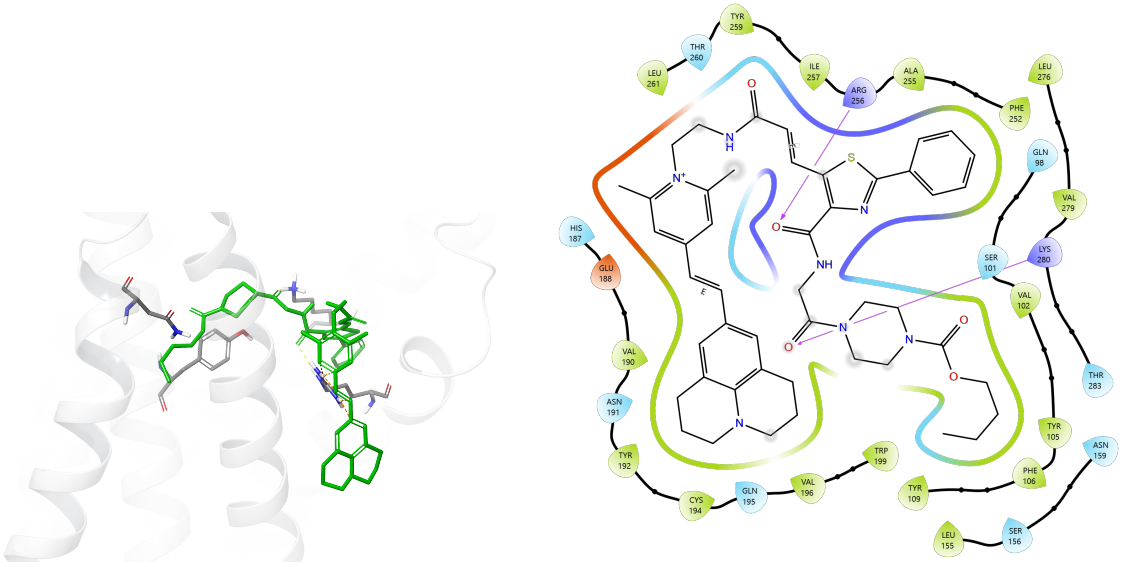

(a) (b)

Figure 27: Glide docking of propenamide **77** at the antagonist bound P2Y12 crystal structure (4NTJ). a) 3D binding pose of propenamide **77**. b) Key residue binding interactions of propenamide **77**.

3.4 Summary

This chapter aimed to identify a suitable structure for developing a NanoBRET ligand library. To achieve this, existing literature ligands were triaged based on their ability to adopt binding poses consistent with the established binding conformation of P2Y12 antagonists. A SBDD approach using *in silico* docking was employed to evaluate whether selected ligands conformed to the known binding pose. Subsequently, NanoBRET probes and the analogous truncated linkers were docked, and the structures were evaluated.

The results from the truncated fluorescent probes were promising. Not only were the amide linker modifications predicted to be tolerated, but they also gained H-bonding interactions with Tyr259 or Thr260. The scores of propanamides **82b** and **c**, and propenamide **83b** were similar to those of the ethyl ester benchmarks, suggesting that the binding affinity could conceivably be experimentally conserved. However, methoxyethyl propenamide **83c** was the only ligand that did not display binding poses resembling those of P2Y12 antagonists. This was potentially due to

the linker rigidity restricting the orientation of the linker and clashes with Tyr259. Consequently, no ligand poses that reflected the co-crystallisation ligand binding pose was observed.

Molecular docking studies on P2Y12 NanoBRET fluorescent probes yielded limited insights to understanding the binding interactions or pose. The suggested poses for the propenamide series were likely affected by a grid size that was too small, potentially forcing unrealistic orientations, especially for the rigid propenamide series. Additionally, it would be unlikely for the high-affinity thiazoles **60** and **61** to be displaced by the fluorophores. Therefore, manually assigning key ligand binding interactions or enlarging the Glide grid could remedy these unrealistic poses.

The molecular docking of the truncated fluorescent probes gave insight in the amide modification tolerance. The orientation of either the propenamide or propanamide moieties on thiazoles **60** and **61** suggests potential suitability for repurposing in NanoBRET assays. Based on the highest GlideScore from the docked truncated compounds, propenoic acid **61** was selected as the lead ligand for NanoBRET probe development.

Chapter 4

Towards the synthesis of NanoBRET probes for P2Y12

4.1 Introduction

Chapter 3 discussed our approaches toward the computational design of P2Y12 NanoBRET probes. This involved the selection of a known P2Y12 ligand as a starting point to build upon propenoic acid **61**, as well as potential linkers and fluorophores. A combination of these components produced a library of possible fluorescent probes. Overall, the results indicated that the carboxylic acid attachment position pointed towards extracellular space as intended and the modifications would likely be tolerated as summarised in **Figure 28**. The compound library from the docking studies was then reviewed for synthetic accessibility and predicted affinity, creating a focused library of compounds to initially synthesise.

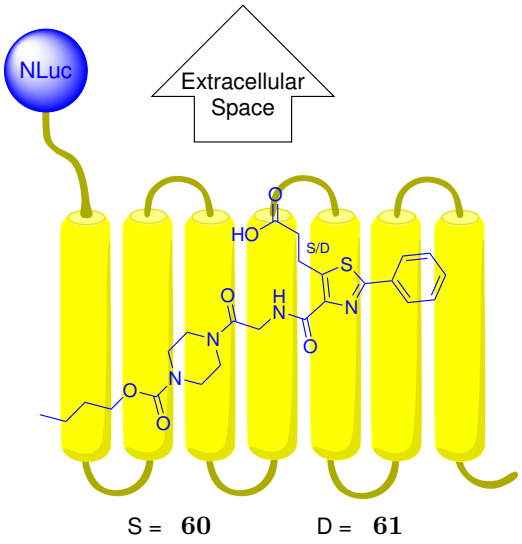

Figure 28: Summary of the Glide docking data: The carboxylic acid faces toward extracellular space and the amide modifications were predicted to be tolerable at P2Y12. S = Single bond, propanoic acid **60**, D = Double bond, propenoic acid **61**.

4.1.1 Chapter aims

The aim of this chapter was to synthesise P2Y12 NanoBRET probe candidates to aid the development of a fluorescence-based competition binding assay. As discussed in **Chapter 3**, the carboxylic acid was modelled to be the ideal position to attach a fluorophore (**Figure 28**). TAMRA and Py-1, were evaluated as fluorophores with suitable properties for our application. Additionally, linkers of various lengths were explored in order to identify the optimal linker length for both affinity and NanoBRET signal strength.

4.1.2 Proposed fluorescent probe library

Propenoic acid **61** was selected as the focus ligand to build the fluorescent probe. Among the truncated amide library, docking studies predicted propenamide **83b** was the highest affinity amide at P2Y12 (**Appendix 1**). We chose to conjugate this ligand to a selection of suitably pre-functionalised commercially available alkyl and PEG linkers. The fluorophore components, Py-1 and TAMRA, were selected for their fluorescence properties and stability.[172] The ligand, linker and fluorophore

components were combined to form a structurally diverse P2Y12 NanoBRET probe library (**Table 7**).

Table 7: Proposed fluorescent probe library based on the results and discussion in **Chapter 3**.

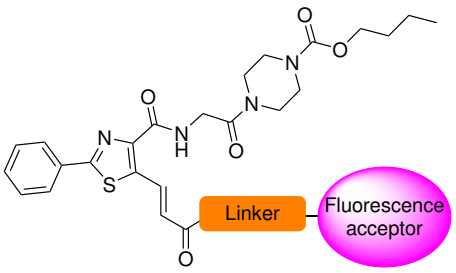

Fluorescence acceptor	Linker	Compound number
Py-1	C_2H_4	**77**
	C_3H_6	**78**
	C_4H_8	**79**
	C_5H_{10}	**84**
	C_6H_{12}	**85**
	PEG1	**80**
	PEG2	**81**
	PEG3	**86**
TAMRA	C_2H_4	**72**
	C_3H_6	**73**
	C_4H_8	**74**
	C_5H_{10}	**87**
	C_6H_{12}	**88**
	PEG1	**75**
	PEG2	**76**
	PEG3	**89**

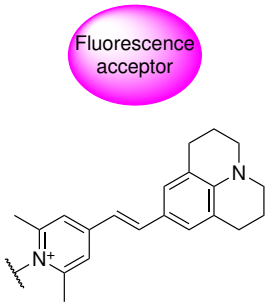

Py1

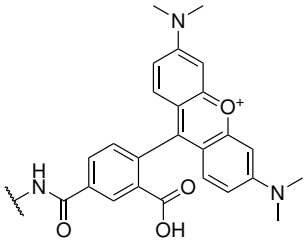

TAMRA

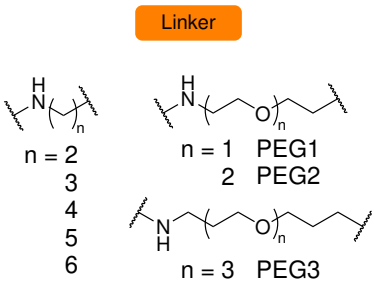

4.2 Synthetic plan

A convergent synthetic approach was chosen for accessing lead **61** with a divergent approach best suited to conjugate the fluorescent probes. Although a reported route to propenoic acid exists **61**, the Suzuki coupling reaction used to achieve the structure from thiazole **90** was poor yielding for a divergent approach and the boronic ester

coupling partner was not commercially available (**Scheme 16**).[184] Thus, an improved synthetic route was explored (**Scheme 17**).

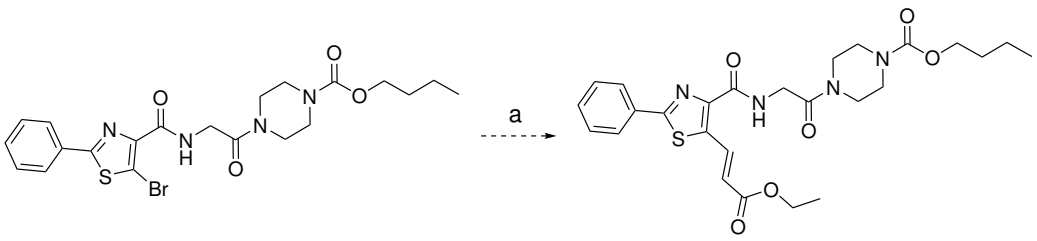

90 **91**

Scheme 16: Caroff and coworkers' olefination of **90** to access ethyl ester **91**. (a) 2-Ethoxycarbonylvinylboronic acid pinacol ester, K_2CO_3, $Pd(PPh_3)_4$, in DME and H_2O, 90 °C, 40 h, 21%.[184]

To access the common carboxylic acid lead **61**, we proposed that ester **92** could be hydrolysed under either acidic or basic conditions. An olefination reaction using Wittig conditions could be completed from thiazole carbaldehyde **94**. The formation of compound **94** could be achieved from an amide coupling between thiazole **94** and glycine **95**. Thiazole **94** could be obtained from the formylation of thiazole ethyl ester **97** and ester hydrolysis. Cyclisation of thiobenzamide **98** and pyruvate **99** would provide access to thiazole ethyl ester **97**.

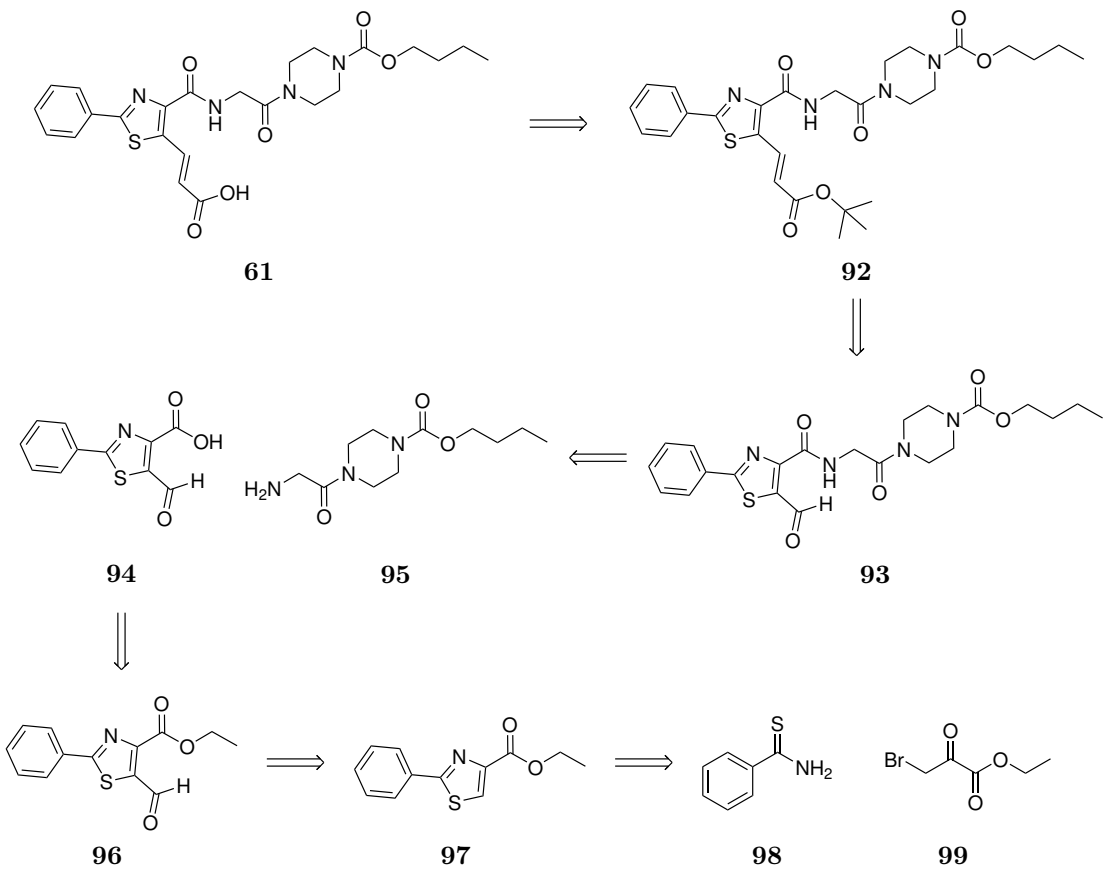

Scheme 17: Proposed retrosynthetic plan to synthesise lead **61** starting from commercially available reagents.

Piperazine **95** could be accessed from the Boc-deprotection of piperazyl glycine derivative **100** under acidic conditions. An S_N2 reaction between piperazine **101** and activated carbamate **102** would yield piperazyl glycine derivative **100**. Careful procedural control could afford mono-amidate piperazine **101** from diamine **104** and Boc-glycine (Boc-Gly-OH) **115**. Accordingly, carbamate **102** could be synthesised from an S_N2 reaction between 1-butanol **106** and carbonyldiimidazole (CDI) **105**. All starting materials in the proposed route were commercially available.

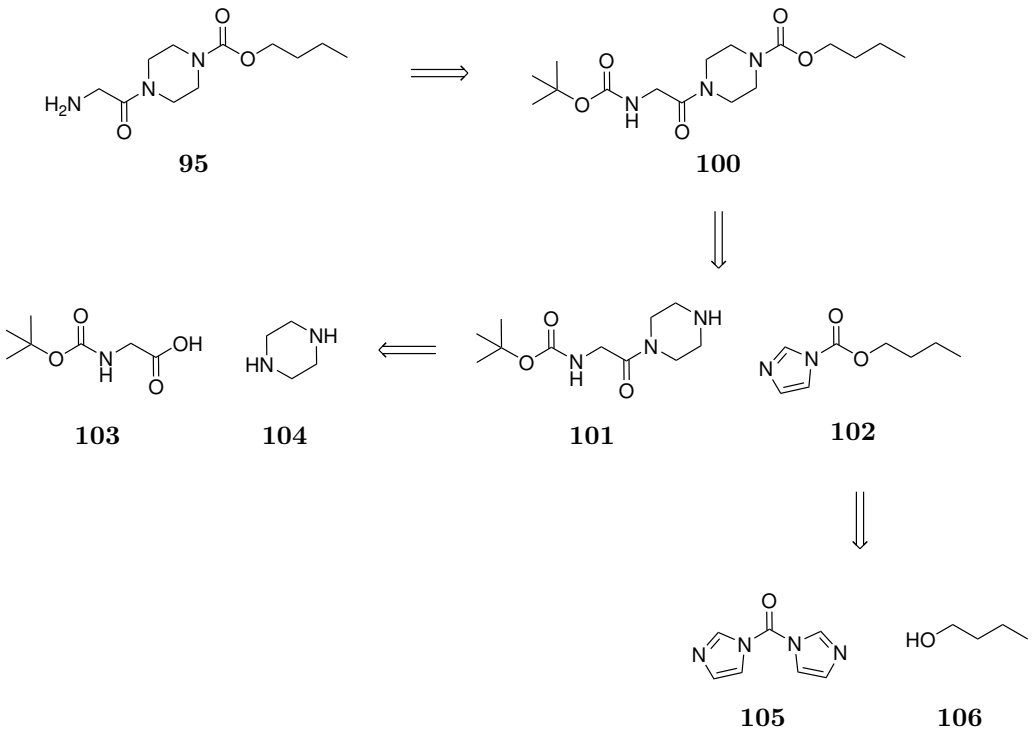

Scheme 18: Proposed retrosynthetic plan to access piperazine **95** starting from commercially available reagents.

Py-1 was not commercially available but could be synthesised following the procedure reported by Höfelschweiger and coworkers.[173] The divergent fluorophore appendage would begin with the linker attachment to lead **61** under standard amide coupling conditions, yielding compounds **107**-**114**. These could then be converted to the free amine under acidic conditions and directly coupled to Py-1 under basic conditions to furnish the Py-1 NanoBRET probe series. A portion of the free amine could alternatively be directly appended to TAMRA under standard amide coupling conditions to furnish the TAMRA NanoBRET probe series.

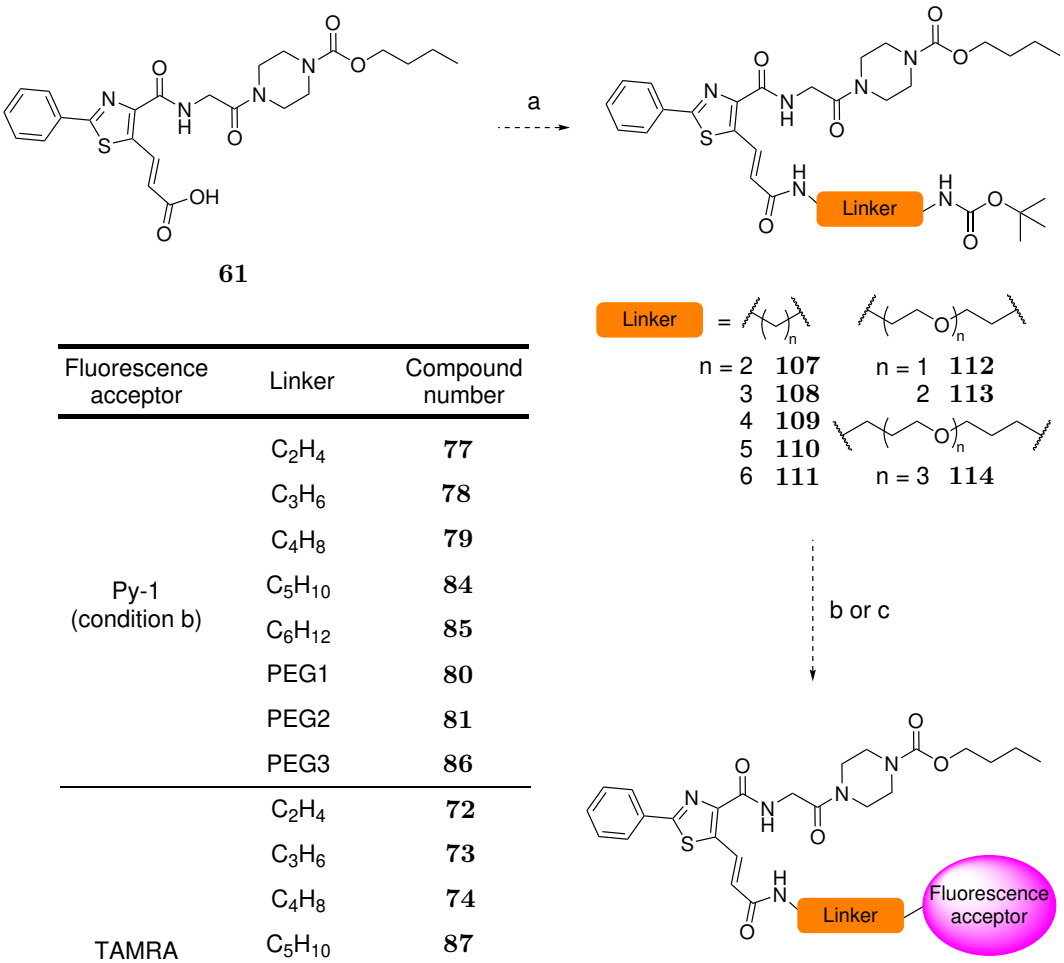

61

Fluorescence acceptor	Linker	Compound number
Py-1 (condition b)	C_2H_4	**77**
	C_3H_6	**78**
	C_4H_8	**79**
	C_5H_{10}	**84**
	C_6H_{12}	**85**
	PEG1	**80**
	PEG2	**81**
	PEG3	**86**
TAMRA (condition c)	C_2H_4	**72**
	C_3H_6	**73**
	C_4H_8	**74**
	C_5H_{10}	**87**
	C_6H_{12}	**88**
	PEG1	**75**
	PEG2	**76**
	PEG3	**89**

Scheme 19: General synthetic plan of lead **61** conjugation with TAMRA and Py1 by using a divergent approach. (a) Boc-diamine linker, HATU, iPr$_2$NEt, DMF, rt, o/n; (b) i) 4 M HCl in dioxane, DCM, rt, 30 min, ii) Py-1, Et$_3$N, in MeOH, 60 °C, 1 h; (c) i) 4 M HCl in dioxane, DCM, rt, 30 min, ii) TAMRA, HATU, iPr$_2$NEt, DMF, rt, o/n.

4.3 Synthesis

4.3.1 Lead synthesis

Piperazine fragment synthesis

To obtain carbamate **102**, CDI was used as a safer alternative to phosgene or triphosgene in the synthesis of an activated intermediate for a carbamate formation

reaction. CDI was treated with 1-butanol under anhydrous conditions to minimise the likelihood of hydrolytic decomposition. The reaction was monitored using TLC analysis, and upon completion and purification *via* flash chromatography, the desired product **102** was obtained in good yield (83%, **Scheme 20**). Excess equivalents of butanol did not significantly impact the yield (entry 2, **Appendix 4**), due to the reduced reactivity of the carbamate product versus the activated urea starting material. However, a short series of optimisation experiments concluded that a 1:1 ratio of CDI and butanol achieved the best yield (entry 3, **Appendix 4**).

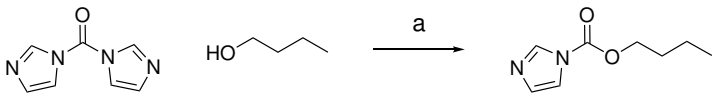

105 **106** **102**

Scheme 20: Synthesis of reactive butylimidazole carbamate intermediate **102** for subsequent butyl carbamate formation. (a) DCM, 0 °C - rt, o/n, 83%.

Concurrently, Boc-Gly-OH **115** was coupled to piperazine **104** to give amide **101**. This was initially attempted by pre-stirring Boc-Gly-OH **115** with EDC and HOBt to form the activated ester before adding excess quantities of piperazine solution dropwise (**Table 8**). However, this reacted too quickly and exclusively generated the diamide product. Re-attempting the reaction with neat piperazine afforded some product when added to the stirred activated ester solution. Unfortunately, the rate of the dimerisation reaction was still observed to be faster than dissolution of solid piperazine, leading to low yields (18%). Thus an attempt was made to slowly generate the active ester species *via* slow addition of hexafluorophosphate azabenzotriazole tetramethyl uronium (HATU) to a solution of Boc-Gly-OH and piperazine. A slow addition was performed at low temperatures to reduce the speed of substitution. TLC analysis and a ninhydrin stain were used to visualise the free amine starting material and product.

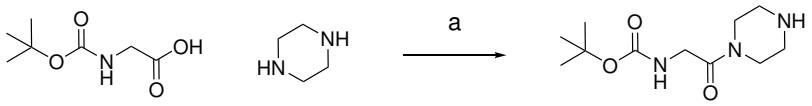

115 **104** **101**

Scheme 21: Amide coupling of piperazine and Boc-Gly-OH to synthesise piperazine **101**. (a) HATU, iPr$_2$NEt, DMF, 0 °C - rt, o/n, 83%.

An attempt to purify the product using standard additive-free flash chromatography conditions was unsuccessful as the free amine of the product would streak due to its interaction with the slightly acidic silica medium. A non-nucleophilic organic base, Et_3N, was used to neutralise the interactions to aid in the rate of elution and resolution of the fractions. This achieved good yields on test scale (83%, entry 3, **Table 8**), but significant reduction in yield occurred upon scaling up the reaction. This posed practical challenges for synthesising large quantities of intermediate **101**. As such, a more robust strategy to synthesise piperazine core (**100**) that did not rely on the precise experimental control was explored.

Table 8: Optimisation of the amide coupling conditions to increase yield of the monoamide as shown in **Scheme 21**.

Entry	Conditions	Outcome
1	Boc-Gly-OH, EDC, HOBt and Et_3N in DCM was added slowly to piperazine (5 eq.) in DCM, rt	Exclusive formation of diamide product
2	Piperazine (5 eq.) was added to stirring solution of Boc-Gly-OH, EDC, HOBt and Et_3N in DCM, rt	18% yield
3	HATU in DMF added slowly to piperazine (5 eq.), Boc-Gly-OH and iPr$_2$NEt DMF, 0 °C - rt	83% yield
4	HATU in DMF added slowly to piperazine (5 eq.), Boc-Gly-OH and iPr$_2$NEt DMF, 0 °C - rt (Scaled up)	33% yield

The synthesis of piperazine core **100** *via* commercially available Boc-piperazine **116** as the starting material could improve regioselectivity. Boc-piperazine **116** was first treated with activated carbamate **102** under basic conditions to access dicarbamate **117** in excellent yields (97%, step a, **Scheme 22**). The work-up was performed quickly with dilute hydrochloric acid to remove the imidazole and triethylamine by-products whilst minimising the chance of Boc-deprotection.

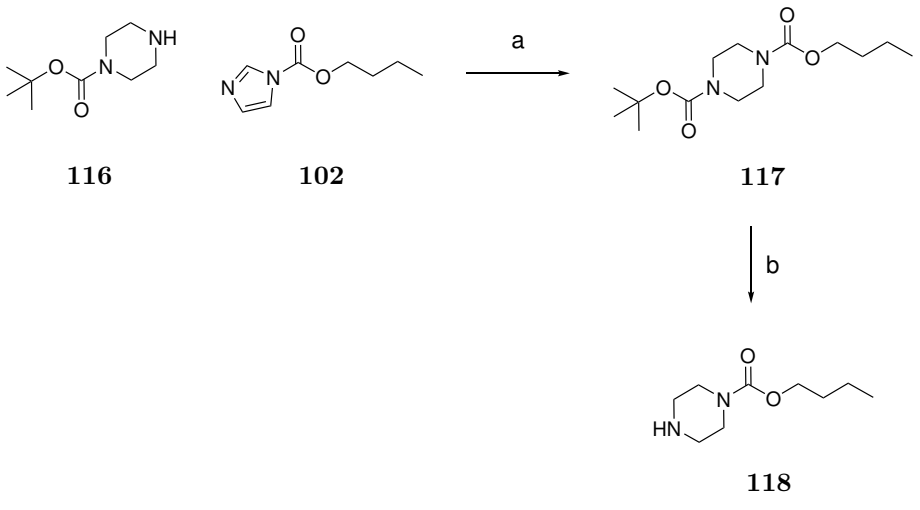

116 **102** **117** **118**

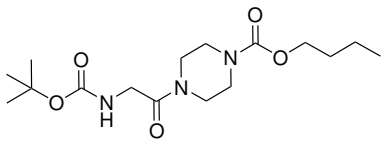

100

Scheme 22: Top: Synthesis of butyl piperazine carbamate **118** *via* forming the dicarbamate **117** with *N*-Boc-Piperazine. (a) Et_3N, DCM, rt, 71 h, 97%; (b) 4 M HCl in dioxane, DCM, rt, 1 h, quant. Bottom: Structure of piperazine core **100**.

Dicarbamate **117** was then deprotected under acidic conditions to access free amine **118**. The mechanism for the Boc-deprotection of **117** is shown in **Scheme 23**). The tertiary carbocation **120** stability allowed the liberation of isobutylene **121** and the subsequent collapse of carbamate intermediate **122**. Expulsion of isobutylene resulted in a shift of the overall equilibrium towards the collapse of the Boc group *via* loss of carbon dioxide. On the other hand, the *n*-butyl chain **124** is unable to generate a stable carbocation to liberate itself. As a result, the *n*-butyl carbamate was more stable than Boc-group under acidic conditions and selectively generated amine **118**. The by-products of the Boc-deprotection are volatile, so the product

was used without further purification.

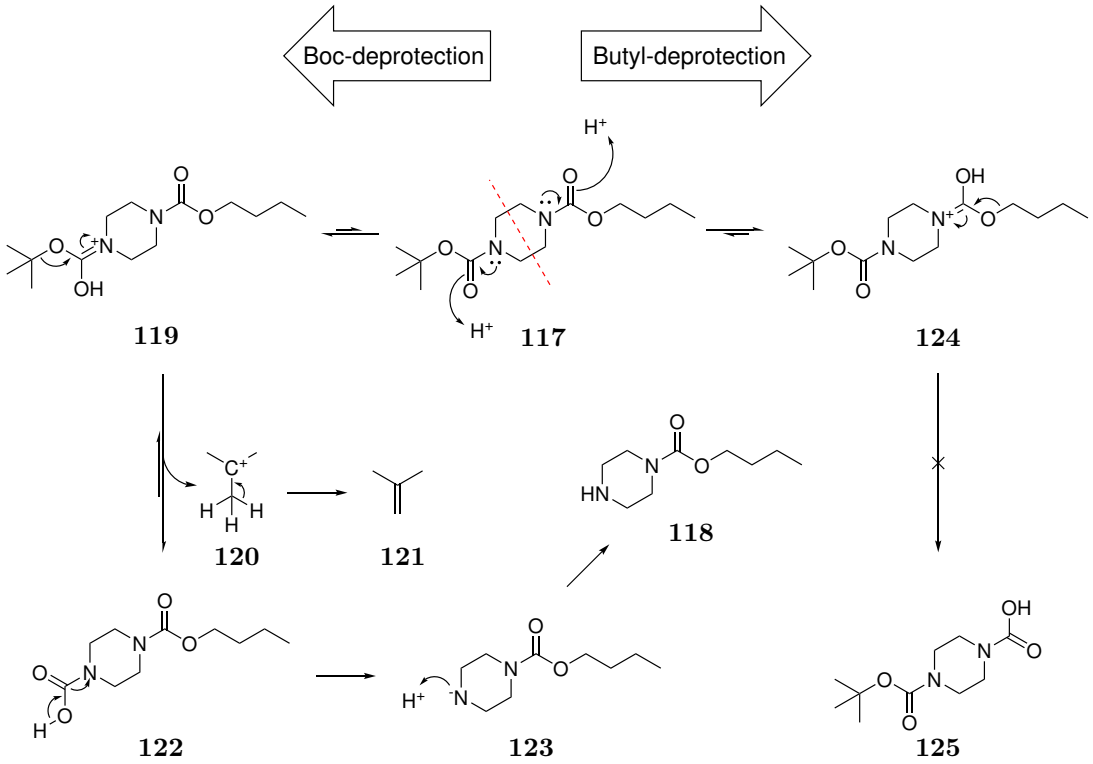

Scheme 23: Proposed mechanism for the selective deprotection of dicarbamate **117** to yield **118**.

To complete the synthesis of the piperazine core, free amine **101** was treated with carbamate **102** under basic conditions to access disubstituted piperazine **100** in excellent yields (97%, procedure a, **Scheme 24**). Alternatively, piperazine **118** was treated with Boc-Gly-OH under HATU amide coupling conditions to access disubstituted piperazine **100** also in excellent yields (97%, procedure b, **Scheme 24**). The latter route proved more robust and was used for subsequent synthesis.

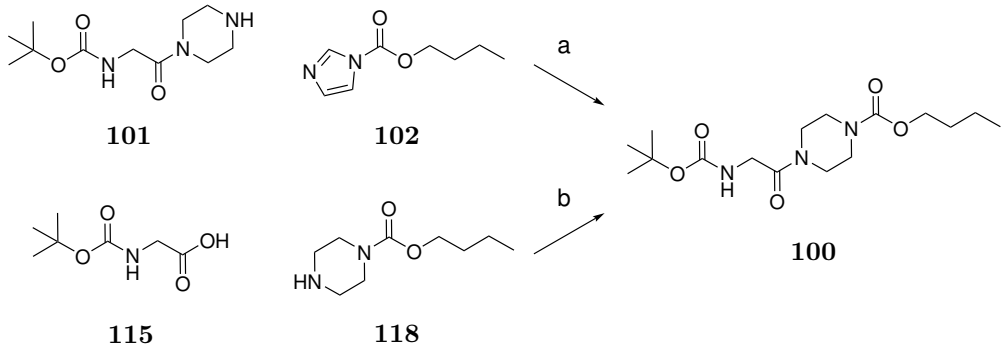

Scheme 24: Synthesis of the piperazine **100** from piperazine **101** and **118**. (a) Et_3N, DCM, rt, o/n, 97%; (b) HATU, $i Pr_2NEt$, DMF, rt, o/n, 97%.

Thiazole core synthesis

To access precursor **97** for the thiazole olefination, the thiazole core was prepared to couple with piperazine **100**. Thiazole **97** was synthesised *via* Hantzsch thiazole synthesis from the condensation between thiobenzamide **98** and ethyl bromopyruvate **99** under reflux (**Scheme 25**). The crude product was purified *via* flash chromatography, resulting in a viscous oil. To remove any trapped solvents, the product was concentrated with Et_2O three times to isolate thiazole **97** in excellent yields (97%). The presence of an aromatic proton signal at 8.15 ppm and two additional aromatic carbon signals at 130.7 and 148.0 ppm in the NMR spectra confirmed successful thiazole ring formation (**Appendix 11** and **Appendix 12**).

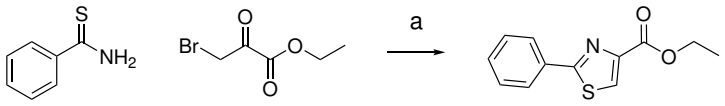

98 **99** **97**

Scheme 25: Synthesis of thiazole core **97** *via* the condensation of thiobenzamide **98** and pyruvate **99**. (a) THF, reflux, o/n, 97%.

Thiazole olefination — Wittig reaction

Our first strategy to olefinate this thiazole entailed the use of a Wittig reaction and avoidance of precious metal catalysis. To access aldehyde **96** required for this transformation, Vilsmeier reagent was generated *in situ* from $POCl_3$ in DMF and added to thiazole **97**, before stirring the reaction at 90 °C (entry 1, **Table 9**). The reaction was monitored by TLC analysis, but unreacted starting material remained, prompting an increase in temperature to 115 °C. Although a UV-visible product was observed using TLC analysis, staining with dinitrophenylhydrazine (DNP) did not suggest aldehyde formation. Raising the temperature further to 140 °C resulted in a brown solution and complex reaction mixture, likely due to decomposition of the Vilsmeier reagent. Trace amounts of what we assumed to be the desired product within the crude mixture was observed *via* TLC with DNP staining.

Table 9: Attempts towards the formylation of thiazole **97**. $^{\alpha}$ Assessed likely presence of carbaldehyde by co-spotting against starting material on TLC with DNP staining. $^{\beta}$ Determined by mass spectrometry.

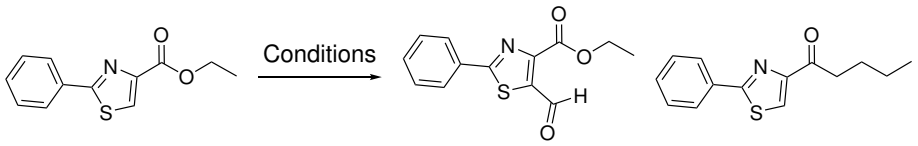

97 **96** **126**

Entry	Conditions	Outcome
1	$POCl_3$ (4 equiv.), DMF, 0–140 °C, 48 h	Trace product + S.M.$^{\alpha}$
2	$POCl_3$ (10 equiv.), DMF, 0–115 °C, 20 h	Trace product + S.M.$^{\alpha}$
3	$POCl_3$ (4 equiv.), Et_3N, cat. DMAP, DMF, 0–115 °C, 20 h	Trace product + S.M.$^{\alpha}$
4	i) *n*-BuLi, THF, -78 °C, ii) DMF	Butyl ketone **126** (major)
5	i) *n*-BuLi, Et_2O, -78 °C, ii) DMF	Complex mixture (trace product + butyl ketone **126** + S.M.)$^{\alpha\beta}$
6	i) *n*-BuLi, toluene, -78 °C, ii) DMF	Complex mixture (trace product + butyl ketone **126** + S.M.)$^{\alpha\beta}$
7	i) *n*-BuLi, THF (5 x dilution of entry 4), -78 °C, ii) DMF	S.M.$^{\alpha}$
8	i) *n*-BuLi, diisopropylamine, Et_2O, -78 °C, ii) DMF	Complex mixture$^{\alpha}$

A second attempt at formylation of **97**, while maintaining a temperature below the decomposition point, produced no significant improvements. It was thought that the phosphoric acid by-product, generated from the *in situ* formation of the Vilsmeier reagent, had protonated the unreacted thiazole **97**. This could draw electron density away from the 5-position and deactivate it for a nucleophilic attack on the Vilsmeier

reagent. Excess Et_3N was added to neutralise the phosphoric acid, and DMAP was introduced as catalyst to facilitate the Vilsmeier-Haack reaction. However, even with the measures taken to facilitate the formylation, it was unable to formylate at the deactivated 5-position. A reactive organolithium intermediate was envisioned to improve the nucleophilicity at the 5-position and facilitate the formylation.

Lithiation of thiazole **97** at the 5-position was attempted through lithium-hydrogen exchange with *n*-butyllithium (*n*-BuLi). Despite cold temperatures favouring the lithium-halogen exchange reaction over the substitution reaction, the *n*-BuLi was too reactive and perhaps unsuprisingly formed the *n*-butyl ketone **126** as the major product. *n*-BuLi predominantly exists as the monomeric form in THF,[185,186] which could have been too nucleophilic and substituted the ethyl ester. To moderate the reactivity and tune the selectivity, solvent trials with toluene and Et_2O were performed to investigate the clustering of organolithium species in the reaction to attenuate the nucleophilic reactivity of *n*-BuLi.[186] Both solvents prevented the *n*-BuLi from directly substituting the ethyl ester, but a complex mixture was generated after treatment with DMF (entries 5 and 6, **Table 9**). No consumption of starting material **97** was observed under more dilute reaction conditions in THF. Trials with lithium diisopropylamine as a more sterically hindered lithiating reagent resulted in a complex reaction mixture. The 5-position on the thiazole proved highly unreactive and incompatible with many sets of reaction conditions.[187] This prompted the exploration of a palladium-catalysed carbon-carbon coupling approach to facilitate the olefination.

Thiazole olefination — C-H activation

We first envisioned that palladium-catalysed C-H activation could be employed to olefinate the 5-position of thiazole **97**. The di-ester **127** would be challenging to selectively hydrolyse. Thus, thiazole **129** was decided as the olefination substrate.

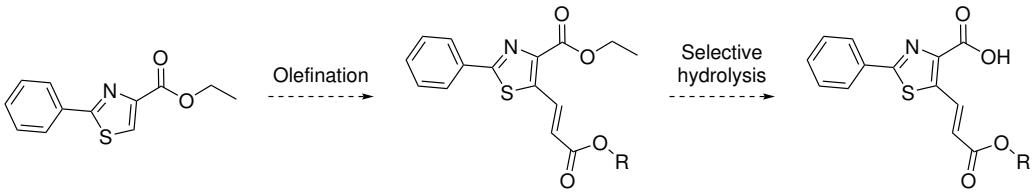

97 **127** **128**

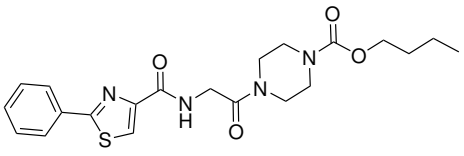

129

Scheme 26: Top: Olefination of thiazole **97** would result in di-ester **127**. This intermediate would be challenging to selectively hydrolyse. Bottom: Thiazole **129** was decided to be the olefination substrate to circumvent the need for selective hydrolysis.

Carboxylic acid **131** was synthesised *via* Hantzsch thiazole synthesis from the condensation between thiobenzamide **98** and bromopyruvic acid **130** under reflux (**Scheme 27**). The reaction was monitored by TLC analysis, but full consumption of starting material was not observed. The reaction was halted, and the desired product **131** was obtained in 33% yield.

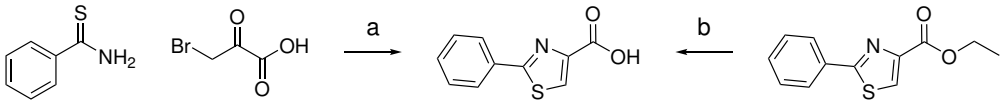

98 **130** **131** **97**

Scheme 27: Synthesis of thiazole core **131** and **97**. (a) 1,4-dioxane, reflux, o/n, 33%; (b) LiOH, H_2O/THF, o/n, quant.

The proposed mechanism to form compound **131** was through a bimolecular nucleophilic substitution (S_N2) between thiobenzamide **98** and bromopyruvic acid **130**, followed by the deprotonation of amine **132** by thiobenzamide **98** (**Scheme 28**). Although the S_N2 reaction generates bromide anions, the thiobenzamide was predicted to be a stronger base to abstract free protons. This would result in the protonation of thiobenzamide **98**, prohibiting its ability to participate in further S_N2 reactions. Moreover, the presence of carboxylic acids (e.g. **131** and **130**) could increase the

acidity of the reaction mixture, potentially also deactivating thiobenzamide **98**. The poor isolated yield could have resulted from the stalled reaction due to these issues.

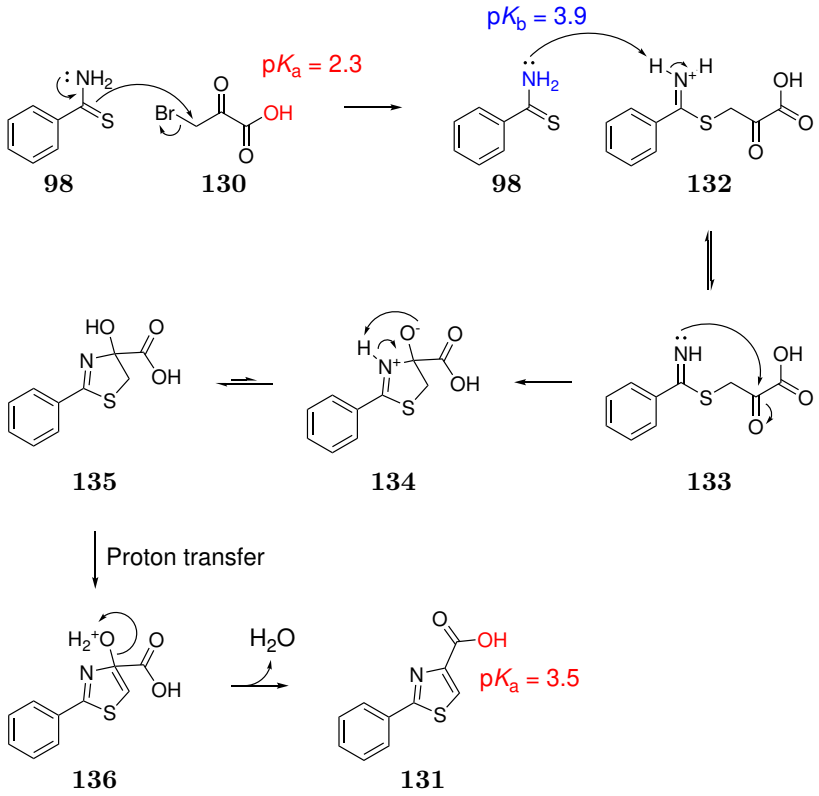

Scheme 28: Proposed mechanism of the Hantzsch thiazole synthesis and protonation of thiobenzamide. The pK_a and pK_b were predicted using MolGpka.[131]

As an alternative approach, previously synthesised ethyl ester **97** could be hydrolysed to afford carboxylic acid **131** under standard LiOH mediated hydrolysis conditions. The product was first purified by washing the basic reaction mixture with EtOAc. The aqueous layer was then acidified to pH $\approx$ 2 and extracted with EtOAc, affording the desired product in quantitative yields.

To access thiazole **129**, piperazine **100** was Boc-deprotected with hydrochloride in dioxane to expose the free amine **95** (step a, **Scheme 29**). This was carried through without further purification and coupled with carboxylic acid **131** under standard HATU amide coupling conditions (step b, **Scheme 29**). The crude product was purified *via* flash chromatography eluting with acetone in hexane. However, dimethylurea **138** co-eluted with the desired product, necessitating an aqueous work-up with citric acid to extract the dimethyl urea by-product. Pure product **129** was

isolated in quantitative yields.

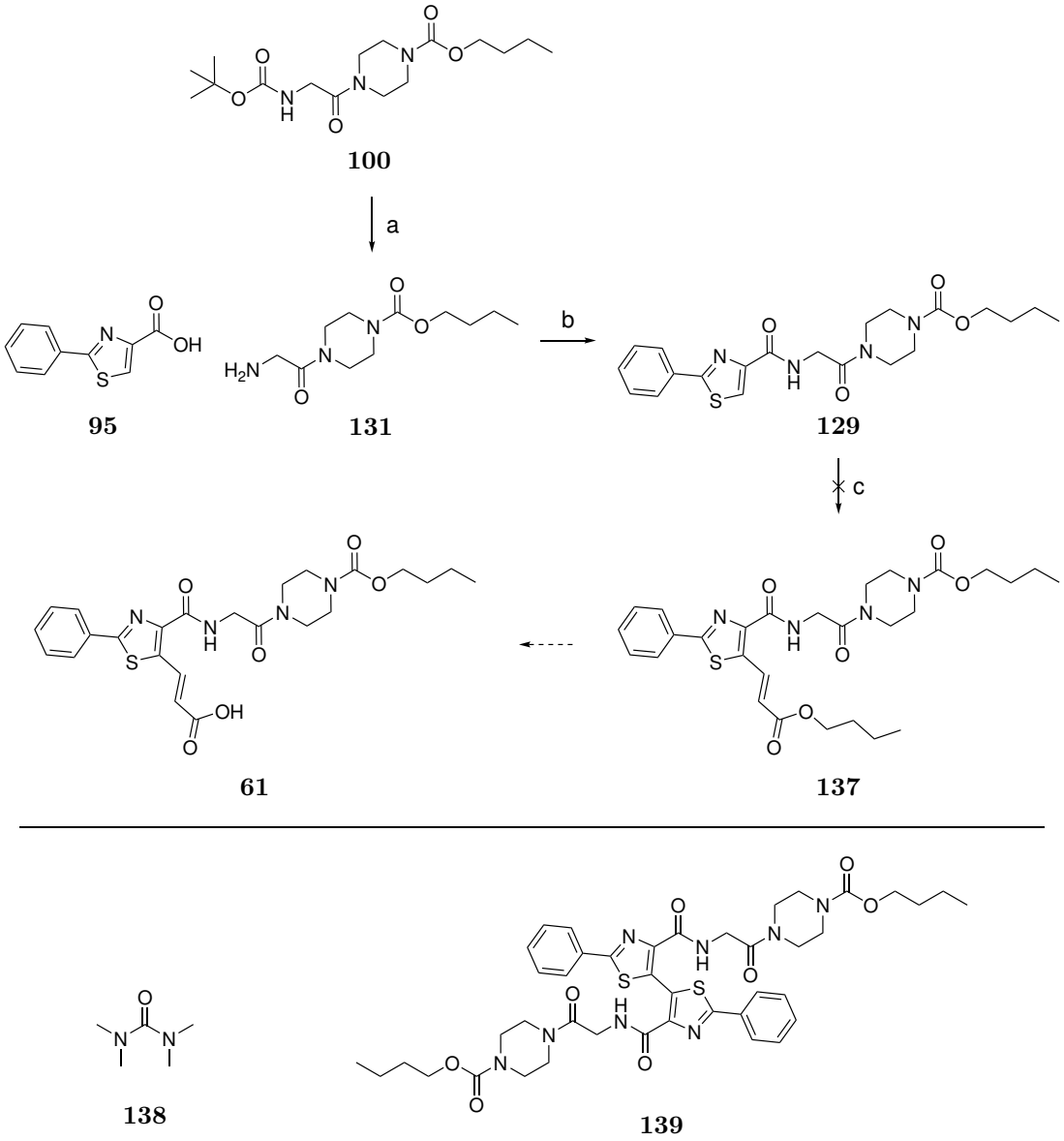

Scheme 29: Synthetic route towards compound **61** *via* C-H activation of compound **129**. Homocoupled starting material was the major product **139**. (a) 4 M HCl in dioxane, DCM, rt, 30 min, quant.; (b) HATU, iPr$_2$NEt, DMF, rt, o/n, quant.; (c) Butyl acrylate, Pd(OAc)$_2$ (10 mol%), AgOAc, DMF/DMSO, 115 °C, 48 h.

Thiazole **129** was subsequently submitted to palladium cross-coupling conditions (entry 1, **Table 10**).[188] TLC analysis indicated the incomplete consumption of starting materials. In addition to the recovered starting material **129**, the homocoupled product **139** was also isolated *via* flash chromatography purification. Mass spectrometry (881 [M+Na]$^+$, **Appendix 13**) and a similar spectrum to the starting material, without the expected thiazole proton at 8.09 ppm, (**Appendix 14**) were

evidence for homocoupled product **139** formation. Although the desired product was not formed, evidently oxidative insertion of compound **129** had occurred. However, homocoupling to form **139** suggests that reductive elimination to form the desired olefinated product was slow.

Jeffery and coworkers have shown that addition of tetrabutylammonium (TBA) salts to Heck reactions effectively mediate reagent transfer.[189,190] Compound **129** was therefore resubmitted to the palladium-catalysed C-H activation reaction with TBA(HSO_4) (entry 2, **Table 10**). The product was isolated *via* flash chromatography, and while mass spectrometry suggested that **137** had formed (ESI^+: 579 $[M+Na]^+$, ESI^-: 555 $[M-1]^-$), the yield was extremely low, with insufficient material isolated to perform NMR analysis. In parallel with the previous reaction, *tert*-amyl alcohol (*t*-AmylOH) was trialled to investigate the effects of a polar protic solvent (entry 3, **Table 10**). It was thought that the solvent could donate electron density to the palladium catalyst, add steric bulk and improve the reductive elimination step. However, a similar outcome was achieved as the previous experiment, with only trace formation of **137**.

Table 10: Attempts to olefinate thiazole **129** with butyl acrylate *via* palladium catalysed C-H activation.

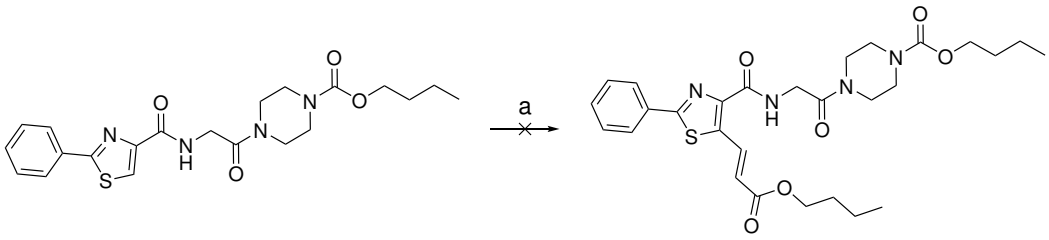

129 **137**

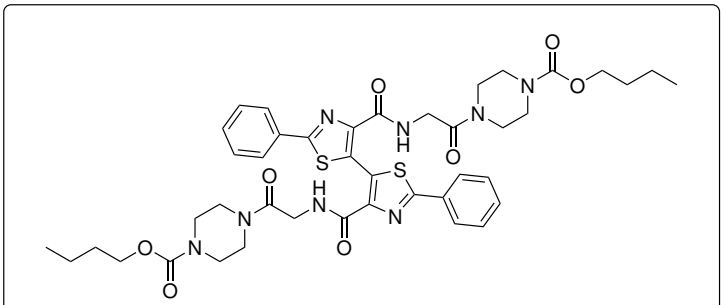

139

Entry	Conditions	Outcome
1	Butyl acrylate, $Pd(OAc)_2$ (10 mol%), AgOAc, DMF/DMSO, under N_2, 115 °C, 48 h, degassed and dry	Homocoupled product **139** and S.M.
2	Butyl acrylate, $Pd(OAc)_2$ (10 mol%), AgOAc, TBA(HSO_4), DMF/DMSO, under N_2, 115 °C, 120 h, degassed and dry	Trace product **137** and S.M.
3	Butyl acrylate, $Pd(OAc)_2$ (10 mol%), AgOAc, TBA(HSO_4), *t*-AmylOH, under N_2, 115 °C, 120 h, degassed and dry	Trace product **137** and S.M.

The C-H activation route proved unsuitable for accessing the desired product **137**. Suspected palladium catalyst poisoning and the formation of homocoupled by-product **139** were persistent challenges. Lack of reported studies that overcome these challenges made systematic optimisation challenging. Consequently, we directed our focus toward the better-studied Heck reaction to olefinate the thiazole.

Thiazole olefination — Heck reaction

The Heck cross-coupling reaction involves formation of a new C-C bond between an aryl or vinyl (pseudo)halide and a suitably activated alkene. For this strategy to be used, we first required a halogenated analogue of our thiazole core. Therefore, the synthesis of the bromothiazole derivative **140** was investigated to enable attempts at the Heck coupling reaction.

Table 11: Optimisation of thiazole **97** bromination. $^{\alpha}$ Co-elution of fractions. $^{\beta}$ Recovery of starting material. N.R. = No reaction. S.M. = Starting material.

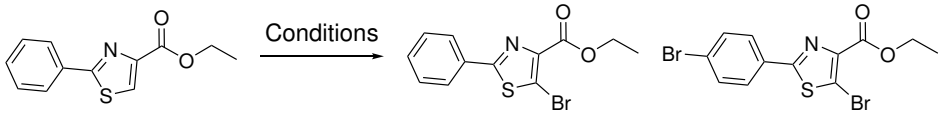

97 **140** **141**

Entry	Conditions	Outcome
1	Br_2, Et_2O, rt, 18 h	9% yield **140** + dibromothiazole **141**$^{\alpha}$ + 81% S.M.$^{\beta}$
2	Br_2, MeCN, reflux, 18 h	71% yield **140** + dibromothiazole **141**$^{\alpha}$ + 16% S.M.$^{\beta}$
3	NBS (2 eq.), MeCN, reflux, 17 h	37% yield **140** + dibromothiazole **141**$^{\beta}$
4	NBS (1 eq.), MeCN, reflux, 16 h	N.R.$^{\beta}$
5	NBS (1 eq.), MeCN (PureSolv), reflux, 19 h	51% yield **140** + 39% S.M.$^{\beta}$
6	NBS (1 eq.), cat. Iodine, MeCN (PureSolv), 35 °C, 19 h	85% yield **140** + S.M.$^{\beta}$

Initial attempts to brominate thiazole **97** and form bromothiazole **140** used elemental bromine (entries 1 and 2, **Table 11**). When the reaction was performed

in Et_2O, the solvent evaporated rapidly under the exothermic reaction condition and concentrated the reaction mixture in an uncontrolled fashion. Product purification using flash chromatography proved challenging. The desired product **140** eluted over many fractions, expending excessive solvent volumes, and co-eluting with dibrominated by-product **141** (**Appendix 15**). This resulted in poor yields of bromothiazole **140** (9%) and substantial recovery of starting material (81%).

To address the solvent evaporation issue, the reaction was performed in acetonitrile (MeCN). While the yield of bromothiazole **140** improved significantly (71%, entry 2, **Table 11**), purification challenges persisted. The co-elution of mono- and di-brominated thiazoles complicated the purification by flash chromatography. It was surmised that suppression of the formation of dibromothiazole **141** would simplify purification. The high concentration of reactive elemental bromine in the reaction mixture was believed to be contributing to dibromination, therefore alternative bromine sources were investigated to access **140**.

Liu and coworkers reported the regioselective mono-bromination at the 5-position on thiazoles using *N*-bromosuccinimide (NBS) — a reagent commonly used to generate low concentrations of elemental bromine in a controlled manner.[191] Following these procedures, thiazole **97** was treated with 2 equivalents of NBS in MeCN under reflux. The reaction mixture turned brown, indicating the release of elemental bromine, and TLC analysis indicated the consumption of starting material. The major isolated products were once again identified as di- and mono-brominated thiazoles **140** and **141** (entry 3, **Table 11**). The equivalence of NBS was therefore reduced to limit the formation of dibrominated thiazole **141** (entry 4, **Table 11**). Unexpectedly, no reaction was observed. The presence of residual water in MeCN could have generated hydrobromic acid or hypobromites **Scheme 30**. These species did not appear to act as brominating agents for thiazole **97**.

The reaction was repeated under anhydrous conditions to exclusively generate elemental bromine (entry 5, **Table 11**). This resulted in 51% yield of desired product **97** and 39% starting material. To further optimise the reaction, iodine was added as

a catalyst and generated the desired product **140** in excellent yield (85%, entry 6, **Table 11**).

The bromination mechanism was proposed to proceed *via* the homolysis of bromine. Although NBS typically serves as a source of electrophilic bromine, it can also undergo *in situ* decomposition to generate elemental bromine, which then homolyses to form bromine radicals. These radicals regioselectively attack the 5-position of thiazole. Addition of the iodine catalyst could form a reactive iodine monobromide intermediate *in situ* and more readily undergo homolysis.[192] The lower temperatures and concentration of elemental bromine in solution allow for the regioselectivity of the bromination.

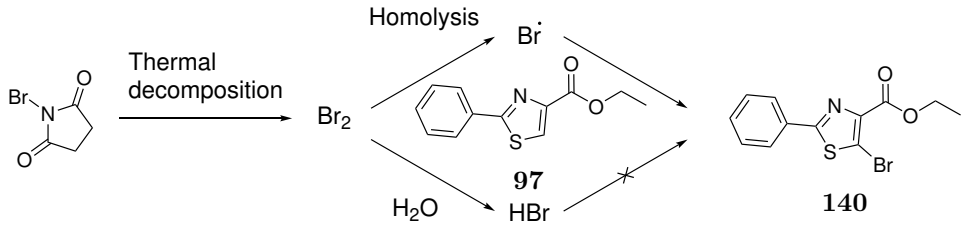

Scheme 30: Mechanism of the bromination reaction, starting with the thermal decomposition of NBS to generate free bromine, which could then react with the thiazole or be deactivated in the presence of water.

We next proceeded to investigate the Heck reaction required to olefinate the thiazole core. We first performed reaction optimisation using thiazole **97** as a test compound, rather directly attempting our primary strategy of late-stage introduction of the olefin. This choice was made to limit loss of late-stage material, as previously encountered during C-H activation studies.

Tert-butyl acrylate was chosen as a suitable coupling partner, as it could be deprotected *via* either acidic or basic hydrolysis. Thiazole **97** was reacted with *tert*-butyl acrylate, Cy_2NMe, $PdCl_2$(dbpf) and TBACl under nitrogen following the robust condition reported by Murray and coworkers (**Scheme 31**).[193,194] TLC analysis confirmed formation of a new product, but the reaction did not progress to completion. It was therefore halted and purified *via* flash chromatography, resulting in isolation of desired di-ester product **142** in good yield (70%). The remainder of the starting material was converted to the dehalogenated by-product **97**. Since the

reaction was carried out at high temperatures near the boiling point of *tert*-butyl acrylate (124-127 °C),[195] the reaction was attempted once again in a sealed tube to ensure the acrylate remained in solution. Pleasingly, this further improved the yield of desired product **142** (91%).

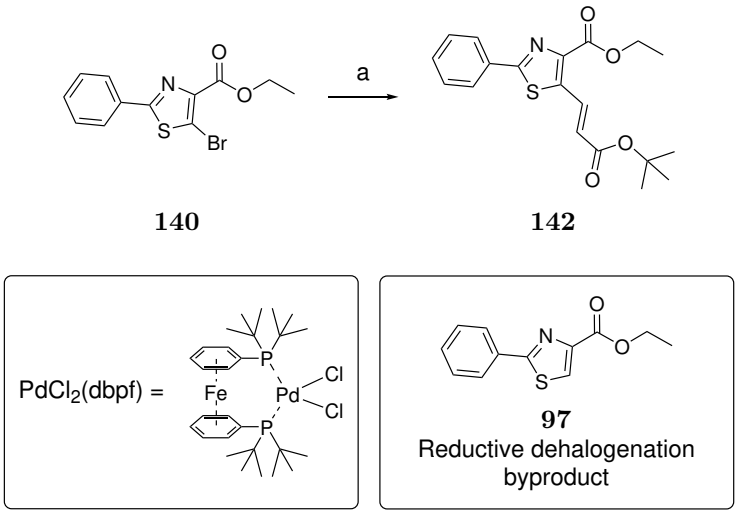

140 **142**

Scheme 31: Olefination of thiazole **140** under Heck reaction conditions. (a) *Tert*-butyl acrylate, Cy_2NMe, $PdCl_2$(DBPF) (2 mol%), TBACl, DMA, under N_2, 80 °C, 71 h, 85%.

With the Heck coupling conditions optimised on bromothiazole **97**, we proceeded to synthesise bromothiazole **144** to allow incorporation of this high-yielding cross-coupling reaction at a later stage of the synthesis. This began by submitting thiazole **140** to LiOH catalysed hydrolysis conditions (step a, **Scheme 32**) and yielded the desired product **143** in excellent yield (92%). Subsequently, piperazine **95** and bromothiazole **143** were treated with HATU under basic conditions to access amide **144**.

Amide **144** was next submitted to our optimised Heck coupling conditions (step c, **Scheme 32**). Gratifyingly, the reaction translated well to the more complex substrate, and desired product **92** was obtained in 89% yield following purification *via* flash chromatography. In contrast to the previous C-H activation strategy to olefinate the thiazole, this strategy used lower quantities of palladium catalyst, improved conversion, and selectively generated the desired product **92**. The choice of ligand was crucial in the success of this olefination strategy, as use of the electron-rich

bidentate ligand suppressed formation of the homocoupled product. This olefination strategy was scaled up to half a gram without sacrificing yields.

Finally, *tert*-butyl ester **92** was treated with TFA to deprotect the *tert*-butyl ester. This afforded the desired product **61** in quantitative yield, which was used in subsequent steps without further purification.

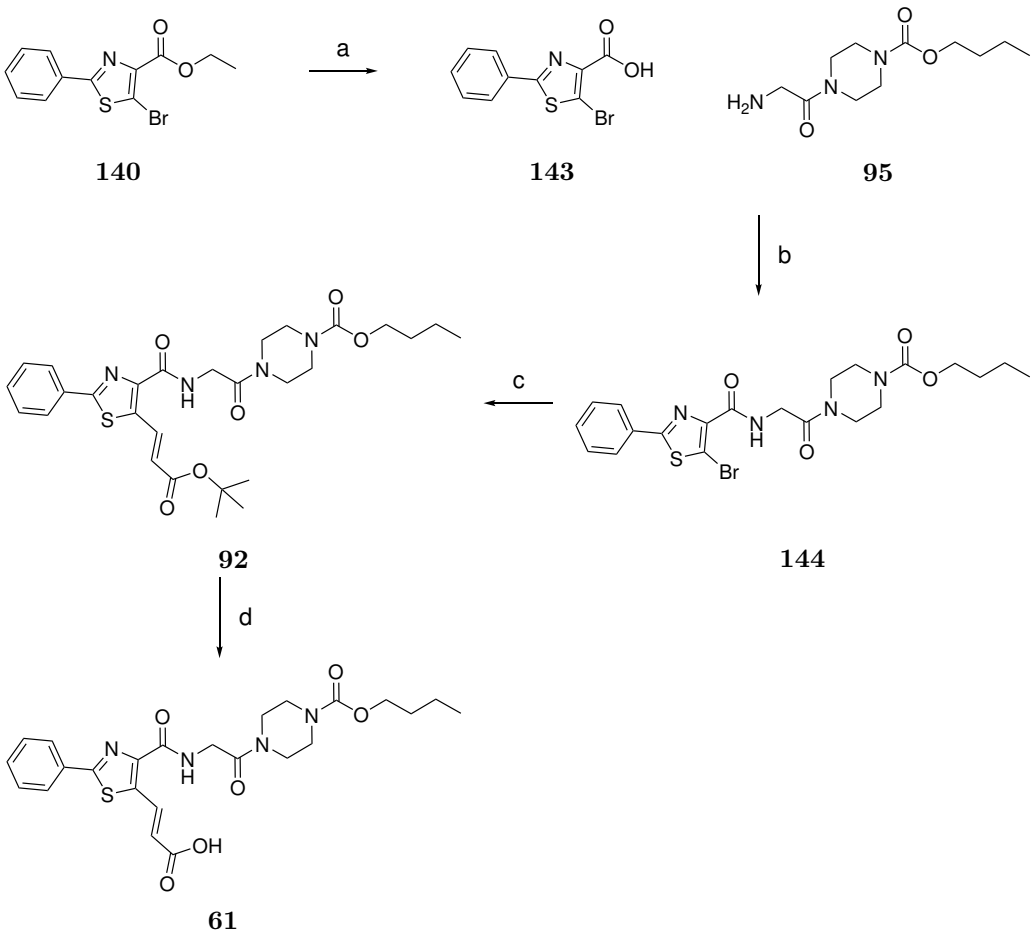

Scheme 32: Synthesis of lead **61** *via* Heck reaction conditions. (a) LiOH, in H_2O and THF, rt, o/n, 92%; (b) HATU, *i*Pr_2NEt, DMF, rt, o/n, 85%; (c) *Tert*-butyl acrylate, Cy_2NMe, $PdCl_2$(DBPF) (2 mol%), TBACl, DMA, 80 °C, 65 h, 89%; (d) TFA, DCM, rt, 3 h, quant.

4.3.2 Py-1 synthesis

In preparation for the conjugation of carboxylic acid **61** to our desired fluorophores, Py-1 precursor **149** was synthesised as the key intermediate for accessing Py-1 probe series **77**-**86**. Julolidine carbaldehyde **146** and pyrylium salt **148** were first synthesised from common lab reagents following the procedure reported by

Höfelschweiger and coworkers.[173]

Julolidine carbaldehyde **146** was synthesised through *in situ* generation of the Vilsmeier reagent with $POCl_3$ and DMF, followed by treatment with julolidine. The crude product was purified by flash chromatography to yield the desired product **146** (78%). Concurrently, pyrylium salt **148** was prepared *via* the condensation of acetic anhydride in the presence of *t*-BuOH. The crude product was recrystallised to obtain pyrylium **148** (34%). Julolidine carbaldehyde **146** was then treated with pyrylium salt **148** under reflux in methanol, resulting in an immediate colour change from colourless to blue. The crude product was purified by flash chromatography to afford Py-1 precursor **149** in quantitative yield.

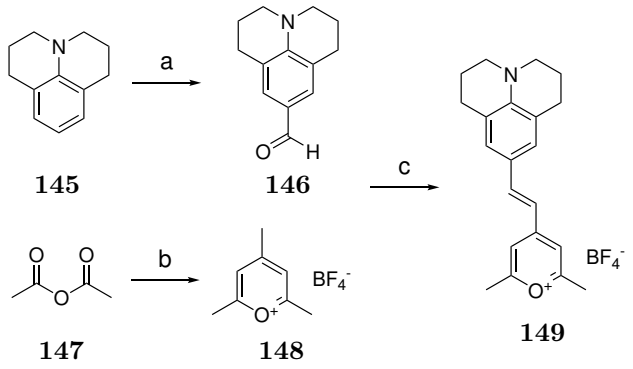

Scheme 33: Synthesis of Py-1 from commercially available lab reagents. (a) $POCl_3$, DMF, 0–90 °C, 20 h, 78%; (b) *t*-BuOH, 48% w/v aq. HBF_4, 5–100 °C, 5 min, 34%; (c) MeOH, reflux, 21 h, quant.

The mechanism for the synthesis of pyrylium **148** begins with the protonation of *tert*-butanol (*t*-BuOH), liberating isobutylene **153** and water. The isobutylene **153** attacks the protonated acetic anhydride **154**, forming intermediate **155**. Deprotonation by a suitable conjugate base in solution (e.g. acetate) generates alkene **156**, followed by elimination of acetic acid to form intermediate **157**, which can tautomerise to intermediate **158**. The nucleophilicity of the terminal alkene of **158** is greater than that of a saturated alkene **157**. This allows intermediate **158** to react with acetic anhydride **154**, forming intermediate **159** that undergoes proton transfer and elimination of acetic acid once more to form intermediate **161**. The final steps involve cyclisation, aromatisation, and dehydration to drive the reaction

to the pyrylium salt **148**. Various protonation sites and counterion exist throughout the intermediates, but these have been simplified in this mechanism for clarity.

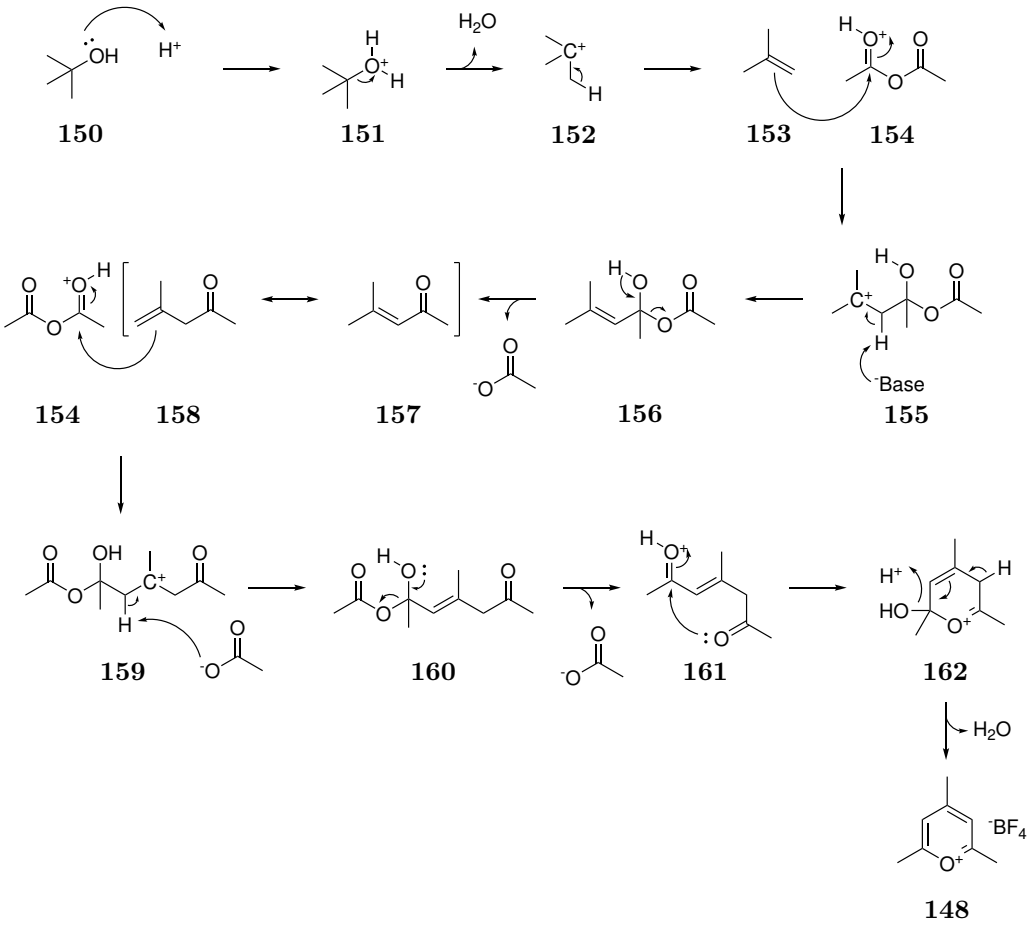

Scheme 34: Proposed mechanism for the synthesis of trimethylpyrylium tetrafluoroborate.

4.3.3 Linker and fluorophore conjugation

The conjugation of the Py-1 and TAMRA probes **77**-**89** began by appending linkers to the thiazole P2Y12 ligand. Then *via* a divergent strategy, the Py-1 and TAMRA fluorophores could be appended (**Scheme 19**).

Linker conjugation

A small selection of mono-Boc-protected amine linkers, readily available within our research group, was appended to carboxylic acid **61** using standard HATU amide coupling conditions (step a, **Scheme 35**). TLC analysis confirmed the complete conversion of starting material **61** and the reaction was subsequently halted. The

crude products were purified *via* flash chromatography, yielding the respective compounds **107**, **108** and **112**. However, flash chromatography was unable to separate an oily residue from the desired products.

Analysis by mass spectrometry did not reveal the presence of any species in addition to the desired product, but ^{1}H NMR spectroscopy revealed additional peaks in the aliphatic region (1.80-1.63, 1.32-1.18 and 0.90-0.79 ppm). This suggested the product was likely lipophilic and co-eluted with aliphatic impurities. Attempts were made to remove this byproduct by partitioning the crude product in MeCN and hexane, but after concentration, the impurity persisted when analysed by ^{1}H NMR spectroscopy. Trituration with hexane was also attempted, but the product formed a very fine suspension which proved challenging to filter to separate it from the greasy residue. Even after filtering and dissolving the product again, the byproduct continued to persist in the samples. Recrystallisation was attempted, but it was challenging to determine whether the oily product had dissolved on small-scale. To achieve a more reliable purification process, reverse-phase column chromatography was employed using C18 silica as the stationary phase, buffering with TFA to improve resolution. This purification strategy successfully removed the byproduct and afforded the respective products **107**, **108** and **112** in moderate to quantitative yields (step a, **Scheme 35**).

Py-1 analogues

With the purified Boc-protected amines **107**, **108** and **112** in hand, Boc-deprotection was performed using hydrogen chloride in dioxane in preparation for the final conjugation step. The crude free amines **163**, **164** and **165** were directly used in conjugation with Py-1 precursor **149**. Upon heating, the solution changed colour from blue to red and was monitored *via* TLC analysis until complete consumption of starting material was observed. Unfortunately, although attempts were made to isolate products **77**, **78** and **80** by flash chromatography using multiple eluent systems, ^{1}H NMR analysis showed multiple impurities across the spectrum. After

three days at ambient temperature, the compounds had decomposed into brown oily residues.

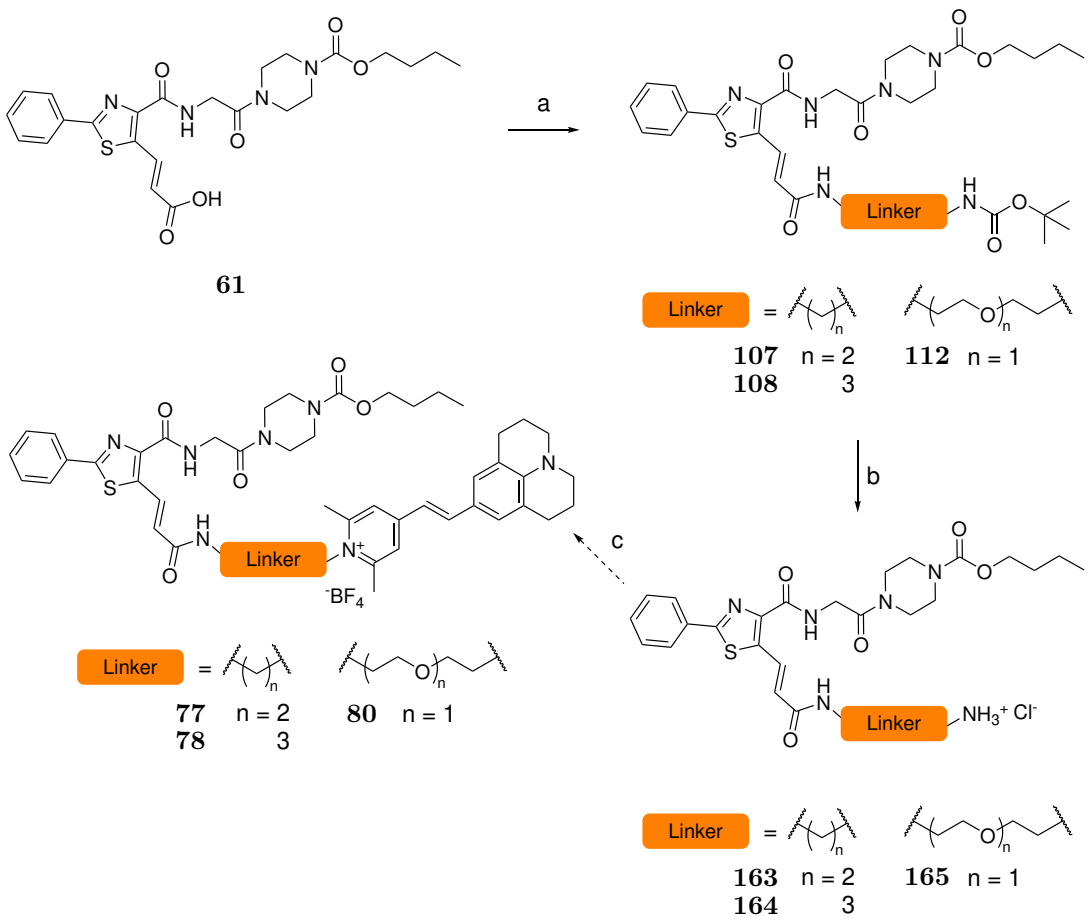

Scheme 35: Appending *N*-Boc-diaminelinkers to the lead **61** and subsequent attempts to Py-1 **149** conjugation. (a) *N*-Boc-diaminelinker, HATU, iPr$_2$NEt, DMF, rt, o/n, 62% - quant.; (b) 4 M HCl in dioxane, DCM, rt, 30 min, quant.; (c) Py-1 precursor **149**, MeCN, 60 °C, o/n.

A literature report recommended aqueous salt eluent systems to purify the pyridinium salt analogues.[196] Using sodium tetrafluoroborate in a gradient of water and acetone, the counterion was maintained as tetrafluoroborate. Despite this system aiding elution, NMR analysis indicated the product remained impure. Purification *via* reverse-phase chromatography was attempted without an acidic buffer component, and the product remained bound to the stationary phase. Buffering the solution with Et_3N or acetic acid, the product also remained bound to the stationary phase. Ultimately, TFA had to be used for the mobile phase and product **77** then eluted. Although mass spectrometry indicated the presence of the desired product, NMR

analysis was challenging with **77** observed to be poorly soluble in organic solvents.

The purification challenges were not exclusive to compound **77**, but applied to the other analogues in the Py-1 series. Instability of the product to atmospheric conditions and light made the series undesirable for the purposes of this project. Therefore, our attention turned towards preparation of the TAMRA fluorescent probes.

TAMRA analogues

To synthesise fluorescent probes **72**, **73** and **75**, the respective amines **163**, **164** and **165** were treated with HATU and $i\text{Pr}_2\text{NEt}$ to conjugate the ligand (**Scheme 36**). Mass spectrometry analysis suggested the formation of products **72**, **73** and **75**. However, TLC analysis indicated the formation of multiple products with poor resolution, preventing their separation, isolation, and characterisation. Flash chromatography was even more challenging than TLC analysis suggested, so purification was attempted using preparative TLC. Unfortunately, resolution of the preparative TLC was also poor and only trace quantities of product were isolated, as suggested by mass spectrometry analysis. Insufficient material was isolated for NMR analysis ($<$2 mg), exacerbated by the large molecular weight of the compounds. HPLC analysis revealed the presence of many impurities with similar retention times, prompting the search for a cleaner synthetic method.

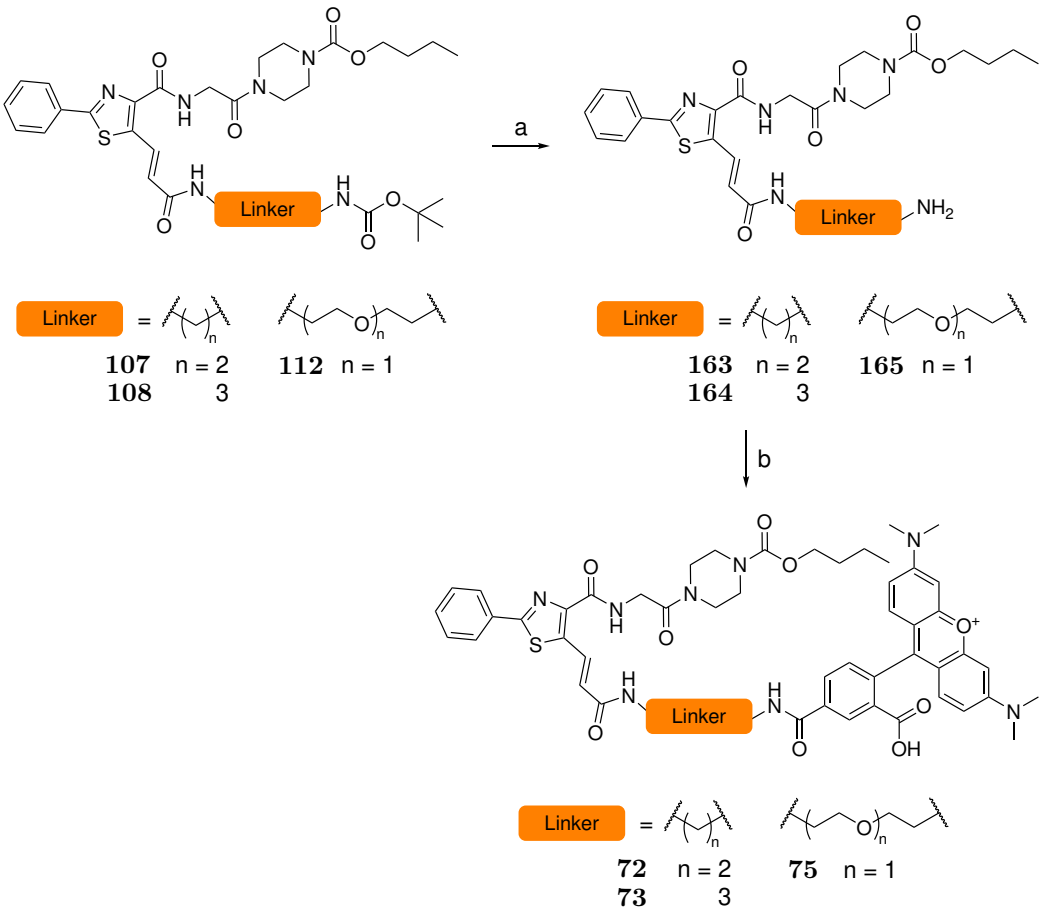

Scheme 36: Conjugation of the ligand with TAMRA. (a) 4 M HCl in dioxane, DCM, rt, 30 min, quant.; (b) TAMRA, HATU, iPr$_2$NEt, DMF, rt, o/n.

TAMRA *N*-hydroxysuccinimide (NHS) ester has commonly been used to aid conjugation with amines.[197,198] Efforts were therefore made to synthesise the TAMRA-NHS active ester **167** to enable facile conjugation with amines **163**, **164** and **165**. TAMRA **166** and NHS were pre-stirred with Et_3N, followed by the addition of diisopropyl carbodiimide (DIC). Attempts to purify the product with MeOH in DCM, buffered with Et_3N, inadvertently resulted in the substitution of the NHS ester with methanol. To mitigate this issue, purification with acetic acid and acetone proved more effective.[199] The isolated major product was the di-NHS ester **168**, with minor quantities of the mono-NHS ester **167** and starting material (entry 1, **Table 12**).

The reaction was repeated at low temperatures to investigate whether regioselectivity could be improved by starting cold and then slowly bringing the mixture to room temperature (entry 2, **Table 12**). However, cooling had an insignificant effect

on the regioselectivity of the reaction, again yielding both products **167** and **168**. The use of EDC to introduce steric bulk to the carbodiimide, with the intention of favouring the 5-position intermediate (entry 3, **Table 12**), also failed to significantly influence regioselectivity.

Table 12: Attempted synthesis and optimisation of TAMRA NHS ester **167**. (a) Conditions (see table). S.M. = starting material; $^{\alpha}$ Suggested by mass spectrometry and TLC analysis.

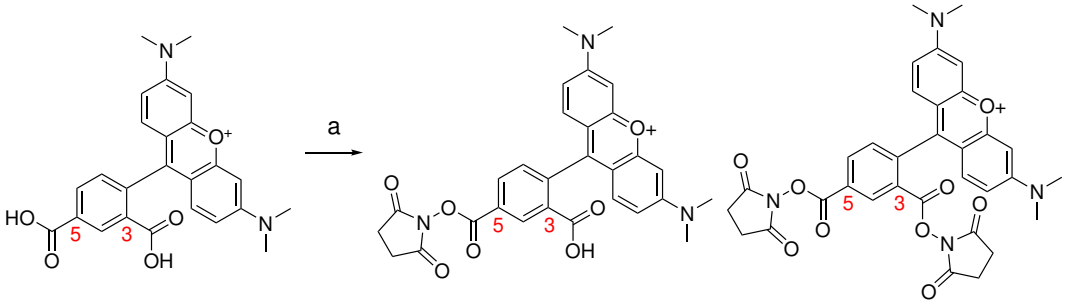

166 **167** **168**

Entry	Condition	Outcome
1	NHS, DIC, Et_3N, DCM, rt, o/n	Di-NHS ester **168** (Major) + Mono-NHS ester **167** (Minor) + S.M.$^{\alpha}$
2	NHS, DIC, Et_3N, DCM, 0 °C - rt, o/n	Di-NHS ester **168** (Major) + Mono-NHS ester **167** (Minor) + S.M.$^{\alpha}$
3	NHS, EDC, Et_3N, DCM, 0 °C - rt, o/n	Di-NHS ester **168** (Major) + Mono-NHS ester **167** (Minor) + S.M.$^{\alpha}$

To form the TAMRA lactone isomer **169** and deactivate the carboxylic acid at the 3-position, TAMRA was pre-stirred with a base (**Scheme 37**).[199,200] However, the formation of di-NHS ester persisted despite the attempt to deactivate the 3-position.

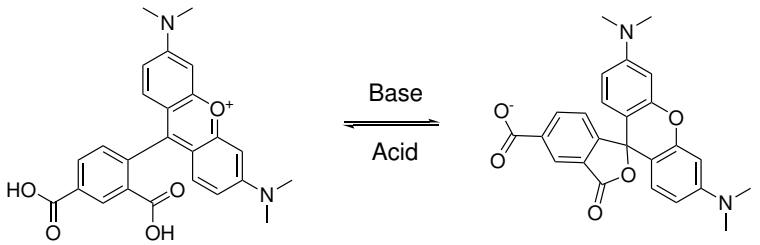

166 **169**

Scheme 37: Structural isomers of TAMRA under acidic and basic conditions.

Given the challenges of pre-functionalising TAMRA, we instead chose to reverse the coupling partners for our final probe conjugation step – preparing activated esters from P2Y12 ligand **61**. Carboxylic acid **61** was esterified under Steglich esterification conditions with suitable alcohols (entries 1 and 2, **Table 13**), resulting in the isolation of activated esters **170** (49%) and **171** (28%). Imidazole-substituted amide derivative **172** was synthesised by treating carboxylic acid **61** with CDI (33%, entry 3, **Table 13**). The NHS-ester was the highest yielding from the trials, and was further optimised by addition of a base ($i\mathrm{Pr}_2\mathrm{NEt}$), resulting in significantly improved yields (89%, entry 4, **Table 13**).

Table 13: Synthesis of activated esters and imidazole-substituted amide **170-172**.

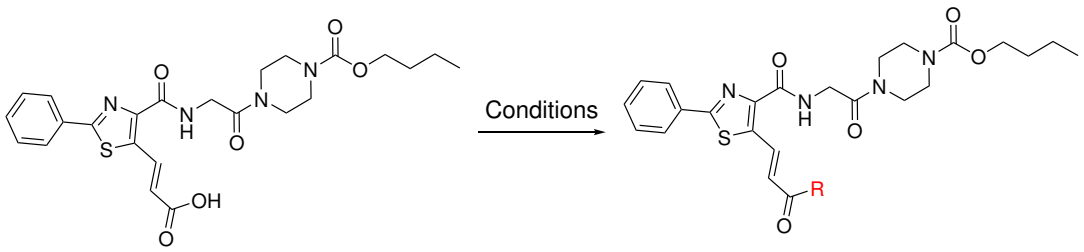

61

R =

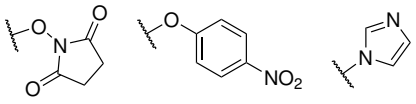

170 **171** **172**

Entry	Conditions	Outcome
1	4-Nitrophenol, EDC, DMAP, DCM, 0 °C - rt, o/n	28% yield of **171**
2	NHS, EDC, DMAP, DCM, 0 °C - rt, o/n	49% yield of **170**
3	CDI, DCM, rt, o/n	33% yield of **172**
4	NHS, DCC, DMAP, iPr$_2$NEt, DMA, 0 °C - rt, o/n	89% yield of **170**

For the conjugation of TAMRA **166** to the linker and the synthesis of compounds **173-180**, a strategy employing standard HATU amide coupling conditions was envisioned. TAMRA was pre-stirred with Et_3N to encourage spirocyclisation to its lactone form, followed by the addition of HATU and the respective amine (step a, **Scheme 38**). Initial purification using normal-phase chromatography resulted in co-elution with impurities. However, subsequent reverse-phase chromatography purification afforded the TAMRA-linker compounds **173-180** in moderate to high yields.

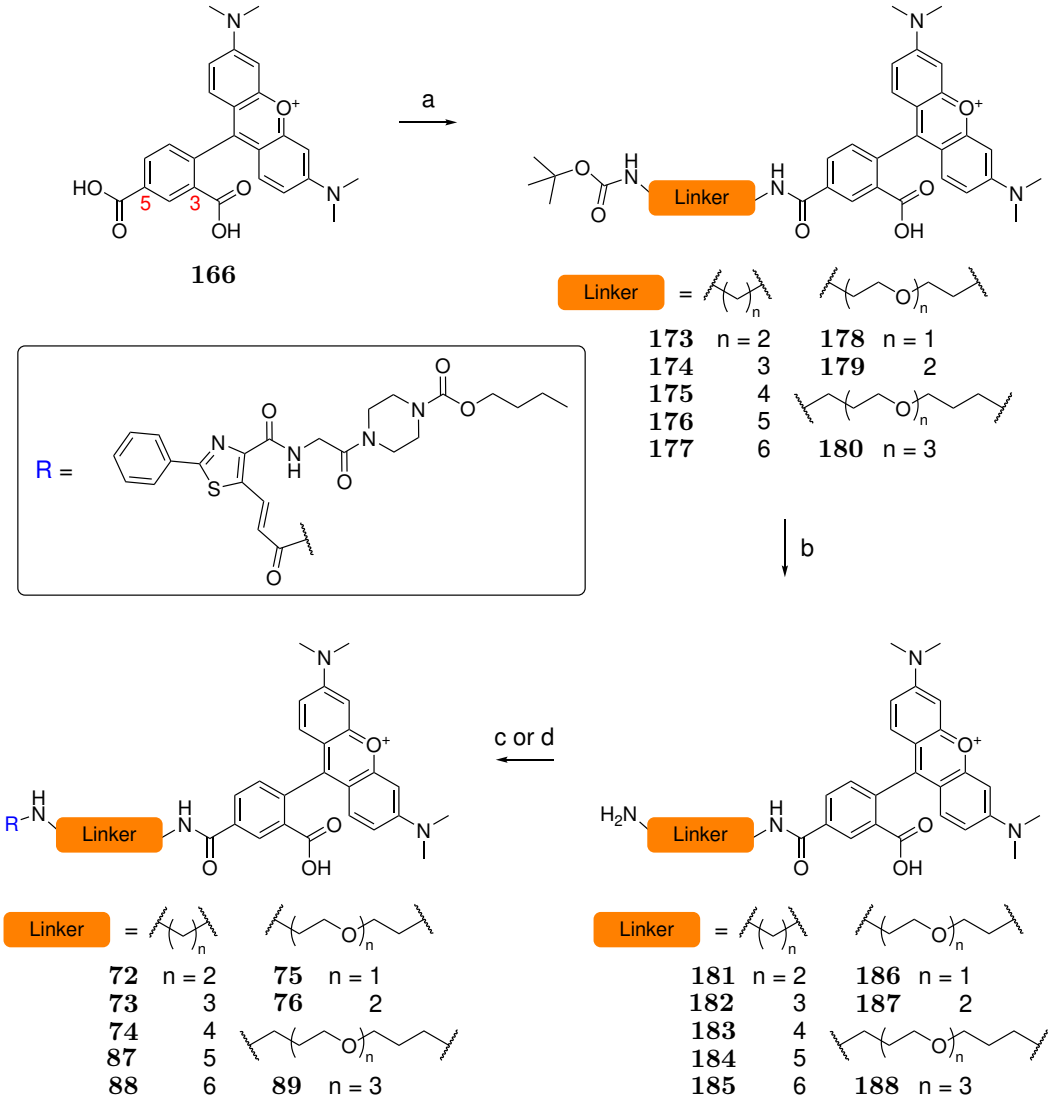

Scheme 38: Synthesis of fluorescent probes **72-89**. (a) *N*-Boc-diamine linker, HATU, Et_3N, DMF, rt, o/n, 33-89%; (b) 4 M HCl in dioxane, DCM, rt, 30 min; (c) 4-Nitrophenyl ester **171**, $i Pr_2NEt$, DCM, rt, o/n, 49% (over 2 steps); (d) NHS ester **170**, $i Pr_2NEt$, DCM, rt, o/n, 43-93%.

Based on ^{1}H NMR spectroscopy, products **173-180** were confirmed to be mono-amidated, but the regioselectivity of the linker attachment was unclear. NMR strategies, including heteronuclear single quantum coherence (HSQC) and heteronuclear multiple-bond coherence (HMBC), failed to definitively identify the hydrogen-carbon correlations for the 3 and 5-position carboxylic acid due to weak signals. Consequently, discriminating the regioisomer of the amides through HMBC would not be possible without definitive evidence of the peak correlations. As an alternative, nuclear Overhauser effect spectroscopy (NOESY) correlation was employed to ascertain

whether unwanted 3-position regioisomers were formed. The absence of NOESY signals between the linker and TAMRA (**Figure 29**) represented tentative evidence for the desired 5-position regioisomer.

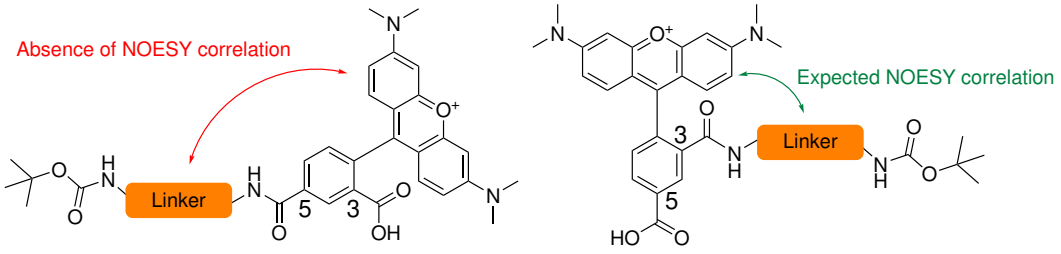

Figure 29: TAMRA-linker compounds regioisomer determination strategy by the presence or absence of an expected NOESY correlation peak.

With regioisomerically pure TAMRA-linker compounds (**173**, **174**, and **178**) in hand, Boc-deprotection was performed using HCl in dioxane (step b, **Scheme 38**). TLC analysis confirmed the complete conversion of the starting materials. The deprotected amines (**181**, **182**, and **186**) were individually suspended in acetonitrile, filtered, and taken up in a solution of Et_3N and chloroform before being concentrated and conjugated with the activated ester (step c or d, **Scheme 38**). The NHS ester **170** substituted more rapidly than the nitrophenol ester **171**. After 2 hours, significant product formation was observed with the NHS ester, while only minor product formation was observed with the nitrophenol ester. The crude products were purified *via* reverse-phase chromatography, buffering with TFA. Pure products **72**, **73**, and **75** were obtained. Unlike the Py-1 series, the products were stable under ambient conditions.

Interestingly, the Boc-deprotected products **175-177**, **179**, and **180**, when conjugated without filtration, produced impurities in the final compounds (**74-88**, **76**, and **89**) that were observable by NMR analysis. However, no observable impurity peaks appeared by mass spectrometry analysis.

The final step prior to biological evaluation of the probes was HPLC analysis to confirm sample purity. Analytical HPLC separated the analytes using a reverse-phase column and a UV-Vis detector read the intensity at a particular wavelength to estimate the purity of the compounds. Analysis of compound **72** showed two analytes

with close retention times (**Appendix 39a**). Intriguingly, the two chromatogram peaks share similar UV-Vis spectra with absorption peaks that were characteristic of the long-wave UV active phenylthiazole propenamide core and TAMRA (343-348 and 556-558 nm). No analyte was detected in the intermediates that shared the same retention time (R_T = 22.2 min), suggesting it is unlikely to be an impurity from the reaction. NMR analysis did not suggest any notable impurities. Apart from the desired product, no other species were observed by matrix-assisted laser desorption/ionisation (MALDI) and atmospheric pressure chemical ionisation (APCI) mass spectrometry. Further purification by a slow reverse phase column was able to separate two impurities, but yielded identical HPLC chromatograms to those acquired before the purification process. Mass spectrometry and NMR analysis confirmed the successful conjugation between active ester **170** and amine **181**, leading to the conclusion that the HPLC analytes could be artefacts of various protonation states, peak tailing, or both, under standard analytical HPLC conditions.[201]

The next step was to identify alternative HPLC conditions for analysing the fluorescent probes. In HPLC analysis, a buffered mobile phase is used to maintain a homogenous pH environment, ensuring the single protonation state throughout the run. TFA is the gold-standard buffering reagent, typically maintaining a pH of 2 with 0.1% v/v concentration in the chromatographic solution. However, this concentration proved insufficient to maintain a single protonation state, leading to multiple analytes for compound **72**. Switching to an ammonium hydroxide buffer with a Waters Xbridge column produced a single analyte in the chromatogram for compound **73** (**Appendix 43**). However, this broad peak raises the possibility of overlap with other analytes in the sample. Many attempts in adjusting the chromatographic solution, column and method were unable to quantify the purity of our final compounds, exhausting all avenues within the given timeframe.

4.3.4 TAMRA analogue fluorescent properties

To assess the suitability of TAMRA analogues **72**, **73**, and **75** for NanoBRET applications, their fluorescent properties were evaluated in methanol under standard conditions (**Appendix 5**). Excitation spectra were recorded using UV-Vis spectrophotometry, and emission spectra were obtained *via* fluorometry, as shown in **Figure 30**. The recorded excitation and emission maxima ($\lambda_{ex} \approx 552$ nm, $\lambda_{em} \approx 578$ nm) were consistent with the characteristic photophysical properties of TAMRA fluorophores,[202] indicating that conjugation to the ligand did not significantly perturb fluorescence behaviour. These results support the potential of these TAMRA analogues for use in NanoBRET-based assays.

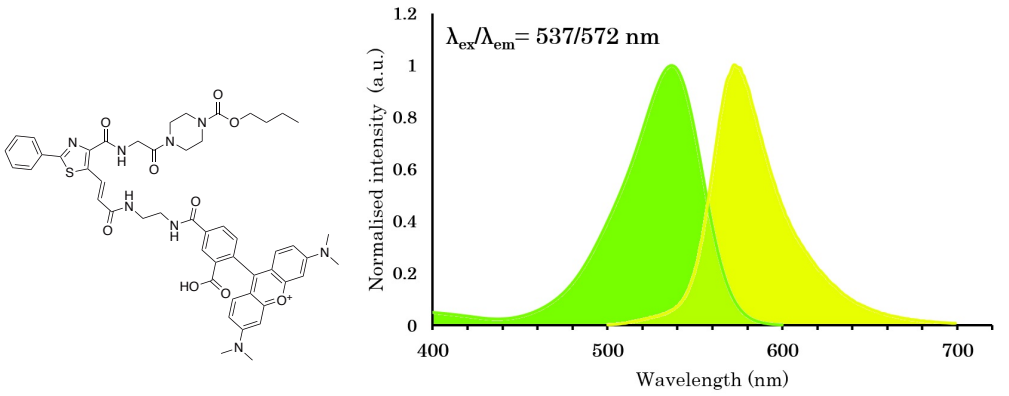

(a)

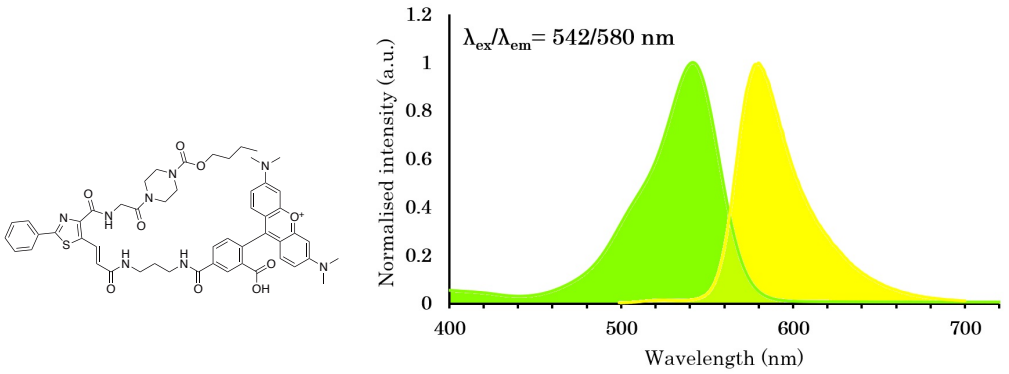

(b)

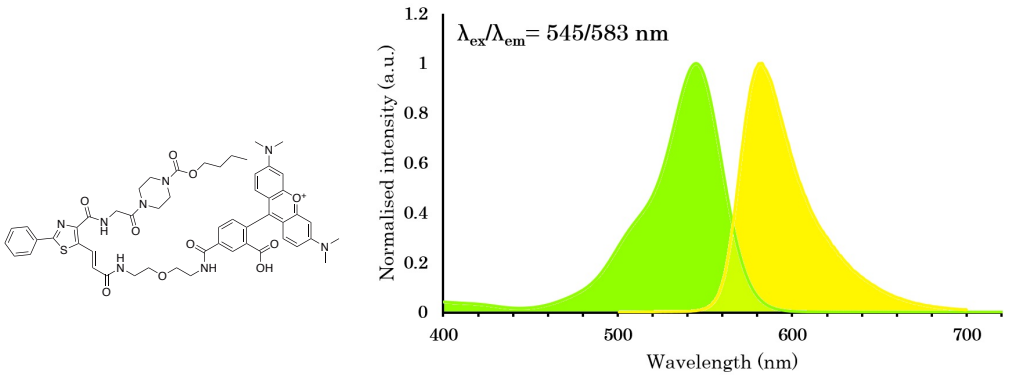

(c)

Figure 30: Excitation and emission spectra of fluorescent probes **72**, **73** and **75** were recorded in MeOH. Experimental conditions are detailed in **Appendix 5**. Data were normalised to the maximal peak excitation and emission. The colours of the excitation and emission spectra correspond to their respective peak wavelengths, converted to RGB using the wavelength-to-RGB calculator from Academo: https://academo.org/demos/wavelength-to-colour-relationship/. a) Excitation and emission spectra of fluorescent probe **72** (left). b) Excitation and emission spectra of fluorescent probe **73** (left). c) Excitation and emission spectra of fluorescent probe **75** (left).

4.4 Concluding remarks

The goal of this chapter was to synthesise a library of P2Y12 probes for the development of a fluorescence-based competition binding assay. The design of the NanoBRET probe library were based on the results from molecular docking in **Chapter 3**. Along the library synthesis, TAMRA and Py-1 were evaluated for their suitability for fluorescence-based competition binding assay. The main focus of the library was to identify the optimal linker length and composition.

The divergent strategy to access the library required scalable procedures to access divergent intermediate **61**. The optimised synthetic route to divergent intermediate **61** was achieved with an overall yield of over 40% yield across 12 steps. Using this intermediate to generate the Py-1 library, the fluorophore was found to be unstable and unsuitable for fluorescence-based competition binding assay. In contrast, the TAMRA analogues were stable and demonstrated the expected fluorescence properties, indicating their suitability for NanoBRET applications. As a result, the TAMRA series became the focus for further optimisation, particularly in evaluating the ideal linker length. Nonetheless, biological evaluation was hampered by purification and analytical HPLC challenges.

HPLC suggested compound **72** was impure, whereas NMR and mass spectrometry suggested the product was pure. The contradiction in observations were speculated to be the presence of multiple ionisation states, peak tailing or a combination of both during the chromatographic separation. Switching to a base-buffered condition caused peak broadening, and further investigation is needed to better resolve the peaks.

Overall, the goals for this chapter have been partially met, though progress is currently hindered by the limitations of the purity evaluation strategy. The biological evaluation of the proposed fluorescent probe library will be crucial in determining the optimal linker length and fluorophore. The binding and BRET ratio data of the fluorescent probes will be assessed for their utility in NanoBRET binding assays. Depending on the results, the fluorescent probes may need further development

or could be used for establishing a NanoBRET P2Y12 competition binding assay protocol. The development of a P2Y12 NanoBRET assay would immediately facilitate the biological evaluation of the PET tracers discussed in **Chapter 2**. This will also open the future horizons for the *de novo* design of P2Y12 PET tracers through HTS.

Chapter 5

Conclusion and future directions

5.1 Summary of our work toward chemical probes for studying P2Y12

Neuroinflammation, the native immune response of the CNS mediated primarily by microglia, is poorly understood in normal physiological conditions and even less so in the context of neurodegenerative diseases. P2Y12 upregulation is suggested to correlate with the critical but understudied anti-inflammatory microglial response in the CNS. PET imaging of P2Y12 using highly targeted small molecule radiotracers could enable cell-specific molecular imaging, that will provide real-time insights into the complex biochemical processes of neuroinflammation. Developing a suite of radiolabelled tool compounds to investigate this receptor is an important first step toward understanding neuroinflammation and its role in health and disease. Previous efforts have been made to repurpose existing P2Y12 ligands from the literature for CNS PET imaging applications, but these ligands cannot cross the BBB or accumulate in the CNS. As a result, the overarching goal of this thesis was to develop new molecules for imaging P2Y12 in the CNS.

In **Chapter 2**, the design and synthesis of fluorinated P2Y12 probes were explored. Results from extensive structure activity relationship (SAR) studies from P2Y12 anti-thrombotic drug discovery campaigns were leveraged to identify a small,

high-affinity lead compound suitable for CNS applications. The lead compound was subsequently modified to incorporate fluorine, with the goal of investigating fluorine tolerability within the binding pocket. A divergent synthetic approach was proposed to furnish our desired compounds, motivating an optimisation campaign to access lead compound **17**. The optimised pathway removed 2 steps from the published synthesis and improved its cumulative yield by 3-fold. This allowed access to gram-scale quantities of the lead compound **17**. Hydrolysis of **17** followed by Steglich esterification successfully produced the desired ester series **19-21**. However, attempts to synthesise the corresponding ketones **22** and **23** via Weinreb ketone synthesis were unsuccessful due to rapid deactivation of the Grignard reagents. During this period of the project, COVID lockdowns significantly limited research capabilities. Latest literature suggested the lead scaffold was CNS impenetrable due to the anionic sulfonylurea moiety under physiological conditions. Thus, attention was turned to the development of fluorescent probes for biological evaluation of the synthesised compounds.

In **Chapter 3**, P2Y12 ligands from literature were reassessed for their potential as starting points for P2Y12 fluorescent probe development. A suitable thiazole scaffold was identified, and molecular docking studies were performed to establish the binding pose of the ligand at P2Y12. The carboxylic acid groups of thiazoles **61** and **60** were suggested to point into the extracellular space by docking studies. Simultaneously, the carboxylic acid group was identified as a synthetic handle for development of a NanoBRET fluorescent probe. Based on these findings, a library of truncated NanoBRET fluorescent probes was designed to investigate the tolerability of the proposed modifications. Docking results suggested that amide linkers would be tolerated within the binding pocket for both scaffolds. Further docking investigation on a library of the full-length fluorescent probes, including the linker and fluorophore, was performed. Although docking of the full-length fluorescent probes showed that short alkyl linkers were favoured, the docking scores of the truncated ligands provided sufficient evidence of tolerability of the modifications at the binding pocket.

In **Chapter 4**, the design and synthesis of fluorescent P2Y12 probes were explored. A library of fluorescent P2Y12 probes was designed based upon lead compound **61**. A divergent synthetic approach was proposed to furnish both TAMRA and Py-1 series **72**-**86**, motivating an optimisation campaign to access large quantities of late-stage divergent intermediate **61**. Highly optimised and robust Heck coupling conditions were developed to overcome the challenges associated with olefination of the thiazole 5-position to yield the *tert*-butyl ester **92**. Optimisation resulted in a cumulative yield of over 40% across 12 steps and facilitated the divergent synthetic approach. Conjugation with fluorophores revealed that Py-1-based probes were unstable under ambient conditions, whereas TAMRA-based probes were stable and further investigated. However, the TAMRA-based probes presented challenges in purity analysis using HPLC that have yet to be fully resolved, delaying their biological evaluation. Subsequently, the optimum linker length has yet to be identified.

5.2 Future directions

In the current landscape, a BBB permeable P2Y12 PET tracer has not yet been developed through the repurposing of literature P2Y12 ligands. Recently, Wildt and coworkers have administered radiolabelled sulfonylurea **17** in mouse models, but they did not observe CNS uptake, even with co-administration of BBB efflux transporter (P-gp) inhibitor tariquidar.[100] Wildt and coworkers have explored the use of *in silico* BBB permeability predictive algorithms to select leads for CNS PET tracer development, but the thienopyrimidine structures were subject to efflux by P-gp transporters.[100] These findings suggest that anti-thrombotic candidates may not be suitable for CNS applications, indicating the potential need for a novel scaffold. Before developing a new tracer, an accessible binding assay must be developed and validated in order to identify a new scaffold.

Fluorescence-based assays offer advantages over traditional radioligand binding assays that improve accessibility. Fluorescent probes exhibit long shelf-lives, and fluorescence-based binding assays require fewer resources, special clearances, or

handling and safety training. Currently, we are developing a fluorescence-based P2Y12 binding assay incorporating NLuc-expressing protein and a BRET acceptor ligand. First, our library of probes will be screened for affinity toward P2Y12 and BRET ratios evaluated. The highest-affinity ligand that generates the strongest BRET ratio will be selected for further validation. It will also be important to validate the NanoBRET binding assay accurately reflects biological binding dynamics that corresponding to native, unlabelled P2Y12.[167] This can be achieved by measuring the affinity of the fluorescent probe for the native ligand using laser irradiation and comparing the results to those obtained from the NanoBRET assay. Alternatively, cross-validation using a competition radioligand binding assay could be used should such a platform become available.[203]

Fragment or HTS would be a viable option for discovery of novel P2Y12 ligands with the advent of a robust and reliable NanoBRET assay. The design of a P2Y12 PET tracer lead candidate from a new scaffold will allow for prudent modifications to promote BBB permeability. To rationalise the development of a BBB permeable P2Y12 PET tracer, *in silico* tools such as docking studies, and prediction of ligand efficiency and BBB permeability using a range of complementary algorithms would inform the ligand design. Leveraging the antagonist-bound crystal structure (PDB: 4NTJ) would support rapid and high-accuracy lead optimisation. Ligand efficiency metrics can help maintain a balance of potency and small molecular size, essential for both binding specificity and BBB permeability.[204] Meanwhile, BBB permeability prediction algorithms can further screen modifications for favourable structural characteristics. This integration of these tools will improve the likelihood of developing a successful P2Y12 PET tracer.

The development of a P2Y12 PET tracer that can image the receptor in the CNS would provide invaluable insight into microglial behaviour during neuroinflammatory events, particularly in neurodegenerative diseases. In addition, the use of fluorescent-based tools for *in vitro* cell imaging could complement these studies, further enhancing understanding of P2Y12 expression and function in different pathological states.

A limited understanding of neurodegenerative disease mechanisms has hindered the development of effective treatments. The identification of key diagnostic or therapeutic targets through *in vivo* tools could streamline the development of drugs for neurodegenerative diseases. Early-stage diagnosis via molecular imaging of receptor expression could prompt timely treatment, potentially improving patient outcomes and slowing disease progression. Evidence also suggests that partial antagonism of P2Y12 may improve lesion repair,[92] a finding that could inform disease-modifying therapies for neurodegenerative conditions. Ultimately, further exploration of P2Y12 in the CNS could elucidate its role in neuroinflammation and advance the development of effective therapeutic strategies.

Chapter 6

Experimental

6.1 Docking studies

The P2Y12 crystal structures (4NTJ, 4PXZ and 4PY0) were prepared using preparation and refinement protocols, directed by the Protein Preparation Wizard embedded in Maestro v13.6 (Schrödinger, LLC, New York, USA). This process includes assigning bond orders, adding hydrogen atoms, and creating zero order bonds to metals and disulphide bonds. The hydrogen bond network within the protein was also optimised with all heteroatom groups within the receptor grid bounding box previously removed and the protein structure minimised to a root mean square deviation (RMSD) of 0.3 Å using the OPLS3 force field

The energy minimised structure of desired ligands was generated using Chemdraw Professional 22.2.0 and Chem3D 22.2.0 (CambridgeSoft Ltd). Following this, ligands were prepared using the LigPrep v4.9 module to generate possible stereoisomers of the ligands. Structures of all potential ionisation states at pH 7 ± 2 were generated. Tautomers were generated and geometries were optimised using OPLS3 force field. Conformers were randomly created for each LigPrep-processed ligand, yielding up to 64 conformers using the ConfGen package.

The receptor grid generation tool in Glide v8.4 was used to characterise the binding site for these docking studies. Binding sites were centred on either the ligand

of the active site or were centred on key residues. A Coulomb-van der Waals scaling factor of 1.0 for receptor van der Waals radii was applied to protein atoms with a partial charge of less than 0.25 e and a similar factor of 0.8 was applied to ligand atoms with a partial charge cutoff of less than 0.15 e. Rotations of hydroxyl and thiol groups were not allowed. All ligands were docked into the receptor grid using Glide v8.4, with all docking carried out using the Extra Precision (XP) scoring function.

6.2 General experimental details

All solvents and reagents were purchased from commercial sources. Anhydrous solvents were obtained from an Innovative Technology PureSolv7 purification system and dried over 5 Å molecular sieves. All reagents were weighed out under ambient conditions. Reactions that calls for anhydrous conditions were kept under nitrogen or argon.

Analytical TLC was performed using Merck aluminium backed silica gel 60 F254 (0.2 mm) plates that were all visualised with UV light (254 or 365 nm), with solvent reported as volume:volume ratio. Otherwise visualised with vanillin, anisaldehyde, ninhydrin, dinitrophenylhydrazide, potassium permanganate and bromocresol green stains. Flash chromatography was performed using Merck Kieselgel 60 (230-400 mesh) or Chem-Supply Silica Gel 60 (0.04-0.06 mm, 230-400 mesh), unless otherwise stated. Reverse phase chromatography was performed on Biotage® Isolera™ One with a ILOK™-SL pre-packed SL4 irregular C18 60 Å column (40-63 µm). Preparative TLC was performed using Analtech glass backed silica gel 60, 10 µm particle (1000 microns thickness) and visualised under visible light. Eluent mixture reported as the percentage of total solution, and the addition of buffers as a volume percentage of the total solution where stated. Hexane and petroleum benzine 40-60 boiling range were used interchangeably.

Melting points were recorded using an Optimelt Automated melting point apparatus from Stanford Research Systems and were measured in open capillary tubes. Decomposition temperature was taken from when the initial colour change has

occurred.

Nuclear magnetic resonance spectra were recorded at 300 K using either a Bruker AVANCE NEO 300 (300 MHz), AVANCE III 400 (400 MHz), AVANCE III 500 (500 MHz) and AVANCE NEO 500 (500 MHz) spectrometer. ^{1}H chemical shifts are expressed as parts per million (ppm) with $CDCl_3$ (δ 7.26), CD_3OD (δ 3.31), DMSO-d_6 (δ 2.50) and CD_3CN (δ 1.94) as reference and are reported as chemical shift (δ); ; multiplicity (s = singlet, br = broad singlet, d = doublet, dd = doublet of doublets, dt = doublet of triplets, q = quartet, t = triplet, td = triplet of doublets, tt = triplet of triplets, m = multiplet); coupling constants (J) reported in Hz; relative integral. Proton decoupled ^{13}C chemical shifts are expressed as parts per million (ppm) with residual $CDCl_3$ (δ 77.16), CD_3OD (δ 49.00), DMSO-d_6 (δ 39.52) and CD_3CN (δ 1.32, 118.26) as reference and reported as chemical shift (δ). Proton decoupled ^{19}F chemical shifts are reported as parts per million (ppm).

Low-resolution mass spectra (LRMS) were recorded using electrospray ionisation (ESI) on a Bruker AmaZon SL ion trap spectrometer. High-resolution mass spectrometry (HRMS) was performed on a Bruker Apex Qe 7T Fourier Transform Ion Cyclotron Resonance mass spectrometer equipped with an Apollo II ESI/MALDI dual source. Samples were run with syringe infusion at 150 µL/hr on a Cole Palmer syringe pump into the ESI source. HRMS samples were run by Dr. Nicholas Proschogo.

High performance liquid chromatography (HPLC) analysis of organic purity was conducted on a Waters Alliance e2690 instrument using either a SunFire™ C18 column (5 µm, 2.1 × 150 mm) or XBridge™ C18 column (5 µm, 2.1 × 150 mm) and detected using a Waters 2998 photodiode array detector analysing between 210-700 nm. Condition a: Separation was achieved using water + 0.1% TFA (solvent A) and MeCN + 0.1% TFA (solvent B) at a flow rate of 0.2 mL/min and a gradient of 10-100% B over 30 minutes. Condition b: Separation was achieved using water + 0.1% TFA (solvent A) and MeCN + 0.1% TFA (solvent B) at a flow rate of 0.2 mL/min and a gradient of 1-100% B over 30 minutes. Condition c: separation was

achieved using water + 0.1% ammonium hydroxide (solvent A) and MeCN + 0.1% ammonium hydroxide (solvent B) at a flow rate of 0.2 mL/min and a gradient of 10-100% B over 30 minutes.

The DMSO solvent used in photophysical studies was of analytical grade (UNIVAR, Ajax Finechem). All coumpounds were prepared as a DMSO (UNIVAR, Ajax Finechem) stock solution diluted to the appropriate concentration using MeOH (LiChrosolv®, Merck). Emission property characterisations were performed on a Horiba FluoroMax®-4 spectrofluorometer equipped with a temperature controlled multicell holder with temperature control enabled (25 °C) using a quartz cuvette (10 mm pathlength). Excitation property characterisations were performed on a Cary 4000 UV-Vis spectrophotometer using a quartz cuvette (10 mm pathlength).

(31) Ethyl 5-cyano-2-methyl-6-oxo-1,6-dihydropyridine-3-carboxylate

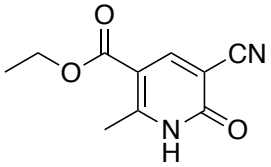

N,*N*-Dimethylformamide dimethyl acetal (DMF-DMA, 46 mL, 0.35 mol) in EtOH (82 mL, 1.4 mol) was stirred with ethyl acetoacetate (40 mL, 0.31 mol) for 3 h at 42 °C until the starting material was consumed as observed by TLC. The mixture was cooled to room temperature (rt) before the slow addition of triethylamine (Et_3N, 4.4 mL, 32 mmol) and malononitrile (24 g, 0.36 mol) in EtOH (180 mL) while maintaining between 25-36 °C. This was allowed to stir for a further 18 h at rt. Acetic acid (22 mL, 0.38 mol) was then added dropwise, keeping the temperature below 25 °C, resulting in a precipitate. The reaction mixture was heated to 75 °C, water (560 mL) was added, and the reaction mixture was cooled to 0 °C. The precipitate was collected, washed with water (3 × 200 mL), and dried *in vacuo* to afford the title compound as an orange solid (43 g, 67%). **mp:** 213-215 °C; **^{1}H NMR (300 MHz, DMSO-d_6):** δ 12.94 (br, 1H), 8.43 (s, 1H), 4.22 (q, J = 7.0 Hz, 2H), 2.60 (d, J = 1.4 Hz, 3H), 1.28 (t, J = 7.1 Hz, 3H) ppm; **LRMS (ESI$^+$)** *m/z*: 229 $[M+Na]^+$. Spectroscopic data consistent with literature.[130]

(27) Ethyl 6-chloro-5-cyano-2-methylnicotinate

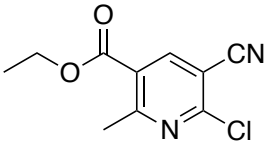

Pyridinone **31** (0.50 g, 2.4 mmol) was dissolved in a solution of phosphoryl chloride (0.36 mL, 3.9 mmol) in MeCN (1.5 mL) and stirred under nitrogen for 22 h at reflux. The mixture was cooled to 0 °C before adding methyl *tert*-butyl ether (3 mL), water (3 mL) and stirred for 30 min at 20 °C. The layers were separated

and the aqueous layer was extracted again with methyl *tert*-butyl ether (1 mL). The combined organic layer was washed with water (2 mL), aq. potassium carbonate (5% w/v, 2 mL), water (2 mL), dried over $MgSO_4$ and concentrated *in vacuo*. EtOH (3 × 10 mL) was added and concentrated *in vacuo* repeatedly to afford the title compound as a yellow solid (0.48 g, 87%). **mp:** 65-66 °C; **^{1}H NMR (300 MHz, $CDCl_3$ with 0.1% v/v TMS):** δ 8.49 (s, 1H), 4.42 (q, J = 7.1 Hz, 2H), 2.90 (s, 3H), 1.42 (t, J = 7.1 Hz, 3H) ppm; **LRMS (ESI$^+$)** *m/z*: 247/249 $[M+Na]^+$. Spectroscopic data consistent with literature.[130]

(32) Ethyl 6-(3-((tert-butoxycarbonyl)amino)azetidin-1-yl)-5-cyano-2-methylnicotinate

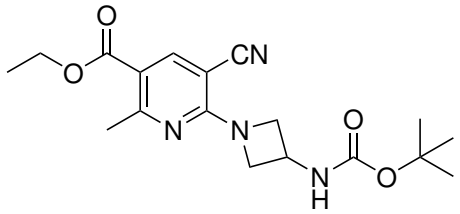

Tert-butyl azetidin-3-ylcarbamate hydrochloride (6.2 g, 30 mmol), nicotinate **27** (6.2 g, 28 mmol), and *i*Pr_2NEt (10 mL, 60 mmol) were dissolved in 1,2-dichloroethane (DCE, 40 mL) and stirred overnight at rt. The mixture was concentrated and then taken up in EtOAc (100 mL), washed with sat. $NaHCO_3$ (2 × 40 mL), brine (40 mL) and dried over $MgSO_4$. This was concentrated *in vacuo* and the crude product was purified by flash chromatography (SiO_2; 14% v/v EtOAc in hexane). Remaining impure fractions were concentrated, recrystallised from EtOAc, and combined with the pure compounds from the column to afford the title compound as white crystals (8.8 g, 93%). **mp:** 173 °C; **^{1}H NMR (300 MHz, $CDCl_3$ with 0.1% v/v TMS):** δ 8.26 (s, 1H), 4.98 (br, 1H), 4.70 (t, J = 8.7 Hz, 2H), 4.59 (br, 1H), 4.30 (q, J = 7.1 Hz, 2H), 4.24-4.15 (m, 2H), 2.70 (s, 3H), 1.46 (s, 9H), 1.37 (t, J = 7.1 Hz, 3H) ppm; **LRMS (ESI$^+$)** *m/z*: 383 $[M+Na]^+$. Spectroscopic data consistent with literature.[99]

(33) 2,2,2-Trichloroethyl ((5-chlorothiophen-2-yl)sulfonyl)carbamate

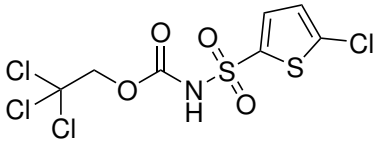

NaOH (8.1 g, 200 mmol) in water (100 mL) was added to 5-chlorothiophene-2-sulfonamide (15 g, 76 mmol) in DCE (350 mL). 2,2,2-Trichloroethyl chloroformate (13.5 mL, 98 mmol) was added dropwise to vigorously stirring 5-chlorothiophene-2-sulfonamide mixture at 0 °C. After complete addition, the mixture was brought up to rt and further stirred for 7 h. The mixture was acidified to pH < 1 with concentrated HCl, extracted with DCM (500 mL), followed by washing the organic layer with brine (100 mL) and drying over $MgSO_4$, and concentrating *in vacuo*. The crude product was purified by flash chromatography (SiO_2; 5-25% v/v EtOAc in hexane) to afford the title compound as a white solid (8.5 g, 30%). **mp:** 69-76 °C; **^{1}H NMR (300 MHz, $CDCl_3$ with 0.1% v/v TMS):** δ 8.31 (br, 1H), 7.70 (d, J = 4.2 Hz, 1H), 6.98 (d, J = 4.1 Hz, 1H), 4.75 (s, 2H) ppm; **LRMS (ESI$^-$)** m/z: 372 $[M\text{-}H]^-$. Spectroscopic data consistent with literature.[99]

(44) 6-(3-Aminoazetidin-1-yl)-5-cyano-2-methylnicotinate hydrochloride

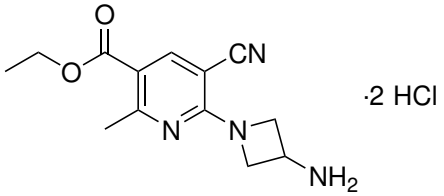

Hydrogen chloride in 1,4-dioxane (4 M, 14 mL, 56 mmol) was added slowly to a stirring suspension of Boc-amine **32** (0.98 g, 2.7 mmol) in DCM (10 mL), which was then left stirring for 18 h at rt. The reaction mixture was concentrated to afford the title compound as a white solid, which was carried through without further purification. **^{1}H NMR (400 MHz, DMSO-d_6):** δ 8.61 (br, 3H), 8.34 (s, 1H),

4.57 (t, J = 9.0 Hz, 2H), 4.36-4.27 (m, 2H), 4.24 (q, J = 7.1 Hz, 2H), 4.17-4.09 (m, 1H), 2.64 (s, 3H), 1.30 (t, J = 7.1 Hz, 3H) ppm (rapid proton exchange made the pyridinium proton more difficult to observe); **LRMS (ESI$^+$)** m/z: 261 $[M+H]^+$.

(17) Ethyl 6-(3-(3-((5-chlorothiophen-2-yl)sulfonyl)ureido)-azetidin-1-yl)-5-cyano-2-methylnicotinate

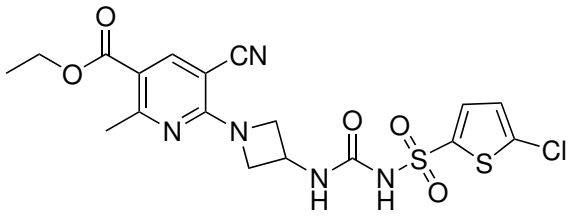

2-Chloropyridine (80 µL, 0.85 mmol) was added to amine **44** (0.10 g, 0.29 mmol) in dry DCM (1 mL), to which trifluoromethanesulfonic anhydride (50 µL, 0.30 mmol) was added dropwise. The resulting reaction mixture was stirred for 50 min at rt under nitrogen atmosphere. Et_3N (0.23 mL, 1.7 mmol) was added dropwise, followed by the addition of 5-chlorothiophene-2-sulfonamide (0.19 g, 0.86 mmol) and stirring overnight at rt. The reaction mixture was diluted in chloroform (50 mL), washed with water (25 mL), brine (25 mL) and dried over $MgSO_4$. This was concentrated *in vacuo* and the crude product was purified by flash chromatography (SiO_2; 30-50% v/v EtOAc in hexane and then 30-50% v/v EtOAc in hexane + 0.5% AcOH) to afford the title compound as a white solid (68 mg, 49%). **^{1}H NMR (300 MHz, DMSO-d_6):** δ 11.24 (br, 1H), 8.29 (s, 1H), 7.59 (d, J = 4.1 Hz, 1H), 7.38 (s, 1H), 7.23 (d, J = 4.1 Hz, 1H), 4.52 (m, 3H), 4.22 (q, J = 7.1 Hz, 2H), 4.14 (d, J = 6.3 Hz, 2H), 2.61 (s, 3H), 1.29 (t, J = 7.1 Hz, 3H) ppm; **LRMS (ESI$^-$)** m/z: 482/484 $[M-H]^-$; **HRMS (ESI$^+$)** m/z: $C_{20}H_{20}N_4O_4$ $[M+H]^+$ calculated: 484.0511/486.0478, found: 484.0509/486.0480. Spectroscopic data consistent with literature.[99]

(34) 6-(3-(3-((5-Chlorothiophen-2-yl)sulfonyl)ureido)azetidin-1-yl)-5-cyano-2-methylnicotinic acid

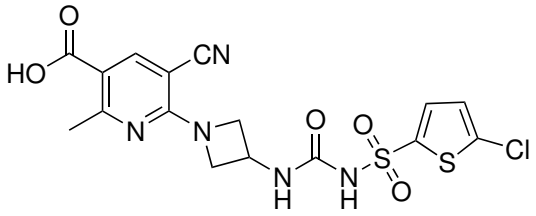

Aq. LiOH (3 M, 0.5 mL, 1.5 mmol) was added to ester **17** (0.02 g, 41 µmol) in THF and water (50% v/v, 1 mL) at rt, the reaction was stopped when there is complete consumption of starting material by TLC. The mixture was diluted with water (50 mL) and washed with EtOAc (25 mL). The aqueous layer was acidified with concentrated HCl until pH < 3, extracted with EtOAc (3×25 mL), washed with water (25 mL), brine (25 mL) and dried over $MgSO_4$. The product was concentrated *in vacuo* to afford the title compound as an off-white solid (18 mg, quant.). **^{1}H NMR (300 MHz, DMSO-d_6):** δ 12.81 (br, 1H), 11.37 (br, 1H), 8.25 (s, 1H), 7.56 (d, J = 4.1 Hz, 1H), 7.34 (br, 1H), 7.22 (d, J = 4.1 Hz, 1H), 4.51-4.49 (m, 3H), 4.12 (d, J = 5.8 Hz, 2H), 2.61 (s, 3H) ppm; **^{13}C NMR (126 MHz, DMSO-d_6):** δ 166.5, 164.8, 158.3, 151.8, 146.5, 139.5, 136.4, 133.5, 127.9, 117.4, 114.6, 86.6, 58.9, 40.8, 25.9; **LRMS (ESI$^-$)** *m/z*: 454/456 $[M\text{-}H]^-$; **HRMS (ESI$^+$)** *m/z*: $C_{16}H_{12}ClN_5O_5S_2$ $[M\text{-}2H]^-$ calculated: 226.4990/227.4975, found: 226.4989/227.4975.

(35) 6-(3-(3-((5-Chlorothiophen-2-yl)sulfonyl)ureido)azetidin-1-yl)-5-cyano-*N*-methoxy-*N*,2-dimethylnicotinamide

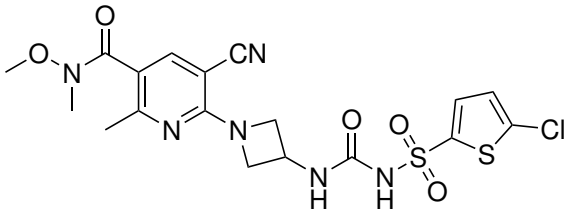

Pyridine (60 µL, 0.70 mmol) was added to nicotinic acid **34** (0.16 g, 0.35 mmol) and *N*,*O*-dimethylhydroxylamine hydrochloride (45 mg, 0.45 mmol) in THF (3 mL) at rt. 1-Ethyl-3-(3-dimethylaminopropyl)carbodiimide (EDC, 0.13 g, 0.70 mmol)

and pyridine (60 µL, 0.70 mmol) were added to the reaction mixture and stirred for 22 h at rt. The crude mixture was diluted with EtOAc (100 mL), washed with water (100 mL), aq. citric acid (10% w/v, 100 mL), brine (100 mL) and then dried over $MgSO_4$. This was concentrated *in vacuo* and the crude product was purified by flash chromatography (SiO_2; 70% v/v EtOAc in hexane, 70-100% v/v EtOAc in hexane + 0.5% AcOH) to afford the title compound as a white solid (0.14 g, 83%). $\boldsymbol{R_f}$ 0.42 (20% v/v EtOAc/hexane + 3 drops AcOH); **^{1}H NMR (500 MHz, DMSO-d_6):** δ 11.43 (br, 1H), 7.92 (s, 1H), 7.62 (d, J = 4.1 Hz, 1H), 7.54 (br, 1H), 7.25 (d, J = 4.1 Hz, 1H), 4.50-4.43 (m, 3H), 4.10-4.06 (m, 2H), 3.48 (s, 3H), 3.22 (s, 3H), 2.31 (s, 3H); **^{13}C NMR (126 MHz, DMSO-d_6):** δ 167.0 (deduced from HSQC and HMBC, **Appendix 9** and **Appendix 10**), 159.3, 158.0, 151.1, 141.9, 138.8, 136.1, 133.2, 127.5, 119.6, 117.2, 85.7, 61.0, 58.4, 40.4, 30.7, 22.8; **LRMS (ESI$^-$)** m/z: 497/499 $[M\text{-}H]^-$; **HRMS (ESI$^-$)** m/z: $C_{18}H_{19}ClN_6O_5S_2$ $[M\text{-}H]^-$ calculated: 497.0474/499.0444, found: 497.0474/499.0442.

General procedure for esterification of nicotinic acid 34

EDC was added to iPr$_2$NEt, nicotinic acid **34**, HOBt and fluorinated alcohol in dry DCM (0.11 mmol/mL) under nitrogen atmosphere and stirred overnight at rt. The reaction mixture was diluted with DCM (230 mL/mmol), washed with water (90 mL/mmol), brine (90 mL/mmol) and dried over $MgSO_4$. This was concentrated *in vacuo* and the crude product was purified by flash chromatography (SiO_2; 10-40% v/v EtOAc in hexane, 40% v/v EtOAc in hexane + 0.5% AcOH) and recrystallised with MeCN to afford the respective compound.

(19) 4-Fluoroethyl 6-(3-(3-((5-chlorothiophen-2-yl)sulfonyl)-ureido)azetidin-1-yl)-5-cyano-2-methylnicotinate

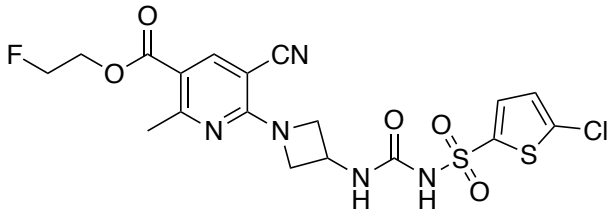

Followed *general procedure for esterification of nicotinic acid **34*** with EDC (84 mg, 0.44 mmol), *i*Pr_2NEt (90 µL, 0.53 mmol), nicotinic acid **34** (100 mg, 0.22 mmol), HOBt (19 mg, 0.11 mmol) and 2-fluoroethanol (40 µL, 0.68 mmol) to afford the title compound as off-white crystals (95 mg, 86%). **^{1}H NMR (300 MHz, DMSO-d_6):** δ 11.38 (br, 1H), 8.32 (s, 1H), 7.60 (d, J = 4.1 Hz, 1H), 7.41 (d, J = 5.6 Hz, 1H), 7.24 (d, J = 4.1 Hz, 1H), 4.86–4.77 (dd, J = 4.7, 3.2 Hz 1H), 4.70–4.61 (dd, J = 4.7, 3.2 Hz 1H), 4.60–4.44 (m, 4H), 4.39 (dd, J = 4.7, 3.2 Hz, 1H), 4.15 (d, J = 7.1 Hz, 2H), 2.62 (s, 3H) ppm; **^{13}C NMR (126 MHz, DMSO-d_6):** δ 164.4, 164.1, 157.7, 151.4, 146.0, 133.0, 127.4, 116.8, 112.8, 86.2, 82.3, 81.0, 63.9, 63.7, 58.5, 40.4, 25.3 ppm; **^{19}F NMR (471 MHz, DMSO-d_6):** δ -223.1 (s) ppm; **LRMS (ESI$^-$)** m/z: 500/502 [M-H]$^-$; **HRMS (ESI$^-$)** m/z: $C_{18}H_{16}ClN_5O_5S_2$ [M-H]$^-$ calculated: 500.0271/502.0239, found: 500.0276/502.0249.

(20) 4-Fluoropropyl 6-(3-(3-((5-chlorothiophen-2-yl)sulfonyl)-ureido)azetidin-1-yl)-5-cyano-2-methylnicotinate

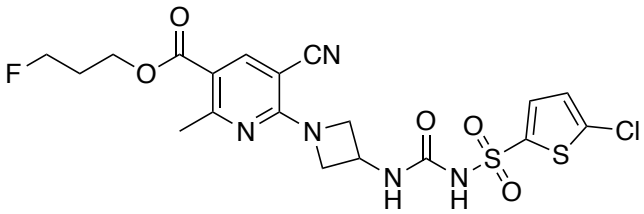

Followed *general procedure for esterification of nicotinic acid **34*** with EDC (84 mg, 0.44 mmol), *i*Pr_2NEt (90 µL, 0.53 mmol), nicotinic acid **34** (92 mg, 0.20 mmol), HOBt (17 mg, 0.13 mmol) and 3-fluoro-1-propanol (40 µL, 0.50 mmol) to afford the title compound as off-white crystals (67 mg, 61%). **^{1}H NMR (500 MHz, DMSO-d_6):** δ 11.39 (br, 1H), 8.34 (s, 1H), 7.60 (d, J = 4.1 Hz, 1H), 7.40 (d, J = 6.0 Hz, 1H), 7.24 (d, J = 4.1 Hz, 1H), 4.64 (t, J = 5.9 Hz, 1H), 4.55 (t, J = 5.9

Hz, 1H), 4.53–4.47 (m, 3H), 4.28 (t, J = 6.2 Hz, 2H), 4.15 (m, 2H), 2.61 (s, 3H), 2.13–2.08 (m, 1H), 2.08–2.02 (m, 1H) ppm; **^{13}C NMR (126 MHz, DMSO-d_6):** δ 164.7 (2 × C peaks), 158.2, 146.5, 133.4, 127.9, 117.4, 113.6, 86.6, 82.2, 80.9, 61.3 (2 × C peaks), 59.0, 40.8, 29.7, 29.5, 25.8; **^{19}F NMR (471 MHz, DMSO-d_6):** δ -220.2 (s) ppm; **LRMS (ESI$^-$)** m/z: 514/516 [M-H]$^-$; **HRMS (ESI$^-$)** m/z: $C_{19}H_{18}ClN_5O_5S_2$ [M-H]$^-$ calculated: 514.0427/516.0395, found: 514.0433/516.0406.

(21) 4-Fluorobutyl 6-(3-(3-((5-chlorothiophen-2-yl)sulfonyl)-ureido)azetidin-1-yl)-5-cyano-2-methylnicotinate

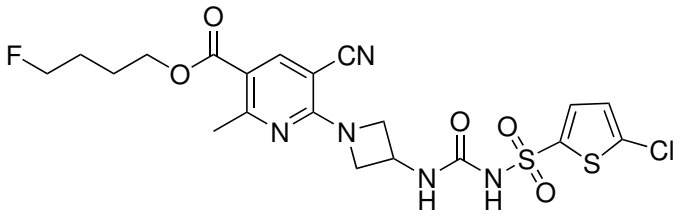

Followed *general procedure for esterification of nicotinic acid **34*** with EDC (84 mg, 0.44 mmol), iPr$_2$NEt (90 µL, 0.53 mmol), nicotinic acid **34** (92 mg, 0.20 mmol), HOBt (20 mg, 0.14 mmol) and 4-fluoro-1-butanol (80 µL, 0.57 mmol) to afford the title compound as off-white crystals (37 mg, 32%). **^{1}H NMR (500 MHz, DMSO-d_6):** δ 11.38 (br, 1H), 8.30 (s, 1H), 7.59 (d, J = 4.1 Hz, 1H), 7.37 (s, 1H), 7.23 (d, J = 4.1 Hz, 1H), 4.57–4.46 (m, 4H), 4.44 (t, J = 6.0 Hz, 1H), 4.22 (t, J = 6.0 Hz, 2H), 4.18–4.11 (m, 2H), 2.61 (s, 3H), 1.82–1.71 (m, 4H) ppm; **^{13}C NMR (126 MHz, DMSO- d_6):** δ 164.3, 164.2, 157.7, 145.8, 132.8, 127.3, 116.9, 113.2, 86.2, 84.2, 82.9, 64.1, 58.5, 40.4, 26.7, 26.5, 25.3, 24.2 (2 × C peaks) ppm; **^{19}F NMR (471 MHz, DMSO-d_6):** δ -217.1 (s) ppm; **LRMS (ESI$^-$)** m/z: 528/530 [M-H]$^-$; **HRMS (ESI$^-$)** m/z: $C_{20}H_{20}ClN_5O_5S_2$ [M-H]$^-$ calculated: 528.0584/530.0552, found: 528.0590/530.0564.

(102) Butyl 1*H*-imidazole-1-carboxylate

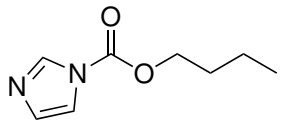

1-Butanol (2.9 mL, 31 mmol) was added dropwise to a stirred solution of 1,1′-carbonyldiimidazole (CDI, 5.1 g, 32 mmol) in dry DCM (25 mL) at 0 °C. The reaction mixture was brought up to rt and stirred for 70 h, and then concentrated under a flow of nitrogen. The mixture was suspended in Et_2O (150 mL) and filtered through a Celite® pad, which washed with further Et_2O (100 mL). After concentrating *in vacuo*, the resulting crude product was purified by flash chromatography (SiO_2; 5-15% v/v acetone in hexane) to afford the title compound as a clear oil (4.4 g, 83%). $\boldsymbol{R_f}$ 0.21 (10% v/v acetone in hexane); **^{1}H NMR (300 MHz, $CDCl_3$ with 0.1% v/v TMS):** δ 8.12 (s, 1H), 7.42 (s, 1H), 7.07 (s, 1H), 4.41 (t, J = 6.6 Hz, 2H), 1.83-1.74 (m, 2H), 1.51-1.43 (m, 2H), 1.01-0.98 (t, J = 7.4 Hz, 3H) ppm; **^{13}C NMR (75 MHz, $CDCl_3$ with 0.1% v/v TMS):** δ 148.8, 137.1, 130.6, 117.1, 68.2, 30.5, 19.0, 13.6 ppm; **LRMS (ESI^+)** *m/z*: 256 $[M+H]^+$; **HRMS (ESI^+)** *m/z*: $C_8H_{12}N_2O_2$ $[M+Na]^+$ calculated: 191.0791, found: 191.0792.

(101) *Tert*-butyl (2-oxo-2-(piperazin-1-yl)ethyl)carbamate

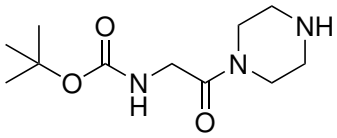

HATU (0.28 g, 0.73 mmol) in dry DMF (1 mL) was dropwise to a stirred solution of piperazine (0.26 g, 3 mmol), Boc-Gly-OH (0.10 g, 0.59 mmol) and iPr$_2$NEt (0.14 mL, 0.82 mmol) in dry DMF (3 mL) at rt. The reaction mixture was stirred for 14 h and then quenched with sat. aq. sodium carbonate, extracted with EtOAc (3 × 20 mL) and the organic layer was washed with sat. aq. Na_2SO_4 (20 mL). The crude product was concentrated under a flow of nitrogen and purified by flash chromatography (SiO_2; 5-10% v/v MeOH in DCM and then 10% v/v MeOH in DCM + 0.5% Et_3N) to afford the title compound as a white solid (0.12 g, 83%). $\boldsymbol{R_f}$ 0.27 (10% v/v MeOH in DCM + 5 drops Et_3N); **^{1}H NMR (300 MHz, $CDCl_3$ with**

0.1% v/v TMS): δ 5.52 (br, 1H), 3.93 (d, J = 4.4 Hz, 2H), 3.59 (t, J = 5.1 Hz, 2H), 3.34 (t, J = 5.1 Hz, 2H), 2.86-2.82 (m, 4H), 1.44 (s, 9H) ppm; **LRMS (ESI$^+$)** m/z: 266 ([M+Na]$^+$). Spectroscopic data consistent with literature.[205]

(117) Butyl 4-((*tert*-butoxycarbonyl)glycyl)piperazine-1-carboxylate

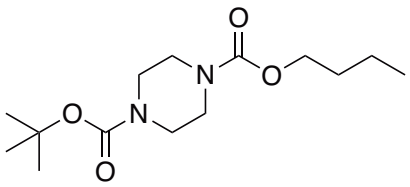

1-Boc-piperazine (2.6 g, 13 mmol) and Et_3N (1.9 mL, 13 mmol) in DCM (10 mL) was added to carbamate **102** (2.2 g, 13 mmol) and stirred for 71 h at rt. The reaction mixture was concentrated under a flow of nitrogen and taken up in EtOAc (200 mL), washed with 0.25 M aq. HCl (2 × 100 mL), brine (50 mL) and dried over $MgSO_4$. This was concentrated *in vacuo* and the crude product was purified by flash chromatography (SiO_2; 5-20% v/v acetone in hexane) to afford the title compound as a white solid (3.7 g, 97%). **^{1}H NMR (300 MHz, $CDCl_3$ with 0.1% v/v TMS):** 4.07 (t, J = 6.6 Hz, 2H), 3.40 (m, 8H), 1.65-1.55 (m, 2H), 1.44 (s, 9H), 1.41–1.29 (m, 2H), 0.92 (t, J = 7.3 Hz, 3H) ppm; **LRMS (ESI$^+$)** m/z: 309 [M+Na]$^+$; **HRMS (ESI$^+$)** m/z: $C_{14}H_{26}N_2O_4$ [M+Na]$^+$ calculated: 309.1785, found: 309.1786. Spectroscopic data consistent with literature.[149]

(100) Butyl 4-((*tert*-butoxycarbonyl)glycyl)piperazine-1-carboxylate

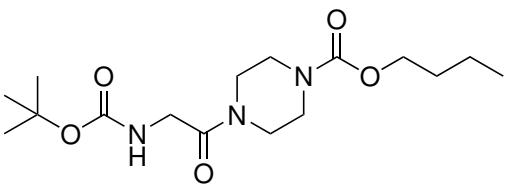

Procedure 1: Via piperazine 101

Piperazine **101** (1.3 g, 5.3 mmol) and Et_3N (0.74 mL, 5.3 mmol) in DCM (13 mL) was added to carbamate **102** (0.92 g, 5.5 mmol) in DCM (13 mL) and stirred for 23 h at rt. The reaction mixture was concentrated under a flow of nitrogen and purified by flash chromatography (SiO_2; 10-20% v/v acetone in hexane) to afford the title compound as a white solid (1.8 g, 97%).

Procedure 2: Via piperazine 117

Hydrogen chloride in 1,4-dioxane solution (4 M, 16 mL, 64 mmol) was added to Boc-piperazine **117** (3.7 g, 13 mmol) in DCM (16 mL) under nitrogen and stirred for 1 h at rt. This was concentrated and used without further purification. The crude amine and iPr$_2$NEt (6.8 mL, 30 mmol) in DMF (23 mL) was added to HATU (5.8 g, 15 mmol) and Boc-Gly-OH (2.3 g, 13 mmol) in DMF (15 mL) over 11 min at 0 °C. The reaction mixture was brought up to rt and stirred for 22 h. The crude product was concentrated under a flow of nitrogen, taken up in EtOAc (250 mL), washed with aq. citric acid (10% w/v, 100 mL), brine (100 mL) and dried over $NaSO_4$. The product was recrystallised from EtOAc:toluene:MeCN (4:2:1) to afford the title compound as a white solid (3.8 g, 86%). $\boldsymbol{R_f}$ 0.41 (30% v/v acetone in hexane); **^{1}H NMR (500 MHz, $CDCl_3$ with 0.1% v/v TMS):** δ 5.47 (br, 1H), 4.10 (t, J = 6.6 Hz, 2H), 3.96 (d, J = 4.6 Hz, 2H), 3.61 (t, J = 5.2 Hz, 2H), 3.51-3.46 (m, 4H), 3.37 (t, J = 5.2 Hz, 2H), 1.65-1.59 (m, 2H), 1.45 (s, 9H), 1.40-1.34 (m, 2H), 0.94 (t, J = 7.4 Hz, 3H) ppm; **^{13}C NMR (126 MHz, $CDCl_3$ with 0.1% v/v TMS):** δ 167.2, 155.8, 155.4, 79.8, 65.8, 44.2, 42.3, 41.8, 31.0, 28.4, 19.2, 13.7 ppm; **LRMS (ESI$^+$)** m/z: 366 ([M+Na]$^+$); **HRMS (ESI$^+$)** m/z: $C_{16}H_{29}N_3O_5$ [M+Na]$^+$ calculated: 366.1999, found: 366.1995.

(97) Ethyl 2-phenylthiazole-4-carboxylate

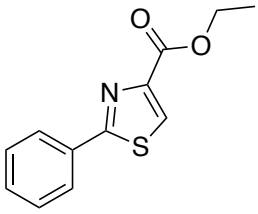

Ethyl-3-bromopyruvate (3.9 g, 20 mmol) was added dropwise to a solution of thiobenzamide (2.0 g, 15 mmol) in THF (40 mL) and heated at reflux for 27 h. The crude product was concentrated *in vacuo* and then purified by flash chromatography (SiO_2; 5-7% Et_2O, 20% v/v toluene in hexane). The solution was repeatedly concentrated *in vacuo* from Et_2O to afford the title compound as a viscous yellow oil (3.0 g, 97%). $\boldsymbol{R_f}$ 0.53 (20% v/v acetone in hexane); **^{1}H NMR (300 MHz, $CDCl_3$ with 0.1% v/v TMS):** δ 8.16 (s, 1H), 8.06-7.97 (m, 2H), 7.50-7.42 (m, 3H), 4.45 (q, J = 7.1 Hz, 2H), 1.43 (t, J = 7.1 Hz, 2H) ppm; **^{13}C NMR (75 MHz, $CDCl_3$ with 0.1% v/v TMS):** δ 168.9, 161.4, 148.0, 132.8, 130.7, 129.0, 127.1, 127.0, 61.5, 14.4 ppm; **LRMS (ESI^+)** *m/z*: 169 $[M+H]^+$. Spectroscopic data consistent with literature.[191]

(131) 2-Phenylthiazole-4-carboxylic acid

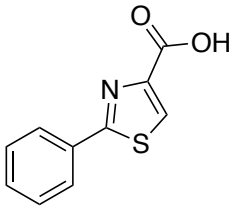

LiOH (0.58 g, 24 mmol) was added to a solution of ethyl 2-phenylthiazole-4-carboxylate (0.30 g, 1.3 mmol) in water in THF (50% v/v, 9 mL) and stirred for 8 h at rt. The reaction mixture was washed with EtOAc (3 × 50 mL), the aqueous layer was acidified to pH < 1 with concentrated HCl and extracted with EtOAc (3 × 50 mL). The organic layer was washed with brine (50 mL) and dried over Na_2SO_4. This was concentrated *in vacuo* to obtain an off-white solid. This was recrystallised from toluene to afford the title compound as off-white crystals (0.22 g, 83%). $\boldsymbol{R_f}$ 0.43 (10% v/v MeOH in DCM); **^{1}H NMR (300 MHz, DMSO-d_6):** δ 12.73 (br,

1H), 8.50 (s, 1H), 7.99-7.95 (m, 2H), 7.56-7.51 (m, 3H) ppm; **^{13}C NMR (75 MHz, CD_3CN):** δ 148.8, 137.1, 130.6, 117.1, 68.2, 30.5, 19.0, 13.6 ppm; **LRMS (ESI^+)** *m/z*: 256 $[M+H]^+$. Spectroscopic data consistent with literature.[191]

(95) Butyl 4-glycylpiperazine-1-carboxylate hydrochloride

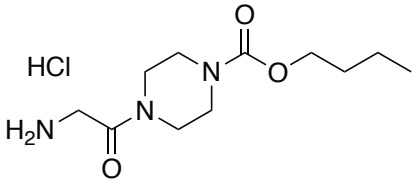

Hydrogen chloride in 1,4-dioxane solution (4 M, 3.1 mL, 12 mmol) was added dropwise to Boc-carbamate **100** (190 mg, 0.56 mmol) in dry DCM (2.1 mL) and stirred at rt for 30 min. Upon complete consumption of starting material as observed by TLC, the reaction mixture was concentrated under a flow of nitrogen and the crude material used without further purification. **LRMS (ESI^+)** *m/z*: 266 $[M+Na]^+$; **HRMS (ESI^+)** *m/z*: $C_{11}H_{21}N_3O_3$ $[M+H]^+$ calculated: 244.1656, found: 244.1656.

(129) Butyl 4-((2-phenylthiazole-4-carbonyl)glycyl)piperazine-1-carboxylate

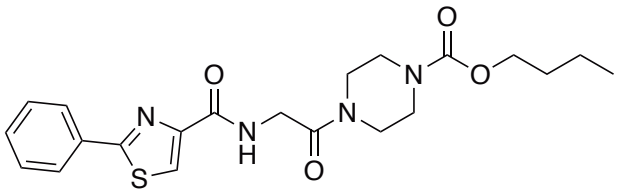

Hydrogen chloride in 1,4-dioxane solution (4 M, 3.1 mL, 12 mmol) was added dropwise to Boc-carbamate **100** (190 mg, 0.56 mmol) in dry DCM (2.1 mL) and stirred at rt for 30 min. Upon complete consumption of starting material as observed by TLC, the reaction mixture was concentrated under a flow of nitrogen and used without further purification. HATU (0.26 g, 0.67 mmol) in DMF (2.1 mL) were added dropwise to carboxylic acid **131** (0.11 g, 0.52 mmol), the crude amine **95** and *i*Pr_2NEt (0.43 mL, 2.4 mmol) in DMF (2.1 mL) and stirred at rt for 18 h. The

reaction mixture was concentrated under flow of nitrogen, taken up with EtOAc (200 mL), washed with aq. citric acid (10% w/v, 100 mL), water (100 mL), brine (50 mL) and dried over $MgSO_4$. This was concentrated *in vacuo* and the crude product was purified by flash chromatography (SiO_2; 5-40% v/v acetone in hexane) to afford the title compound as an off-white solid (0.21 g, quant.). $\boldsymbol{R_f}$ 0.14 (20% v/v acetone in hexane); **^{1}H NMR (500 MHz, $CDCl_3$ with 0.1% v/v TMS):** δ 8.36 (t, J = 4.6 Hz, 1H), 8.09 (s, 1H), 8.01-7.99 (m, 2H), 7.47-7.45 (m, 3H), 4.32 (d, J = 4.5 Hz, 2H), 4.12 (t, J = 6.7 Hz, 2H), 3.69 (t, J = 5.3 Hz, 2H), 3.57-3.49 (m, 6H), 1.67–1.62 (m, 2H), 1.43–1.36 (m, 2H), 0.95 (t, J = 7.4 Hz, 2H) ppm; **^{13}C NMR (126 MHz, $CDCl_3$ with 0.1% v/v TMS):** δ 168.5, 166.8, 161.3, 155.6, 150.4, 132.9, 130.8, 129.2, 126.9, 123.2, 66.0, 44.6, 42.0, 41.4, 31.2, 19.3, 13.9 ppm; **LRMS (ESI$^+$)** *m/z*: 453 $[M+Na]^+$; **HRMS (ESI$^+$)** *m/z*: $C_{21}H_{26}N_4O_4S$ $[M+Na]^+$ calculated: 453.1567, found: 453.1567.

(140) Ethyl 5-bromo-2-phenylthiazole-4-carboxylate

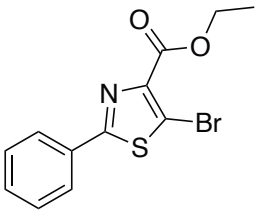

Iodine (0.48 g, 1.7 mmol) was added to a solution of thiazole **97** (2.7 g, 12 mmol) and *N*-bromosuccinimide (2.1 g, 12 mmol) in dry MeCN (37 mL) under nitrogen atmosphere at 35 °C. The resulting mixture and stirred for 24 h. The reaction was quenched with 5% aq. sodium thiosulfate, extracted with Et_2O (3 × 150 mL), washed with brine (150 mL) and dried over $MgSO_4$. This was concentrated *in vacuo* and the crude product was purified by flash chromatography (SiO_2; 0-5.5% v/v ether in hexane, 5.5-10% ether and 20% v/v toluene in hexane) to afford the title compound as a waxy off-white solid (3.1 g, 85%). $\boldsymbol{R_f}$ 0.73 (40% v/v ether in hexane); **^{1}H NMR (500 MHz, $CDCl_3$ with 0.1% v/v TMS):** δ 7.92-7.90 (m, 2H), 7.47-7.45 (m, 3H), 4.47 (q, J = 7.1 Hz, 2H), 1.45 (t, J = 7.1 Hz, 3H) ppm; **^{13}C**

NMR (126 MHz, $CDCl_3$ with 0.1% v/v TMS): δ 168.0, 161.3, 144.6, 132.5, 131.2, 129.2, 126.8, 116.5, 77.4, 77.4, 77.2, 76.9, 62.0, 14.4 ppm; **LRMS (ESI^+)** *m/z*: 645/647/649 $[2M+Na]^+$; **HRMS (ESI^+)** *m/z*: $C_{12}H_{11}BrNO_2S$ $[M+H]^+$ calculated: 311.9688/313.9668, found: 311.9684/313.9664.

(142) Ethyl (*E*)-5-(3-(*tert*-butoxy)-3-oxoprop-1-en-1-yl)-2-phenylthiazole-4-carboxylate

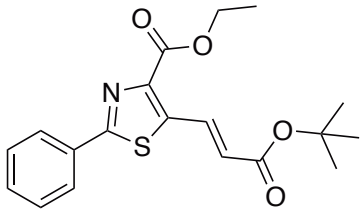

Tert-butyl acrylate (1.2 mL, 8.4 mmol) and Cy_2NMe (0.54 mL, 2.5 mmol) in dry DMA (3 mL) was degassed with nitrogen sparging and added to ethyl 5-bromo-2-phenylthiazole-4-carboxylate (0.51 g, 1.7 mmol), TBACl (43 mg, 0.17 mmol) and $PdCl_2(dbpf)_2$ (21 mg, 0.034 mmol, 2 mol%) in a sealed tube under nitrogen atmosphere. The reaction mixture was then stirred for 71 h at 80 °C. This was concentrated under a flow of nitrogen and the crude product was purified by flash chromatography (SiO_2; 10-20% v/v acetone in hexane, 2.5% increments) to afford the title compound as an off-white solid (0.50 g, 85%). $\boldsymbol{R_f}$ 0.56 (20% v/v acetone in hexane); **^{1}H NMR (300 MHz, $CDCl_3$ with 0.1% v/v TMS):** δ 8.47 (d, J = 15.9 Hz, 1H), 8.03–7.92 (m, 2H), 7.46 (m, 3H), 6.27 (d, J = 15.9 Hz, 1H), 4.48 (q, J = 7.1 Hz, 2H), 1.54 (s, 9H), 1.47 (t, J = 7.1 Hz, 3H) ppm; **^{13}C NMR (75 MHz, $CDCl_3$ with 0.1% v/v TMS):** δ 166.9, 165.0, 161.9, 145.3, 141.2, 133.0, 132.5, 131.4, 129.2, 127.2, 126.3, 81.4, 62.0, 28.3, 14.5 ppm; **LRMS (ESI^+)** *m/z*: 741 $[2M+Na]^+$; **HRMS (ESI^+)** *m/z*: $C_{19}H_{21}NO_4S$ $[M+Na]^+$ calculated: 382.1084, found: 382.1083.

(143) 5-Bromo-2-phenylthiazole-4-carboxylic acid

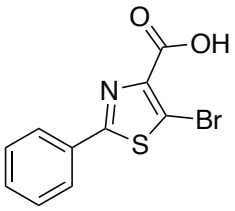

LiOH (0.59 g, 25 mmol) was added to ester **140** (2.6 g, 8.2 mmol) in water (24 mL) and THF (24 mL), and stirred for 18 h at rt. The reaction mixture was washed with ether (200 mL), the aqueous layer was acidified to pH < 4 with concentrated HCl. This was extracted with EtOAc (3 $\times$ 100 mL), washed with brine (100 mL), dried over Na_2SO_4 and concentrated *in vacuo*. The crude product was recrystallised (60% v/v toluene in hexane) to afford the title compound as off-white crystals (2.1 g, 92%). $\boldsymbol{R_f}$ 0.09 (20% v/v EtOAc in DCM + 5 drops AcOH); **^{1}H NMR (500 MHz, CD_3CN):** δ 7.95-7.93 (m, 2H), 7.55-7.50 (m, 3H) ppm; **^{13}C NMR (126 MHz, CD_3CN):** δ 168.5, 161.4, 144.6, 133.0, 132.3, 130.3, 127.3, 117.5 ppm; **LRMS (ESI$^-$)** *m/z*: 282/284 $[M\text{-}H]^-$; **HRMS (ESI$^-$)** *m/z*: $C_{10}H_5BrNO_2S$ $[M\text{-}H]^-$ calculated: 282.9230/283.9209, found: 281.9226/283.9204.

(144) Butyl 4-((5-bromo-2-phenylthiazole-4-carbonyl)glycyl)-piperazine-1-carboxylate

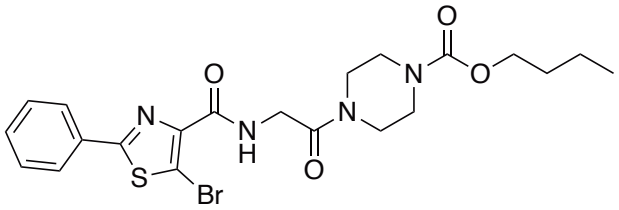

Hydrogen chloride in 1,4-dioxane solution (4 M, 19 mL, 76 mmol) was added dropwise to Boc-carbamate **100** (2.9 g, 8.3 mmol) in dry DCM (30 mL) and stirred at rt for 30 min. Upon complete consumption of starting material as observed by TLC, the reaction mixture was concentrated under a flow of nitrogen and used without further purification. HATU (3.8 g, 9.8 mmol) was added to carboxylic acid **143** (2.2 g, 7.6 mmol), the crude amine **95** and iPr$_2$NEt (6.6 mL, 38 mmol) in DMF (30 mL) and stirred for 17 h at rt. The reaction mixture was concentrated under flow of

nitrogen, taken up in DCM (200 mL), washed with aq. citric acid (10% w/v, 100 mL), water (100 mL), brine (100 mL) and dried over Na_2SO_4. This was concentrated *in vacuo* and the crude product was recrystallised from water and MeCN (50% v/v water in MeCN) to afford the title compound as an off-white solid (3.3 g, 85%). $\boldsymbol{R_f}$ 0.49 (30% v/v acetone in hexane); **^{1}H NMR (500 MHz, $CDCl_3$ with 0.1% v/v TMS):** δ 8.37 (t, J = 4.7 Hz, 1H), 7.90-7.88 (m, 2H), 7.48-7.44 (m, 3H), 4.28 (d, J = 4.6 Hz, 2H), 4.12 (t, J = 6.7 Hz, 2H), 3.69-3.67 (m, 2H), 3.57-3.47 (m, 6H), 1.66–1.61 (m, 2H), 1.42–1.37 (m, 2H), 0.95 (t, J = 7.3 Hz, 3H) ppm; **^{13}C NMR (126 MHz, $CDCl_3$ with 0.1% v/v TMS):** δ 167.4, 166.8, 160.8, 155.5, 144.7, 132.3, 131.2, 129.3, 126.6, 113.2, 65.9, 44.6, 43.7, 42.0, 41.3, 31.1, 19.3, 13.9 ppm; **LRMS (ESI$^+$)** *m/z*: 531/533 $[M+Na]^+$; **HRMS (ESI$^+$)** *m/z*: $C_{21}H_{25}BrN_4O_4S$ $[M+Na]^+$ calculated: 531.0672/533.0652, found: 531.06814/533.0661.

(92) Butyl (*Z*)-4-((5-(3-(*tert*-butoxy)-3-oxoprop-1-en-1-yl)-2-phenylthiazole-4-carbonyl)glycyl)piperazine-1-carboxylate

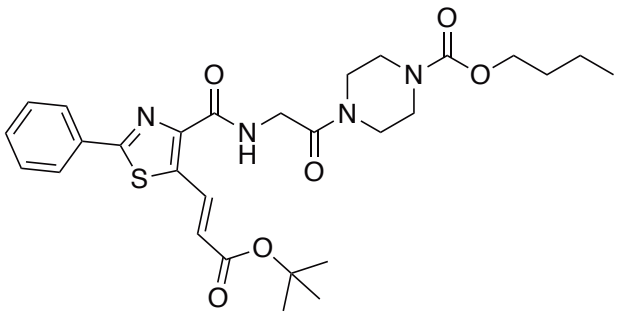

Tert-butyl acrylate (0.86 mL, 5.9 mmol) and Cy_2NMe (0.38 mL, 1.8 mmol) in dry DMA (2 mL) was degassed and added to bromothiazole **144** (0.61 g, 1.2 mmol), TBACl (33 mg, 0.12 mmol) and $PdCl_2(dbpf)_2$ (16 mg, 0.024 mmol, 2 mol%) in a sealed tube under inert atmosphere. The reaction mixture was stirred at 80 °C for 65 h and then concentrated under a flow of nitrogen, taken up in EtOAc (150 mL), washed with water (100 mL), brine (100 mL) and dried over Na_2SO_4. This was concentrated under the flow of nitrogen and the crude product was purified by flash chromatography (SiO_2; 10-18% v/v acetone in hexane) to afford the title compound

as an off-white solid (0.59 g, 89%). $\boldsymbol{R_f}$ 0.24 (40% v/v EtOAc in hexane); **^{1}H NMR (300 MHz, $CDCl_3$ with 0.1% v/v TMS):** δ 8.75 (d, J = 16.0 Hz, 1H), 8.48 (t, 1H), 8.02–7.91 (m, 2H), 7.51–7.39 (m, 3H), 6.21 (d, J = 16.0 Hz, 1H), 4.30 (d, J = 4.5 Hz, 2H), 4.12 (t, J = 6.5 Hz, 3H), 3.72-3.63 (m, 2H), 3.58-3.42 (m, 6H), 1.70–1.57 (m, 2H), 1.53 (s, 9H), 1.47–1.31 (m, 2H), 0.95 (t, J = 7.3 Hz, 3H) ppm; **^{13}C NMR (75 MHz, DMSO-d_6):** δ 166.7, 166.3, 165.2, 161.7, 155.5, 146.2, 138.8, 133.4, 132.4, 131.4, 129.2, 127.0, 125.9, 81.1, 65.9, 44.6, 42.0, 41.3, 31.1, 28.3, 19.3, 13.9 ppm; **LRMS (ESI$^+$)** m/z: 579 $[M+Na]^+$; **HRMS (ESI$^+$)** m/z: $C_{28}H_{36}N_4O_6S$ $[M+Na]^+$ calculated: 579.2248, found: 579.2242.

(61) (*Z*)-3-(4-((2-(4-(butoxycarbonyl)piperazin-1-yl)-2-oxo-ethyl)carbamoyl)-2-phenylthiazol-5-yl)acrylic acid

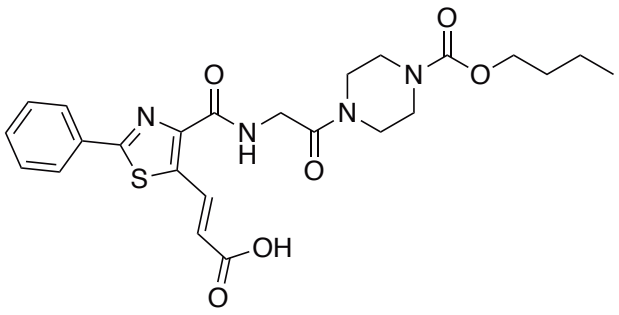

TFA (2.0 mL, 26 mmol) was added to *tert*-butyl ester **92** (0.59 g, 1.1 mmol) in dry DCM (12 mL) and stirred for 3 h at rt. The reaction mixture was concentrated under the flow of nitrogen, taken up in EtOAc and Et_2O (50% v/v, 200 mL) and washed with 1 M aq. NaOH (3 × 100 mL). The aq. layer was acidified with concentrated HCl to pH < 4, extracted with EtOAc (3 × 70 mL) and dried over Na_2SO_4. This was concentrated under the flow of nitrogen and the crude product was recrystallised (70% EtOAc and 5% v/v MeCN in hexane) to afford the title compound as off-white crystals (530 mg, quant.). $\boldsymbol{R_f}$ 0.20 (20% v/v acetone in hexane); **^{1}H NMR (500 MHz, DMSO-d_6):** δ 8.76 (t, J = 5.5 Hz, 1H), 8.70 (d, J = 15.9 Hz, 1H), 8.08-8.02 (m, 2H), 7.61-7.55 (m, 3H), 6.32 (d, J = 16.0 Hz, 1H), 4.20 (d, J = 5.4 Hz, 2H), 4.02 (t, J = 6.5 Hz, 2H), 3.53-3.42 (m, 6H), 1.61-1.51 (m, 2H), 1.39-1.30 (m, 2H),

0.90 (t, J = 7.4 Hz, 3H) ppm; **^{13}C NMR (126 MHz, DMSO-d_6):** δ 167.1 (2 × C), 166.3, 165.9, 161.0, 154.7, 146.7, 137.4, 131.8, 131.7, 129.5, 126.8, 124.3, 64.8, 43.8, 41.3, 40.8, 30.6, 18.7, 13.7 ppm; **LRMS (ESI$^+$)** m/z: 523 $[M+Na]^+$; **HRMS (ESI$^-$)** m/z: $C_{24}H_{27}N_4O_6S$ $[M-H]^-$ calculated: 499.1657, found: 499.1653.

(146) 2,3,6,7-Tetrahydro-1*H*,5*H*-pyrido[3,2,1-*ij*]quinoline-9-carbaldehyde

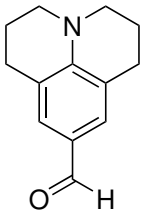

Phosphoryl chloride (0.59 mL, 6.3 mmol) was added dropwise to dry DMF (7.9 mL) under nitrogen atmosphere at 0 °C, the reaction mixture was brought up to rt and stirred for 1 h. The phosphoryl chloride solution was added to julolidine (1.0 g, 5.8 mmol) under nitrogen, which was brought up to 90 °C and stirred for a further 19 h. After the reaction mixture was cooled to rt, it was diluted with water (50 mL), quenched with sat. aq. bicarb solution until pH ≈ 7, extracted with EtOAc (3 × 400 mL), washed with brine (200 mL) and then concentrated *in vacuo*. The crude product was purified by flash chromatography (SiO_2; 5-15% v/v acetone in hexane) to afford the title compound as a yellow solid (0.90 g, 78%). $\boldsymbol{R_f}$ 0.31 (15% v/v acetone in hexane); **^{1}H NMR (300 MHz, $CDCl_3$ with 0.1% v/v TMS):** δ 9.60 (s, 1H), 7.29 (s, 2H), 3.29 (t, J = 6.3 Hz, 4H), 2.76 (t, J = 6.3 Hz, 4H), 2.00-1.92 (m, 4H) ppm; **^{13}C NMR (75 MHz, $CDCl_3$ with 0.1% v/v TMS):** δ 190.3, 148.0, 129.6, 124.2, 120.5, 50.2, 27.8, 21.4 ppm; **LRMS (ESI$^+$)** m/z: 425 $[2M+Na]^+$. Spectroscopic data consistent with literature.[206,207]

(148) 2,4,6-Trimethylpyrylium tetrafluoroborate

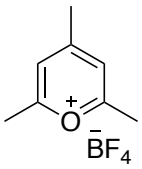

Tetrafluoroboric acid (48% w/v, 5.8 mL, 44 mmol) was added dropwise to a stirring solution of *t*-BuOH (3.1 g, 42 mmol) in acetic anhydride (50 mL, 0.53 mol) while maintaining below 100 °C. The reaction mixture was cooled to 80 °C and then rapidly to 5 °C. Diethyl ether (130 mL) was added, the white precipitate was filtered and collected. The crude product was recrystallised from EtOH in MeOH (50% v/v) with 10 drops of tetrafluoroboric acid to afford the title compound as white crystals (3.0 g, 34%). **^{1}H NMR (300 MHz, CD_3OD):** δ 7.87 (s, 2H), 2.88 (s, 6H), 2.72 ppm (s, 3H); **LRMS (ESI$^+$)** *m/z*: 123 $[M]^+$. Spectroscopic data consistent with literature.[208]

(149) (*E*)-2,6-dimethyl-4-(2-(2,3,6,7-tetrahydro-1*H*,5*H*-pyrido[3,2,1-*ij*quinolin-9-yl)vinyl)pyrylium tetrafluoroborate

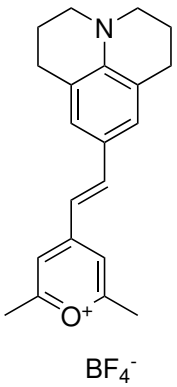

Julolidine carbaldehyde **146** (0.48 g, 2.4 mmol) in MeOH (6 mL) was added to pyrylium **148** (0.76 g, 3.6 mmol) in MeOH (6 mL) and refluxed for 21 h. The reaction mixture was concentrated *in vacuo* and purified by flash chromatography (SiO_2; 5% v/v acetone in DCM, 10% v/v MeOH in $CHCl_3$) to afford the title compound as a fine blue powder (0.94 g, quant.). $\boldsymbol{R_f}$ 0.20 (10% v/v MeOH in $CHCl_3$); **^{1}H NMR (500 MHz, CD_3OD):** δ 7.90 (d, J = 14.7 Hz, 1H), 7.32-7.30 (br, 2H), 6.68 (d, J = 14.7 Hz, 1H), 3.48 (t, J = 5.8 Hz, 4H), 2.77 (t, J = 6.2 Hz, 4H), 2.02-1.98

(m, 4H) ppm; **LRMS (ESI$^+$)** *m/z*: 306 $[M]^+$. Spectroscopic data consistent with literature.[173]

General amide coupling condition appending linkers to Actelion lead

HATU (1.3 eq.) was added to carboxylic acid **61** (1 eq.), Boc-diamine linker (1.3 eq.) and *i*Pr_2NEt (5 eq.) in DMF (6.3 mL/mmol) and stirred for 19 h at rt. The reaction mixture was concentrated under a flow of nitrogen, taken up in EtOAc (500 mL/mmol), washed with aq. citric acid (10% w/v, 250 mL/mmol), brine (250 mL/mmol) and then dried over $MgSO_4$. This was concentrated under a flow of nitrogen and the crude product was purified by flash chromatography (SiO_2; 10-30% v/v EtOAc in hexane, 10-30% v/v acetone in hexane) to afford the respective compounds.

(107) Butyl (*E*)-4-((5-(3-((2-((*tert*-butoxycarbonyl)amino)-ethyl)amino)-3-oxoprop-1-en-1-yl)-2-phenylthiazole-4-carbonyl)glycyl)piperazine-1-carboxylate

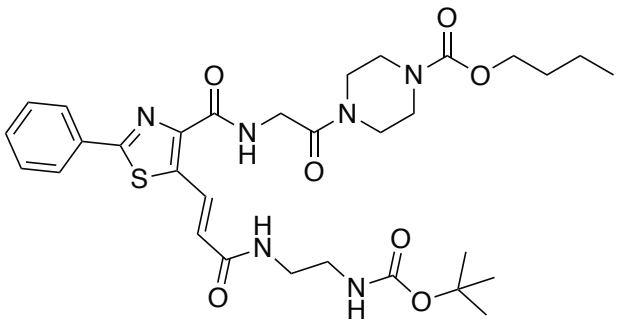

Followed ***general amide coupling conditions to append linkers*** with HATU (40 mg, 0.10 mmol), carboxylic acid **61** (41 mg, 0.080 mmol), *N*-Boc-ethylenediamine (17 mg, 0.10 mmol) and *i*Pr_2NEt (71 µL, 0.40 mmol) to afford the title compound as an off-white solid (33 mg, 64%). $\boldsymbol{R_f}$ 0.54 (30% v/v acetone in hexane); **^{1}H NMR (500 MHz, $CDCl_3$ with 0.1% v/v TMS):** δ 8.65 (d, J = 15.6 Hz, 1H), 8.44 (t,

J = 4.5 Hz, 1H), 7.94 (d, J = 7.1 Hz, 2H), 7.44 (q, J = 7.5 Hz, 3H), 6.60 (s, 1H), 6.30 (d, J = 15.9 Hz, 1H), 5.06 (s, 1H), 4.30 (d, J = 4.6 Hz, 2H), 4.12 (t, J = 6.7 Hz, 2H), 3.72–3.65 (m, 2H), 3.53 (m, 8H), 3.34 (m, 2H), 1.68–1.60 (m, 2H), 1.44 (s, 9H), 1.43-1.36 (m, 2H), 0.95 (t, J = 7.4 Hz, 3H) ppm; **LRMS (ESI$^+$)** *m/z*: 665 [M+Na]$^+$; **HRMS (ESI$^+$)** *m/z*: $C_{31}H_{43}N_6O_7S$ [M+H]$^+$ calculated: 643.2909, found: 643.2916.

(108) Butyl (*E*)-4-((5-(3-((3-((*tert*-butoxycarbonyl)amino)-propyl)amino)-3-oxoprop-1-en-1-yl)-2-phenylthiazole-4-carbonyl)glycyl)piperazine-1-carboxylate

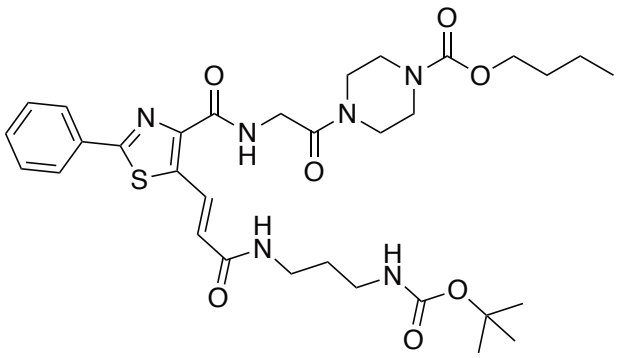

Followed ***general amide coupling conditions to append linkers*** with HATU (11 mg, 0.029 mmol), carboxylic acid **61** (10 mg, 0.020 mmol), *N*-Boc-1,3-propanediamine (4.3 mg, 0.025 mmol) and *i*Pr$_2$NEt (1 drop) to afford the title compound as an off-white solid (12 mg, 90%). $\boldsymbol{R_f}$ 0.61 (40% v/v acetone in Et$_2$O); **^{1}H NMR (500 MHz, CDCl$_3$ with 0.1% v/v TMS):** δ 8.56 (d, J = 15.8 Hz, 1H), 8.43 (t, J = 4.6 Hz, 1H), 7.86 (d, J = 7.5 Hz, 2H), 7.49-7.32 (m, 3H), 6.88 (t, J = 6.3 Hz, 1H), 6.27 (d, J = 15.8 Hz, 1H), 4.26 (d, J = 4.5 Hz, 2H), 4.09 (t, J = 6.6 Hz, 2H), 3.64 (m, 2H), 3.50 (m, 6H), 3.36 (q, J = 6.4 Hz, 2H), 3.17 (q, J = 6.1 Hz, 2H), 1.66 (m, 2H), 1.64–1.58 (m, 2H), 1.43 (s, 9H), 1.37 (m, 2H), 0.93 (t, J = 7.4 Hz, 3H) ppm; **^{13}C NMR (101 MHz, CDCl$_3$ with 0.1% v/v TMS):** δ 166.9, 165.9, 165.6, 161.9, 157.0, 155.6, 145.8, 139.0, 132.3, 131.3, 130.1, 129.2, 127.0, 79.6, 65.9, 44.5, 43.7, 42.0, 41.3, 37.4, 36.5, 31.1, 30.2, 28.6, 19.3, 13.9 ppm;

LRMS (ESI$^+$) *m/z*: 709 [M+Na]$^+$; **HRMS (ESI$^+$)** *m/z*: $C_{33}H_{46}N_6O_8S$ [M+Na]$^+$ calculated: 709.2990, found: 709.2988.

(112) Butyl (*E*)-4-((5-(2,2-dimethyl-4,12-dioxo-3,8-dioxa-5,11-diazatetradec-13-en-14-yl)-2-phenylthiazole-4-carbonyl)glycyl)piperazine-1-carboxylate

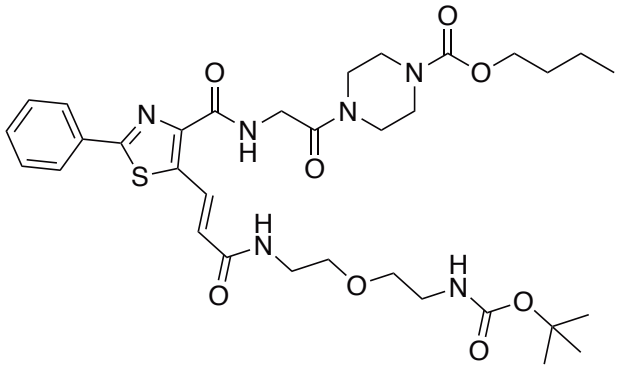

Followed ***general amide coupling conditions to append linkers*** with HATU (20 mg, 0.052 mmol), carboxylic acid **61** (20 mg, 0.040 mmol), *tert*-butyl (2-(2-aminoethoxy)ethyl)carbamate (9.0 mg, 0.044 mmol) and iPr$_2$NEt (2 drops) to afford the title compound as an off-white solid (28 mg, quant.). $\boldsymbol{R_f}$ 0.54 (30% v/v acetone in hexane); **^{1}H NMR (300 MHz, CDCl$_3$ with 0.1% v/v TMS):** δ 8.64 (d, J = 15.9 Hz, 1H), 8.46 (t, J = 4.2 Hz, 1H), 7.92 (d, J = 7.9 Hz, 2H), 7.50–7.37 (m, 3H), 6.58 (s, 1H), 6.37 (d, J = 15.9 Hz, 1H), 5.05 (s, 1H), 4.29 (d, J = 4.5 Hz, 2H), 4.11 (t, J = 6.6 Hz, 2H), 3.67 (m, 2H), 3.60–3.39 (m, 12H), 3.32 (m, 2H), 1.70–1.56 (m, 2H), 1.43 (s, 9H), 1.42-1.3 (m, 2H), 0.94 (t, J = 7.3 Hz, 3H) ppm; **^{13}C NMR (101 MHz, CDCl$_3$ with 0.1% v/v TMS):** δ 166.8, 165.8, 165.4, 161.8, 156.4, 155.5, 145.9, 139.1, 132.4, 131.3, 130.0, 129.2, 127.2, 127.0, 79.6, 70.5, 69.7, 65.9, 44.5, 43.5, 42.0, 41.3, 39.7, 31.2, 28.6, 19.3, 13.9 ppm; **LRMS (ESI$^+$)** *m/z*: 679 [M+Na]$^+$; **HRMS (ESI$^+$)** *m/z*: $C_{32}H_{44}N_6O_7S$ [M+Na]$^+$ calculated: 679.2884, found: 679.2894.

(72) (*E*)-9-(4-((2-(3-(4-((2-(4-(butoxycarbonyl)piperazin-1-yl)-2-oxoethyl)carbamoyl)-2-phenylthiazol-5-yl)acrylamido)-ethyl)carbamoyl)-2-carboxyphenyl)-3,6-bis(dimethylamino)-xanthylium

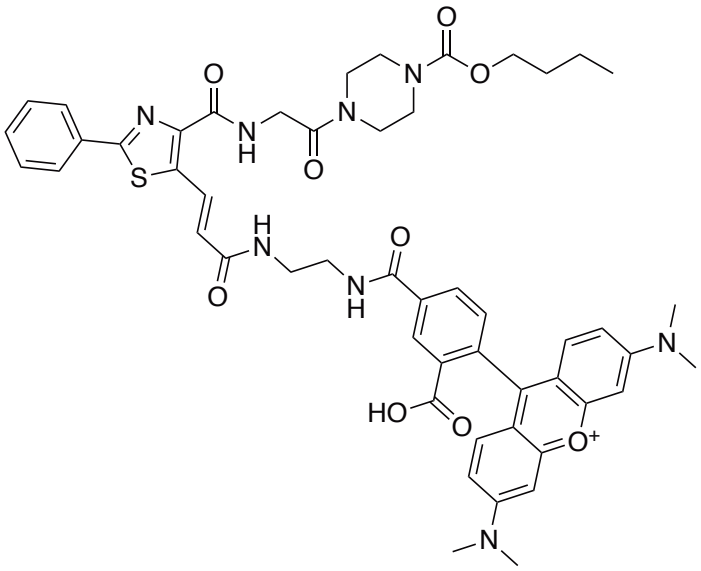

Hydrogen chloride in 1,4-dioxane solution (4 M, 40 µL, 0.16 mmol) was added to Boc-carbamate **173** (9 mg, 0.016 mmol) in dry DCM (0.4 mL) and stirred for 40 min at rt. The reaction mixture was concentrated under a flow of nitrogen, taken up in MeCN (5 mL), filtered, and the solid was rinsed with MeCN. The solid was taken up in Et_3N and chloroform (0.1% v/v, 20 mL) and concentrated under a flow of nitrogen. Activated ester **170** (8.5 mg, 0.014 mmol) in DCM (0.35 mL) was added to the crude amine product, to which $i Pr_2NEt$ (7.5 µL, 0.043 mmol) was added, followed by stirring for 3 h at rt. This was concentrated under a flow of nitrogen and the crude product was purified by reverse phase chromatography (C18, 10-100% v/v MeCN in water + 0.05% TFA) to afford the title compound as a purple solid (12.6 mg, 93%). $\boldsymbol{R_f}$ 0.33 (10% v/v MeOH in DCM); **^{1}H NMR (500 MHz, DMSO-d_6):** δ 9.26 (s, 1H), 9.02 (t, J = 5.5 Hz, 1H), 8.72 (m, 2H), 8.57 (d, J = 15.7 Hz, 1H), 8.50 (t, J = 5.8 Hz, 1H), 8.32 (dd, J = 7.9, 2.0 Hz, 1H), 8.05 (m, 2H), 7.63–7.54 (m, 4H), 7.11 – 6.99 (m, 4H), 6.95 (d, J = 2.4 Hz, 2H), 6.56 (d, J = 15.7 Hz, 1H), 4.20 (d, J = 5.4 Hz, 2H), 4.03 (t, J = 6.5 Hz, 2H), 3.54–3.42 (m, 4H), 3.41–3.36

(m, 3H), 3.27 (s, 12H), 1.60-1.53 (m, 2H), 1.40-1.31 (m, 2H), 0.91 (t, J = 7.4 Hz, 3H) ppm; **LRMS (ESI$^+$)** m/z: 955 $[M]^+$; **HRMS (ESI$^+$)** m/z: $C_{51}H_{55}N_8O_9S$ $[M]^+$ calculated: 955.3807, found: 955.3796; **HPLC (λ = 220 nm), condition a:** 84.9%, t_R = 22.686 min. 2D NMR spectra are shown in **Appendix 16** and **Appendix 17**.

(73) (*E*)-9-(4-((3-(3-(4-((2-(4-(butoxycarbonyl)piperazin-1-yl)-2-oxoethyl)carbamoyl)-2-phenylthiazol-5-yl)acrylamido)-propyl)carbamoyl)-2-carboxyphenyl)-3,6-bis(dimethylamino)-xanthylium

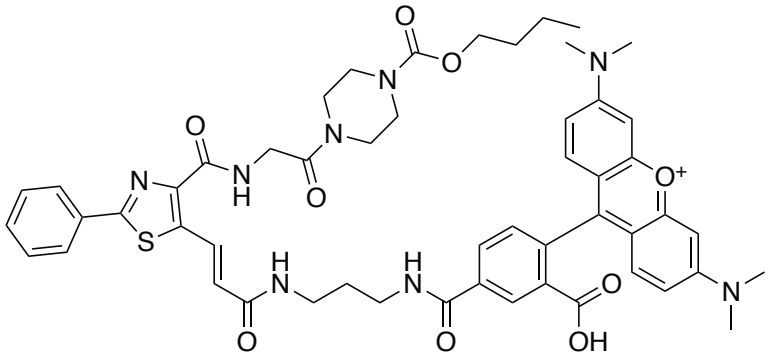

Hydrogen chloride in 1,4-dioxane solution (4 M, 40 µL, 0.16 mmol) was added to Boc-carbamate **174** (12 mg, 0.021 mmol) in dry DCM (0.4 mL) and stirred for 40 min at rt. The crude product was concentrated under the flow of nitrogen, taken up in MeCN (5 mL), filtered and rinsed with MeCN. The solid was taken up in Et_3N and chloroform (0.1% v/v, 20 mL) and concentrated under a flow of nitrogen. Activated ester **170** (11 mg, 0.019 mmol) in DCM (0.42 mL) was added to the crude amine product, to which iPr$_2$NEt (9.8 µL, 0.056 mmol) was added and stirred for 3 h at rt. This was concentrated under a flow of nitrogen and the crude product was purified by reverse phase chromatography (C18, 10-100% v/v MeCN in water + 0.05% TFA) to afford the title compound as a purple solid (8.5 mg, 47%). $\boldsymbol{R_f}$ 0.19 (10% v/v MeOH in DCM); **^{1}H NMR (500 MHz, DMSO-d_6):** δ 8.91 (t, J = 5.8 Hz, 1H), 8.70 (m, 2H), 8.53 (dd, J = 15.8, 1.5 Hz, 1H), 8.37 (t, J = 5.8 Hz, 1H), 8.31 (d, J = 8.0 Hz,

1H), 8.02 (d, J = 7.0 Hz, 2H), 7.62–7.52 (m, 4H), 7.03 (m, 4H), 6.92 (s, 2H), 6.54 (d, J = 15.7 Hz, 1H), 4.19 (d, J = 5.5 Hz, 2H), 4.02 (t, J = 6.5 Hz, 3H), 3.56-3.33 (m, 10H, deduced from HSQC and HMBC, **Appendix 18** and **Appendix 19**), 3.30 (q, J = 6.4 Hz, 2H), 3.25 (s, 12H), 1.79 (m, 2H), 1.56 (m, 2H), 1.33 (m, 2H), 0.89 (t, J = 7.4 Hz, 4H) ppm; **LRMS (ESI$^+$)** m/z: 991 $[M+Na]^+$; **HRMS (MALDI$^+$)** m/z: $C_{52}H_{57}N_8O_9S$ $[M]^+$ calculated: 969.3964, found: 969.3970; **HPLC (λ = 215 nm), condition b:** 65.5%, t_R = 24.357 min.

(75) (*E*)-9-(4-((2-(2-(3-(4-((2-(4-(butoxycarbonyl)piperazin-1-yl)-2-oxoethyl)carbamoyl)-2-phenylthiazol-5-yl)acrylamido)-ethoxy)ethyl)carbamoyl)-2-carboxyphenyl)-3,6-bis(dimethyl-amino)xanthylium

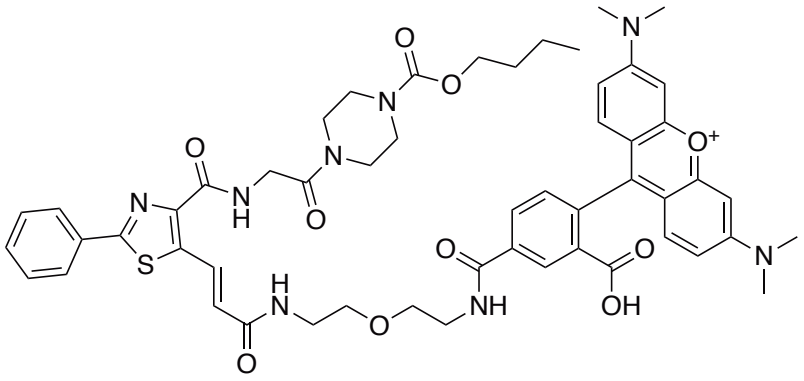

Hydrogen chloride in 1,4-dioxane solution (4 M, 40 µL, 0.16 mmol) was added to Boc-carbamate **178** (11 mg, 0.018 mmol) in dry DCM (0.4 mL) and stirred for 40 min at rt. The crude product was concentrated under the flow of nitrogen, taken up in MeCN (5 mL), and filtered over Celite® pad discarding the filtrate. The filtrant was taken up in solid was taken up in Et_3N and chloroform (0.1% v/v, 20 mL) and concentrated under the flow of nitrogen. Activated ester **171** (10 mg, 0.016 mmol) in DCM (0.33 mL) was added to the crude TAMRA product, to which iPr$_2$NEt (8.4 µL, 0.048 mmol) was added and stirred for 3 h at rt. This was concentrated under a flow of nitrogen and the crude product was purified by reverse phase chromatography (C18, 10-100% v/v MeCN in water + 0.05% TFA) to afford the title compound as

a purple solid (7.8 mg, 49%). $\boldsymbol{R_f}$ 0.27 (10% v/v MeOH in DCM); **^{1}H NMR (500 MHz, DMSO-d_6):** δ 8.82 (t, J = 5.3 Hz, 1H), 8.68 (s, 1H), 8.58 (t, J = 5.2 Hz, 1H), 8.52 (d, J = 15.7 Hz, 1H), 8.36 (m, 2H), 7.91 (d, J = 7.4 Hz, 2H), 7.60-7.51 (m, 2H), 7.49 (t, J = 7.4 Hz, 2H), 6.93 (s, 4H), 6.79 (s, 2H), 6.54 (d, J = 15.7 Hz, 1H), 4.10 (d, J = 5.3 Hz, 2H), 4.03 (t, J = 6.5 Hz, 2H), 3.63 (t, J = 5.4 Hz, 2H), 3.67-3.33 (m, 14H), 3.19 (s, 12H), 1.61–1.51 (m, 2H), 1.40-1.28 (m, 2H), 0.90 (t, J = 7.3 Hz, 3H) ppm; **HRMS (MALDI$^+$)** m/z: $C_{53}H_{59}N_8O_{10}S$ $[M]^+$ calculated: 999.4069, found: 999.4075; **HPLC (λ = 215 nm), condition b:** 93.8%, t_R = 23.381 min. 2D NMR spectra are shown in **Appendix 20** and **Appendix 21**.

(170) Butyl (*E*)-4-((5-(3-((2,5-dioxopyrrolidin-1-yl)oxy)-3-oxoprop-1-en-1-yl)-2-phenylthiazole-4-carbonyl)glycyl)piperazine-1-carboxylate

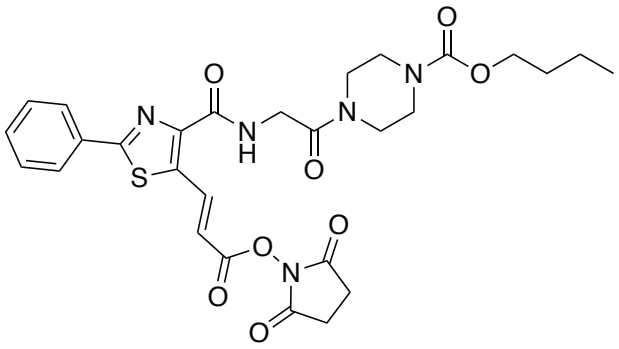

DCC (26 mg, 0.11 mmol) and iPr$_2$NEt (25 mg, 0.2 mmol) were sequentially added to carboxylic acid **61** (48 mg, 0.1 mmol), NHS (14 mg, 0.12 mmol), and DMAP (7.1 mg, 0.058 mmol) in dry DMA (0.50 mL) under nitrogen and stirred for 19 h at rt. This was concentrated under a flow of nitrogen and the crude product was purified by flash chromatography (SiO_2; 10-50% v/v acetone in hexane) to afford the title compound as an off-white solid (51 mg, 89%). $\boldsymbol{R_f}$ 0.29 (30% v/v acetone in hexane); **^{1}H NMR (500 MHz, $CDCl_3$ with 0.1% v/v TMS):** δ 9.16 (d, J = 16.1 Hz, 1H), 8.49 (t, J = 4.6 Hz, 1H), 7.97 (d, J = 6.8 Hz, 2H), 7.53 – 7.37 (m, 3H), 6.38 (d, J = 16.0 Hz, 1H), 4.27 (d, J = 4.5 Hz, 2H), 4.10 (t, J = 6.6 Hz, 2H),

3.67 (t, J = 5.2 Hz, 2H), 3.58–3.44 (m, 6H), 2.86 (s, 4H), 1.65 – 1.57 (m, 2H), 1.42 – 1.33 (m, 2H), 0.93 (t, J = 7.4 Hz, 3H) ppm; **^{13}C NMR (126 MHz, $CDCl_3$ with 0.1% v/v TMS):** δ 169.3, 168.1, 166.6, 161.2, 161.0, 155.5, 148.0, 139.6, 136.9, 132.0, 131.9, 129.3, 127.2, 116.2, 65.9, 44.5, 43.6 (2 × C peaks), 42.0, 41.2, 31.1, 25.7, 19.2, 13.8 ppm; **LRMS (ESI$^+$)** *m/z*: 620 $[M+Na]^+$; **HRMS (ESI$^+$)** *m/z*: $C_{28}H_{31}N_5O_8S$ $[M+Na]^+$ calculated: 620.1786, found: 620.1775.

(171) Butyl (*E*)-4-((5-(3-(4-nitrophenoxy)-3-oxoprop-1-en-1-yl)-2-phenylthiazole-4-carbonyl)glycyl)piperazine-1-carboxylate

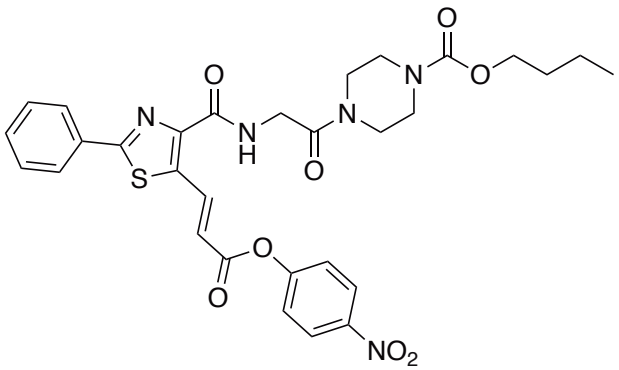

EDC (29 mg, 0.15 mmol) and DMAP (25 mg, 0.2 mmol) were added to carboxylic acid **61** (50 mg, 0.1 mmol) and 4-nitrophenol (22 mg, 0.15 mmol) in dry DCM (0.5 mL) under nitrogen and stirred for 24 h at rt. The reaction mixture was diluted with DCM (50 mL), washed with 1 M aq. HCl (15 mL), sat. aq. bicarb solution (15 mL), water (15 mL), brine (15 mL) and then dried over Na_2SO_4. This was concentrated under a flow of nitrogen and the crude product was purified by flash chromatography (SiO_2; 10-50% v/v acetone in hexane) to afford the title compound as an off-white solid (17 mg, 28%). $\boldsymbol{R_f}$ 0.16 (20% v/v acetone in hexane); **^{1}H NMR (500 MHz, $CDCl_3$ with 0.1% v/v TMS):** δ 9.16 (d, J = 15.9 Hz, 1H), 8.53 (t, J = 4.6 Hz, 1H), 8.33–8.26 (dt, J = 9.1, 2.2 Hz, 2H), 8.00 (dt, J = 6.7, 1.6 Hz, 2H), 7.54–7.46 (m, 3H), 7.40–7.34 (dt, J = 9.1, 2.1 Hz, 2H), 6.43 (d, J = 16.0 Hz, 1H), 4.30 (d, J = 4.5 Hz, 2H), 4.12 (t, J = 6.7 Hz, 2H), 3.72–3.63 (m, 2H), 3.61–3.43 (m, 6H),

1.67-1.59 (m, 2H), 1.43–1.34 (m, 2H), 0.94 (t, J = 7.4 Hz, 3H) ppm; **^{13}C NMR (126 MHz, $CDCl_3$ with 0.1% v/v TMS):** δ 167.7, 166.5, 163.3, 161.5, 155.6, 155.5, 147.5, 145.5, 137.6, 137.4, 132.1, 131.8, 129.3, 127.2, 125.3, 122.6, 121.2, 66.0, 44.5, 43.6 (2 × C peaks), 42.0, 41.3, 31.1, 19.3, 13.9 ppm; **LRMS (ESI$^+$)** m/z: 644 $[M+Na]^+$; **HRMS (ESI$^+$)** m/z: $C_{30}H_{31}N_5O_8S$ $[M+Na]^+$ calculated: 644.1786, found: 644.1777.

(172) Butyl (*E*)-4-((5-(3-(1*H*-imidazol-1-yl)-3-oxoprop-1-en-1-yl)-2-phenylthiazole-4-carbonyl)glycyl)piperazine-1-carboxylate

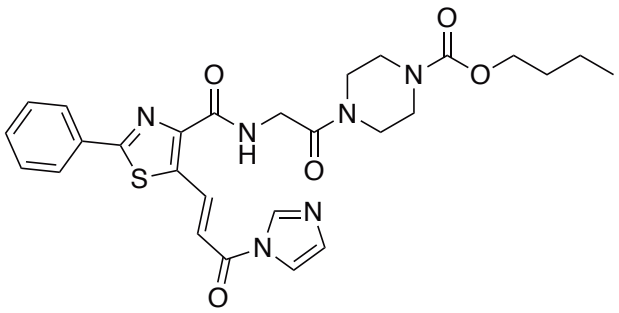

CDI (22 mg, 0.12 mmol) was added to (*Z*)-3-(4-((2-(4-(butoxycarbonyl)piperazin-1-yl)-2-oxoethyl)carbamoyl)-2-phenylthiazol-5-yl)acrylic acid (48 mg, 0.1 mmol) in dry DCM (0.25 mL) under nitrogen and stirred for 14 h at rt. This was concentrated under a flow of nitrogen and the crude product was purified by flash chromatography (SiO_2; 10-70% v/v acetone in hexane) to afford the title compound as an off-white solid (17 mg, 33%). $\boldsymbol{R_f}$ 0.27 (20% v/v acetone in hexane); **^{1}H NMR (500 MHz, $CDCl_3$ with 0.1% v/v TMS):** δ 9.23 (d, J = 15.5 Hz, 1H), 8.50 (s, 1H), 8.28 (s, 1H), 7.98 (d, J = 1.8 Hz, 1H), 7.60 (s, 1H), 7.52–7.43 (m, 3H), 7.15 (s, 1H), 6.88 (d, J = 15.5 Hz, 1H), 4.30 (d, J = 4.5 Hz, 2H), 4.12 (t, J = 6.7 Hz, 3H), 3.67 (d, J = 5.4 Hz, 2H), 3.58–3.45 (m, 6H), 1.63 (m, 2H), 1.39 (m, 2H), 0.94 (t, J = 7.4 Hz, 3H) ppm; **^{13}C NMR (126 MHz, $CDCl_3$ with 0.1% v/v TMS):** δ 167.8, 166.5, 161.2, 160.9, 155.5, 148.3, 139.1, 137.0, 136.4, 132.0, 131.9, 131.4, 129.4, 129.4, 127.2, 119.7, 116.5, 65.9, 44.5, 43.5 (2 × C peaks), 42.0, 41.3, 31.1, 19.3, 13.9 ppm;

LRMS (ESI$^+$) *m/z*: 573 [M+Na]$^+$; **HRMS (ESI$^+$)** *m/z*: $C_{27}H_{31}N_6O_5S$ [M+H]$^+$ calculated: 551.2071, found: 551.2069.

General amide coupling condition appending linkers to TAMRA

Et_3N (5 eq.) was added to 5-TAMRA (1 eq.) in DMA (43 mL/mmol) and stirred for 5 min at rt, to which HATU (1.3 eq.) and then Boc-diamine linker (1.3 eq.) in DMA (43 mL/mmol) were added to the 5-TAMRA solution. This was stirred for 22 h and then purified by reverse phase chromatography (10-100% v/v MeCN in water + 0.1% Et_3N) to afford the respective compounds.

(173) 9-(4-((2-((*Tert*-butoxycarbonyl)amino)ethyl)carbamoyl)-2-carboxyphenyl)-3,6-bis(dimethylamino)xanthylium

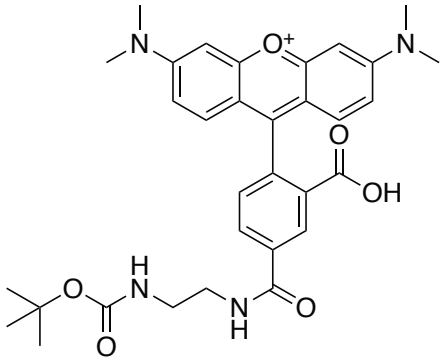

Followed ***general amide coupling condition appending linkers to TAMRA*** with Et_3N (16 µL, 0.12 mmol), 5-TAMRA (10 mg, 0.023 mmol), HATU (11 mg, 0.030 mmol) and *N*-Boc-ethylenediamine (4.8 mg, 0.030 mmol) to afford the title compound as a purple solid (9.6 mg, 72%). $\boldsymbol{R_f}$ 0.41 (10% v/v MeOH in DCM); **^{1}H NMR (300 MHz, $CDCl_3$ with 0.1% v/v TMS):** δ 8.45 (s, 1H), 8.16 (dd, J = 8.0, 1.6 Hz, 1H), 7.69 (t, J = 4.2 Hz, 1H), 7.23 (d, J = 8.0 Hz, 1H), 6.60 (d, J = 8.9 Hz, 2H), 6.49 (d, J = 2.5 Hz, 2H), 6.40 (dd, J = 8.9, 2.6 Hz, 2H), 5.16 (m, 1H), 3.61 (q, J = 5.1 Hz, 2H), 3.42 (m, 2H), 2.99 (s, 12H), 1.44 (s, 9H) ppm; **^{13}C NMR (126 MHz, $CDCl_3$ with 0.1% v/v TMS):** δ 169.2,

166.6, 157.7, 154.8, 153.3, 152.6, 136.1, 133.7, 129.0, 124.9, 123.8, 109.1, 106.8, 98.5, 80.3, 42.4, 40.4, 28.5 ppm; **LRMS (ESI$^+$)** *m/z*: 573 $[M]^+$; **HRMS (ESI$^+$)** *m/z*: $C_{32}H_{37}N_4O_6$ $[M]^+$ calculated: 573.2708, found: 573.27129. 2D NMR spectra are shown in **Appendix 22** and **Appendix 23**.

(174) 9-(4-((2-((*Tert*-butoxycarbonyl)amino)propyl)carbamoyl)-2-carboxyphenyl)-3,6-bis(dimethylamino)xanthylium

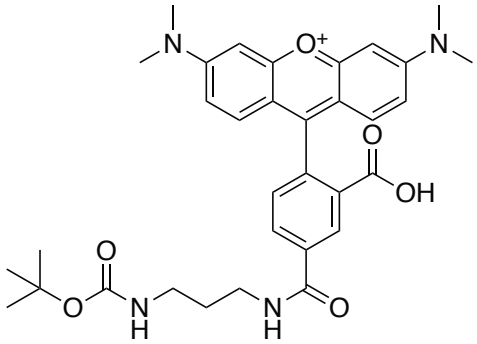

Followed ***general amide coupling condition appending linkers to TAMRA*** with Et_3N (16 µL, 0.12 mmol), 5-TAMRA (10 mg, 0.023 mmol), HATU (11 mg, 0.030 mmol) and *N*-Boc-1,3-propanediamine (5.2 mg, 0.030 mmol) to afford the title compound as a purple solid (12 mg, 89%). R_f 0.41 (10% v/v MeOH in DCM); **^{1}H NMR (400 MHz, DMSO-d_6):** δ 8.78 (t, J = 5.6 Hz, 1H), 8.44 (s, 1H), 8.22 (dd, J = 8.0, 1.8 Hz, 1H), 7.31 (d, J = 8.0 Hz, 1H), 6.81 (t, J = 5.7 Hz, 1H), 6.59–6.41 (m, 6H), 3.30 (m, 2H), 3.01 (q, J = 6.6 Hz, 2H), 2.94 (s, 12H), 1.67 (m, 2H), 1.38 (s, 9H) ppm; **^{13}C NMR (101 MHz, DMSO-d_6):** δ 168.4, 164.7, 155.6, 154.8, 152.1, 152.0, 136.2, 134.4, 128.4, 126.9, 124.2, 123.1, 109.0, 105.6, 98.0, 84.8, 77.5, 39.8, 37.8, 37.2, 29.4, 28.2 ppm; **LRMS (ESI$^+$)** *m/z*: 587 $[M]^+$; **HRMS (ESI$^+$)** *m/z*: $C_{33}H_{39}N_4O_6$ $[M]^+$ calculated: 587.2864, found: 587.2856. 2D NMR spectra are shown in **Appendix 24** and **Appendix 25**.

(175) 9-(4-((4-((*Tert*-butoxycarbonyl)amino)butyl)carbamoyl)-2-carboxyphenyl)-3,6-bis(dimethylamino)xanthylium

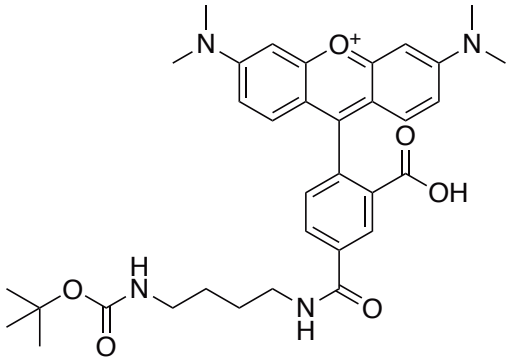

Followed ***general amide coupling condition appending linkers to TAMRA*** with Et_3N (16 µL, 0.12 mmol), 5-TAMRA (10 mg, 0.023 mmol), HATU (11 mg, 0.030 mmol) and *N*-Boc-1,4-butanediamine (5.6 mg, 0.030 mmol) to afford the title compound as a purple solid (12 mg, 88%). $\boldsymbol{R_f}$ 0.41 (10% v/v MeOH in DCM); **^{1}H NMR (500 MHz, DMSO-d_6):** δ 8.80 (t, J = 5.6 Hz, 1H), 8.43 (s, 1H), 8.22 (dd, J = 8.0, 1.6 Hz, 1H), 7.30 (d, J = 8.0 Hz, 1H), 6.79 (t, J = 5.8 Hz, 1H), 6.56–6.40 (m, 6H), 3.32-3.27 (m, 2H), 2.97-2.91 (m, 14H), 1.55-1.50 (m, 2H), 1.48–1.41 (m, 2H), 1.37 (s, 9H) ppm; **^{13}C NMR (126 MHz, DMSO-d_6):** δ 168.5, 164.7, 155.7, 154.8, 152.2, 152.0, 136.3, 134.5, 128.4, 126.9, 124.2, 123.1, 109.0, 105.6, 98.0, 84.9, 77.4, 39.8, 39.1 (deduced from HSQC and HMBC, **Appendix 26** and **Appendix 27**), 28.3, 27.1, 26.4 ppm; **LRMS (ESI$^+$)** *m/z*: 601 $[M]^+$; **HRMS (ESI$^+$)** *m/z*: $C_{34}H_{41}N_4O_6$ $[M]^+$ calculated: 601.3021, found: 601.3013.

(176) 9-(4-((5-((*Tert*-butoxycarbonyl)amino)pentyl)carbamoyl)-2-carboxyphenyl)-3,6-bis(dimethylamino)xanthylium

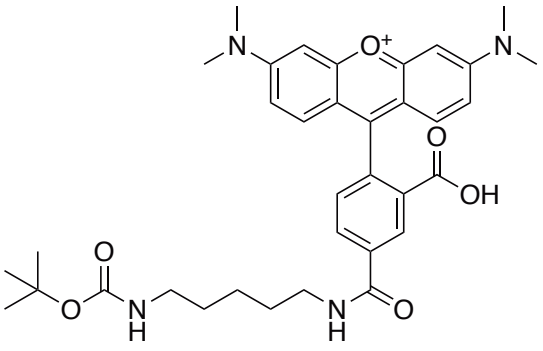

Followed ***general amide coupling condition appending linkers to***

TAMRA with Et_3N (16 µL, 0.12 mmol), 5-TAMRA (10 mg, 0.023 mmol), HATU (11 mg, 0.030 mmol) and *N*-Boc-cadaverine (6.1 mg, 0.030 mmol) to afford the title compound as a purple solid (4.5 mg, 33%). $\boldsymbol{R_f}$ 0.41 (10% v/v MeOH in DCM); **^{1}H NMR (500 MHz, DMSO-d_6):** δ 8.78 (t, J = 5.6 Hz, 1H), 8.43 (s, 1H), 8.21 (dd, J = 8.0, 1.6 Hz, 1H), 7.30 (d, J = 8.0 Hz, 1H), 6.76 (t, J = 5.9 Hz, 1H), 6.56–6.44 (m, 6H), 3.30 (d, J = 6.2 Hz, 2H), 2.94 (s, 12H), 2.93-2.86 (m, 2H), 1.59–1.51 (m, 2H), 1.45-1.38 (m, 2H), 1.36 (s, 9H), 1.34–1.28 (m, 2H) ppm; **^{13}C NMR (126 MHz, DMSO-d_6):** δ 168.5, 164.7, 155.7, 154.8, 152.2, 152.0, 136.3, 134.5, 128.4, 126.9, 124.2, 123.1, 109.0, 105.6, 98.0, 84.8, 77.4, 39.9 (deduced from HSQC and HMBC, **Appendix 28** and **Appendix 29**), 39.7 (deduced from HSQC and HMBC), 39.4 (deduced from HSQC and HMBC), 29.3, 28.7, 28.3, 23.8 ppm; **LRMS (ESI$^+$)** *m/z*: 637 $[M\text{-}H+Na]^+$; **HRMS (ESI$^+$)** *m/z*: $C_{35}H_{43}N_4O_6$ $[M]^+$ calculated: 615.3177, found: 615.3173.

(177) 9-(4-((6-((*Tert*-butoxycarbonyl)amino)hexyl)carbamoyl)-2-carboxyphenyl)-3,6-bis(dimethylamino)xanthylium

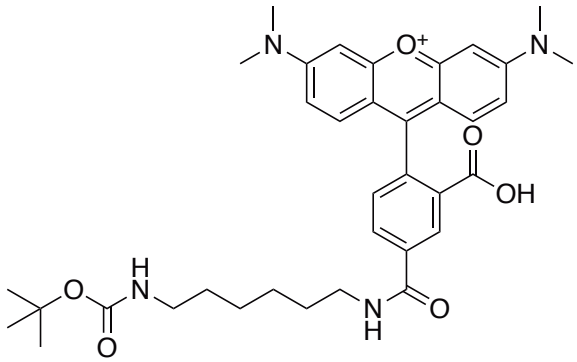

Followed ***general amide coupling condition appending linkers to TAMRA*** with Et_3N (16 µL, 0.12 mmol), 5-TAMRA (10 mg, 0.023 mmol), HATU (11 mg, 0.030 mmol) and *N*-Boc-1,6-hexanediamine (6.5 mg, 0.030 mmol) to afford the title compound as a purple solid (9.9 mg, 74%). $\boldsymbol{R_f}$ 0.41 (10% v/v MeOH in DCM); **^{1}H NMR (500 MHz, DMSO-d_6):** δ 8.78 (t, J = 5.6 Hz, 1H), 8.43 (s, 1H), 8.22 (dd, J = 8.1, 1.6 Hz, 1H), 7.30 (d, J = 8.0 Hz, 1H), 6.75 (t, J =

5.8 Hz, 1H), 6.55–6.48 (m, 6H), 3.33–3.27 (m, 2H), 2.94 (s, 12H), 2.92–2.87 (m, 2H), 1.58–1.51 (m, 2H), 1.42–1.37 (m, 2H), 1.36 (s, 9H), 1.34–1.25 (m, 4H) ppm; **^{13}C NMR (126 MHz, DMSO-d_6):** δ 168.5, 164.7, 155.7, 154.8, 152.2, 152.0, 136.3, 134.5, 128.4, 126.9, 124.2, 123.1, 109.0, 105.6, 98.0, 84.8, 79.2, 77.4, 39.8, 39.7 (deduced from HSQC and HMBC, **Appendix 30** and **Appendix 31**), 39.4 (deduced from HSQC and HMBC), 29.5, 29.0, 28.3, 26.2, 26.1 ppm; **LRMS (ESI$^+$)** *m/z*: 629 $[M]^+$; **HRMS (ESI$^+$)** *m/z*: $C_{36}H_{45}N_4O_6$ $[M]^+$ calculated: 629.3334, found: 629.3326.

(178) 9(4((2(2((*Tert*-butoxycarbonyl)amino)ethoxy)ethyl)carbamoyl)-2-carboxyphenyl)-3,6-bis(dimethylamino)xanthylium

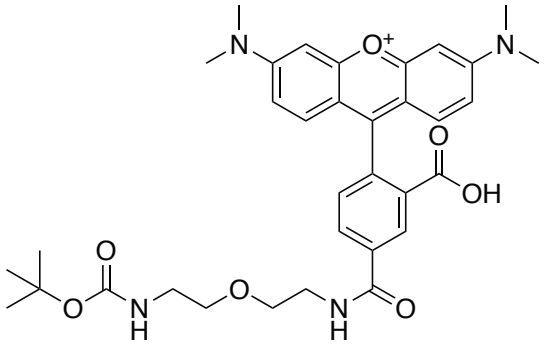

Followed ***general amide coupling condition appending linkers to TAMRA*** with Et_3N (16 µL, 0.12 mmol), 5-TAMRA (10 mg, 0.023 mmol), HATU (11 mg, 0.030 mmol) and *tert*-butyl (2-(2-aminoethoxy)ethyl)carbamate (6.2 mg, 0.030 mmol) to afford the title compound as a purple solid (11 mg, 82%). $\boldsymbol{R_f}$ 0.41 (10% v/v MeOH in DCM); **^{1}H NMR (400 MHz, DMSO-d_6):** δ 8.86 (t, J = 5.5 Hz, 1H), 8.45 (s, 1H), 8.23 (d, J = 8.0 Hz, 1H), 7.31 (d, J = 8.0 Hz, 1H), 6.75 (d, J = 5.9 Hz, 1H), 6.63 – 6.40 (m, 6H), 3.56 (t, J = 5.9 Hz, 2H), 3.47 (t, J = 5.7 Hz, 3H), 3.43 (t, J = 6.2 Hz, 2H), 3.10 (q, J = 5.9 Hz, 2H), 2.94 (s, 12H), 1.36 (s, 9H) ppm; **^{13}C NMR (101 MHz, DMSO-d_6):** δ 168.3, 164.9, 155.6, 154.8, 152.1, 152.0, 136.0, 134.5, 128.4, 126.9, 124.1, 123.2, 109.0, 105.6, 98.0, 84.8, 77.6, 69.0, 68.5, 39.7 (deduced from HSQC and HMBC, **Appendix 32** and **Appendix 33**), 39.3 (deduced from HSQC and HMBC), 28.2 ppm; **LRMS (ESI$^+$)** *m/z*: 617 $[M]^+$;

HRMS (ESI$^+$) *m/z*: $C_{34}H_{41}N_4O_7$ $[M]^+$ calculated: 617.2970, found: 617.2967.

(179) 9-(2-Carboxy-4-((2,2-dimethyl-4-oxo-3,8,11-trioxa-5-aza-tridecan-13-yl)carbamoyl)phenyl)-3,6-bis(dimethylamino)xanthylium

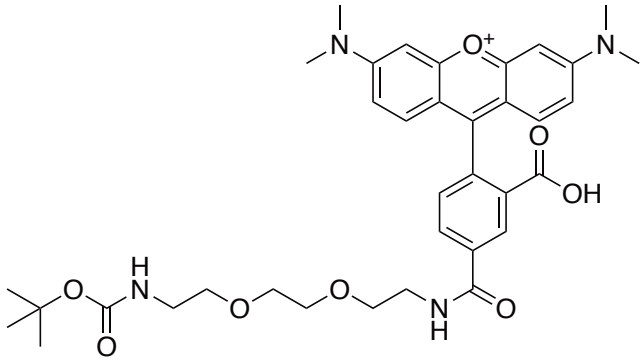

Followed ***general amide coupling condition appending linkers to TAMRA*** with Et_3N (16 µL, 0.12 mmol), 5-TAMRA (10 mg, 0.023 mmol), HATU (11 mg, 0.030 mmol) and *tert*-butyl (2-(2-(2-aminoethoxy)ethoxy)ethyl)carbamate (7.5 mg, 0.030 mmol) to afford the title compound as a purple solid (8.2 mg, 51%). R_f 0.41 (10% v/v MeOH in DCM); **LRMS (ESI$^+$)** *m/z*: 661 $[M]^+$; **^{1}H NMR (500 MHz, DMSO-d_6):** δ 8.88 (t, J = 5.5 Hz, 1H), 8.46 (d, J = 1.5 Hz, 1H), 8.23 (dd, J = 8.0, 1.6 Hz, 1H), 7.31 (d, J = 8.0 Hz, 1H), 6.73 (t, J = 5.3 Hz, 1H), 6.52 (d, J = 8.8 Hz, 2H), 6.50 (s, 2H), 6.48 (dd, J = 8.8, 2.5 Hz, 2H), 3.58 (t, J = 6.0 Hz, 2H), 3.56 (dd, J = 5.4, 2.6 Hz, 2H), 3.52 (dd, J = 5.2, 2.6 Hz, 2H), 3.48 (q, J = 5.8 Hz, 2H), 3.38 (t, J = 6.1 Hz, 2H), 3.05 (q, J = 6.1 Hz, 2H), 2.94 (s, 12H), 1.36 (s, 9H) ppm; **^{13}C NMR (126 MHz, DMSO-d_6):** δ 168.4, 164.8, 155.6, 154.8, 152.2, 152.0, 136.0, 134.5, 128.4, 126.9, 124.2, 123.2, 109.0, 105.6, 98.0, 84.8, 77.6, 69.6, 69.5, 69.2, 68.8, 39.8, 39.7 (deduced from HSQC and HMBC, **Appendix 34** and **Appendix 35**), 39.4 (deduced from HSQC and HMBC), 28.2 ppm; **HRMS (ESI$^+$)** *m/z*: $C_{36}H_{45}N_4O_8$ $[M]^+$ calculated: 661.3232, found: 661.3222.

(180) 9-(2-Carboxy-4-((2,2-dimethyl-4-oxo-3,9,12,15-tetraoxa-5-azaoctadecan-18-yl)carbamoyl)phenyl)-3,6-bis(dimethylamino)xanthylium

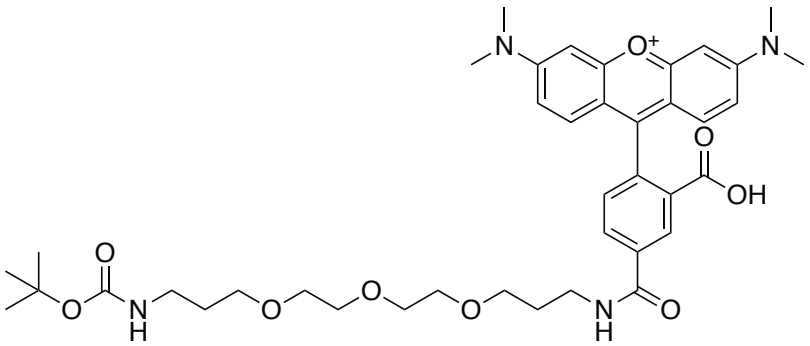

Followed ***general amide coupling condition appending linkers to TAMRA*** with Et_3N (16 µL, 0.12 mmol), 5-TAMRA (10 mg, 0.023 mmol), HATU (11 mg, 0.030 mmol) and *tert*-butyl (3-(2-(2-(3-aminopropoxy)ethoxy)ethoxy)propyl)-carbamate (7.5 mg, 0.023 mmol) to afford the title compound as a purple solid (8.4 mg, 56%). $\boldsymbol{R_f}$ 0.41 (10% v/v MeOH in DCM); **^{1}H NMR (500 MHz, DMSO-d_6):** δ 8.79 (t, J = 5.6 Hz, 1H), 8.43 (s, 1H), 8.22 (d, J = 8.1 Hz, 1H), 7.30 (d, J = 8.0 Hz, 1H), 6.72 (t, J = 5.8 Hz, 1H), 6.58–6.44 (m, 6H), 3.56–3.44 (m, 10H), 3.35-3.30 (m, 4H), 2.98-2.91 (m, 14H), 1.79 (m, 2H), 1.58 (m, 2H), 1.35 (s, 9H) ppm; **^{13}C NMR (126 MHz, DMSO-d_6):** δ 168.4, 164.8, 155.6, 154.8, 152.2, 152.0, 136.3, 134.5, 128.4, 126.9, 124.2, 123.1, 109.0, 105.6, 98.0, 84.8, 79.2, 77.5, 69.8 (2 × C peaks, **Appendix 36** and **Appendix 37**), 69.6 (2 × C peaks), 68.3, 68.1, 39.8, 37.3, 36.9, 29.7, 29.3, 28.3 ppm; **LRMS (ESI$^+$)** m/z: 755 $[M\text{-}H+Na]^+$; **HRMS (ESI$^+$)** m/z: $C_{40}H_{53}N_4O_9$ $[M]^+$ calculated: 733.3807, found: 733.3799.

References

(1) Przedborski, S.; Vila, M.; Jackson-Lewis, V., et al. Series Introduction: Neurodegeneration: What is it and where are we? *J. Clin. Investig.* **2003**, *111*, 3–10.

(2) Parkinson, J. An essay on the shaking palsy. *J. Neuropsychiatry Clin. Neurosci.* **2002**, *14*, 223–236.

(3) Garcia Ruiz, P. J.; Luquin Piudo, R.; Martinez Castrillo, J. C. On Disease Modifying and Neuroprotective Treatments for Parkinson's Disease: Physical Exercise. *Front. Neurol.* **2022**, *13*, 938686.

(4) Kumar, D.; Ashraf, G. M.; Bilgrami, A. L.; Hassan, M. I. Emerging therapeutic developments in neurodegenerative diseases: A clinical investigation. *Drug Discov. Today* **2022**, *27*, 103305.

(5) Thompson, A. J.; Banwell, B. L.; Barkhof, F.; Carroll, W. M.; Coetzee, T.; Comi, G.; Correale, J.; Fazekas, F.; Filippi, M.; Freedman, M. S., et al. Diagnosis of multiple sclerosis: 2017 revisions of the McDonald criteria. *Lancet Neurol.* **2018**, *17*, 162–173.

(6) Tam, R. Y.; Fuehrmann, T.; Mitrousis, N.; Shoichet, M. S. Regenerative Therapies for Central Nervous System Diseases: a Biomaterials Approach. *Neuropsychopharmacology* **2014**, *39*, 169–188.

(7) Durães, F.; Pinto, M.; Sousa, E. Old Drugs as New Treatments for Neurodegenerative Diseases. *Pharmaceuticals* **2018**, *11*, 44.

(8) McGinley, M. P.; Goldschmidt, C. H.; Rae-Grant, A. D. Diagnosis and Treatment of Multiple Sclerosis: A Review. *Jama* **2021**, *325*, 765–779.

(9) Hellwig, S.; Domschke, K.; Meyer, P. T. Update on PET in neurodegenerative and neuroinflammatory disorders manifesting on a behavioural level: imaging for differential diagnosis. *Curr. Opin. Neurol.* **2019**, *32*, 548–556.

(10) Bates, G. P.; Dorsey, R.; Gusella, J. F.; Hayden, M. R.; Kay, C.; Leavitt, B. R.; Nance, M.; Ross, C. A.; Scahill, R. I.; Wetzel, R., et al. Huntington disease. *Nat. Rev. Dis. Primers* **2015**, *1*, 1–21.

(11) Poewe, W.; Seppi, K.; Tanner, C. M.; Halliday, G. M.; Brundin, P.; Volkmann, J.; Schrag, A.-E.; Lang, A. E. Parkinson disease. *Nat. Rev. Dis. Primers* **2017**, *3*, 1–21.

(12) Dupont, A.-C.; Largeau, B.; Guilloteau, D.; Santiago Ribeiro, M. J.; Arlicot, N. The place of PET to assess new therapeutic effectiveness in neurodegenerative diseases. *Contrast Media & Molecular Imaging* **2018**, *2018*, 7043578.

(13) Zhou, J.; Jangili, P.; Son, S.; Ji, M. S.; Won, M.; Kim, J. S. Fluorescent Diagnostic Probes in Neurodegenerative Diseases. *Adv. Mater.* **2020**, *32*, 2001945.

(14) Högel, H.; Rissanen, E.; Vuorimaa, A.; Airas, L. Positron emission tomography imaging in evaluation of MS pathology in vivo. *Mult. Scler. J.* **2018**, *24*, 1399–1412.

(15) Sobański, M.; Zacharzewska-Gondek, A.; Waliszewska-Prosół, M.; Sąsiadek, M. J.; Zimny, A.; Bladowska, J. A Review of Neuroimaging in Rare Neurodegenerative Diseases. *Dement. Geriatr. Cogn. Dis.* **2021**, *49*, 544–556.

(16) Soni, N.; Ora, M.; Bathla, G.; Nagaraj, C.; Boles Ponto, L. L.; Graham, M. M.; Saini, J.; Menda, Y. Multiparametric magnetic resonance imaging and positron emission tomography findings in neurodegenerative diseases: Current status and future directions. *Neuroradiol. J.* **2021**, *34*, 263–288.

(17) Zhu, L.; Ploessl, K.; Kung, H. F. PET/SPECT imaging agents for neurodegenerative diseases. *Chem. Soc. Rev.* **2014**, *43*, 6683–6691.

(18) García, J.-C.; Bustos, R.-H. The genetic diagnosis of neurodegenerative diseases and therapeutic perspectives. *Brain Sci.* **2018**, *8*, 222.

(19) Hauser, S. L.; Cree, B. A. Treatment of Multiple Sclerosis: A Review. *Am. J. Med.* **2020**, *133*, 1380–1390.

(20) Chitnis, T.; Weiner, H. L., et al. CNS inflammation and neurodegeneration. *J. Clin. Investig.* **2017**, *127*, 3577–3587.

(21) Carson, M. J.; Thrash, J. C.; Walter, B. The cellular response in neuroinflammation: The role of leukocytes, microglia and astrocytes in neuronal death and survival. *Clin. Neurosci. Res.* **2006**, *6*, 237–245.

(22) Ghadery, C.; Best, L. A.; Pavese, N.; Tai, Y. F.; Strafella, A. P. PET Evaluation of Microglial Activation in Non-Neurodegenerative Brain Diseases. *Curr. Neurol. Neurosci. Rep.* **2019**, *19*, 1–12.

(23) Tiepolt, S.; Patt, M.; Aghakhanyan, G.; Meyer, P. M.; Hesse, S.; Barthel, H.; Sabri, O. Current radiotracers to image neurodegenerative diseases. *EJNMMI radiopharm. chem.* **2019**, *4*, 1–23.

(24) Ramesh, G.; MacLean, A. G.; Philipp, M. T. Cytokines and Chemokines at the Crossroads of Neuroinflammation, Neurodegeneration, and Neuropathic Pain. *Mediators Inflamm.* **2013**, *2013*, 480739.

(25) Mukhara, D.; Oh, U.; Neigh, G. N. Neuroinflammation. *Handb. Clin. Neurol.* **2020**, *175*, 235–259.

(26) Kwon, H. S.; Koh, S.-H. Neuroinflammation in neurodegenerative disorders: the roles of microglia and astrocytes. *Transl. Neurodegener.* **2020**, *9*, 42.

(27) Edvinsson, L.; Haanes, K. A.; Warfvinge, K. Does inflammation have a role in migraine? *Nat. Rev. Neurol.* **2019**, *15*, 483–490.

(28) Lyman, M.; Lloyd, D. G.; Ji, X.; Vizcaychipi, M. P.; Ma, D. Neuroinflammation: The role and consequences. *Neurosci. Res.* **2014**, *79*, 1–12.

(29) Barnham, K. J.; Masters, C. L.; Bush, A. I. Neurodegenerative diseases and oxidative stress. *Nat. Rev. Drug Discov.* **2004**, *3*, 205–214.

(30) Kujoth, G. C.; Hiona, A.; Pugh, T. D.; Someya, S.; Panzer, K.; Wohlgemuth, S. E.; Hofer, T.; Seo, A.; Sullivan, R.; Jobling, W., et al. Mitochondrial DNA Mutations, Oxidative Stress, and Apoptosis in Mammalian Aging. *Science* **2005**, *309*, 481–484.

(31) Madabhushi, R.; Pan, L.; Tsai, L.-H. DNA Damage and Its Links to Neurodegeneration. *Neuron* **2014**, *83*, 266–282.

(32) Becher, B.; Spath, S.; Goverman, J. Cytokine networks in neuroinflammation. *Nat. Rev. Immunol.* **2017**, *17*, 49–59.

(33) Smith, J. A.; Das, A.; Ray, S. K.; Banik, N. L. Role of pro-inflammatory cytokines released from microglia in neurodegenerative diseases. *Brain Res. Bull.* **2012**, *87*, 10–20.

(34) Dhuriya, Y. K.; Sharma, D. Necroptosis: a regulated inflammatory mode of cell death. *J. Neuroinflammation* **2018**, *15*, 1–9.

(35) Tansey, M. G.; Goldberg, M. S. Neuroinflammation in Parkinson's disease: Its role in neuronal death and implications for therapeutic intervention. *Neurobiol. Dis.* **2010**, *37*, 510–518.

(36) Huang, E. J.; Reichardt, L. F. Neurotrophins: Roles in Neuronal Development and Function. *Annu. Rev. Neurosci.* **2001**, *24*, 677–736.

(37) Park, K.; Lee, D.; Joe, E.; Kim, S.; Jin, B. Neuroprotective role of microglia expressing interleukin-4. *J. Neurosci. Res.* **2005**, *81*, 397–402.

(38) Sawada, M.; Suzumura, A.; Hosoya, H.; Marunouchi, T.; Nagatsu, T. Interleukin-10 Inhibits Both Production of Cytokines and Expression of Cytokine Receptors in Microglia. *J. Neurochem.* **1999**, *72*, 1466–1471.

(39) Tang, Y.; Le, W. Differential Roles of M1 and M2 Microglia in Neurodegenerative Diseases. *Mol. Neurobiol.* **2016**, *53*, 1181–1194.

(40) Teleanu, D. M.; Niculescu, A.-G.; Lungu, I. I.; Radu, C. I.; Vladâcenco, O.; Roza, E.; Costăchescu, B.; Grumezescu, A. M.; Teleanu, R. I. An Overview of Oxidative Stress, Neuroinflammation, and Neurodegenerative Diseases. *Int. J. Mol. Sci.* **2022**, *23*, 5938.

(41) Yang, Q.-Q.; Zhou, J.-W. Neuroinflammation in the central nervous system: Symphony of glial cells. *Glia* **2019**, *67*, 1017–1035.

(42) Zeis, T.; Enz, L.; Schaeren-Wiemers, N. The immunomodulatory oligodendrocyte. *Brain Res.* **2016**, *1641*, 139–148.

(43) Garland, E. F.; Hartnell, I. J.; Boche, D. Microglia and astrocyte function and communication: what do we know in humans? *Front. Neurosci.* **2022**, *16*, 824888.

(44) Jha, M. K.; Jo, M.; Kim, J.-H.; Suk, K. Microglia-Astrocyte Crosstalk: An Intimate Molecular Conversation. *Neuroscientist* **2018**, *25*, 227–240.

(45) Villa, A.; Klein, B.; Janssen, B.; Pedragosa, J.; Pepe, G.; Zinnhardt, B.; Vugts, D. J.; Gelosa, P.; Sironi, L.; Beaino, W., et al. Identification of new molecular targets for PET imaging of the microglial anti-inflammatory activation state. *Theranostics* **2018**, *8*, 5400.

(46) Lee, E.; Eo, J.-C.; Lee, C.; Yu, J.-W. Distinct Features of Brain-Resident Macrophages: Microglia and Non-Parenchymal Brain Macrophages. *Mol. Cells* **2021**, *44*, 281–291.

(47) Perry, V. H.; Nicoll, J. A.; Holmes, C. Microglia in neurodegenerative disease. *Nat. Rev. Neurol* **2010**, *6*, 193–201.

(48) Walker, F. R.; Beynon, S. B.; Jones, K. A.; Zhao, Z.; Kongsui, R.; Cairns, M.; Nilsson, M. Dynamic structural remodelling of microglia in health and disease: A review of the models, the signals and the mechanisms. *Brain Behav. Immun.* **2014**, *37*, 1–14.

(49) Paolicelli, R. C.; Sierra, A.; Stevens, B.; Tremblay, M.-E.; Aguzzi, A.; Ajami, B.; Amit, I.; Audinat, E.; Bechmann, I.; Bennett, M., et al. Microglia states and nomenclature: A field at its crossroads. *Neuron* **2022**, *110*, 3458–3483.

(50) Parvathenani, L. K.; Tertyshnikova, S.; Greco, C. R.; Roberts, S. B.; Robertson, B.; Posmantur, R. P2X7 Mediates Superoxide Production in Primary Microglia and Is Up-regulated in a Transgenic Mouse Model of Alzheimer's Disease. *J. Biol. Chem.* **2003**, *278*, 13309–13317.

(51) McGeer, P. L.; McGeer, E. G. The inflammatory response system of brain: implications for therapy of Alzheimer and other neurodegenerative diseases. *Brain Res. Rev.* **1995**, *21*, 195–218.

(52) Le Feuvre, R.; Brough, D.; Rothwell, N. Extracellular ATP and P2X7 receptors in neurodegeneration. *Eur. J. Pharmacol.* **2002**, *447*, 261–269.

(53) Xu, L.; He, D.; Bai, Y. Microglia-Mediated Inflammation and Neurodegenerative Disease. *Mol. Neurobiol.* **2016**, *53*, 6709–6715.

(54) Bergström, M.; Grahnen, A.; Långström, B. Positron emission tomography microdosing: a new concept with application in tracer and early clinical drug development. *Eur. J. Clin. Pharmacol.* **2003**, *59*, 357–366.

(55) Bailey, D. L.; Maisey, M. N.; Townsend, D. W.; Valk, P. E., *Positron emission tomography*; Springer: 2005; Vol. 2.

(56) Rong, J.; Haider, A.; Jeppesen, T. E.; Josephson, L.; Liang, S. H. Radiochemistry for positron emission tomography. *Nat. Commun.* **2023**, *14*, 3257.

(57) Jacobson, O.; Kiesewetter, D. O.; Chen, X. Fluorine-18 Radiochemistry, Labeling Strategies and Synthetic Routes. *Bioconjugate Chem.* **2015**, *26*, 1–18.

(58) Hou, L.; Rong, J.; Haider, A.; Ogasawara, D.; Varlow, C.; Schafroth, M. A.; Mu, L.; Gan, J.; Xu, H.; Fowler, C. J., et al. Positron Emission Tomography Imaging of the Endocannabinoid System: Opportunities and Challenges in Radiotracer Development. *J. Med. Chem.* **2020**, *64*, 123–149.

(59) Meikle, S. R.; Badawi, R. D., *Positron Emission Tomography: Basic Sciences*; Springer: 2005, pp 93–126.

(60) Rahmim, A.; Lodge, M. A.; Karakatsanis, N. A.; Panin, V. Y.; Zhou, Y.; McMillan, A.; Cho, S.; Zaidi, H.; Casey, M. E.; Wahl, R. L. Dynamic whole-body PET imaging: principles, potentials and applications. *Eur. J. Nucl. Med. Mol. Imaging* **2019**, *46*, 501–518.

(61) Cherry, S. R.; Jones, T.; Karp, J. S.; Qi, J.; Moses, W. W.; Badawi, R. D. Total-body PET: maximizing sensitivity to create new opportunities for clinical research and patient care. *J. Nucl. Med.* **2018**, *59*, 3–12.

(62) Sui, X.; Tan, H.; Yu, H.; Xiao, J.; Qi, C.; Cao, Y.; Chen, S.; Zhang, Y.; Hu, P.; Shi, H. Exploration of the total-body PET/CT reconstruction protocol with ultra-low ^{18}F-FDG activity over a wide range of patient body mass indices. *EJNMMI Phys.* **2022**, *9*, 17.

(63) Alberts, I.; Hünermund, J.-N.; Prenosil, G.; Mingels, C.; Bohn, K. P.; Viscione, M.; Sari, H.; Vollnberg, B.; Shi, K.; Afshar-Oromieh, A., et al. Clinical performance of long axial field of view PET/CT: a head-to-head intra-individual comparison of the Biograph Vision Quadra with the Biograph Vision PET/CT. *Eur. J. Nucl. Med. Mol. Imaging* **2021**, *48*, 2395–2404.

(64) Beaino, W.; Janssen, B.; Vugts, D. J.; de Vries, H. E.; Windhorst, A. D. Towards PET imaging of the dynamic phenotypes of microglia. *Clin. Exp. Immunol.* **2021**, *206*, 282–300.

(65) Wu, C.; Li, F.; Niu, G.; Chen, X. PET Imaging of Inflammation Biomarkers. *Theranostics* **2013**, *3*, 448.

(66) Chauveau, F.; Boutin, H.; Van Camp, N.; Dollé, F.; Tavitian, B. Nuclear imaging of neuroinflammation: a comprehensive review of [^{11}C]PK11195 challengers. *Eur. J. Nucl. Med. Mol. Imaging* **2008**, *35*, 2304–2319.

(67) Maeda, J.; Suhara, T.; Zhang, M.-R.; Okauchi, T.; Yasuno, F.; Ikoma, Y.; Inaji, M.; Nagai, Y.; Takano, A.; Obayashi, S., et al. Novel peripheral benzodiazepine receptor ligand [^{11}C]DAA1106 for PET: An imaging tool for glial cells in the brain. *Synapse* **2004**, *52*, 283–291.

(68) Huang, G.; Qiu, Y.; Bi, L.; Wei, H.; Li, G.; Li, Z.; Ye, P.; Yang, M.; Shen, Y.; Liu, H., et al. PET Imaging of P2X7 Receptor (P2X7R) for Neuroinflammation with Improved Radiosynthesis of Tracer [^{18}F]4A in Mice and Non-human Primates. *ACS Chem. Neurosci.* **2022**, *13*, 3464–3476.

(69) Lee, N.; Choi, J. Y.; Ryu, Y. H. The development status of PET radiotracers for evaluating neuroinflammation. *Nucl. Med. Mol. Imaging* **2024**, 1–17.

(70) De Picker, L. J.; Morrens, M.; Branchi, I.; Haarman, B. C.; Terada, T.; Kang, M. S.; Boche, D.; Tremblay, M.-E.; Leroy, C.; Bottlaender, M., et al. TSPO PET brain inflammation imaging: A transdiagnostic systematic review and meta-analysis of 156 case-control studies. *Brain Behav. Immun.* **2023**.

(71) Burnstock, G. Purine and purinergic receptors. *Brain Neurosci. Adv.* **2018**, *2*, 2398212818817494.

(72) Burnstock, G. Physiology and pathophysiology of purinergic neurotransmission. *Physiological reviews* **2007**, *87*, 659–797.

(73) Unwin, N. Neurotransmitter action: Opening of ligand-gated ion channels. *Cell* **1993**, *72*, 31–41.

(74) Zarrinmayeh, H.; Territo, P. R. Purinergic Receptors of the Central Nervous System: Biology, PET Ligands, and Their Applications. *Mol. Imaging* **2020**, *19*, 1536012120927609.

(75) Hille, B. Modulation of ion-channel function by G-protein-coupled receptors. *Trends Neurosci.* **1994**, *17*, 531–536.

(76) Iovino, L.; Tremblay, M.; Civiero, L. Glutamate-induced excitotoxicity in Parkinson's disease: The role of glial cells. *Journal of pharmacological sciences* **2020**, *144*, 151–164.

(77) Burnstock, G.; Knight, G. E. Cellular distribution and functions of P2 receptor subtypes in different systems. *Int Rev Cytol* **2004**, *240*, 31–304.

(78) Burnstock, G. Purinergic signalling and disorders of the central nervous system. *Nature reviews Drug discovery* **2008**, *7*, 575–590.

(79) Beaino, W.; Janssen, B.; Kooij, G.; van der Pol, S. M.; van Het Hof, B.; van Horssen, J.; Windhorst, A. D.; de Vries, H. E. Purinergic receptors P2Y12R and P2X7R: potential targets for PET imaging of microglia phenotypes in multiple sclerosis. *J. Neuroinflammation* **2017**, *14*, 1–16.

(80) Hide, I.; Shiraki, H.; Masuda, A.; Maeda, T.; Kumagai, M.; Kunishige, N.; Yanase, Y.; Harada, K.; Tanaka, S.; Sakai, N. P2Y2 receptor mediates dying cell removal via inflammatory activated microglia. *Journal of Pharmacological Sciences* **2023**, *153*, 55–67.

(81) Yang, X.; Lou, Y.; Liu, G.; Wang, X.; Qian, Y.; Ding, J.; Chen, S.; Xiao, Q. Microglia P2Y6 receptor is related to Parkinson's disease through neuroinflammatory process. *Journal of neuroinflammation* **2017**, *14*, 1–12.

(82) Bhattacharya, A.; Ceusters, M. Targeting neuroinflammation with brain penetrant P2X7 antagonists as novel therapeutics for neuropsychiatric disorders. *Neuropsychopharmacology* **2020**, *45*, 234.

(83) Dymond, J. S., *Methods in Enzymology*; Elsevier: 2013; Vol. 529, pp 279–289.

(84) Hollopeter, G.; Jantzen, H.-M.; Vincent, D.; Li, G.; England, L.; Ramakrishnan, V.; Yang, R.-B.; Nurden, P.; Nurden, A.; Julius, D., et al. Identification of the platelet ADP receptor targeted by antithrombotic drugs. *Nat.* **2001**, *409*, 202–207.

(85) Sasaki, Y.; Hoshi, M.; Akazawa, C.; Nakamura, Y.; Tsuzuki, H.; Inoue, K.; Kohsaka, S. Selective expression of Gi/o-coupled ATP receptor P2Y12 in microglia in rat brain. *Glia* **2003**, *44*, 242–250.

(86) Mildner, A.; Huang, H.; Radke, J.; Stenzel, W.; Priller, J. $P2Y_{12}$ receptor is expressed on human microglia under physiological conditions throughout development and is sensitive to neuroinflammatory diseases. *Glia* **2017**, *65*, 375–387.

(87) Cox, D. Anti-platelet agents: past, present and future. *ISBT Sci. Ser.* **2020**, *15*, 131–141.

(88) Li, X.; Zhang, G.; Cao, X. The Function and Regulation of Platelet P2Y12 Receptor. *Cardiovasc. Drugs Ther.* **2023**, *37*, 199–216.

(89) Van Giezen, J.; Humphries, R. G. Preclinical and Clinical Studies with Selective Reversible Direct $P2Y_{12}$ Antagonists. *Semin. Thromb. Hemost.* **2005**, *31*, 195–204.

(90) Baqi, Y.; Müller, C. E. Antithrombotic $P2Y_{12}$ receptor antagonists: recent developments in drug discovery. *Drug Discov. Today* **2019**, *24*, 325–333.

(91) Webster, C. M.; Hokari, M.; McManus, A.; Tang, X. N.; Ma, H.; Kacimi, R.; Yenari, M. A. Microglial $P2Y_{12}$ Deficiency/Inhibition Protects against Brain Ischemia. *PLoS One* **2013**, *8*, e70927.

(92) Lou, N.; Takano, T.; Pei, Y.; Xavier, A. L.; Goldman, S. A.; Nedergaard, M. Purinergic receptor P2RY12-dependent microglial closure of the injured blood–brain barrier. *Proc. Natl. Acad. Sci.* **2016**, *113*, 1074–1079.

(93) Tozaki-Saitoh, H.; Tsuda, M.; Miyata, H.; Ueda, K.; Kohsaka, S.; Inoue, K. $P2Y_{12}$ Receptors in Spinal Microglia Are Required for Neuropathic Pain after Peripheral Nerve Injury. *J. Neurosci.* **2008**, *28*, 4949–4956.

(94) Müller, C. E.; Namasivayam, V. Recommended tool compounds and drugs for blocking P2X and P2Y receptors. *Purinergic Signal.* **2021**, *17*, 633–648.

(95) Maeda, J.; Minamihisamatsu, T.; Shimojo, M.; Zhou, X.; Ono, M.; Matsuba, Y.; Ji, B.; Ishii, H.; Ogawa, M.; Akatsu, H., et al. Distinct microglial response against Alzheimer's amyloid and tau pathologies characterized by P2Y12 receptor. *Brain Commun.* **2021**, *3*, fcab011.

(96) Arnott, J. A.; Planey, S. L. The influence of lipophilicity in drug discovery and design. *Expert Opin. Drug Discov.* **2012**, *7*, 863–875.

(97) Waring, M. J. Lipophilicity in drug discovery. *Expert Opin. Drug Discov* **2010**, *5*, 235–248.

(98) Doan, K. M. M.; Humphreys, J. E.; Webster, L. O.; Wring, S. A.; Shampine, L. J.; Serabjit-Singh, C. J.; Adkison, K. K.; Polli, J. W. Passive permeability and P-glycoprotein-mediated efflux differentiate central nervous system (CNS) and non-CNS marketed drugs. *J. Pharmacol. Exp. Ther.* **2002**, *303*, 1029–1037.

(99) Bach, P.; Boström, J.; Brickmann, K.; Van Giezen, J.; Groneberg, R. D.; Harvey, D. M.; O'Sullivan, M.; Zetterberg, F. Synthesis, structure–property relationships and pharmacokinetic evaluation of ethyl 6-aminonicotinate sulfonylureas as antagonists of the $P2Y_{12}$ receptor. *Eur. J. Med. Chem.* **2013**, *65*, 360–375.

(100) Van der Wildt, B.; Janssen, B.; Pekošak, A.; Stéen, E. J. L.; Schuit, R. C.; Kooijman, E. J.; Beaino, W.; Vugts, D. J.; Windhorst, A. D. Novel Thienopyrimidine-Based PET Tracers for $P2Y_{12}$ Receptor Imaging in the Brain. *ACS Chem. Neurosci.* **2021**, *12*, 4465–4474.

(101) Bach, P.; Boström, J.; Brickmann, K.; van Giezen, J.; Hovland, R.; Petersson, A. U.; Ray, A.; Zetterberg, F. A novel series of piperazinyl-pyridine ureas as antagonists of the purinergic $P2Y_{12}$ receptor. *Bioorg. Med. Chem. Lett.* **2011**, *21*, 2877–2881.

(102) Zhang, L.; Villalobos, A.; Beck, E. M.; Bocan, T.; Chappie, T. A.; Chen, L.; Grimwood, S.; Heck, S. D.; Helal, C. J.; Hou, X., et al. Design and Selection Parameters to Accelerate the Discovery of Novel Central Nervous System Positron Emission Tomography (PET) Ligands and Their Application in the Development of a Novel Phosphodiesterase 2A PET Ligand. *J. Med. Chem.* **2013**, *56*, 4568–4579.

(103) Jackson, I. M.; Buccino, P. J.; Azevedo, E. C.; Carlson, M. L.; Luo, A. S.; Deal, E. M.; Kalita, M.; Reyes, S. T.; Shao, X.; Beinat, C., et al. Radiosynthesis and initial preclinical evaluation of [^{11}C]AZD1283 as a potential P2Y12R PET radiotracer. *Nucl. Med. Biol.* **2022**, *114*, 143–150.

(104) Marvin 24.3.131, 2024, ChemAxon.

(105) Lee, C. S. et al. Fused heterocyclic compound, International Patent WO2010-027236A2, 2010.

(106) Wager, T. T.; Hou, X.; Verhoest, P. R.; Villalobos, A. Central Nervous System Multiparameter Optimization Desirability: Application in Drug Discovery. *ACS Chem. Neurosci.* **2016**, *7*, 767–775.

(107) Pike, V. W. Considerations in the Development of Reversibly Binding PET Radioligands for Brain Imaging. *Curr. Med. Chem.* **2016**, *23*, 1818–1869.

(108) Waring, M. J.; Arrowsmith, J.; Leach, A. R.; Leeson, P. D.; Mandrell, S.; Owen, R. M.; Pairaudeau, G.; Pennie, W. D.; Pickett, S. D.; Wang, J., et al. An analysis of the attrition of drug candidates from four major pharmaceutical companies. *Nat. Rev. Drug Discov.* **2015**, *14*, 475–486.

(109) Mandal, S.; Mandal, S. K., et al. Rational drug design. *Eur. J. Pharmacol.* **2009**, *625*, 90–100.

(110) Ma, B. B.; Montgomery, A. P.; Chen, B.; Kassiou, M.; Danon, J. J. Strategies for targeting the P2Y12 receptor in the central nervous system. *Bioorg. Med. Chem. Lett.* **2022**, *71*, 128837.

(111) Sabe, V. T.; Ntombela, T.; Jhamba, L. A.; Maguire, G. E.; Govender, T.; Naicker, T.; Kruger, H. G. Current trends in computer aided drug design and a highlight of drugs discovered via computational techniques: A review. *Eur. J. Med. Chem* **2021**, *224*, 113705.

(112) Bruno, A.; Costantino, G.; Sartori, L.; Radi, M. The In Silico Drug Discovery Toolbox: Applications in Lead Discovery and Optimization. *Curr. Med. Chem.* **2019**, *26*, 3838–3873.

(113) Wager, T. T.; Hou, X.; Verhoest, P. R.; Villalobos, A. Moving Beyond Rules: The Development of a Central Nervous System Multiparameter Optimization (CNS MPO) Approach To Enable Alignment of Druglike Properties. *ACS Chem. Neurosci.* **2010**, *1*, 435–449.

(114) Zhang, L.; Villalobos, A. Strategies to facilitate the discovery of novel CNS PET ligands. *EJNMMI radiopharm. chem.* **2017**, *1*, 1–12.

(115) Gupta, M.; Lee, H. J.; Barden, C. J.; Weaver, D. F. The Blood–Brain Barrier (BBB) Score. *J. Med. Chem.* **2019**, *62*, 9824–9836.

(116) Stéen, E. J. L.; Vugts, D. J.; Windhorst, A. D. The Application of In Silico Methods for Prediction of Blood-Brain Barrier Permeability of Small Molecule PET Tracers. *Front. Nucl. Med.* **2022**, *2*, 853475.

(117) Ioakimidis, L.; Thoukydidis, L.; Mirza, A.; Naeem, S.; Reynisson, J. Benchmarking the Reliability of QikProp. Correlation between Experimental and Predicted Values. *QSAR Comb. Sci.* **2008**, *27*, 445–456.

(118) Jorgensen, W. L.; Duffy, E. M. Prediction of drug solubility from structure. *Adv. Drug Deliv. Rev.* **2002**, *54*, 355–366.

(119) Fan, Y.; Unwalla, R.; Denny, R. A.; Di, L.; Kerns, E. H.; Diller, D. J.; Humblet, C. Insights for Predicting Blood-Brain Barrier Penetration of CNS Targeted Molecules Using QSPR Approaches. *J. Chem. Inf. Model.* **2010**, *50*, 1123–1133.

(120) Fogel, D. B. Factors associated with clinical trials that fail and opportunities for improving the likelihood of success: A review. *Contemp. Clin. Trials Commun.* **2018**, *11*, 156–164.

(121) Turcotte, E.; Wiens, L. W.; Grierson, J. R.; Peterson, L. M.; Wener, M. H.; Vesselle, H. Toxicology evaluation of radiotracer doses of 3′-deoxy-3′-[^{18}F]-fluorothymidine (^{18}F-FLT) for human PET imaging: Laboratory analysis of serial blood samples and comparison to previously investigated therapeutic FLT doses. *BMC Nucl. Med.* **2007**, *7*, 1–9.

(122) Cheng, H. C. The power issue: Determination of K_B or K_i from IC_{50}: A closer look at the Cheng–Prusoff equation, the Schild plot and related power equations. *J. Pharmacol. Toxicol. Methods* **2001**, *46*, 61–71.

(123) Kalantzi, K. I.; Tsoumani, M. E.; Goudevenos, I. A.; Tselepis, A. D. Pharmacodynamic properties of antiplatelet agents: current knowledge and future perspectives. *Expert Rev. Clin. Pharmacol.* **2012**, *5*, 319–336.

(124) Lonsdale, R.; Ward, R. A. Structure-based design of targeted covalent inhibitors. *Chem. Soc. Rev.* **2018**, *47*, 3816–3830.

(125) ChemDraw 23.1.1.3, 2024, Revvity Signals Software.

(126) Seelig, A. The role of size and charge for blood–brain barrier permeation of drugs and fatty acids. *J. Mol. Neurosci.* **2007**, *33*, 32–41.

(127) Paoletta, S.; Sabbadin, D.; Von Kügelgen, I.; Hinz, S.; Katritch, V.; Hoffmann, K.; Abdelrahman, A.; Straßburger, J.; Baqi, Y.; Zhao, Q., et al. Modeling ligand recognition at the $P2Y_{12}$ receptor in light of X-ray structural information. *J. Comput. Aided Mol. Des.* **2015**, *29*, 737–756.

(128) Parlow, J. J.; Burney, M. W.; Case, B. L.; Girard, T. J.; Hall, K. A.; Hiebsch, R. R.; Huff, R. M.; Lachance, R. M.; Mischke, D. A.; Rapp, S. R., et al. Piperazinyl-glutamate-pyrimidines as potent P2Y12 antagonists for inhibition of platelet aggregation. *Bioorg. Med. Chem. Lett.* **2009**, *19*, 6148–6156.

(129) Andersen, S. M.; Aurell, C.-J.; Zetterberg, F.; Bollmark, M.; Ehrl, R.; Schuisky, P.; Witt, A. Development of a Multi-Kilogram-Scale Synthesis of AZD1283: A Selective and Reversible Antagonist of the $P2Y_{12}$ Receptor. *Org. Process Res. Dev.* **2013**, *17*, 1543–1551.

(130) Bell, S. J.; McIntyre, S.; Garcia, C. F.; Kitson, S. L.; Therkelsen, F.; Andersen, S. M.; Zetterberg, F.; Aurell, C.-J.; Bollmark, M.; Ehrl, R. Development of an Efficient and Practical Route for the Multikilogram Manufacture of Ethyl 5-Cyano-2-methyl-6-oxo-1, 6-dihydropyridine-3-carboxylate and Ethyl

6-Chloro-5-cyano-2-methylnicotinate, Key Intermediates in the Preparation of P2Y12 Antagonists. *Org. Process Res. Dev.* **2012**, *16*, 819–823.

(131) Pan, X.; Wang, H.; Li, C.; Zhang, J. Z.; Ji, C. MolGpka: A Web Server for Small Molecule pK_a Prediction Using a Graph-Convolutional Neural Network. *J. Chem. Inf. Model.* **2021**, *61*, 3159–3165.

(132) Dyer, E.; Newborn Jr, G. E. Thermal Degradation of Carbamates of Methylene-bis-(4-phenyl Isocyanate). *J. Am. Chem. Soc.* **1958**, *80*, 5495–5498.

(133) Azad, S.; Kumamoto, K.; Uegaki, K.; Ichikawa, Y.; Kotsuki, H. A new practical method for the synthesis of unsymmetrical ureas via high-pressure-promoted condensation of 2, 2, 2-trichloroethyl carbamates (Troc-carbamates) with amines. *Tetrahedron Lett.* **2006**, *47*, 587–590.

(134) Dauvergne, J.; Wellington, K.; Chibale, K. Unprecedented observation of sulfonamides in the transesterification of N-unsubstituted carbamates with sulfonyl chlorides. *Tetrahedron Lett.* **2004**, *45*, 43–47.

(135) Caplow, M. Kinetics of Carbamate Formation and Breakdown. *J. Am. Chem. Soc.* **1968**, *90*, 6795–6803.

(136) Spyropoulos, C.; Kokotos, C. G. One-Pot Synthesis of Ureas from Boc-Protected Amines. *J. Org. Chem.* **2014**, *79*, 4477–4483.

(137) Banwell, M. G.; Bissett, B. D.; Busato, S.; Cowden, C. J.; Hockless, D. C.; Holman, J. W.; Read, R. W.; Wu, A. W. Trifluoromethanesulfonic anhydride–4-(N,N-dimethylamino)pyridine as a reagent combination for effecting Bischler--Napieraiski cyclisation under mild conditions: application to total syntheses of the Amaryllidaceae alkaloids N-methylcrinasiadine, anhydrolycorinone, hippadine and oxoassoanine. *J. Chem. Soc., Chem. Commun.* **1995**, 2551–2553.

(138) In, J.; Hwang, S.; Kim, C.; Seo, J. H.; Kim, S. Synthesis of 3, 4-Dihydroisoquinolin-1-ones from N-Boc-(β-Arylethyl) carbamates via Isocyanate Intermediates. *Eur. J. Org. Chem.* **2013**, *2013*, 965–971.

(139) Tashrifi, Z.; Mohammadi-Khanaposhtani, M.; Larijani, B.; Mahdavi, M. Triflic anhydride (Tf_2O): An efficient catalyst for electrophilic activation of amides. *ChemistrySelect* **2021**, *6*, 5320–5328.

(140) Gastaldi, S.; Weinreb, S. M.; Stien, D. Diiodosilane: A reagent for mild, efficient conversion of carbamates to ureas via isocyanates. *J. Org. Chem.* **2000**, *65*, 3239–3240.

(141) Linnell, R. Dissociation constants of 2-substituted pyridines. *J. Org. Chem.* **1960**, *25*, 290–290.

(142) Movassaghi, M.; Hill, M. D. A versatile cyclodehydration reaction for the synthesis of isoquinoline and β-carboline derivatives. *Org. Lett.* **2008**, *10*, 3485–3488.

(143) Lin, H.-S.; Paquette, L. A. A convenient method for determining the concentration of Grignard reagents. *Synth. Commun.* **1994**, *24*, 2503–2506.

(144) Matsubara, K.; Ishibashi, T.; Koga, Y. C- F Bond-Cleavage Reactions of Fluoroalkanes with Magnesium Reagents and without Metal Catalysts. *Org. Lett.* **2009**, *11*, 1765–1768.

(145) Toy, L.; Huber, M. E.; Lee, M.; Bartolomé, A. A.; Ortiz Zacarías, N. V.; Nasser, S.; Scholl, S.; Zlotos, D. P.; Mandour, Y. M.; Heitman, L. H., et al. Fluorophore-Labeled Pyrrolones Targeting the Intracellular Allosteric Binding Site of the Chemokine Receptor CCR1. *ACS Pharmacol. Transl. Sci.* **2024**.

(146) Breen, C. J.; Raverdeau, M.; Voorheis, H. P. Development of a quantitative fluorescence-based ligand-binding assay. *Sci. Rep.* **2016**, *6*, 25769.

(147) Yu, H.-B.; Li, M.; Wang, W.-P.; Wang, X.-L. High throughput screening technologies for ion channels. *Acta Pharmacol. Sin.* **2016**, *37*, 34–43.

(148) Parlow, J. J.; Burney, M. W.; Case, B. L.; Girard, T. J.; Hall, K. A.; Hiebsch, R. R.; Huff, R. M.; Lachance, R. M.; Mischke, D. A.; Rapp, S. R., et al. Piperazinyl-glutamate-pyridines as potent orally bioavailable P2Y12 antago-

nists for inhibition of platelet aggregation. *Bioorg. Med. Chem. Lett.* **2009**, *19*, 4657–4663.

(149) Parlow, J. J.; Burney, M. W.; Case, B. L.; Girard, T. J.; Hall, K. A.; Harris, P. K.; Hiebsch, R. R.; Huff, R. M.; Lachance, R. M.; Mischke, D. A., et al. Piperazinyl glutamate pyridines as potent orally bioavailable P2Y12 antagonists for inhibition of platelet aggregation. *J. Med. Chem.* **2010**, *53*, 2010–2037.

(150) Dhanoa, D.; Becker, O.; Noiman, S.; Reddy, S.; Cheruku, S.; Mele'ndez, R.; Sharadendu, A.; Chen, D.; Marantz, Y.; Shacham, S., et al. New piperidinyl-amino-thieno [2, 3-D] pyrimidine compounds, US Patent US20050222175A1, 2005.

(151) Zech, G.; Hessler, G.; Evers, A.; Weiss, T.; Florian, P.; Just, M.; Czech, J.; Czechtizky, W.; Görlitzer, J.; Ruf, S., et al. Identification of high-affinity P2Y12 antagonists based on a phenylpyrazole glutamic acid piperazine backbone. *J. Med. Chem.* **2012**, *55*, 8615–8629.

(152) Boldron, C.; Besse, A.; Bordes, M.-F.; Tissandié, S.; Yvon, X.; Gau, B.; Badorc, A.; Rousseaux, T.; Barré, G.; Meneyrol, J., et al. N-[6-(4-Butanoyl-5-methyl-1 H-pyrazol-1-yl) pyridazin-3-yl]-5-chloro-1-[2-(4-methylpiperazin-1-yl)-2-oxoethyl]-1 H-indole-3-carboxamide (SAR216471), a novel intravenous and oral, reversible, and directly acting P2Y12 antagonist. *J. Med. Chem.* **2014**, *57*, 7293–7316.

(153) Kirk, I. New Assay, International Patent WO2000033080A2, 1999.

(154) Kirk, I. P. Competition binding assay for detecting P2YADP receptor ligands, US Patent US6455322B1, 2002.

(155) Giordanetto, F.; Bach, P.; Zetterberg, F.; Antonsson, T.; Bylund, R.; Johansson, J.; Sellén, M.; Brown, D.; Hidestål, L.; Berntsson, P., et al. Optimization of ketone-based P2Y12 receptor antagonists as antithrombotic agents: Phar-

macodynamics and receptor kinetics considerations. *Bioorg. Med. Chem. Lett.* **2014**, *24*, 2963–2968.

(156) El-Tayeb, A.; Griessmeier, K. J.; Müller, C. E. Synthesis and preliminary evaluation of [^{3}H]PSB-0413, a selective antagonist radioligand for platelet P2Y12 receptors. *Bioorg. Med. Chem. Lett.* **2005**, *15*, 5450–5452.

(157) Dupuis, A.; Heim, V.; Ohlmann, P.; Gachet, C. In Vitro Binding of [^{3}H]PSB-0413 to $P2Y_{12}$ Receptors. *Curr. Protoc. Pharmacol.* **2015**, *71*, 1–35.

(158) Van Giezen, J.; Nilsson, L.; Berntsson, P.; Wissing, B.; Giordanetto, F.; Tomlinson, W.; Greasley, P. Ticagrelor binds to human P2Y12 independently from ADP but antagonizes ADP-induced receptor signaling and platelet aggregation. *J. Thromb. Haemost.* **2009**, *7*, 1556–1565.

(159) Zhou, S.; Fang, D.; Tan, S.; Lin, W.; Wu, W.; Zheng, K. Investigating the binding mechanism of novel 6-aminonicotinate-based antagonists with P2Y12 by 3D-QSAR, docking and molecular dynamics simulations. *J. Biomol. Struct. Dyn.* **2017**, *35*, 2938–2965.

(160) Ray, M.; Sayeed, A.; Ganshert, M.; Saha, A. Direct Binding Methods to Measure Receptor–Ligand Interactions. *J. Phys. Chem. B* **2023**, *128*, 3–19.

(161) Guo, S.; Zhao, T.; Yun, Y.; Xie, X. Recent progress in assays for GPCR drug discovery. *Am. J. Physiol. Cell Physiol.* **2022**, *323*, C583–C594.

(162) Soave, M.; Briddon, S. J.; Hill, S. J.; Stoddart, L. A. Fluorescent ligands: Bringing light to emerging GPCR paradigms. *Br. J. Pharmacol.* **2020**, *177*, 978–991.

(163) Xu, Y.; Piston, D. W.; Johnson, C. H. A bioluminescence resonance energy transfer (BRET) system: application to interacting circadian clock proteins. *Proc. Natl. Acad. Sci.* **1999**, *96*, 151–156.

(164) Sauvageau, E.; Lefrancois, S. A beginner's guide to bioluminescence resonance energy transfer (BRET). *Biochemist* **2019**, *41*, 36–40.

(165) Machleidt, T.; Woodroofe, C. C.; Schwinn, M. K.; Méndez, J.; Robers, M. B.; Zimmerman, K.; Otto, P.; Daniels, D. L.; Kirkland, T. A.; Wood, K. V. NanoBRET - A Novel BRET Platform for the Analysis of Protein–Protein Interactions. *ACS Chem. Biol.* **2015**, *10*, 1797–1804.

(166) Dale, N. C.; Johnstone, E. K.; White, C. W.; Pfleger, K. D. NanoBRET: the bright future of proximity-based assays. *Front. Bioeng. Biotechnol.* **2019**, *7*, 56.

(167) Stoddart, L. A.; Kilpatrick, L. E.; Hill, S. J. NanoBRET approaches to study ligand binding to GPCRs and RTKs. *Trends Pharmacol. Sci.* **2018**, *39*, 136–147.

(168) Graätz, L.; Müller, C.; Pegoli, A.; Schindler, L.; Bernhardt, G.; Littmann, T. Insertion of Nanoluc into the extracellular loops as a complementary method to establish BRET-based binding assays for GPCRs. *ACS Pharmacol. Transl. Sci.* **2022**, *5*, 1142–1155.

(169) Borroto-Escuela, D. O.; Flajolet, M.; Agnati, L. F.; Greengard, P.; Fuxe, K. Bioluminescence resonance energy transfer methods to study G protein-coupled receptor–receptor tyrosine kinase heteroreceptor complexes. *Methods Cell Biol.* **2013**, *117*, 141–164.

(170) Toy, L.; Huber, M. E.; Schmidt, M. F.; Weikert, D.; Schiedel, M. Fluorescent ligands targeting the intracellular allosteric binding site of the chemokine receptor CCR2. *ACS Chem. Biol.* **2022**, *17*, 2142–2152.

(171) Králová, J.; Jurášek, M.; Mikšátková, L.; Marešová, A.; Fähnrich, J.; Cihlářová, P.; Drašar, P.; Bartůněk, P.; Král, V. Influence of fluorophore and linker length on the localization and trafficking of fluorescent sterol probes. *Sci. Rep.* **2020**, *10*, 22053.

(172) Grätz, L.; Tropmann, K.; Bresinsky, M.; Müller, C.; Bernhardt, G.; Pockes, S. NanoBRET binding assay for histamine H2 receptor ligands using live recombinant HEK293T cells. *Sci. Rep.* **2020**, *10*, 13288.

(173) Höfelschweiger, B. K. The pyrylium dyes: a new class of biolabels. Synthesis, spectroscopy, and application as labels and in general protein assay, Ph.D. Thesis, University of Regensburg, 2005.

(174) Zhang, K.; Zhang, J.; Gao, Z.-G.; Zhang, D.; Zhu, L.; Han, G. W.; Moss, S. M.; Paoletta, S.; Kiselev, E.; Lu, W., et al. Structure of the human P2Y12 receptor in complex with an antithrombotic drug. *Nat.* **2014**, *509*, 115–118.

(175) Zhang, J.; Zhang, K.; Gao, Z.-G.; Paoletta, S.; Zhang, D.; Han, G. W.; Li, T.; Ma, L.; Zhang, W.; Müller, C. E., et al. Agonist-bound structure of the human P2Y12 receptor. *Nat.* **2014**, *509*, 119–122.

(176) Yu, W.-H.; Woessner, J. F. Heparan sulfate proteoglycans as extracellular docking molecules for matrilysin (matrix metalloproteinase 7). *J. Biol. Chem.* **2000**, *275*, 4183–4191.

(177) De Graaf, C.; Foata, N.; Engkvist, O.; Rognan, D. Molecular modeling of the second extracellular loop of G-protein coupled receptors and its implication on structure-based virtual screening. *Proteins: Structure, Function, and Bioinformatics* **2008**, *71*, 599–620.

(178) Caroff, E.; Hilpert, K.; Hubler, F.; Lehmann, D.; Meyer, E.; Renneberg, D. Thiazole derivatives and their use as P2Y12 receptor antagonists, US Patent US8664203B2, 2014.

(179) Gupta, M.; Sharma, R.; Kumar, A. Docking techniques in pharmacology: How much promising? *Comput. Biol. Chem.* **2018**, *76*, 210–217.

(180) Johnston, R. C.; Yao, K.; Kaplan, Z.; Chelliah, M.; Leswing, K.; Seekins, S.; Watts, S.; Calkins, D.; Chief Elk, J.; Jerome, S. V., et al. Epik: p K a and protonation state prediction through machine learning. *Journal of chemical theory and computation* **2023**, *19*, 2380–2388.

(181) Ma, J. C.; Dougherty, D. A. The cation-π interaction. *Chem. Rev.* **1997**, *97*, 1303–1324.

(182) Dougherty, D. A. The cation-π interaction. *Acc. Chem. Res.* **2013**, *46*, 885–893.

(183) Friesner, R. A.; Murphy, R. B.; Repasky, M. P.; Frye, L. L.; Greenwood, J. R.; Halgren, T. A.; Sanschagrin, P. C.; Mainz, D. T. Extra Precision Glide: Docking and Scoring Incorporating a Model of Hydrophobic Enclosure for Protein-Ligand Complexes. *J. Med. Chem.* **2006**, *49*, 6177–6196.

(184) Caroff, E.; Fretz, H.; Hilpert, K.; Houille, O.; Hubler, F.; Meyer, E. Pyrimidine derivatives and their use as P2Y12 receptor antagonists, US Patent US8048881B2, 2011.

(185) Bauer, W.; Winchester, W. R.; Schleyer, P. v. R. Monomeric organolithium compounds in tetrahydrofuran: tert-butyllithium, sec-butyllithium, supermesityllithium, mesityllithium, and phenyllithium. Carbon-lithium coupling constants and the nature of carbon-lithium bonding. *Organomet.* **1987**, *6*, 2371–2379.

(186) Lill, S. O. N., *Lithium compounds in organic synthesis: from fundamentals to applications*; John Wiley & Sons: 2014, pp 33–52.

(187) Cornwall, P.; Dell, C. P.; Knight, D. W. Regioselectivity in the lithiation of methyl-substituted thiazole-and oxazole-carboxylic acids and carboxamides: general methods for the elaboration of trisubstituted thiazoles and oxazoles. *J. Chem. Soc., Perkin Trans.* **1991**, 2417–2428.

(188) Li, Z.; Ma, L.; Tang, C.; Xu, J.; Wu, X.; Yao, H. Palladium (II)-catalyzed oxidative Heck coupling of thiazole-4-carboxylates. *Tetrahedron Lett.* **2011**, *52*, 5643–5647.

(189) Jeffery, T. Heck-type reactions in water. *Tetrahedron Lett.* **1994**, *35*, 3051–3054.

(190) Jeffery, T. On the efficiency of tetraalkylammonium salts in Heck type reactions. *Tetrahedron* **1996**, *52*, 10113–10130.

(191) Liu, L.; Tan, C.; Fan, R.; Wang, Z.; Du, H.; Xu, K.; Tan, J. I 2/TBHP-Mediated tandem cyclization and oxidation reaction: Facile access to 2-substituted thiazoles and benzothiazoles. *Org. Biomol. Chem.* **2019**, *17*, 252–256.

(192) Pramanick, P. K.; Hou, Z.-L.; Yao, B. Mechanistic study on iodine-catalyzed aromatic bromination of aryl ethers by N-bromosuccinimide. *Tetrahedron* **2017**, *73*, 7105–7114.

(193) Murray, P. M.; Bower, J. F.; Cox, D. K.; Galbraith, E. K.; Parker, J. S.; Sweeney, J. B. A robust first-pass protocol for the Heck–Mizoroki reaction. *Org. Process Res. Dev.* **2013**, *17*, 397–405.

(194) Blakemore, D. C.; Doyle, P. M.; Fobian, Y. M., *Synthetic Methods in Drug Discovery: Volume 1*; Royal Society of Chemistry: 2016, pp 143–169.

(195) Haynes, R. K.; Holden, M. Formation of iodides and esters from alcohols and tributyldiiodophosphorane and diiodotriphenylphosphorane. *Aust. J. Chem.* **1982**, *35*, 517–524.

(196) Coe, B. J.; Fielden, J.; Foxon, S. P.; Harris, J. A.; Helliwell, M.; Brunschwig, B. S.; Asselberghs, I.; Clays, K.; Garın, J.; Orduna, J. Diquat derivatives: highly active, two-dimensional nonlinear optical chromophores with potential redox switchability. *J. Am. Chem. Soc.* **2010**, *132*, 10498–10512.

(197) Fili, N.; Toseland, C. P., *Fluorescence and labelling: how to choose and what to do*; Springer: 2014, pp 1–24.

(198) Holmes, K. L.; Lantz, L. M. Protein labeling with fluorescent probes. *Methods Cell Biol.* **2001**, *63*, 185–204.

(199) Brunet, A.; Aslam, T.; Bradley, M. Separating the isomers—Efficient synthesis of the N-hydroxysuccinimide esters of 5 and 6-carboxyfluorescein diacetate and 5 and 6-carboxyrhodamine B. *Bioorg. Med. Chem. Lett.* **2014**, *24*, 3186–3188.

(200) Lyttle, M. H.; Carter, T. G.; Dick, D. J.; Cook, R. M. A tetramethyl rhodamine (Tamra) phosphoramidite facilitates solid-phase-supported synthesis of 5‘-Tamra DNA. *J. Org. Chem.* **2000**, *65*, 9033–9038.

(201) Dong, M. W., *HPLC and UHPLC for Practicing Scientists*; John Wiley & Sons: 2019, pp 199–219.

(202) Quest Graph™ Spectrum [TAMRA (Carboxytetramethylrhodamine)]. AAT Bioquest Inc. https://www.aatbio.com/fluorescence-excitation-emission-spectrum-graph-viewer/tamra$_c$*arboxytetramethylrhodamine*.[*Accessed* : 23*April*2025].

(203) Stéen, J.; Tousiaki, E.-N.; Kingston, L.; van der Wildt, B.; Lenart, N.; Beaino, W.; Verlaan, M.; Zarzycka, B.; Zinnhardt, B.; Denes, A., et al. Characterization of [^{3}H]AZ12464237 as a high affinity, non-nucleotide antagonist radioligand for the P2Y12 receptor. *bioRxiv* **2024**, 2024–10.

(204) Hopkins, A. L.; Keserü, G. M.; Leeson, P. D.; Rees, D. C.; Reynolds, C. H. The role of ligand efficiency metrics in drug discovery. *Nat. Rev. Drug Discov.* **2014**, *13*, 105–121.

(205) Scapecchi, S.; Martini, E.; Manetti, D.; Ghelardini, C.; Martelli, C.; Dei, S.; Galeotti, N.; Guandalini, L.; Romanelli, M. N.; Teodori, E. Structure–activity relationship studies on unifiram (DM232) and sunifiram (DM235), two novel and potent cognition enhancing drugs. *Bioorg. Med. Chem.* **2004**, *12*, 71–85.

(206) Cai, G.; Bozhkova, N.; Odingo, J.; Berova, N.; Nakanishi, K. Circular dichroism exciton chirality method. New red-shifted chromophores for hydroxyl groups. *J. Am. Chem. Soc.* **1993**, *115*, 7192–7198.

(207) Wang, H.; Lu, Z.; Lord, S. J.; Willets, K. A.; Bertke, J. A.; Bunge, S. D.; Moerner, W.; Twieg, R. J. The influence of tetrahydroquinoline rings in dicyanomethylenedihydrofuran (DCDHF) single-molecule fluorophores. *Tetrahedron* **2007**, *63*, 103–114.

(208) Greulich, T. W.; Daniliuc, C. G.; Studer, A. N-aminopyridinium salts as precursors for N-centered radicals–direct amidation of arenes and heteroarenes. *Org. Lett.* **2015**, *17*, 254–257.

Chapter 7

Appendix:

Selected tables

Compound	GlideXP
60	-9.9
82a	-8.8
82b	-7.7
82c	-8.0
61	-8.9
83a	-7.9
83b	-8.6
83c	-$^{\alpha}$

Appendix 1: Top GlideXP scores from truncated NanoBRET probe docking studies. $^{\alpha}$ No binding pose was identified that reflects the ligand pose expected from the crystal structure (4NTJ) by visual inspection.

Compound	GlideXP
67	-6.8
68	-$^{\alpha}$
69	-$^{\alpha}$
70	-7.9
71	-$^{\alpha}$
62	-$^{\alpha}$
63	-$^{\alpha}$
64	-$^{\alpha}$
65	-5.6
66	-$^{\alpha}$

Appendix 2: Top GlideXP scores from propanamide fluorescent probe series docking. $^{\alpha}$ No binding pose was identified that reflects the ligand pose expected from the crystal structure (4NTJ) by visual inspection.

Compound	GlideXP
77	-7.7
78	-$^{\alpha}$
79	-$^{\alpha}$
80	-$^{\alpha}$
81	-$^{\alpha}$
72	-$^{\alpha}$
73	-$^{\alpha}$
74	-$^{\alpha}$
75	-$^{\alpha}$
76	-$^{\alpha}$

Appendix 3: Top GlideXP scores from propenamide series probe docking studies. $^{\alpha}$ No binding pose was identified that reflects the ligand pose expected from the crystal structure (4NTJ) by visual inspection.

Entry	1-Butanol	CDI	Yield (%)
1	1	1.1	65
2	2	1	62
3	1	1	83

Appendix 4: Optimisation of the imidazole carbamate reaction in **Scheme 20** by varying the equivalence. Entries 1 and 2 were concentrated under rotovap, potentially contributing to the lower yields.

Excitation/Emission	Compound	Concentration (µM)	Slit width (nm)
Excitation	**72**	67	-
	73	33	-
	75	33	-
Emission	**72**	100	0.9
	73	100	1
	75	100	0.9

Appendix 5: Experimental conditions for the excitation and emission spectra of TAMRA probes **72**, **73** and **75**. Compound stock solutions (10 mM) were prepared in DMSO and subsequently diluted in MeOH to the desired concentrations. Slit width was optimised based on solution intensity to achieve maximal signal detection. All measurements were conducted using a 10 mm pathlength quartz cuvette.

Selected NMR and MS spectra

(31) Ethyl 5-cyano-2-methyl-6-oxo-1,6-dihydropyridine-3-carboxylate

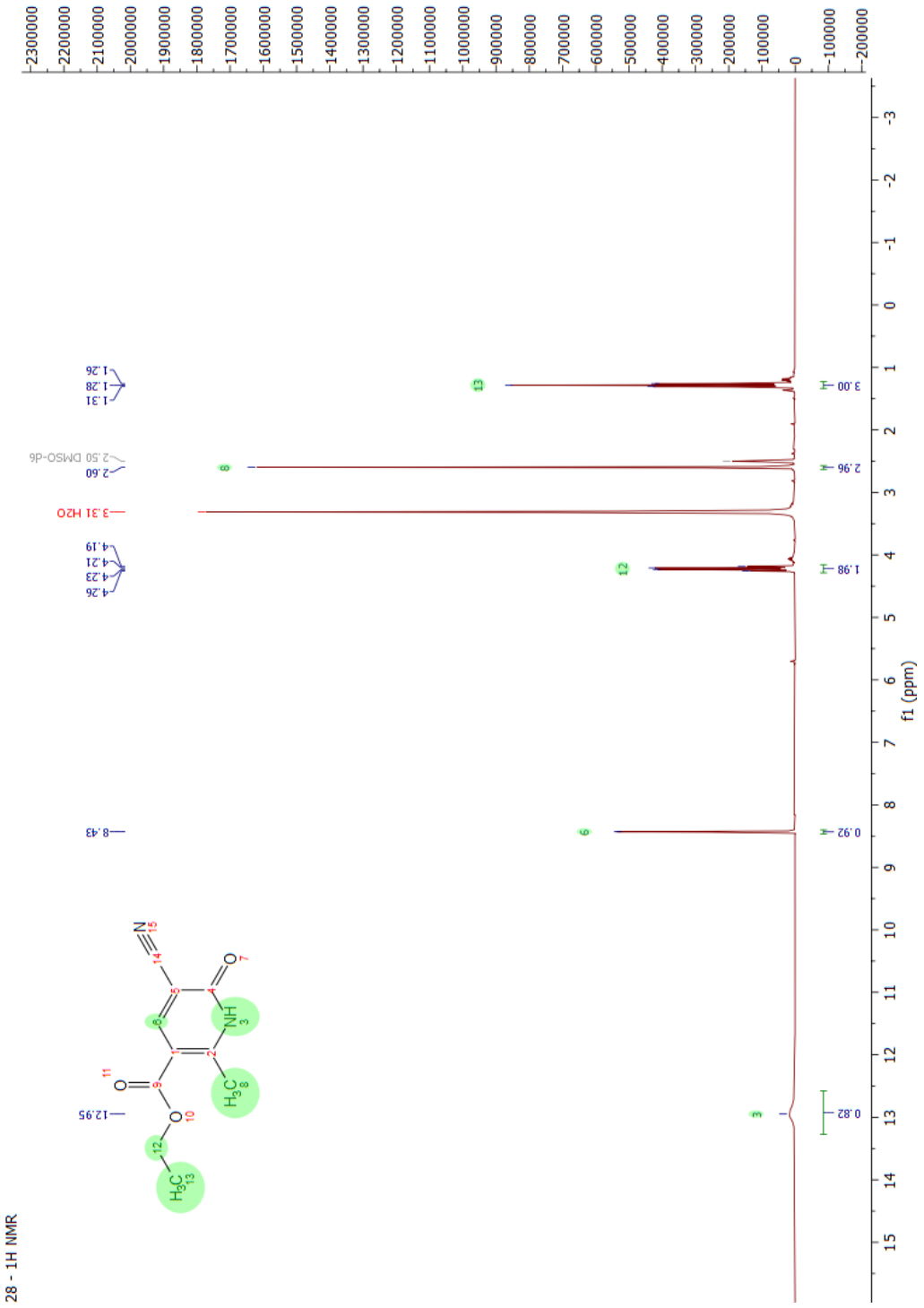

Appendix 6: (**31**) Ethyl 5-cyano-2-methyl-6-oxo-1,6-dihydropyridine-3-carboxylate ^{1}H NMR spectrum.

(27) Ethyl 6-chloro-5-cyano-2-methylnicotinate

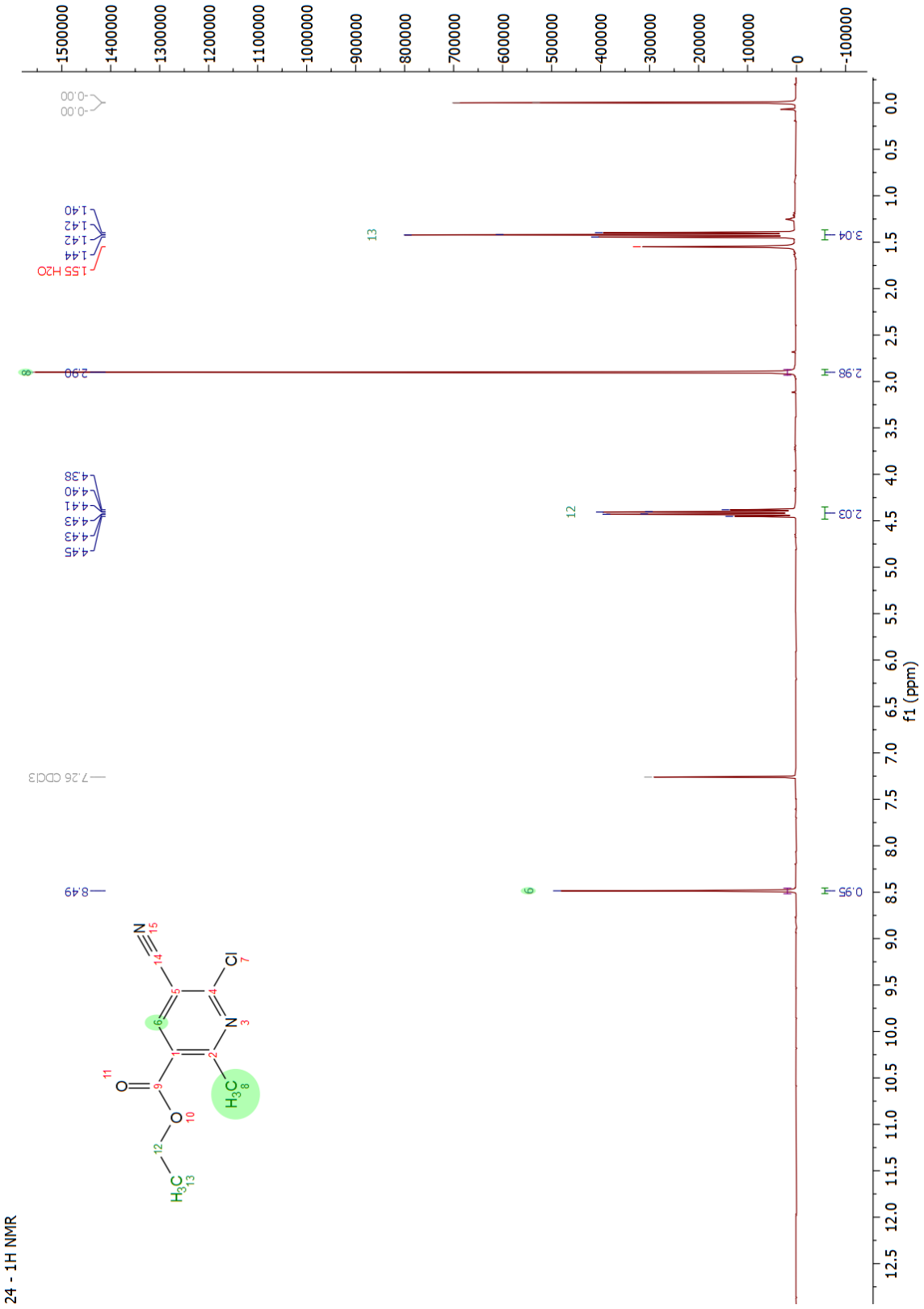

Appendix 7: (**27**) Ethyl 6-chloro-5-cyano-2-methylnicotinate ^{1}H NMR spectrum.

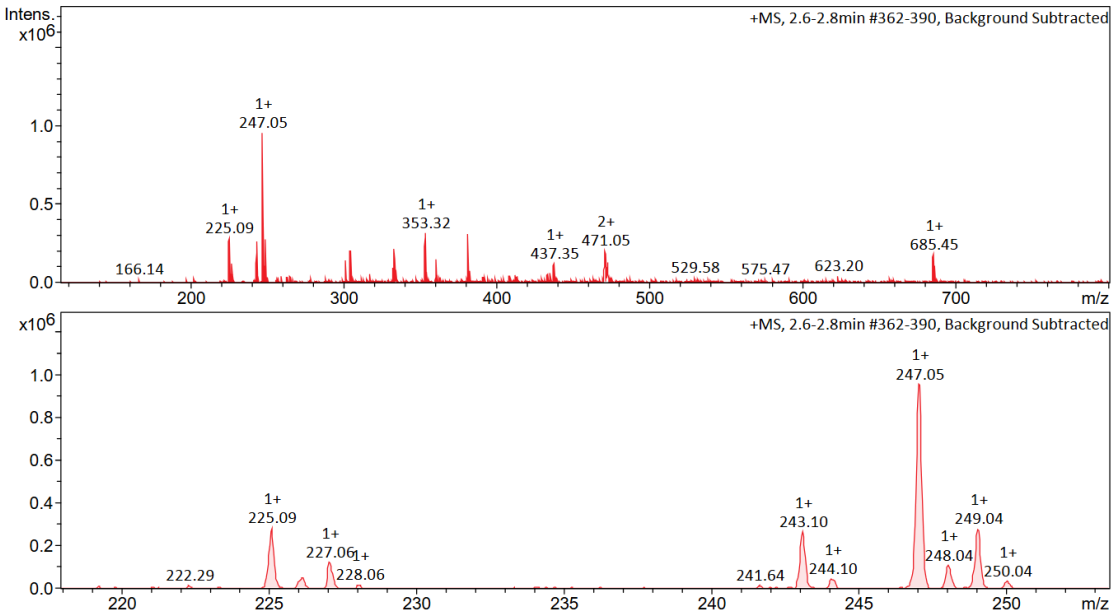

Appendix 8: (**27**) Ethyl 6-chloro-5-cyano-2-methylnicotinate MS spectrum.

(35) 6-(3-(3-((5-Chlorothiophen-2-yl)sulfonyl)ureido)azetidin-1-yl)-5-cyano-*N*-methoxy-*N*,2-dimethylnicotinamide

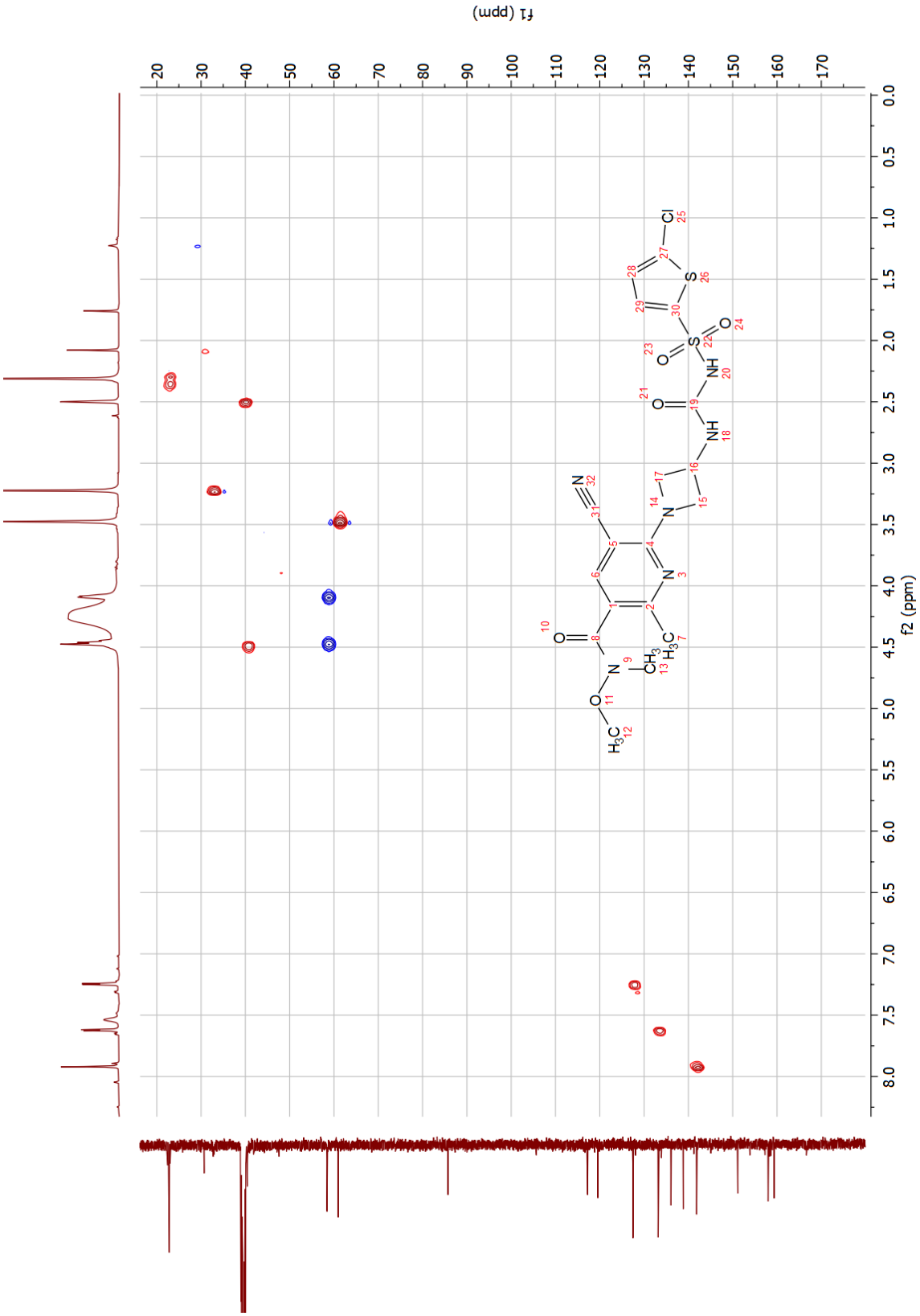

Appendix 9: (**35**) 6-(3-(3-((5-Chlorothiophen-2-yl)sulfonyl)ureido)azetidin-1-yl)-5-cyano-*N*-methoxy-*N*,2-dimethylnicotinamide HSQC.

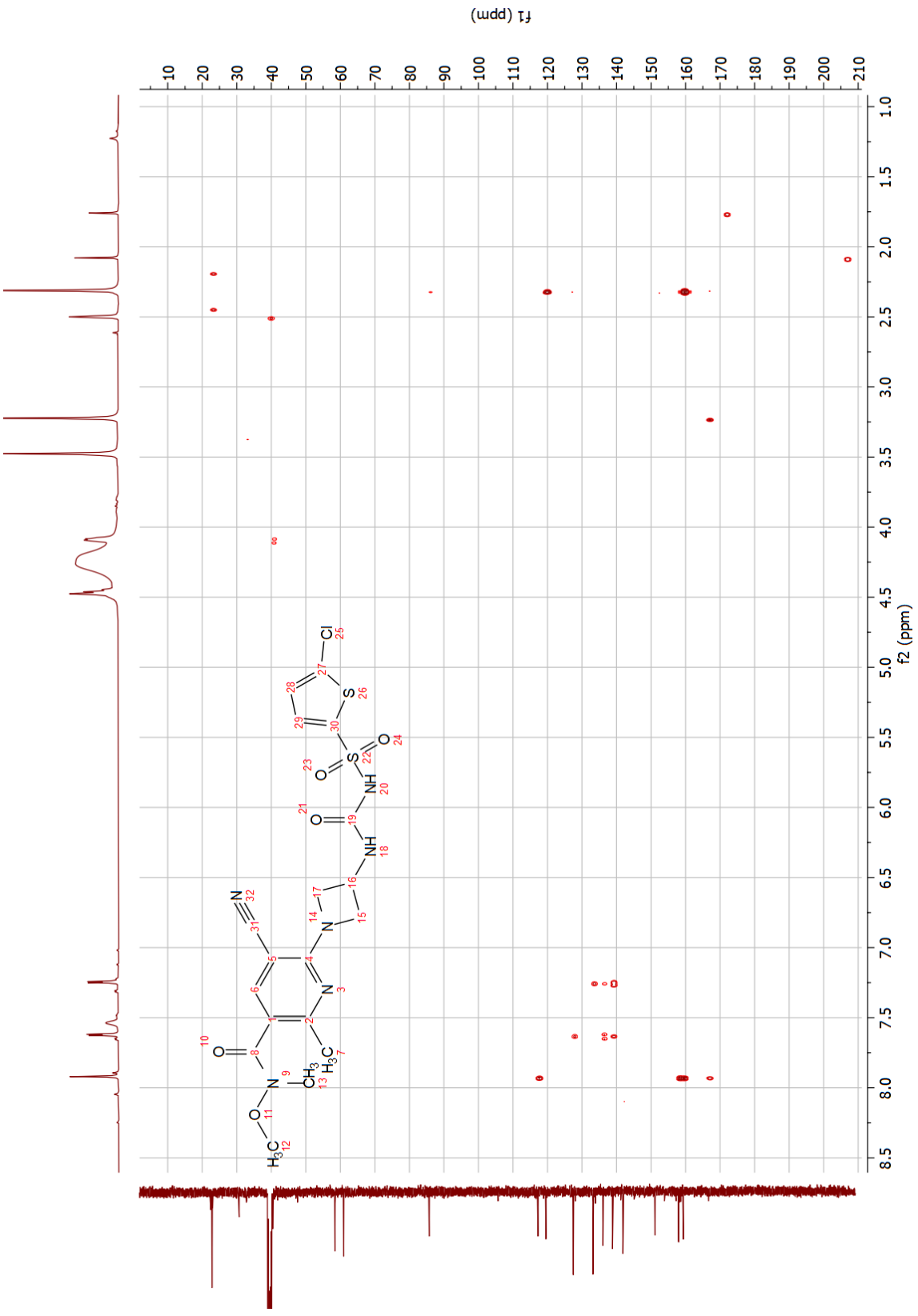

Appendix 10: (**35**) 6-(3-(3-((5-Chlorothiophen-2-yl)sulfonyl)ureido)azetidin-1-yl)-5-cyano-*N*-methoxy-*N*,2-dimethylnicotinamide HMBC.

(97) Ethyl 2-phenylthiazole-4-carboxylate

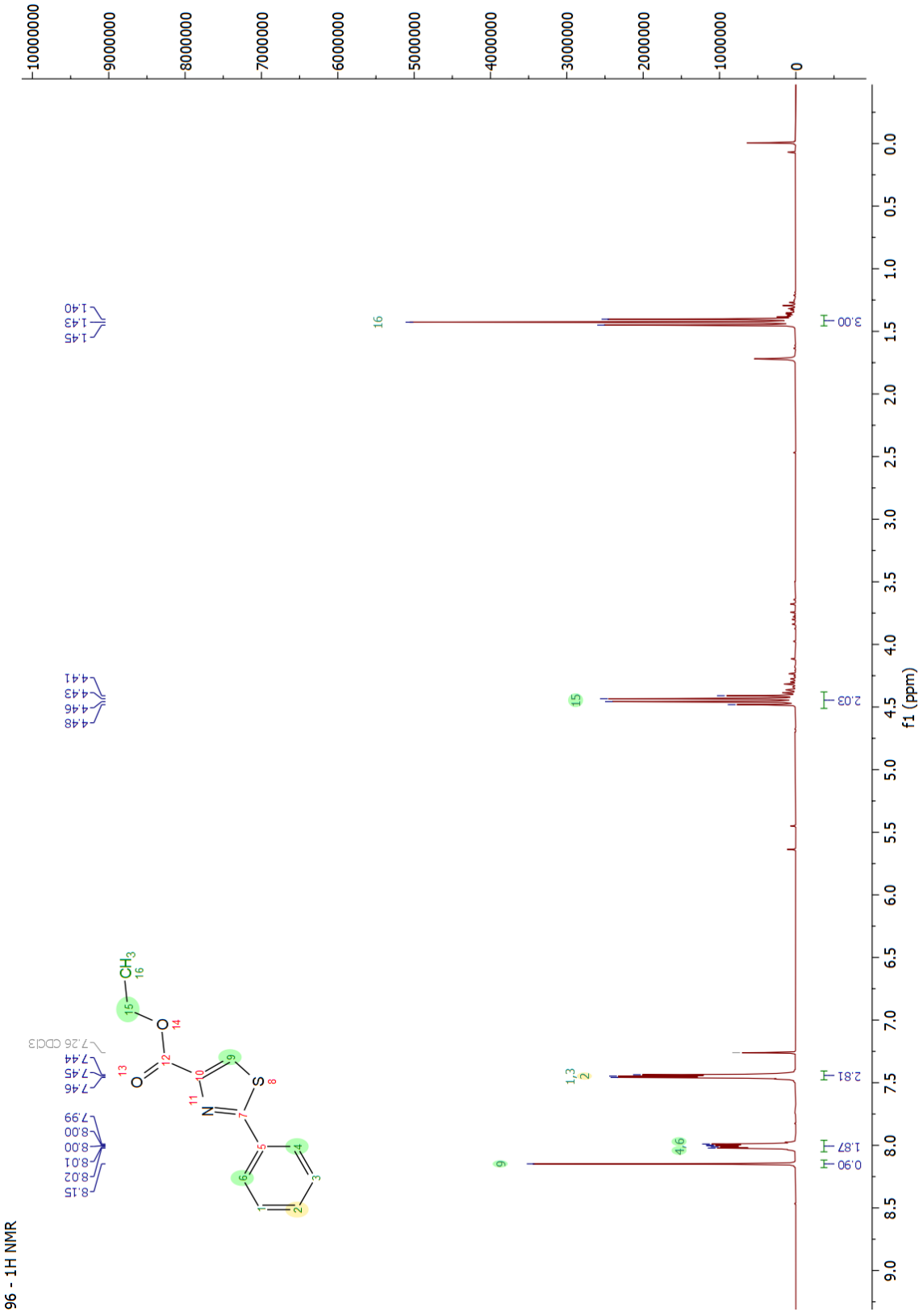

Appendix 11: (**97**) Ethyl 2-phenylthiazole-4-carboxylate ^{1}H NMR spectrum.

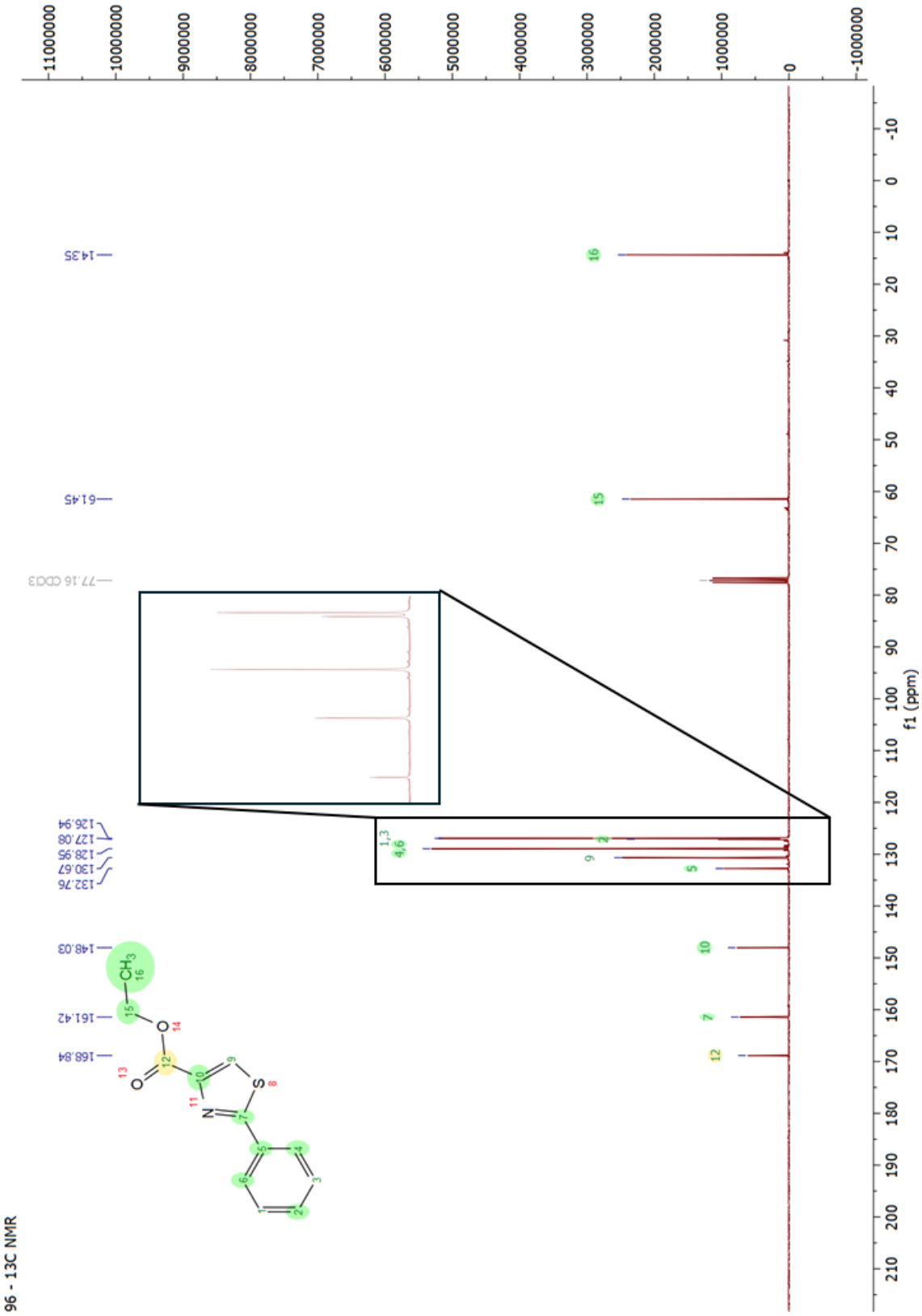

Appendix 12: (**97**) Ethyl 2-phenylthiazole-4-carboxylate ^{13}C NMR spectrum.

(139) Dibutyl 4,4′-(2,2′-((2,2′-diphenyl-[5,5′-bithiazole]-4,4′-dicarbonyl)bis(azanediyl))bis(acetyl))bis(piperazine-1-carboxylate)

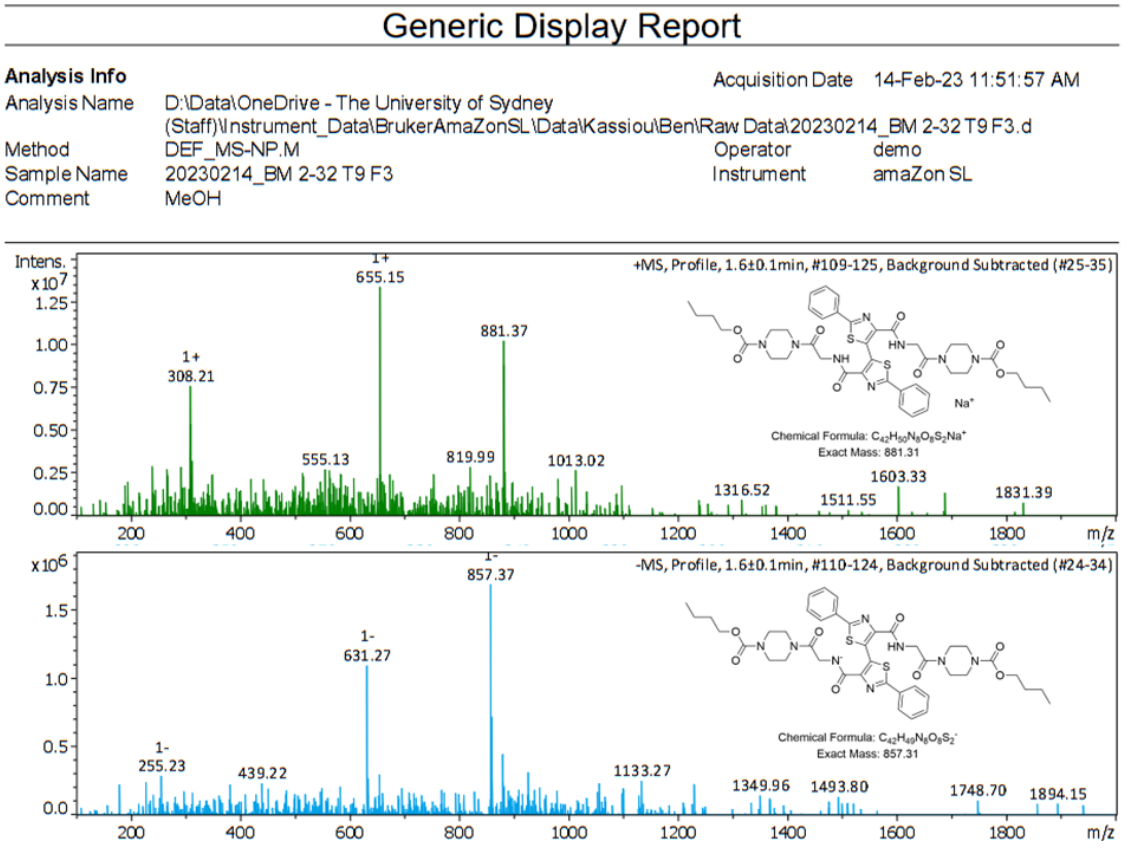

Appendix 13: (**139**) Dibutyl 4,4′-(2,2′-((2,2′-diphenyl-[5,5′-bithiazole]-4,4′-dicarbonyl)bis(azanediyl))bis(acetyl))bis(piperazine-1-carboxylate) MS spectra.

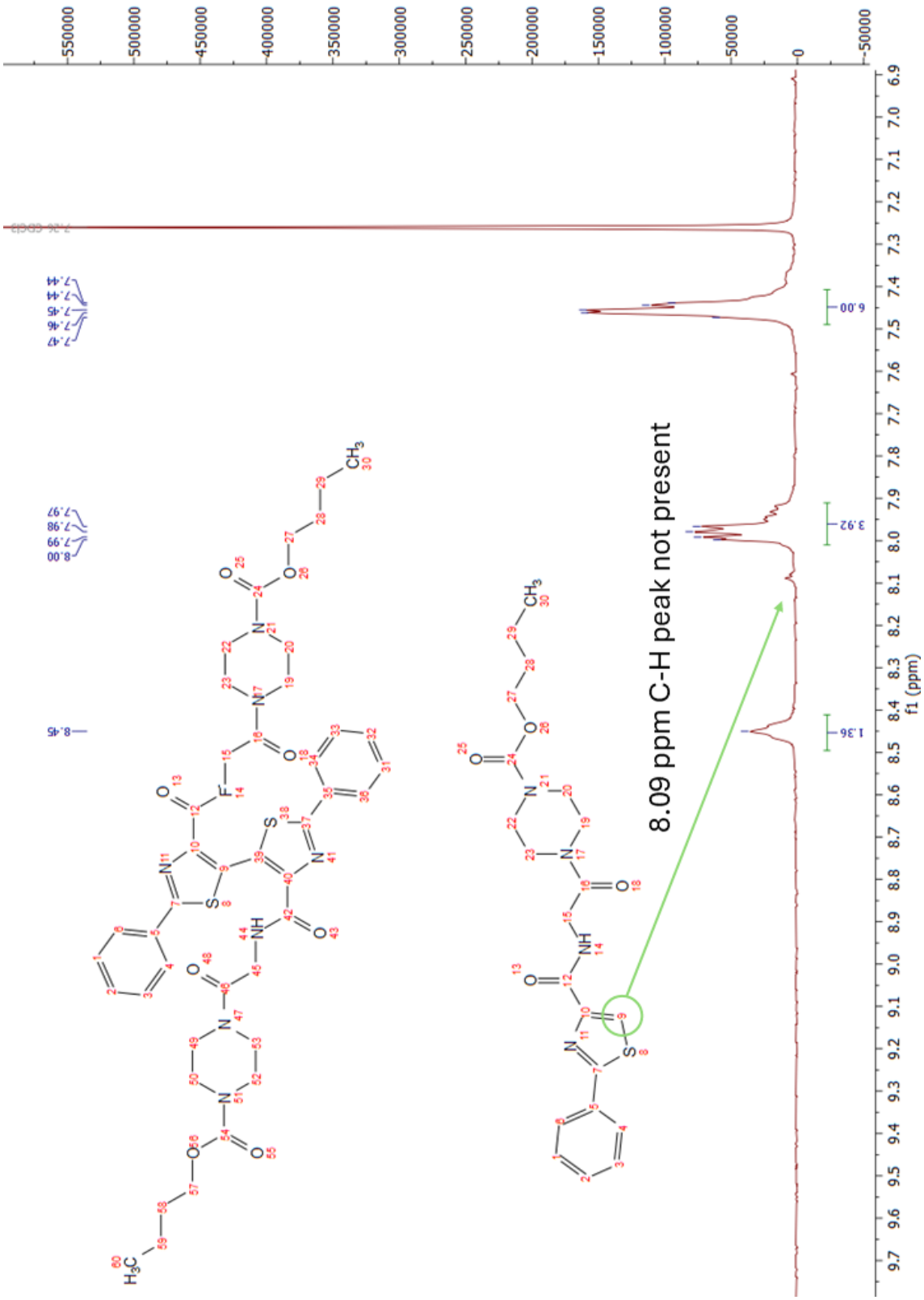

Appendix 14: (**139**) Dibutyl 4,4′-(2,2′-((2,2′-diphenyl-[5,5′-bithiazole]-4,4′-dicarbonyl)bis(azanediyl))bis(acetyl))bis(piperazine-1-carboxylate) ^{1}H NMR spectrum.

(141) Ethyl 5-bromo-2-(4-bromophenyl)thiazole-4-carboxylate-ethyl 5-bromo-2-(4-bromophenyl)thiazole-4-carboxylate

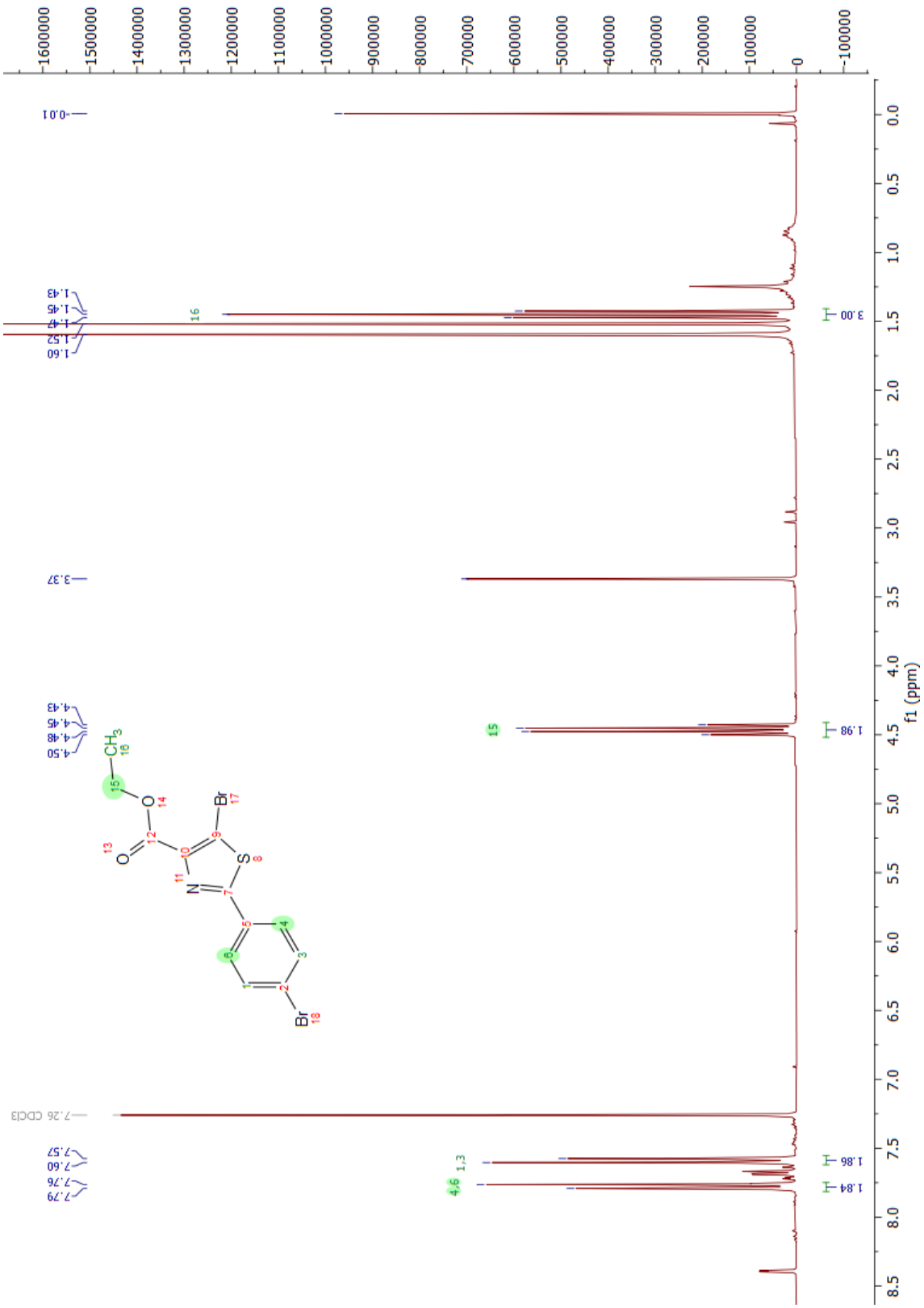

Appendix 15: (**141**) Ethyl 5-bromo-2-(4-bromophenyl)thiazole-4-carboxylateethyl 5-bromo-2-(4-bromophenyl)thiazole-4-carboxylate ^{1}H NMR spectrum.

(72) (*E*)-9-(4-((2-(3-(4-((2-(4-(butoxycarbonyl)piperazin-1-yl)-2-oxoethyl)carbamoyl)-2-phenylthiazol-5-yl)acrylamido)ethyl)-carbamoyl)-2-carboxyphenyl)-3,6-bis(dimethylamino)xanthylium

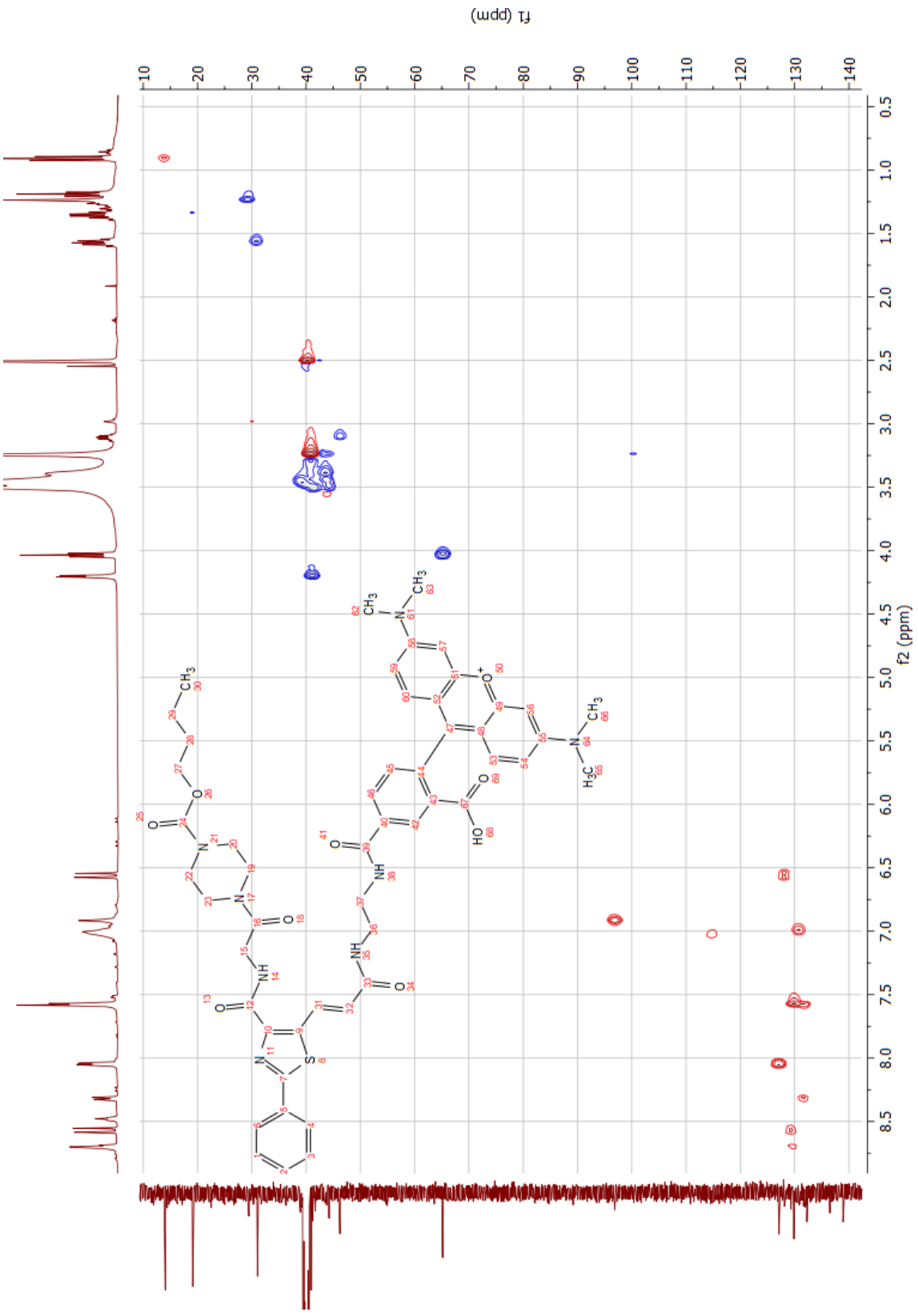

Appendix 16: (**72**) (*E*)-9-(4-((2-(3-(4-((2-(4-(butoxycarbonyl)piperazin-1-yl)-2-oxoethyl)carbamoyl)-2-phenylthiazol-5-yl)acrylamido)ethyl)carbamoyl)-2-carboxyphenyl)-3,6-bis(dimethylamino)xanthylium HSQC.

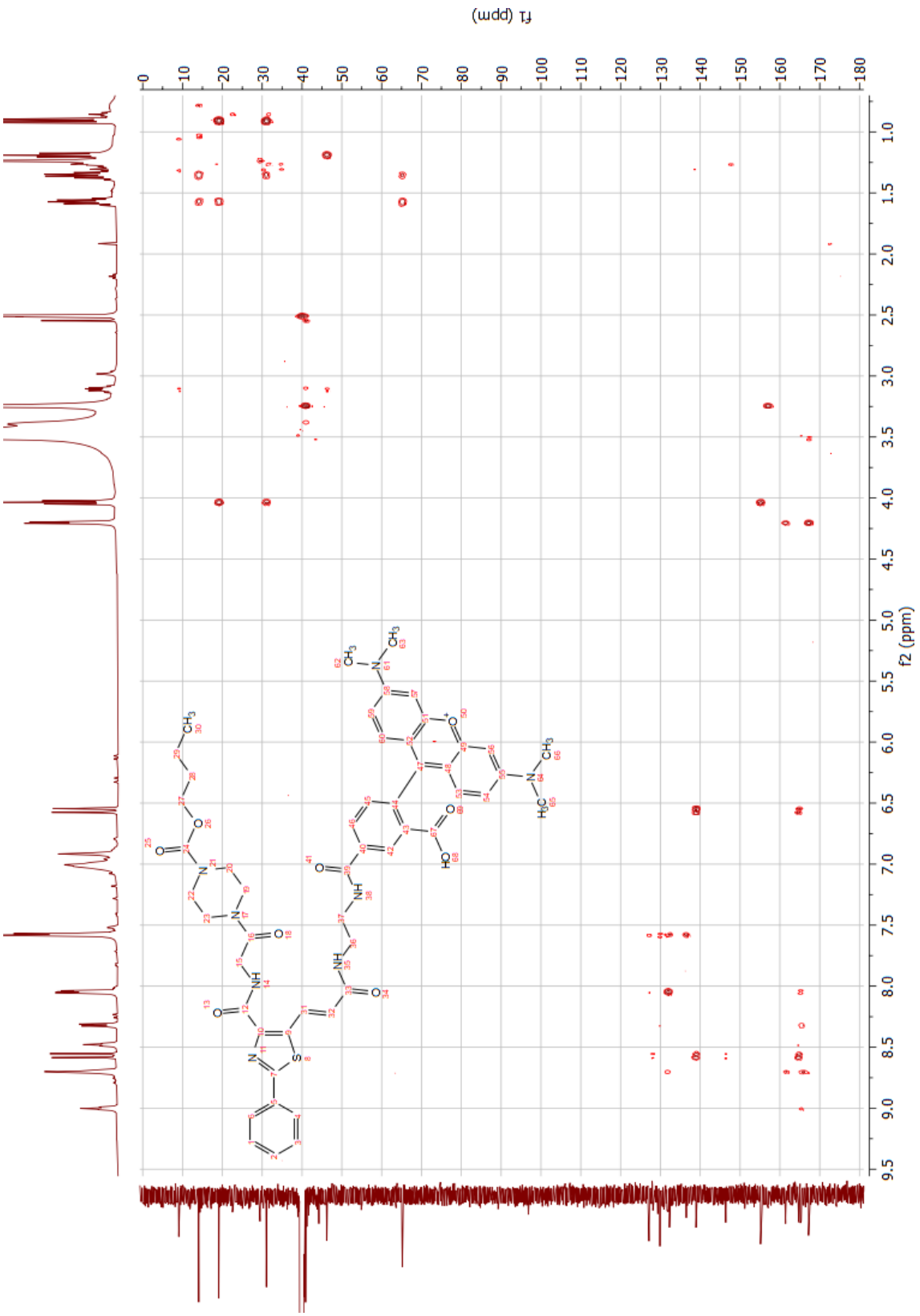

Appendix 17: (**72**) (*E*)-9-(4-((2-(3-(4-((2-(4-(butoxycarbonyl)piperazin-1-yl)-2-oxoethyl)carbamoyl)-2-phenylthiazol-5-yl)acrylamido)ethyl)carbamoyl)-2-carboxyphenyl)-3,6-bis(dimethylamino)xanthylium HMBC.

(73) (*E*)-9-(4-((3-(3-(4-((2-(4-(butoxycarbonyl)piperazin-1-yl)-2-oxoethyl)carbamoyl)-2-phenylthiazol-5-yl)acrylamido)propyl)-carbamoyl)-2-carboxyphenyl)-3,6-bis(dimethylamino)xanthylium

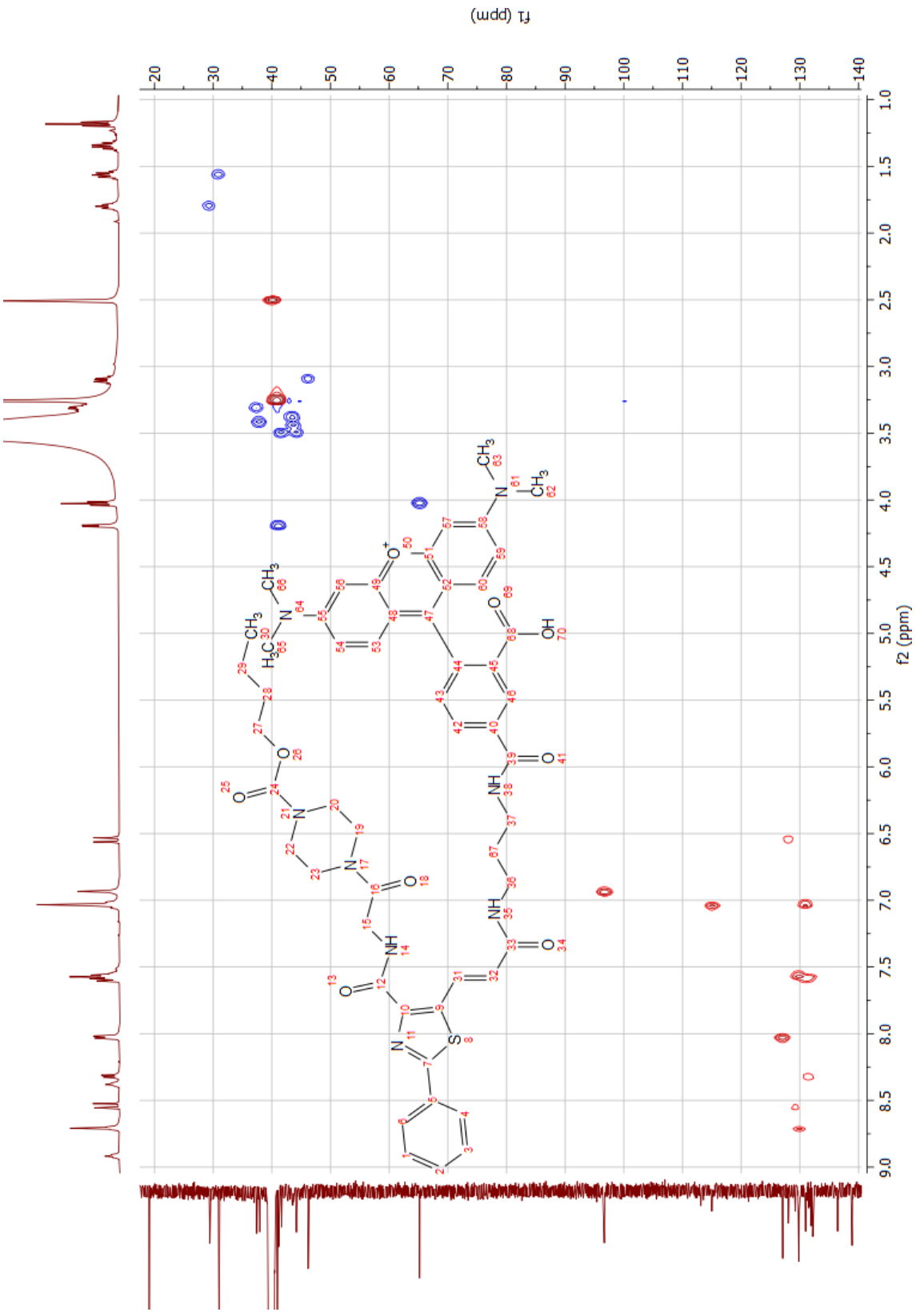

Appendix 18: (**73**) (*E*)-9-(4-((3-(3-(4-((2-(4-(butoxycarbonyl)piperazin-1-yl)-2-oxoethyl)carbamoyl)-2-phenylthiazol-5-yl)acrylamido)propyl)carbamoyl)-2-carboxyphenyl)-3,6-bis(dimethylamino)xanthylium HSQC.

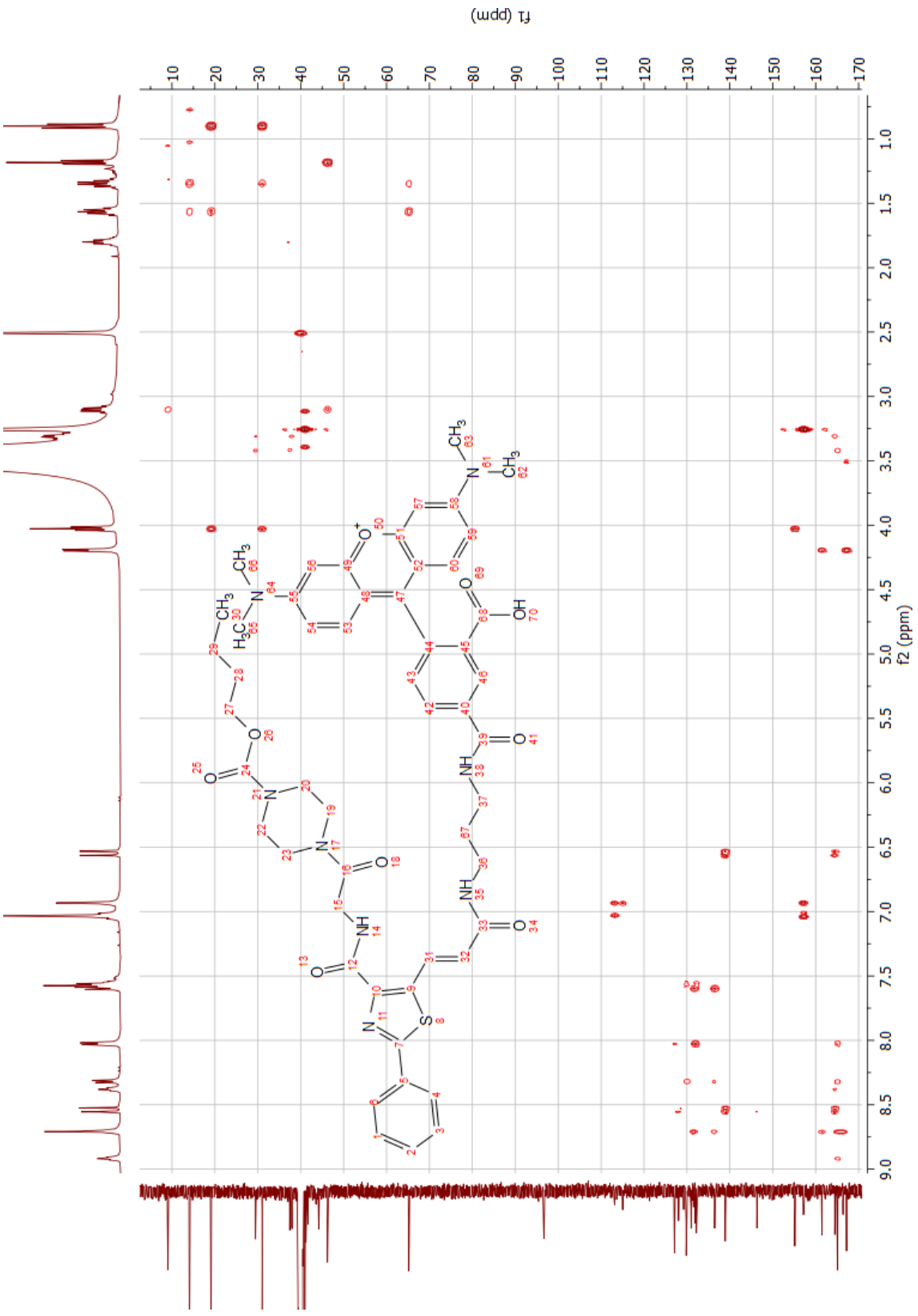

Appendix 19: (**73**) (*E*)-9-(4-((3-(3-(4-((2-(4-(butoxycarbonyl)piperazin-1-yl)-2-oxoethyl)carbamoyl)-2-phenylthiazol-5-yl)acrylamido)propyl)carbamoyl)-2-carboxyphenyl)-3,6-bis(dimethylamino)xanthylium HMBC.

(75) (*E*)-9-(4-((2-(2-(3-(4-((2-(4-(butoxycarbonyl)piperazin-1-yl)-2-oxoethyl)carbamoyl)-2-phenylthiazol-5-yl)acrylamido)ethoxy)-ethyl)carbamoyl)-2-carboxyphenyl)-3,6-bis(dimethylamino)xanthylium

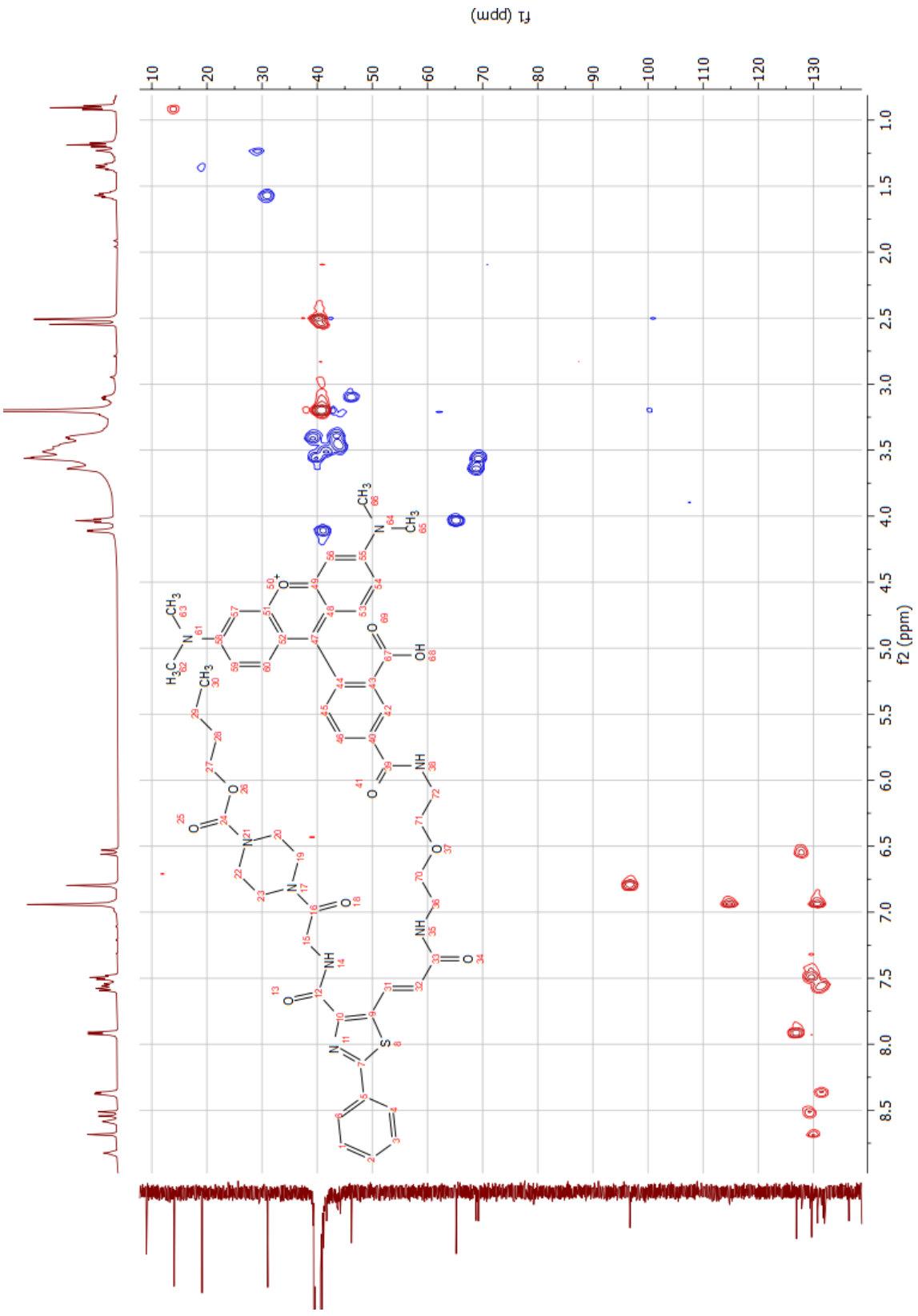

Appendix 20: (**75**) (*E*)-9-(4-((2-(2-(3-(4-((2-(4-(butoxycarbonyl)piperazin-1-yl)-2-oxoethyl)carbamoyl)-2-phenylthiazol-5-yl)acrylamido)ethoxy)ethyl)carbamoyl)-2-carboxyphenyl)-3,6-bis(dimethylamino)xanthylium HSQC.

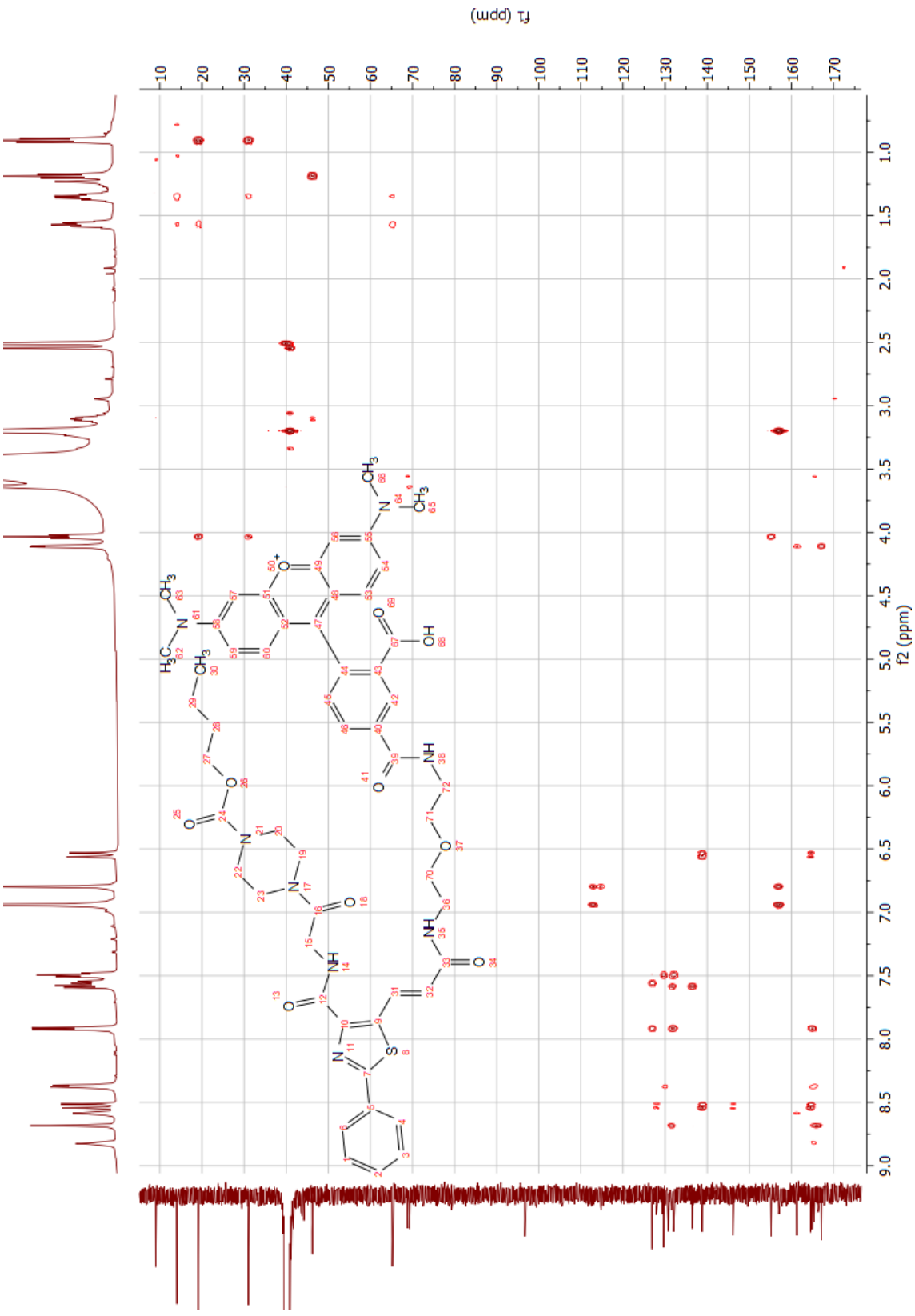

Appendix 21: (**75**) (*E*)-9-(4-((2-(2-(3-(4-((2-(4-(butoxycarbonyl)piperazin-1-yl)-2-oxoethyl)carbamoyl)-2-phenylthiazol-5-yl)acrylamido)ethoxy)ethyl)carbamoyl)-2-carboxyphenyl)-3,6-bis(dimethylamino)xanthylium HMBC.

(173) 9-(4-((2-((*Tert*-butoxycarbonyl)amino)ethyl)carbamoyl)-2-carboxyphenyl)-3,6-bis(dimethylamino)xanthylium

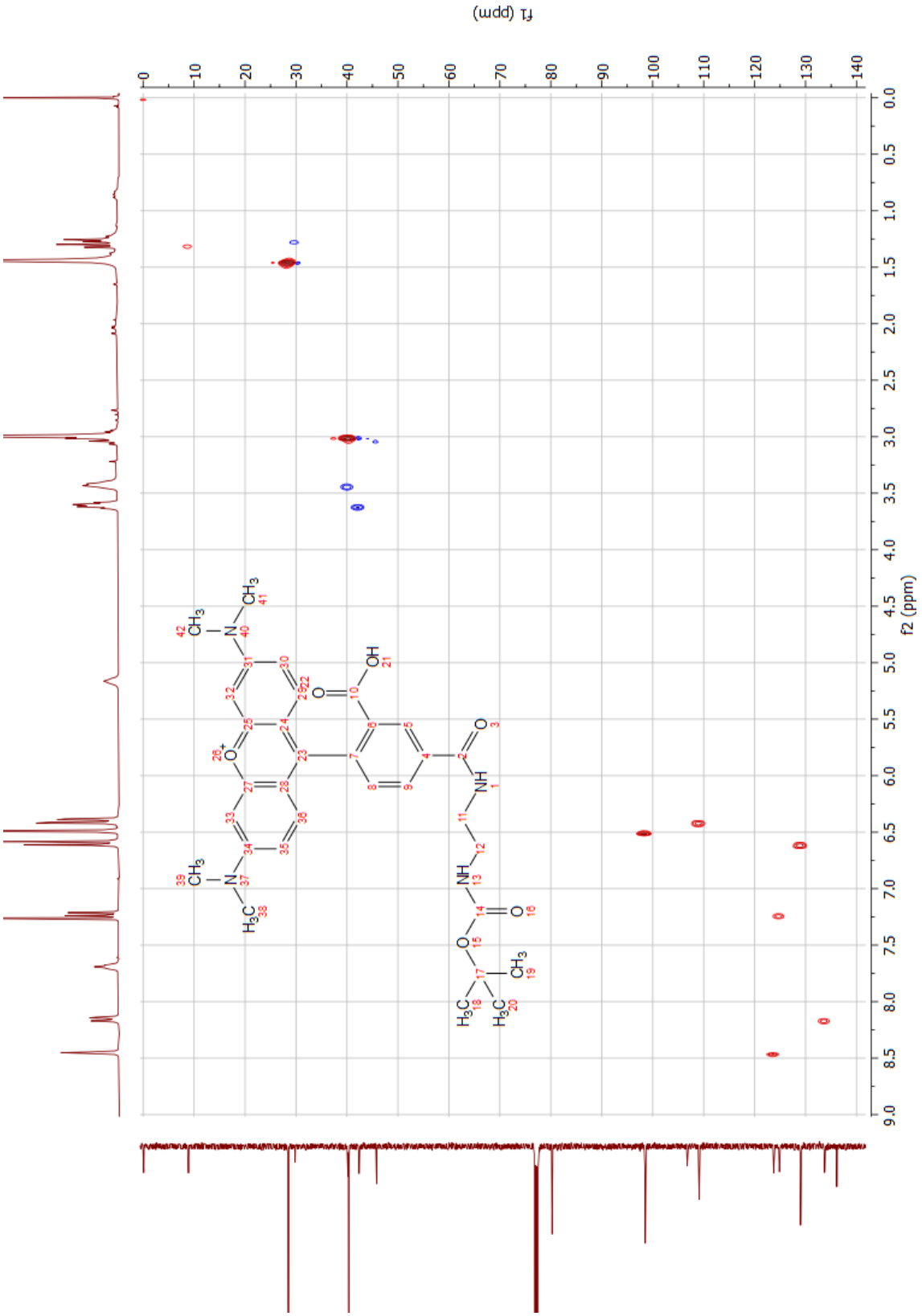

Appendix 22: (**173**) 9-(4-((2-((*Tert*-butoxycarbonyl)amino)ethyl)carbamoyl)-2-carboxyphenyl)-3,6-bis(dimethylamino)xanthylium HSQC.

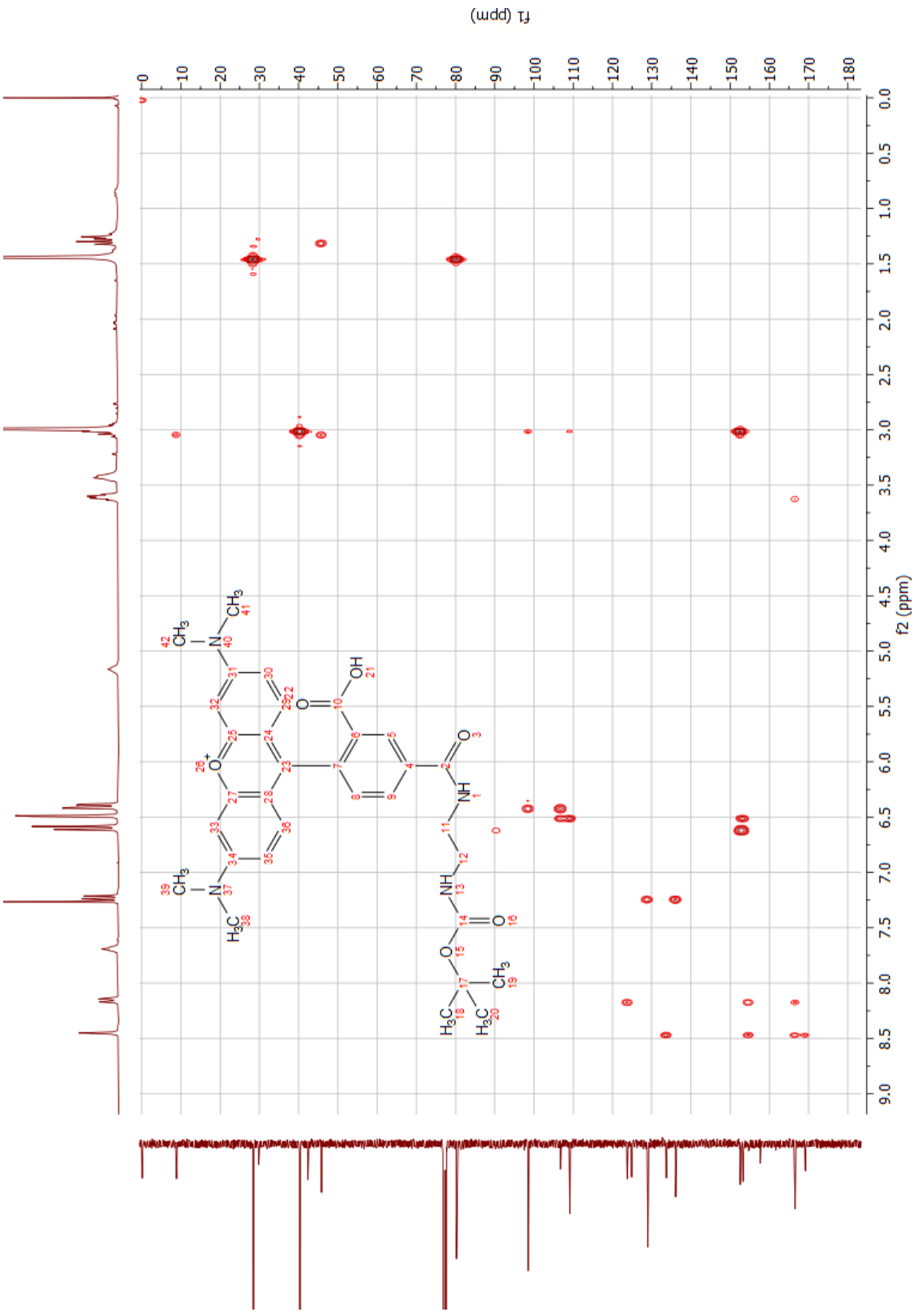

Appendix 23: (**173**) 9-(4-((2-((*Tert*-butoxycarbonyl)amino)ethyl)carbamoyl)-2-carboxyphenyl)-3,6-bis(dimethylamino)xanthylium HMBC.

(174) 9-(4-((2-((*Tert*-butoxycarbonyl)amino)propyl)carbamoyl)-2-carboxyphenyl)-3,6-bis(dimethylamino)xanthylium

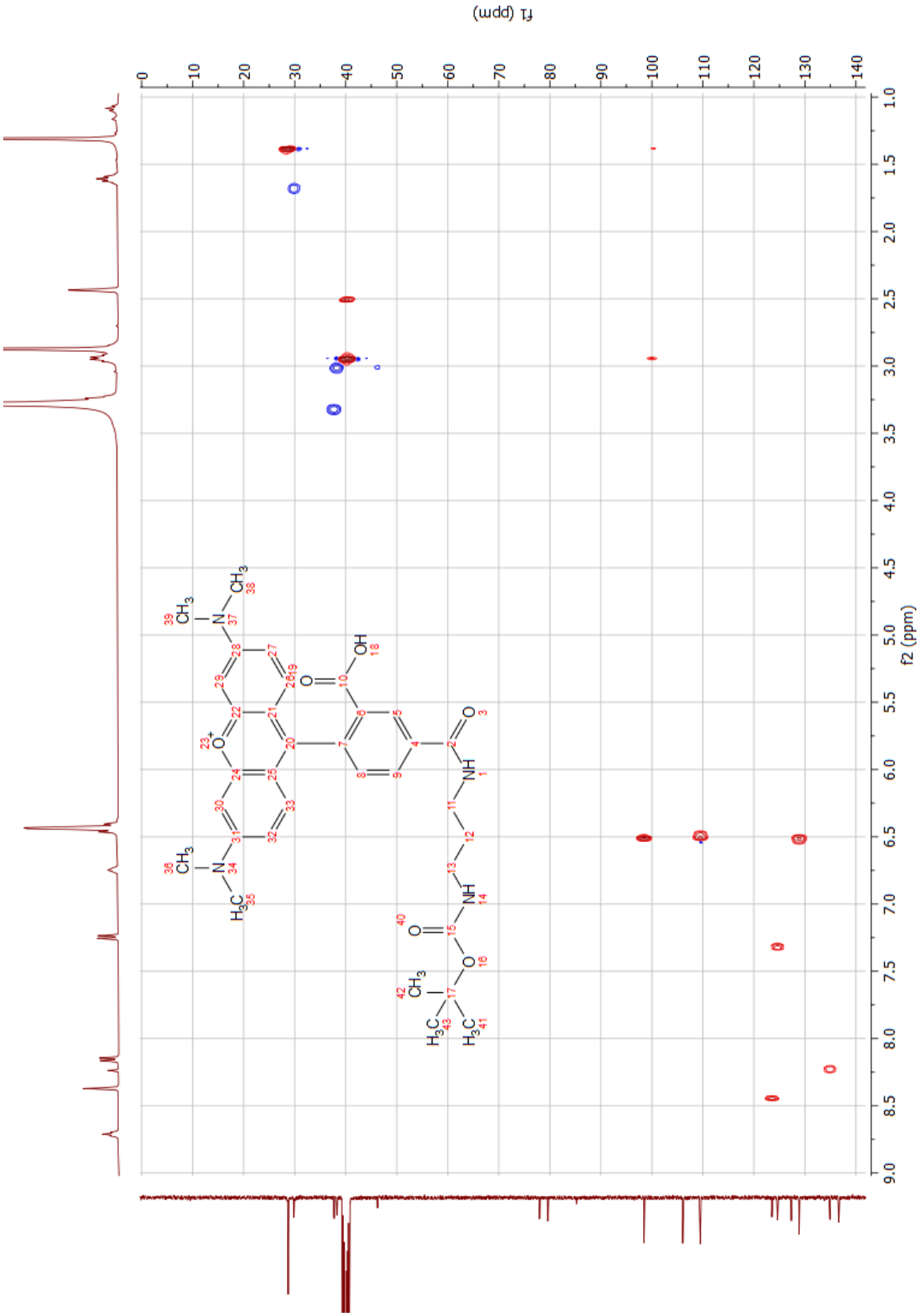

Appendix 24: (**174**) 9-(4-((2-((*Tert*-butoxycarbonyl)amino)propyl)carbamoyl)-2-carboxyphenyl)-3,6-bis(dimethylamino)xanthylium HSQC.

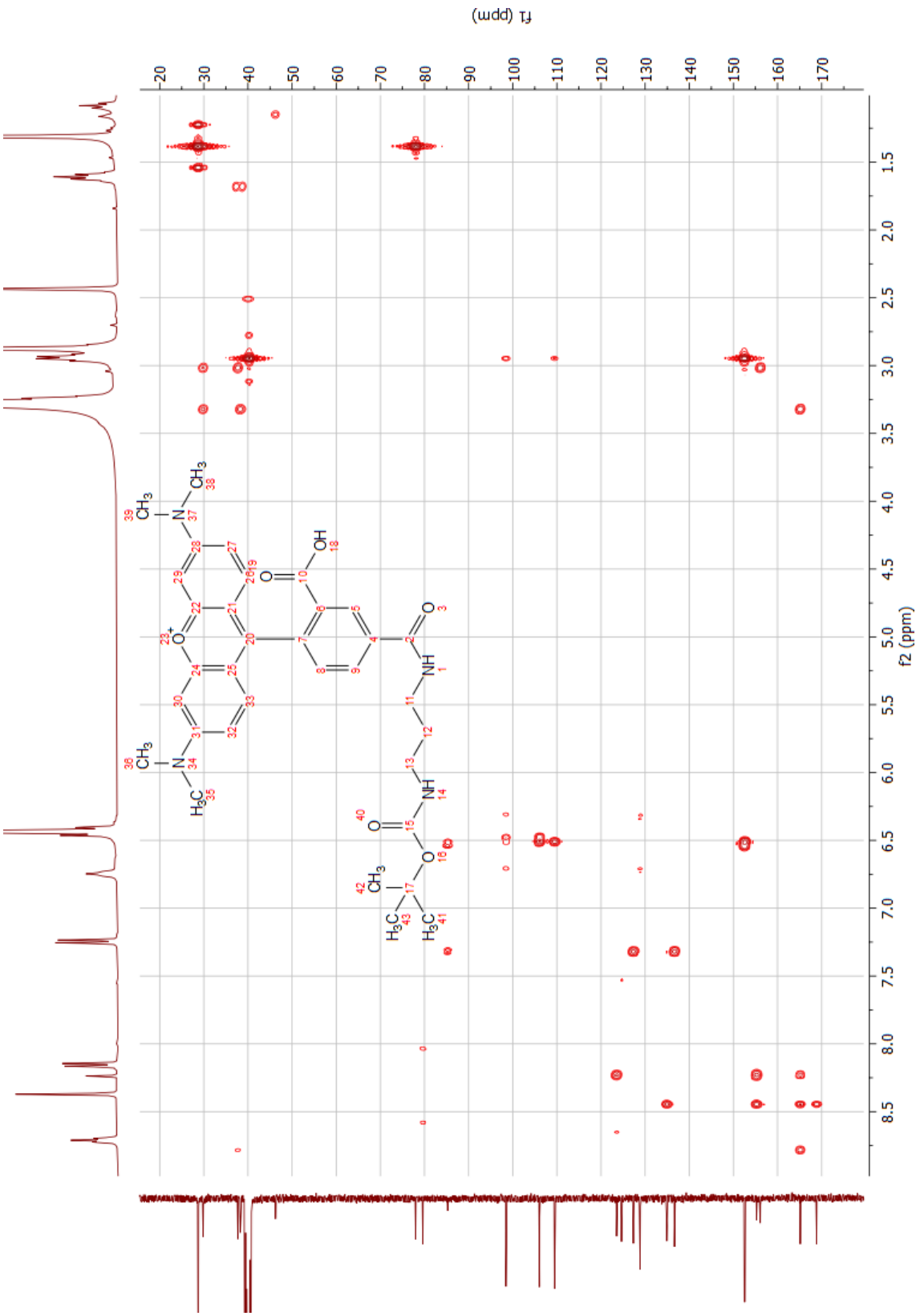

Appendix 25: (**174**) 9-(4-((2-((*Tert*-butoxycarbonyl)amino)propyl)carbamoyl)-2-carboxyphenyl)-3,6-bis(dimethylamino)xanthylium HMBC.

(175) 9-(4-((4-((*Tert*-butoxycarbonyl)amino)butyl)carbamoyl)-2-carboxyphenyl)-3,6-bis(dimethylamino)xanthylium

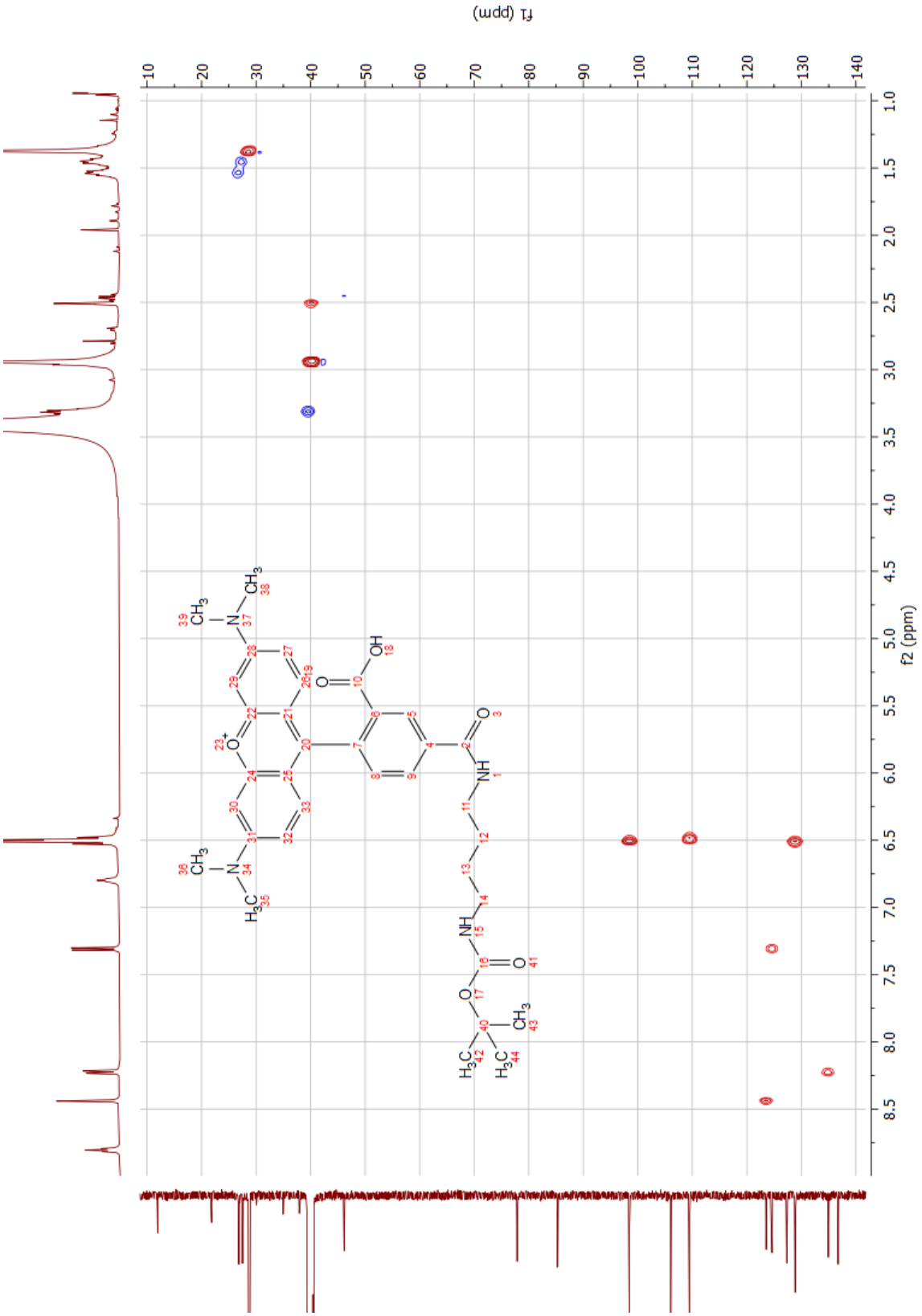

Appendix 26: (**175**) 9-(4-((4-((*Tert*-butoxycarbonyl)amino)butyl)carbamoyl)-2-carboxyphenyl)-3,6-bis(dimethylamino)xanthylium HSQC.

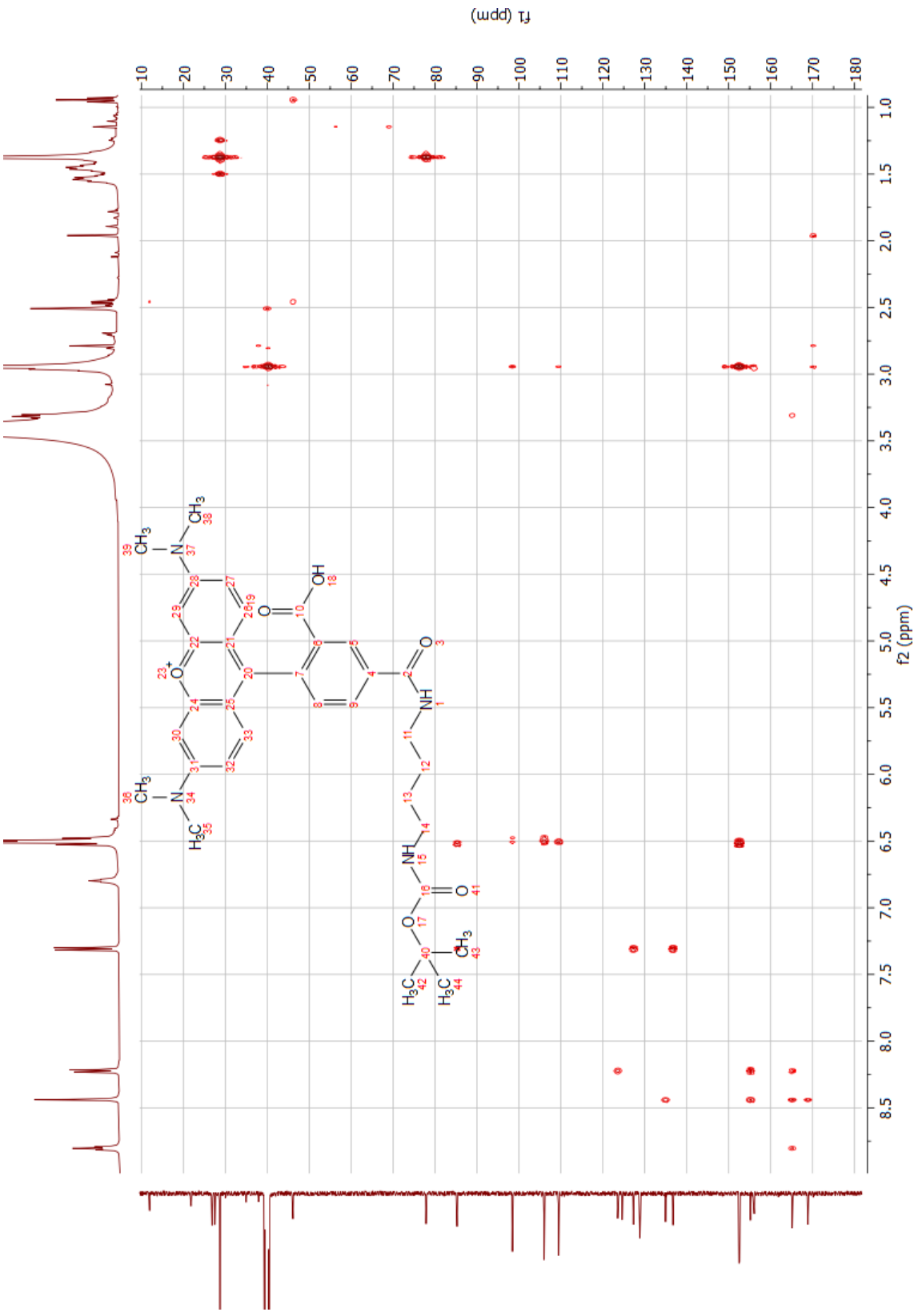

Appendix 27: (**175**) 9-(4-((4-((*Tert*-butoxycarbonyl)amino)butyl)carbamoyl)-2-carboxyphenyl)-3,6-bis(dimethylamino)xanthylium HMBC.

(176) 9-(4-((5-((*Tert*-butoxycarbonyl)amino)pentyl)carbamoyl)-2-carboxyphenyl)-3,6-bis(dimethylamino)xanthylium

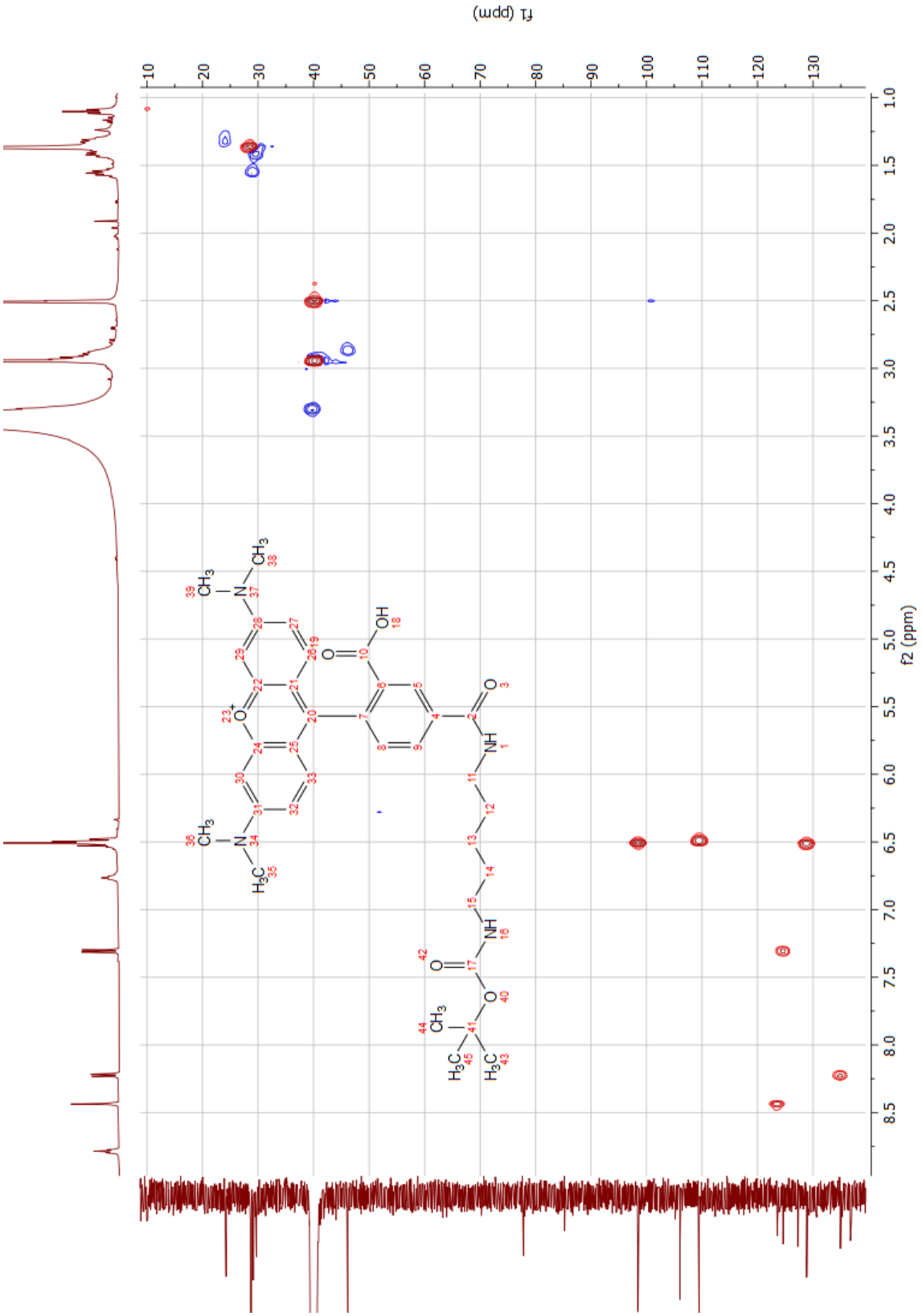

Appendix 28: (**176**) 9-(4-((5-((*Tert*-butoxycarbonyl)amino)pentyl)carbamoyl)-2-carboxyphenyl)-3,6-bis(dimethylamino)xanthylium HSQC.

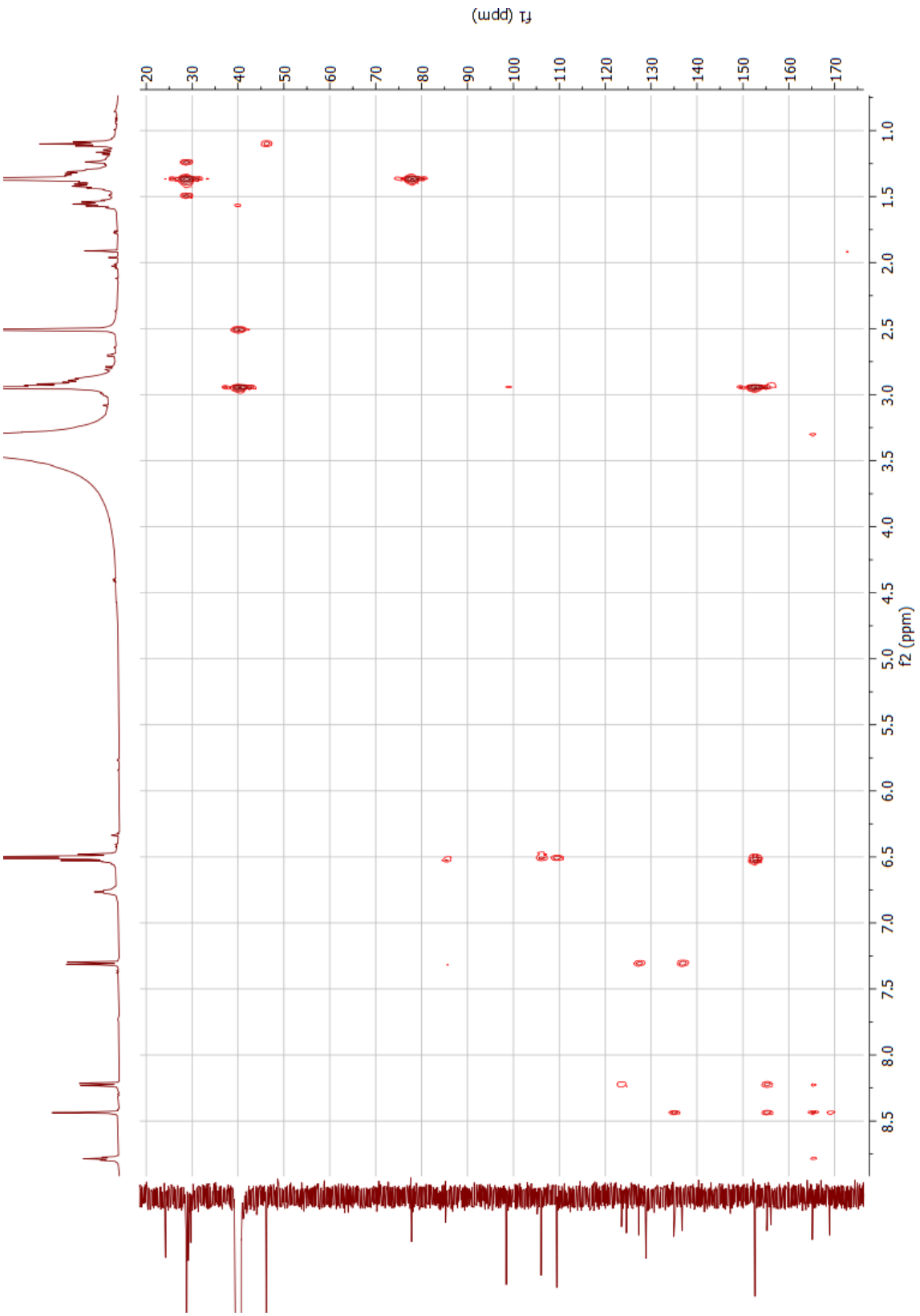

Appendix 29: (**176**) 9-(4-((5-((*Tert*-butoxycarbonyl)amino)pentyl)carbamoyl)-2-carboxyphenyl)-3,6-bis(dimethylamino)xanthylium HMBC.

(177) 9-(4-((6-((*Tert*-butoxycarbonyl)amino)hexyl)carbamoyl)-2-carboxyphenyl)-3,6-bis(dimethylamino)xanthylium

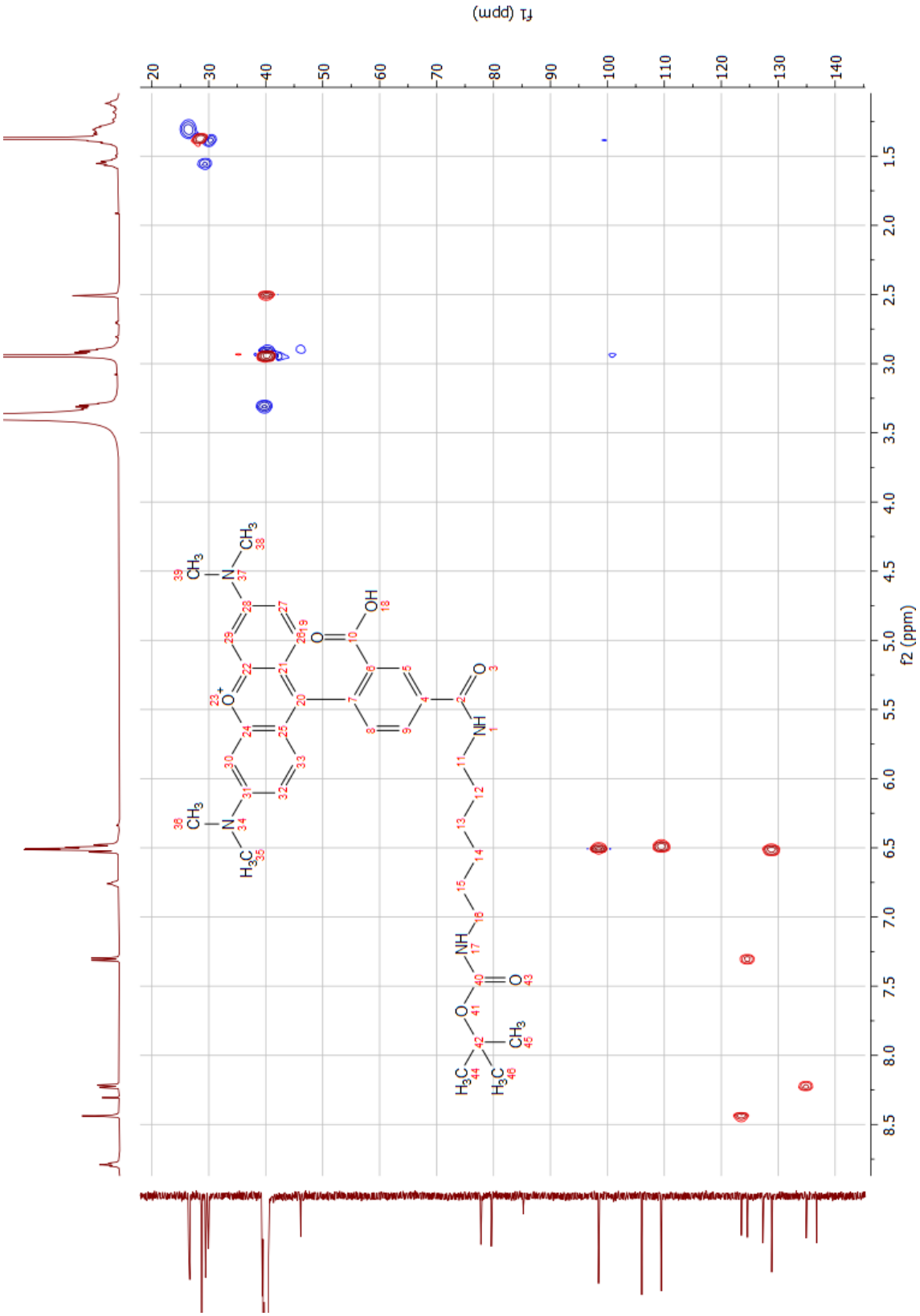

Appendix 30: (**177**) 9-(4-((6-((*Tert*-butoxycarbonyl)amino)hexyl)carbamoyl)-2-carboxyphenyl)-3,6-bis(dimethylamino)xanthylium HSQC.

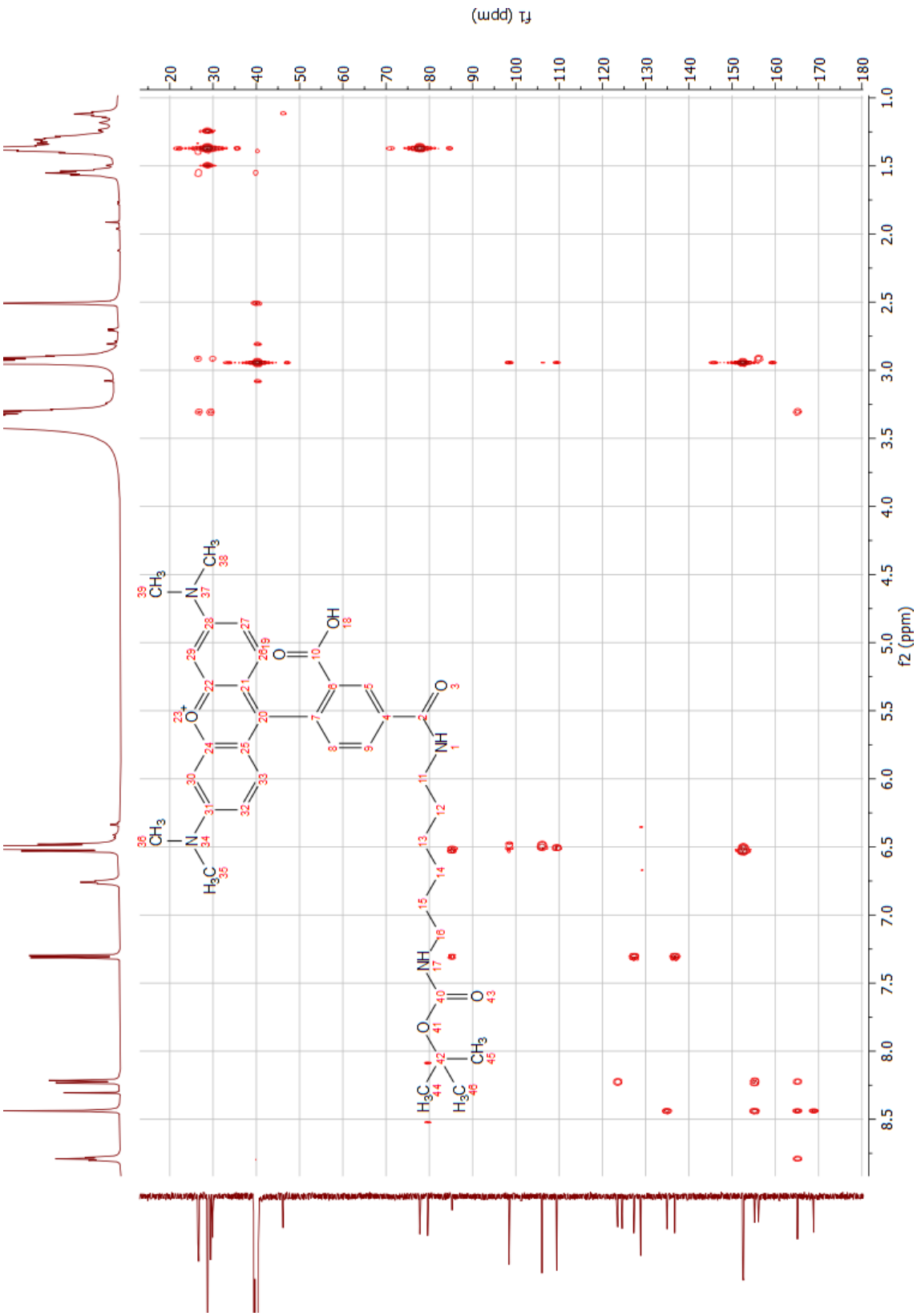

Appendix 31: (**177**) 9-(4-((6-((*Tert*-butoxycarbonyl)amino)hexyl)carbamoyl)-2-carboxyphenyl)-3,6-bis(dimethylamino)xanthylium HMBC.

(178) 9(4((2(2((*Tert*-butoxycarbonyl)amino)ethoxy)ethyl)carbamoyl)-2-carboxyphenyl)-3,6-bis(dimethylamino)xanthylium

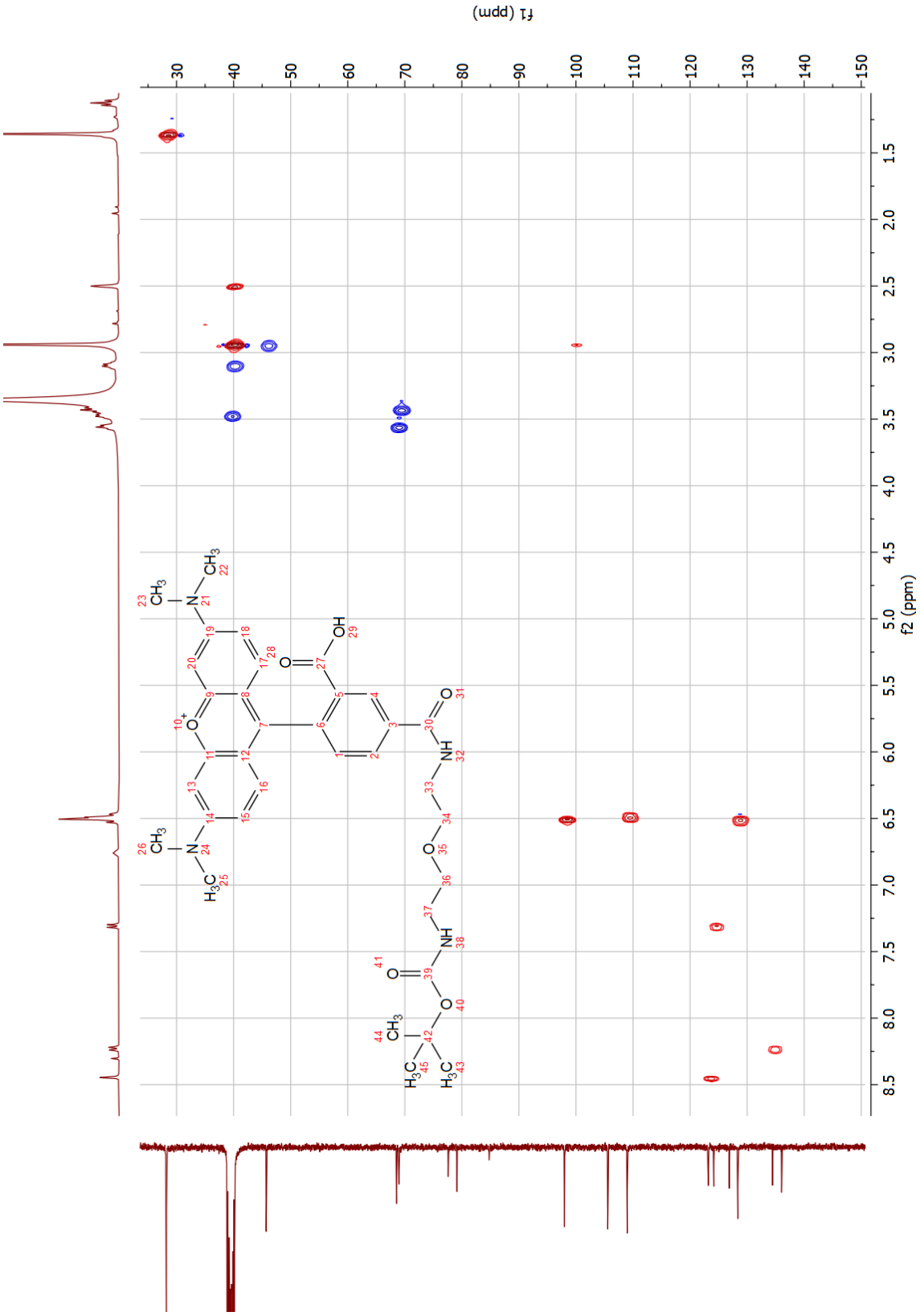

Appendix 32: (**178**) 9(4((2(2((*Tert*-butoxycarbonyl)amino)ethoxy)ethyl)carbamoyl)-2-carboxyphenyl)-3,6-bis(dimethylamino)xanthylium HSQC.

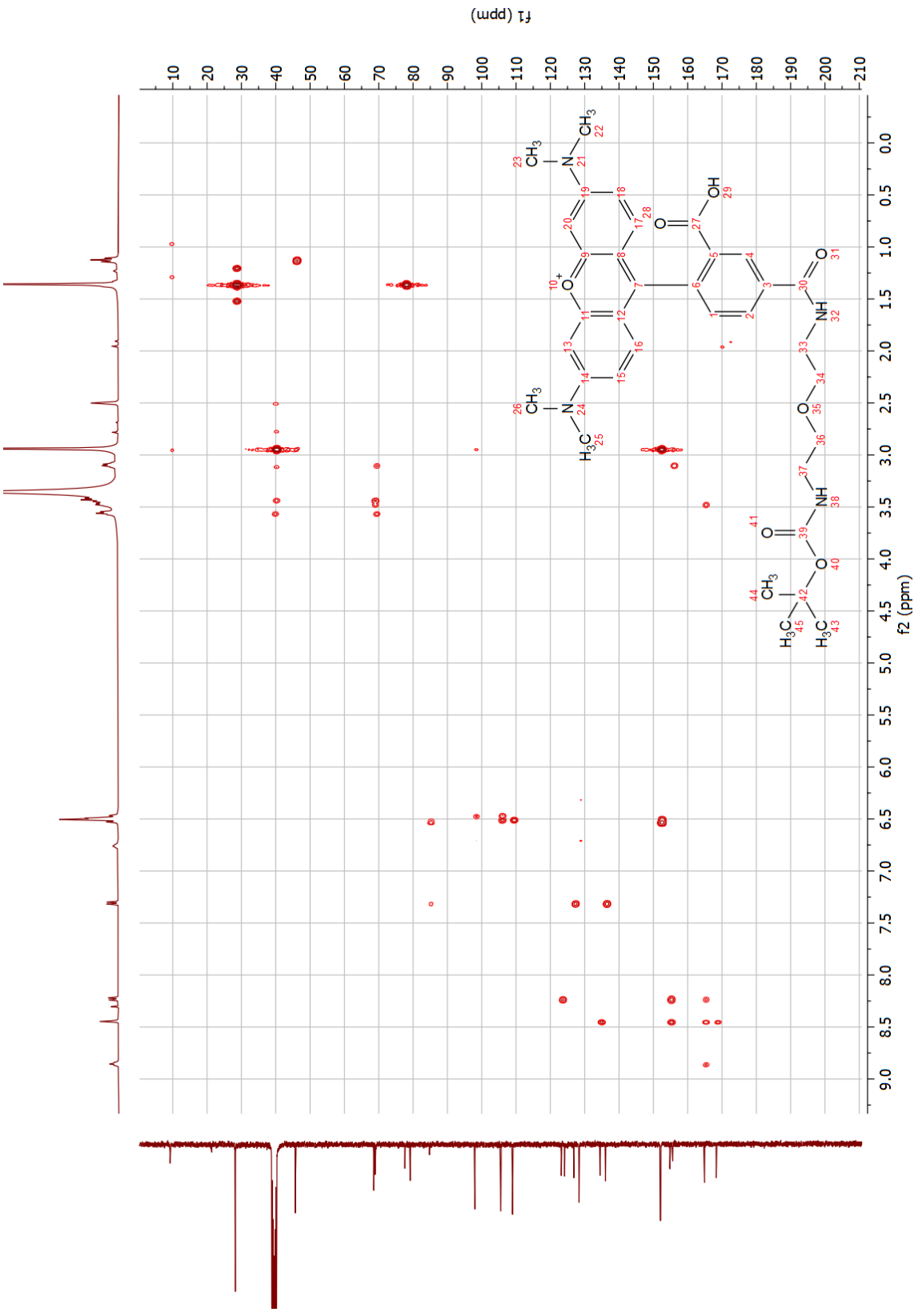

Appendix 33: (**178**) 9(4((2(2((*Tert*-butoxycarbonyl)amino)ethoxy)ethyl)carbamoyl)-2-carboxyphenyl)-3,6-bis(dimethylamino)xanthylium HMBC.

(179) 9-(2-Carboxy-4-((2,2-dimethyl-4-oxo-3,8,11-trioxa-5-aza-tridecan-13-yl)carbamoyl)phenyl)-3,6-bis(dimethylamino)xanthylium

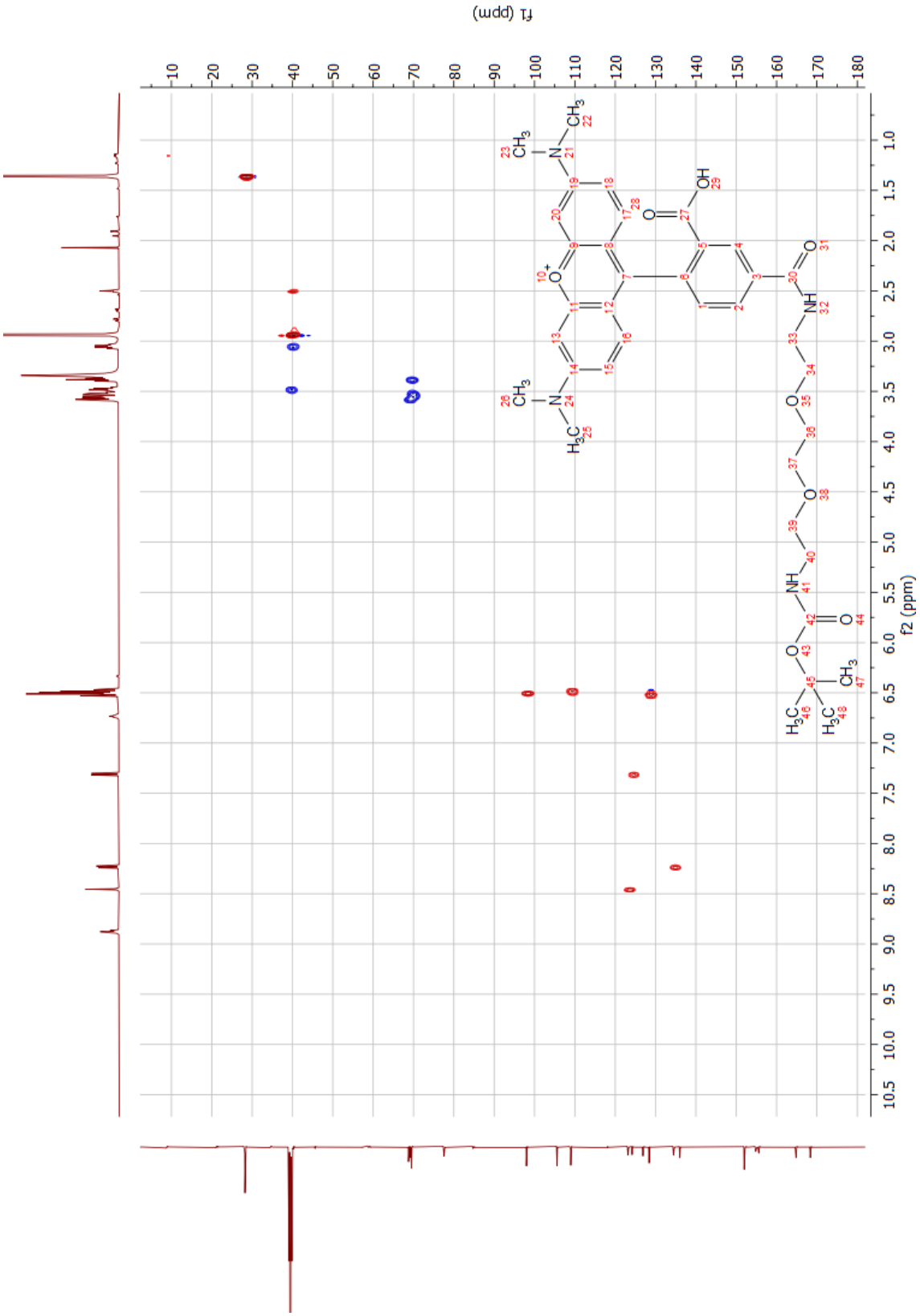

Appendix 34: (**179**) 9-(2-Carboxy-4-((2,2-dimethyl-4-oxo-3,8,11-trioxa-5-azatridecan-13-yl)carbamoyl)phenyl)-3,6-bis(dimethylamino)xanthylium HSQC.

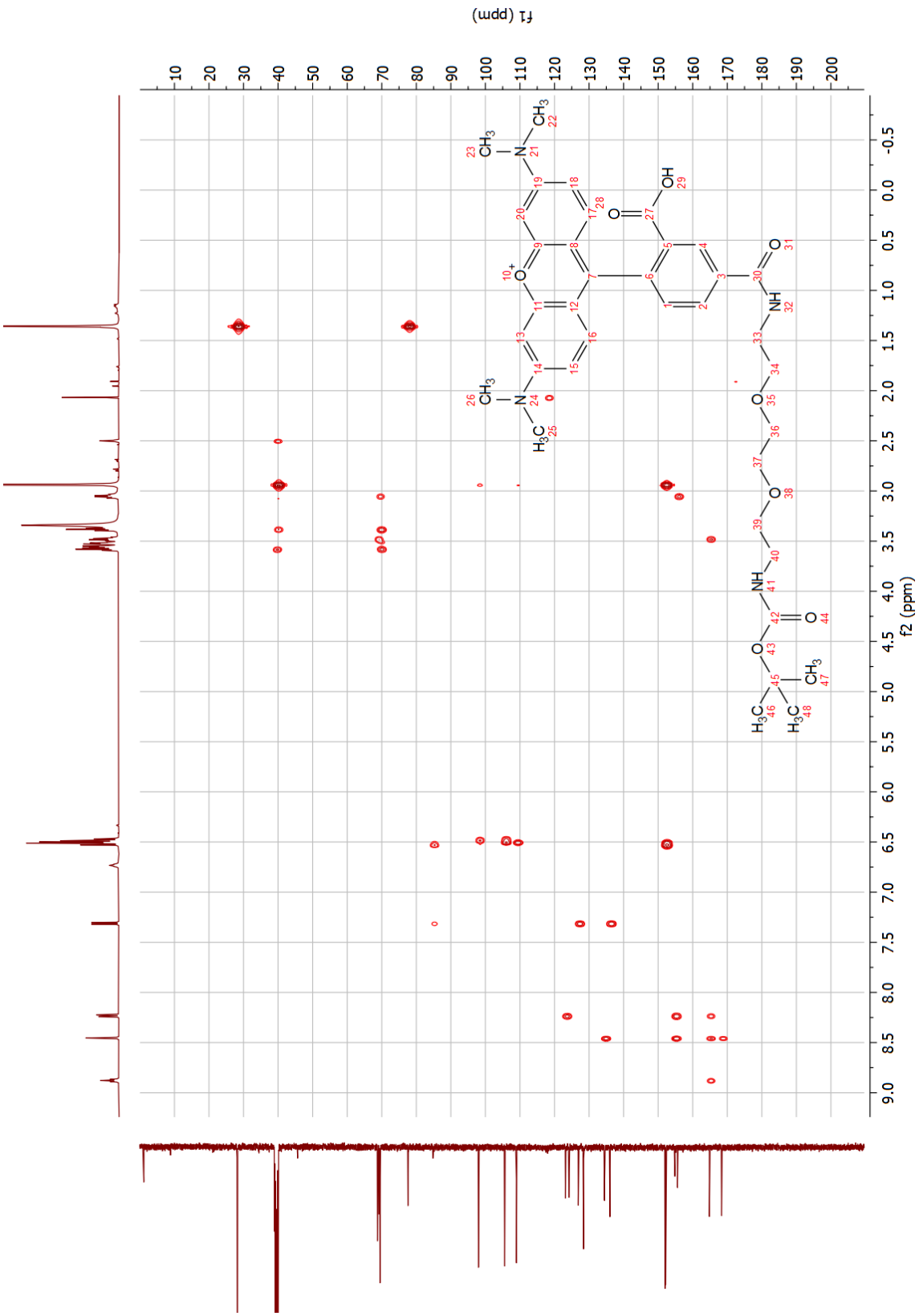

Appendix 35: (**179**) 9-(2-Carboxy-4-((2,2-dimethyl-4-oxo-3,8,11-trioxa-5-azatridecan-13-yl)carbamoyl)phenyl)-3,6-bis(dimethylamino)xanthylium HMBC.

(180) 9-(2-Carboxy-4-((2,2-dimethyl-4-oxo-3,9,12,15-tetraoxa-5-azaoctadecan-18-yl)carbamoyl)phenyl)-3,6-bis(dimethylamino)-xanthylium

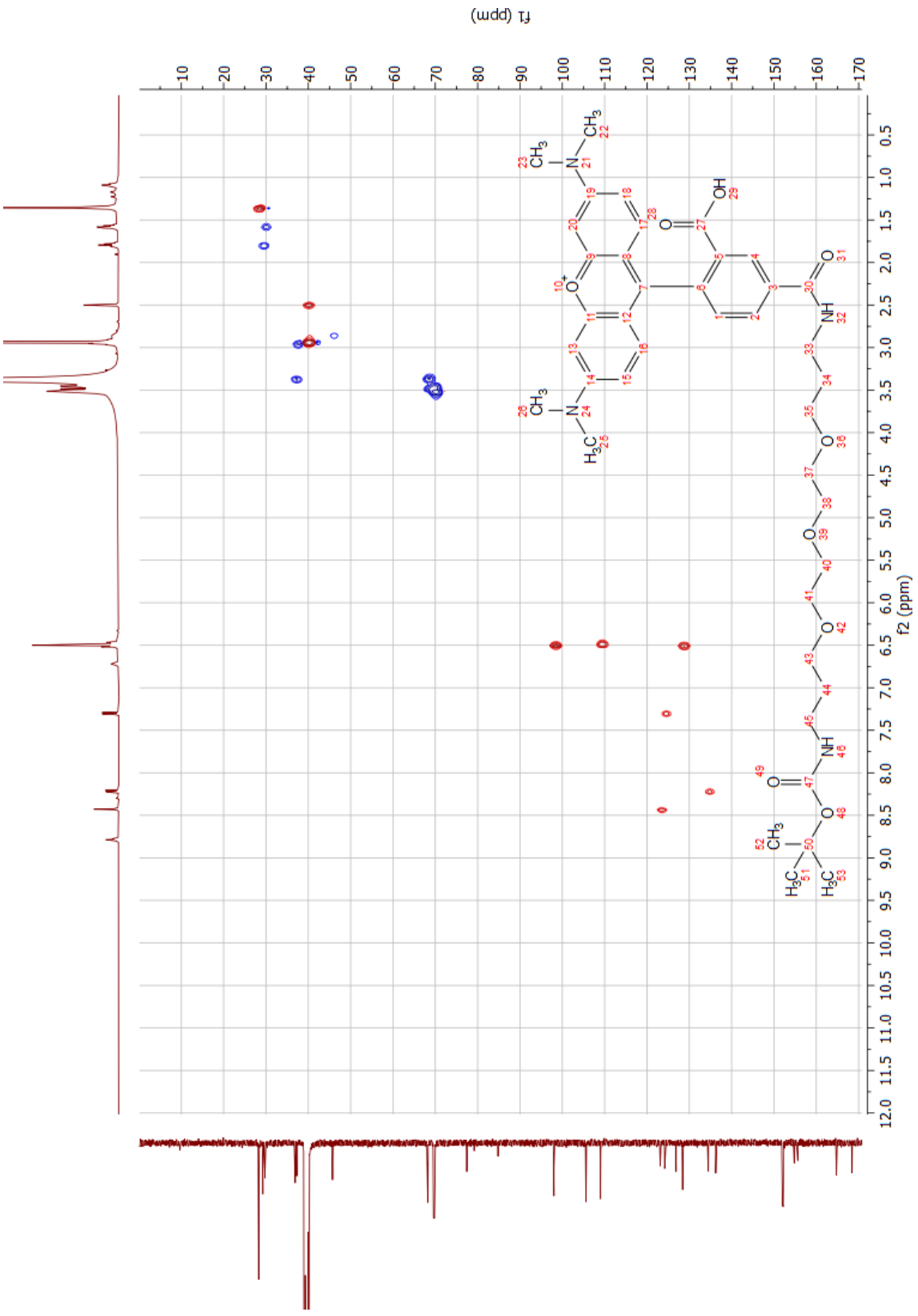

Appendix 36: (**180**) 9-(2-Carboxy-4-((2,2-dimethyl-4-oxo-3,9,12,15-tetraoxa-5-aza-octadecan-18-yl)carbamoyl)phenyl)-3,6-bis(dimethylamino)xanthylium HSQC.

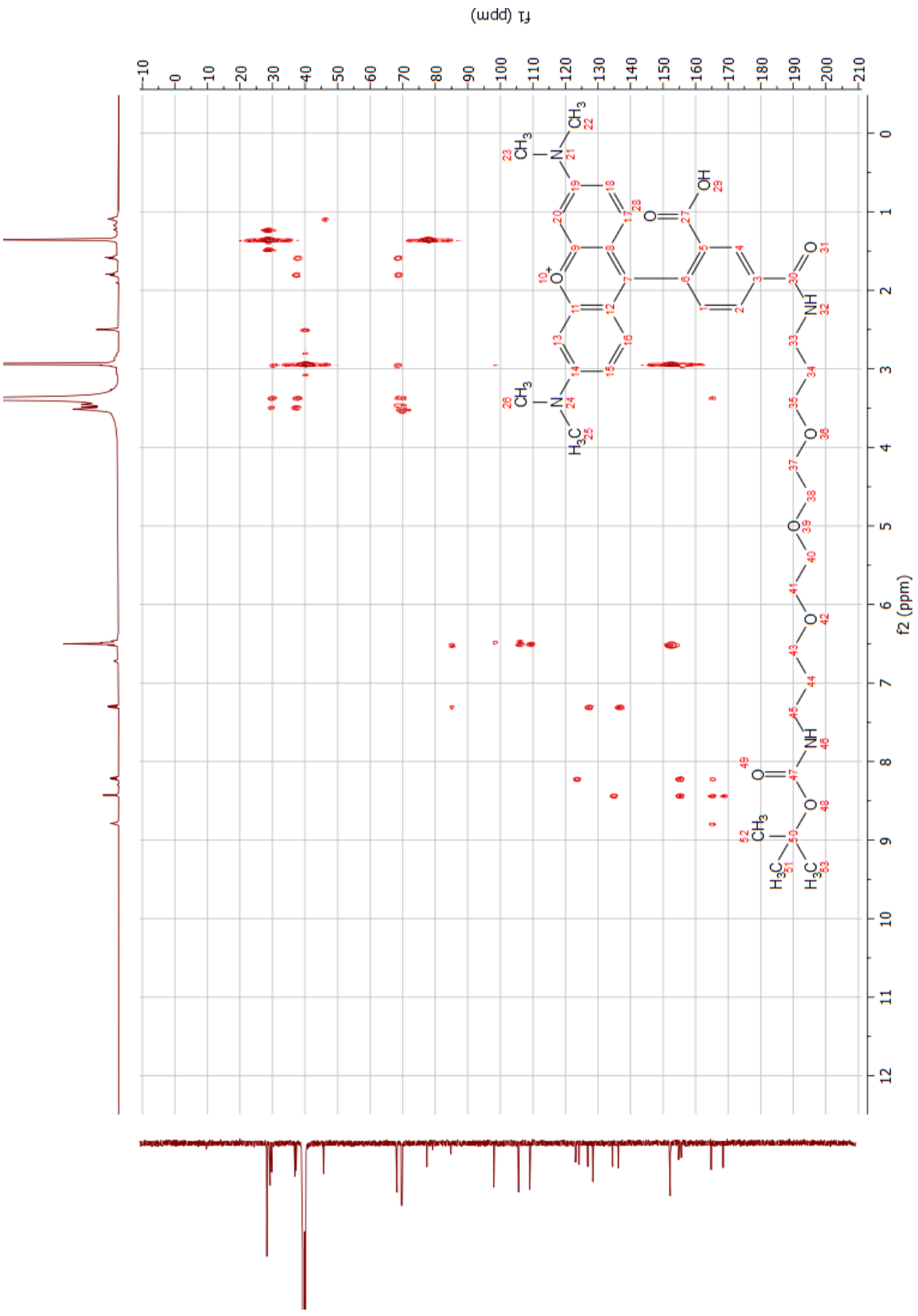

Appendix 37: (**180**) 9-(2-Carboxy-4-((2,2-dimethyl-4-oxo-3,9,12,15-tetraoxa-5-aza-octadecan-18-yl)carbamoyl)phenyl)-3,6-bis(dimethylamino)xanthylium HMBC.

Selected HPLC chromatograms and spectra

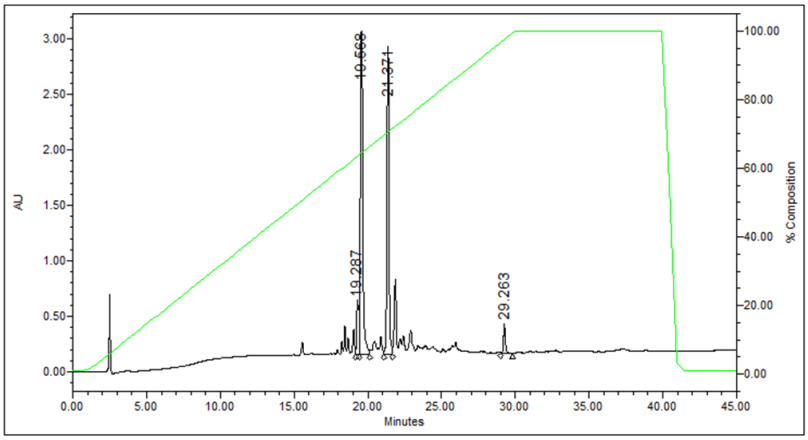

Peak information			
	RT	Area	% Area
1	19.287	5123409	7.22
2	19.568	36508284	51.43
3	21.371	27029221	38.07
4	29.263	2330116	3.28

(a)

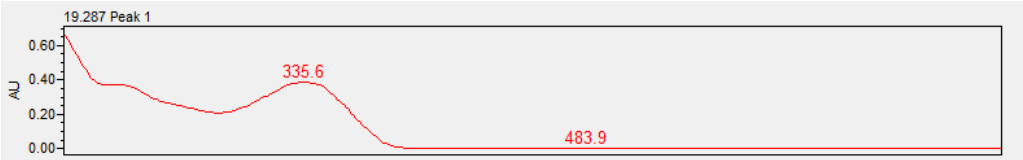

(b)

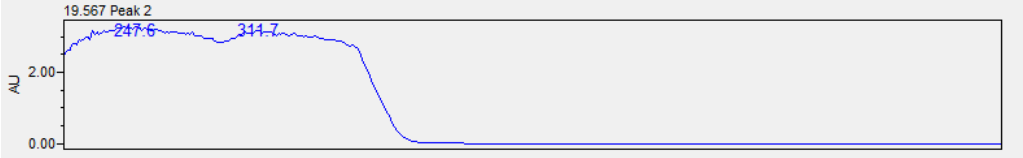

(c)

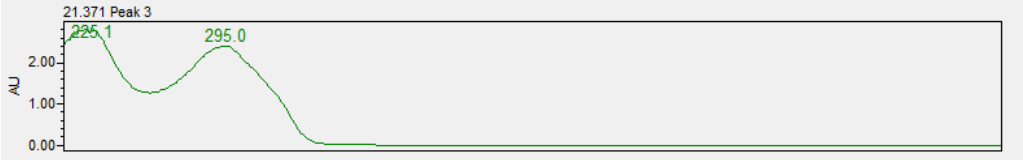

(d)

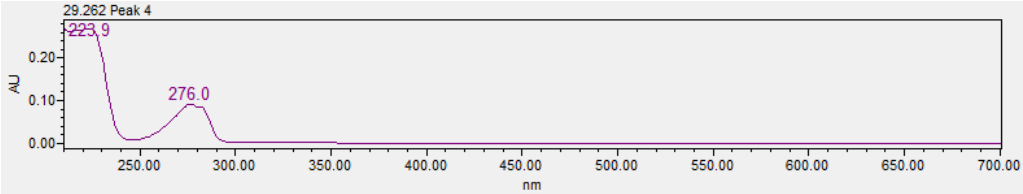

(e)

Appendix 38: HPLC analysis of compound **163**. Eluent: 10-100% A in B. A = MeCN + 0.1% TFA, B = H2O + 0.1% TFA. (a) Chromatogram at 220 nm; (b) Spectrum of analyte at t_R = 19.287 min; (c) Spectrum of analyte at t_R = 19.567 min; (d) Spectrum of analyte at t_R = 21.371 min; (e) Spectrum of analyte at t_R = 29.262 min.

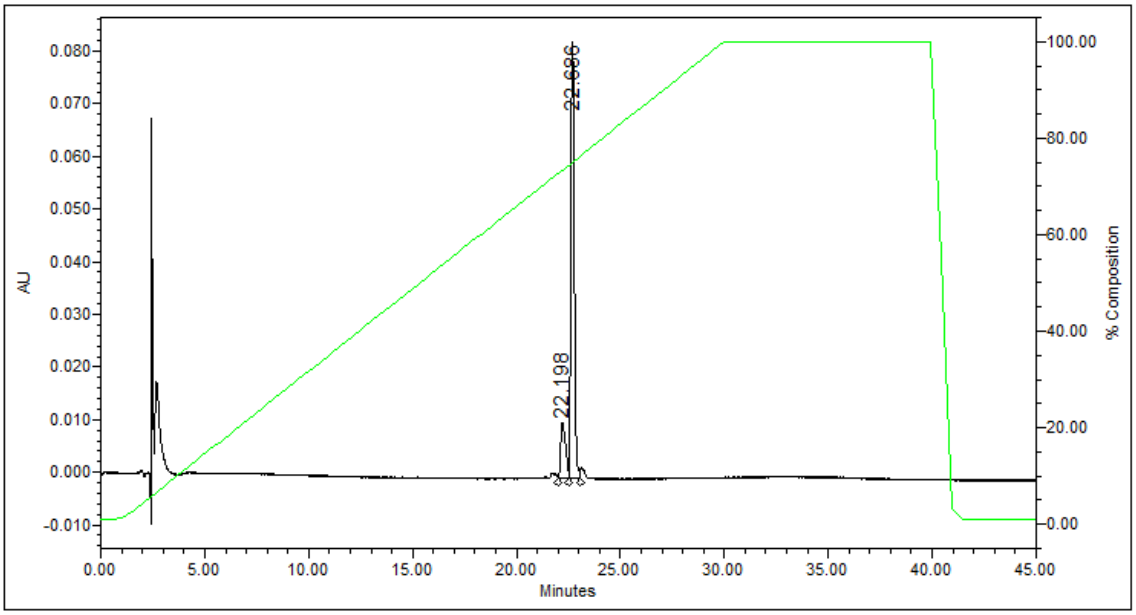

Peak information

	RT	Area	% Area
1	22.198	172616	15.07
2	22.686	972591	84.93

(a)

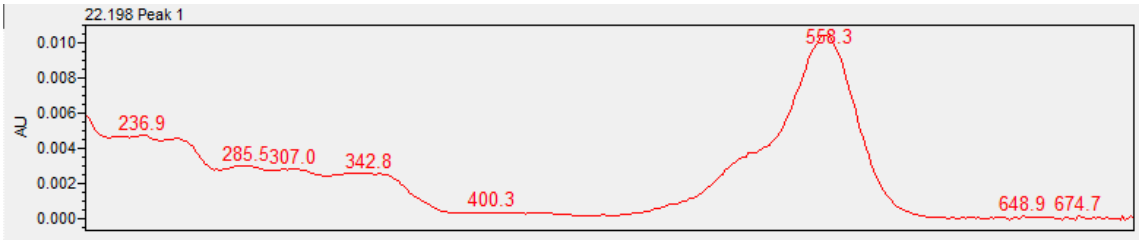

(b)

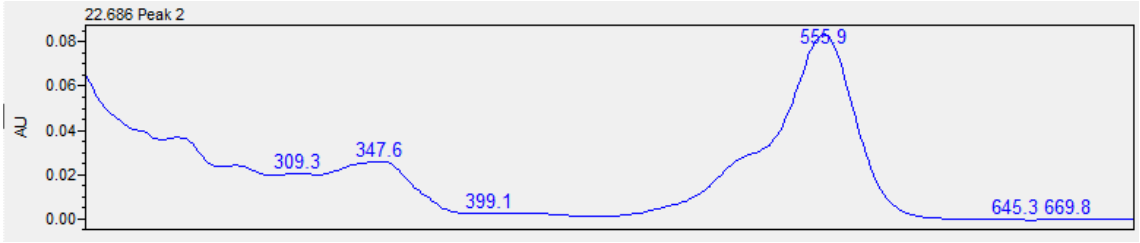

(c)

Appendix 39: HPLC analysis of compound **72**. Eluent: 10-100% A in B. A = MeCN + 0.1% TFA, B = H2O + 0.1% TFA. (a) Chromatogram at 220 nm; (b) Spectrum of analyte at t_R = 22.198 min; (c) Spectrum of analyte at t_R = 22.686 min.

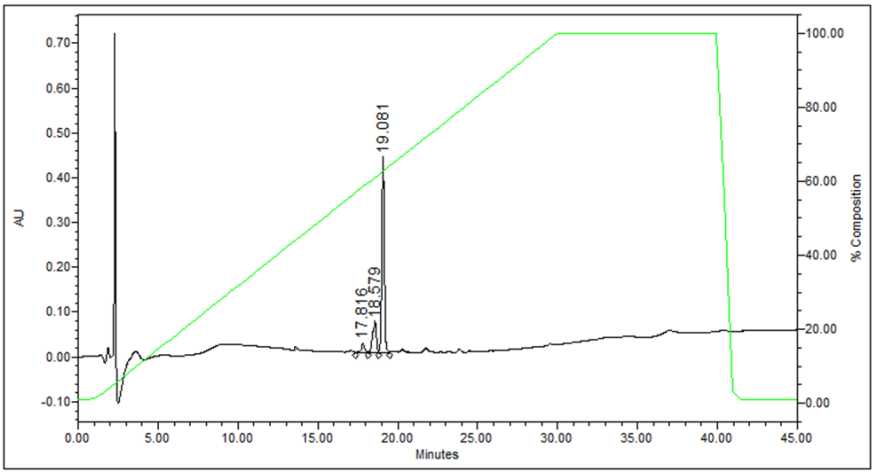

Peak information

	RT	Area	% Area
1	17.816	251661	4.36
2	18.579	1069127	18.52
3	19.081	4452673	77.12

(a)

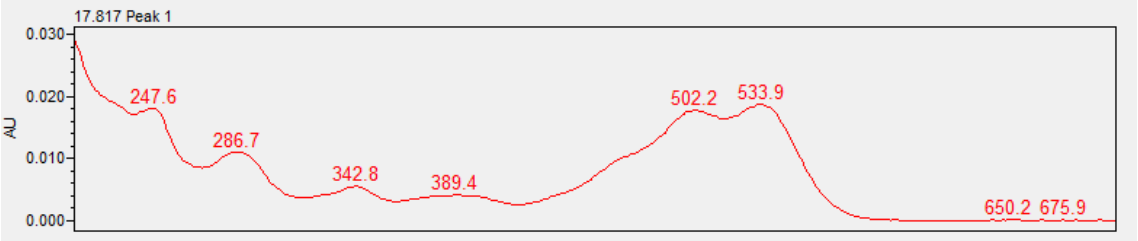

(b)

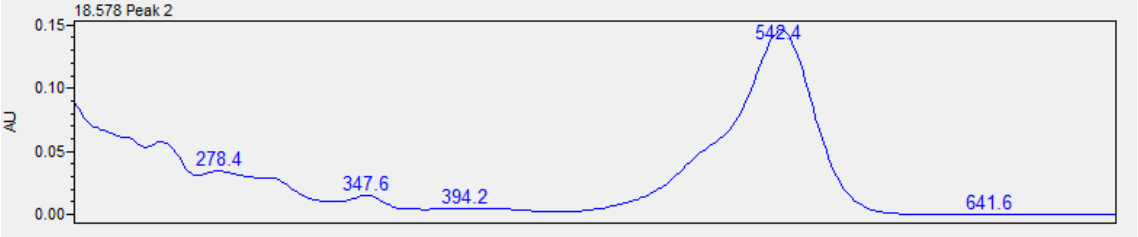

(c)

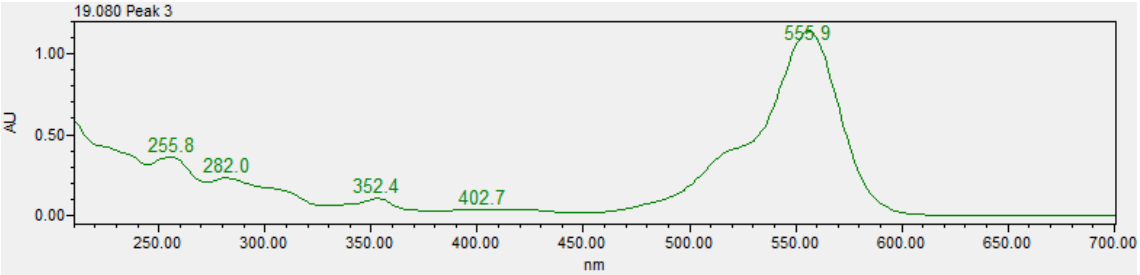

(d)

Appendix 40: HPLC analysis of compound **173**. Eluent: 10-100% A in B. A = MeCN + 0.1% TFA, B = H2O + 0.1% TFA. (a) Chromatogram at 220 nm; (b) Spectrum of analyte at t_R = 17.817 min; (c) Spectrum of analyte at t_R = 18.578 min; (d) Spectrum of analyte at t_R = 19.080 min.

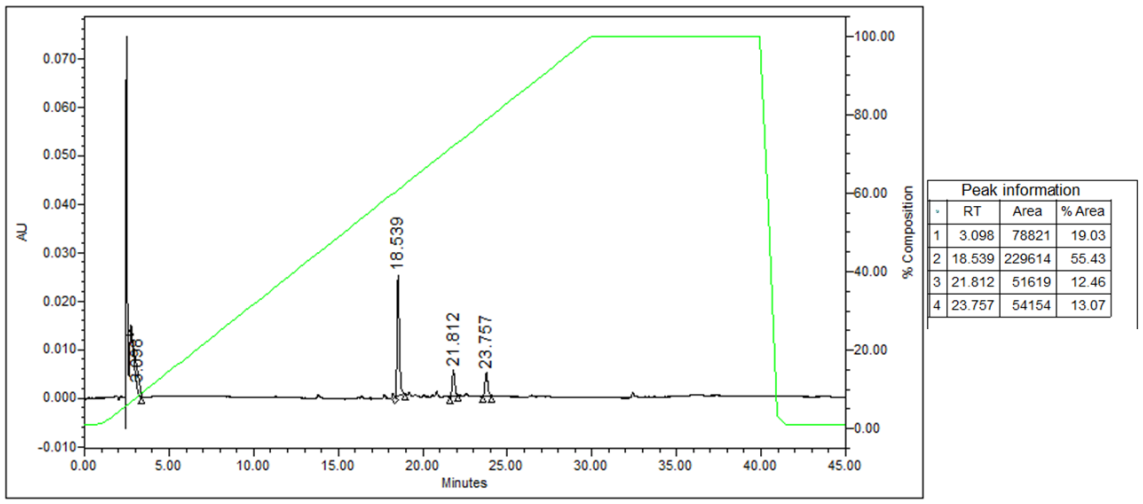

(a)

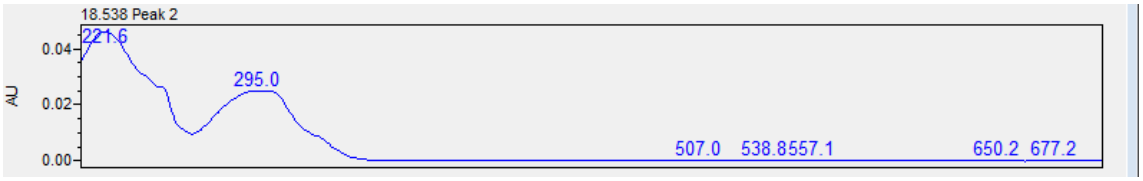

(b)

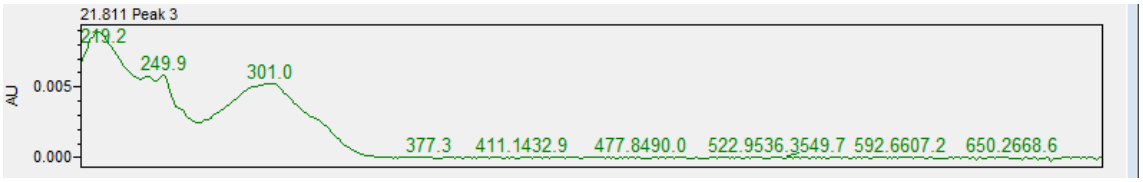

(c)

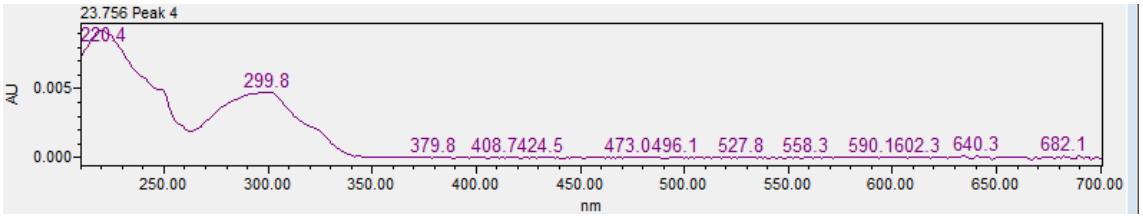

(d)

Appendix 41: HPLC analysis of compound **181**. Eluent: 10-100% A in B. A = MeCN + 0.1% TFA, B = H2O + 0.1% TFA. (a) Chromatogram at 220 nm; (b) Spectrum of analyte at t_R = 18.538 min; (c) Spectrum of analyte at t_R = 21.811 min; (d) Spectrum of analyte at t_R = 23.756 min.

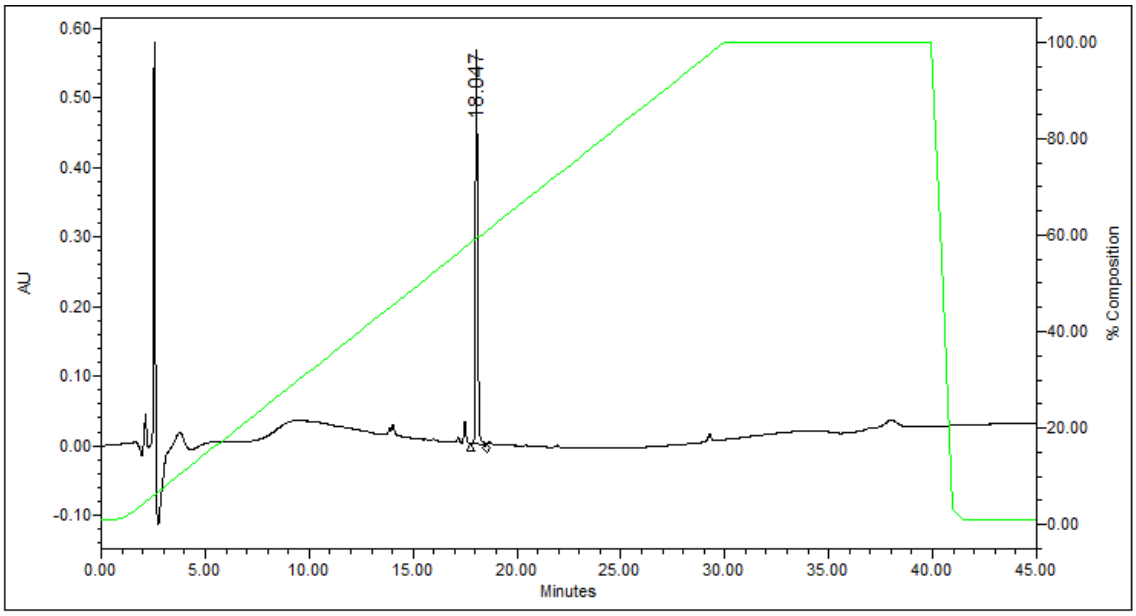

Peak information

	RT	Area	% Area
1	18.047	3918613	100.00

Appendix 42: HPLC analysis of compound **166**, chromatogram of analyte at 220nm.

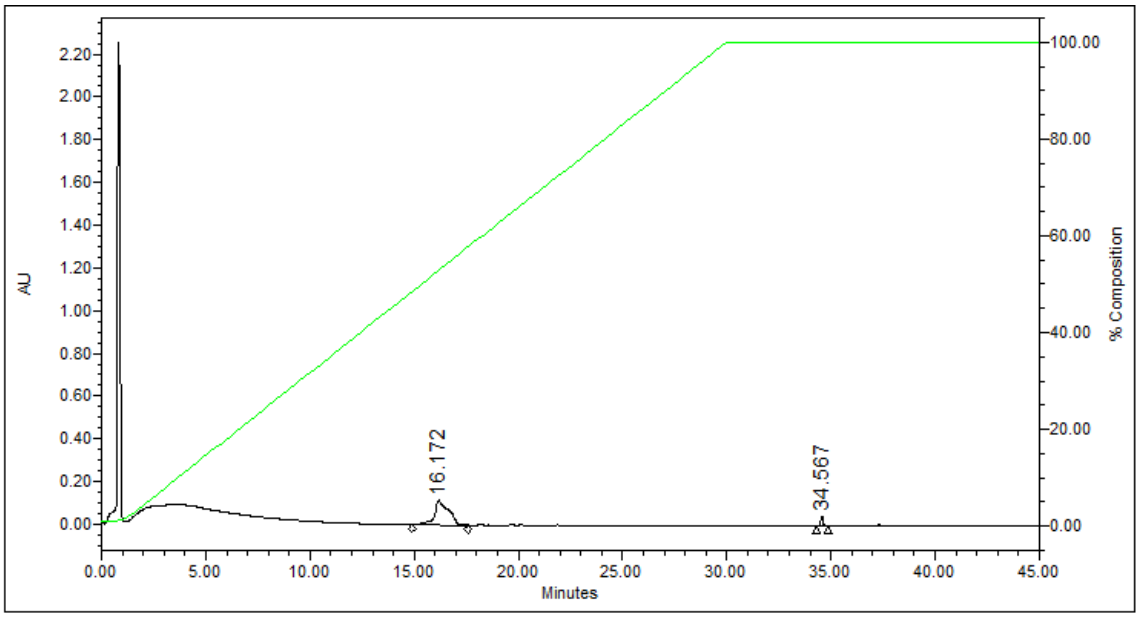

Peak information

	RT	Area	% Area
1	16.172	5443795	94.24
2	34.567	332953	5.76

(a)

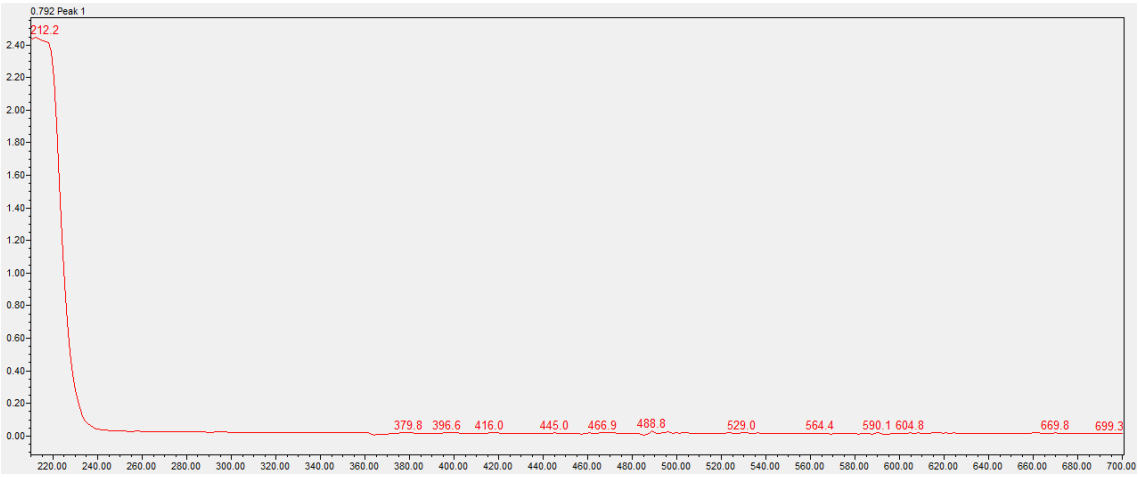

(b)

(c)

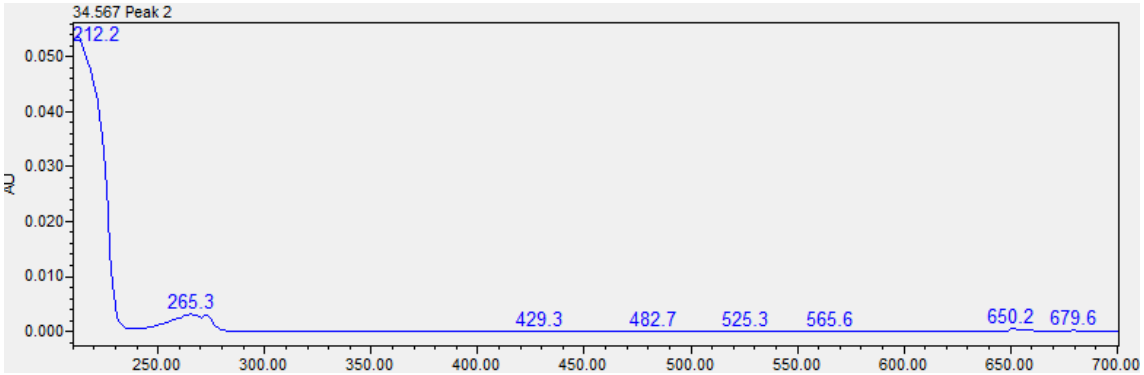

(d)

Appendix 43: HPLC analysis of compound **73**. Eluent: 10-100% A in B. A = MeCN + 0.1% NH_4OH, B = H2O + 0.1% NH_4OH. (a) Chromatogram at 220 nm; (b) Spectrum of analyte at t_R = 0.792 min; (c) Spectrum of analyte at t_R = 16.172 min; (d) Spectrum of analyte at t_R = 34.567 min